

UNIVERSIDADE FEDERAL DE SÃO CARLOS
CENTRO DE CIÊNCIAS EXATAS E DE TECNOLOGIA
DEPARTAMENTO DE QUÍMICA
PROGRAMA DE PÓS-GRADUAÇÃO EM QUÍMICA

**“NANOESTRUCTURED CATALYSTS FOR ORGANIC REACTIONS:
DESIGN, SYNTHESIS AND APPLICATIONS”**

Carolina Guimarães de Souza Lima*

Tese apresentada como parte dos requisitos
para obtenção do título de DOUTORA EM
CIÊNCIAS, área de concentração:
QUÍMICA ORGÂNICA.

Orientador: Prof. Dr. Márcio Weber Paixão

*** bolsista CAPES**

**São Carlos - SP
2016**



UNIVERSIDADE FEDERAL DE SÃO CARLOS

Centro de Ciências Exatas e de Tecnologia
Programa de Pós-Graduação em Química

Folha de Aprovação

Assinaturas dos membros da comissão examinadora que avaliou e aprovou a Defesa de Tese de Doutorado da candidata Carolina Guimarães de Souza Lima, realizada em 29/07/2016:

Prof. Dr. Márcio Weber Paixão
UFSCar

Profa. Dra. Arlene Gonçalves Corrêa
UFSCar

Prof. Dr. Jean Marcel Ribeiro Gallo
UFSCar

Prof. Dr. Igor Polikarpov
USP

Prof. Dr. Luiz Carlos da Silva Filho
UNESP

“Life is not easy for any of us. But what of that? We must have perseverance and above all, confidence in ourselves. We must believe that we are gifted for something and that this thing must be attained.”

Marie Curie

To my husband Thiago and my family.

Acknowledgements

Foremost, I would like to thank my family, especially my mother, Terezinha, which had to be simultaneously my mother and father, and taught me values that will be with me forever.

I also would like to express my gratitude towards my husband, Thiago, who was both my partner in life and in the PhD studies, for having taught me and incentivized me to learn key concepts not only in catalysis and material science, but also in life. Additionally, I thank him for all the help in the development of the experimental work described in Chapters 3 and 4.

Someone once said that "The mediocre teacher tells, the good teacher explains, the superior teacher demonstrates and the great teacher inspires", and, in this spirit, I can say that my supervisor, Prof. Márcio Paixão, was to me a great teacher, for he inspired me to always achieve more. He accepted me without being sure of what I knew and what I could accomplish, and for that I will be always grateful.

I also thank Prof. Rajender Varma and Radek Zboril for their kind supervision during my research stage at the Regional Centre of Advanced Technologies and Materials (RCPTM) of the Palacky University at Olomouc, Czech Republic, as well as the friends I have met there and whom immensely helped me, namely Veronika, Claudia, Josena, Mr. Datta, Ananda, Anuj and Manoj.

My sincere thanks also go to Prof. Arlene Correa, director of the Centre of Excellence for Research in Sustainable Chemistry (CERSusChem), for being such a great teacher and always pleasant to be around; the gatherings at her home at all times made everyone feel welcome and a truthful part of the group.

I also acknowledge Prof. Ricardo Schwab, who was also a part of interesting discussions and provided ideas that helped in the development of this work. Likewise, I thank the fellows of CERSusChem, who made this journey

much more exciting. I learned a little bit with single every one of them, and they have helped me to become a better person and a better chemist: Sandrina (who selflessly taught me so much and helped me to give my first steps in organic synthesis), Floyd Andrade, Julia Monteiro, Karla Feu, Lucas Pozzi, Deborah Araújo, Alexander de la Torre, Lucas Cursino, Rodrigo César, Akbar Ali, Gustavo Piva, Bianca Matsuo and all of the other friends in the lab.

My thanks correspondingly go to CAPES, which provided the fellowships for my PhD studies at UFSCar and for the research period abroad, an experience that enriched me as a person and as a researcher.

Additionally, I earnestly acknowledge the members of the evaluating committee, Prof. Dr. Arlene G. Correa, Prof. Dr. Jean M. R. Gallo, Dr. Luiz Carlos da Silva-Filho and Prof. Dr. Igor Polikarpov for their comments and their invaluable contributions for the final version of this work.

Last but not least, I would like to thank all professors and workers of UFSCar that somehow contributed to the development of the work reported in this thesis, specially Prof. Edson Leite, whom helped in the characterization of the niobium nanocatalyst.

List of Abbreviations

5-HMF	5-Hydroxymethylfurfural
AL	Alkyl Levulinate
ANO	Ammonium Niobate(V) Oxalate
BL	2-Butyl Levulinate
GC	Gas Chromatography
CTAC	Cetyltrimethylammonium Chloride
DABCO	1,4-Diazabicyclo[2.2.2]octane
DES	Deep Eutectic Solvent
DHP	1,4-Dihydropyridine
DHPM	3,4-Dihydropyrimidinone
DLS	Dynamic Light Scattering
DMF	Dimethylfurane
DMSi	Dentritic Mesoporous Silica
DMSO	Dimethylsulfoxide
DPO	5,5-Diethoxypentan-2-one
EDS	Energy-Dispersive X-Ray Spectroscopy
EL	Ethyl Levulinate
FDA	5-Hydroxymethylfurfuryl Alcohol
FDCA	2,5-Furandicarboxylic Acid
FE	2-Propylfurfuryl Ether
FID	Flame Ionization Detector

FT-IR	Fourier Transform Infrared Spectroscopy
FUR	Furfural
FWHM	Full Width at Half Maximum
GVL	γ -Valerolactone
HAADF	High-Angle Annular Dark-Field Imaging
HR-TEM	High-Resolution Transmission Electron Microscopy
ICP-OES	Inductively Coupled Plasma - Optical Emission Spectrometry
LA	Levulinic Acid
MCM	Mobil Composition of Matter
MCR	Multicomponent Reaction
MPTMS	(3-Mercaptopropyl)trimethoxysilane
MPV	Meerwein–Ponndorf–Verley
MS	Mass Spectrometry
MSU	Michigan State University
MTHF	2-Methyltetrahydrofuran
NMR	Nuclear Magnetic Resonance
PDDA	Poly(diallyldimethylammonium chloride)
PL	2-Propyl Levulinate
SBA-15	Santa Barbara-15
SQUID	Superconducting Quantum Interference Device
STEM	Scanning Transmission Electron Microscopy
TCD	Thermal Conductivity Detector
TEA	Triethanolamine

TEM	Transmission Electron Microscopy
TEOS	Tetraethyl Orthosilicate
TG	Thermogravimetric Analysis
TMS	Tetramethylsilane
TPD	Temperature-Programmed Desorption
VSM	Vibrating Sample Magnetometer
XPS	X-Ray Photoelectron Spectroscopy
XRD	X-Ray Diffraction

List of Tables

TABLE 1.1 - Comparison between homogeneous and heterogeneous catalysis..	5
TABLE 1.2 - General features of the methods used to synthesize magnetic nanoparticles.	14
TABLE 2.1 - Optimization of the reaction conditions for the synthesis of DHPMs via Biginelli reaction.	51
TABLE 2.2 Amount of each nanocatalyst employed in the catalyst evaluation reactions.	64
TABLE 3.1 - Position of the bands in the infrared spectra of pyridine absorbed over the magnetically recoverable zeolite catalyst.	99
TABLE 3.2 - Values of the Mössbauer hyperfine parameters, derived from the least-square fitting of the room-temperature ^{57}Fe Mössbauer spectrum, where δ is the isomer shift, ΔE_Q is the quadrupole splitting, B_{hf} is the hyperfine magnetic field, and RA is the relative spectral area of individual spectral components identified during fitting. T-sites denote the tetrahedral cation sites in the crystal structure of Fe_3O_4 (of inverse spinel type) and O-sites stand for the octahedral cation sites in the crystal structure of Fe_3O_4	101
TABLE 4.1 - Textural properties of the silica nanospheres and the functionalized materials.	127

List of Figures

FIGURE 1.1 - Number of papers and citations published on nanocatalysts in the last years.....	6
FIGURE 1.2 - General structure of a semi-heterogeneous catalyst.....	7
FIGURE 1.3 - General methods employed for the immobilization of metal compounds on magnetic supports.....	16
FIGURE 2.1 - Structures of DHMPs that display pharmacological activities. ...	36
FIGURE 2.2 - Diagram showing the polymorphism of niobium oxides at different temperatures.....	41
FIGURE 2.3 - X-ray diffractogram for Fe ₃ O ₄ and the niobium nanocatalyst. ...	44
FIGURE 2.4 - X-ray diffractogram for the copper and nickel nanocatalysts.....	45
FIGURE 2.5 - (a) TEM image, (b) HRTEM image and (c) particle size distribution analysis for the niobium nanocatalyst.....	46
FIGURE 2.6 - (a) BF-STEM image showing the amorphous Nb ₂ O ₅ on the magnetite surface and (b) EDS line profile.....	47
FIGURE 2.7 - EDS elemental maps for Fe ₃ O ₄ @Nb ₂ O ₅ . a) BF-STEM image, b) DF-STEM image, c) Fe map, d) Nb map and e) Fe + Nb map.....	48
FIGURE 2.8 - NH ₃ -TPD curve for Fe ₃ O ₄ and the niobium nanocatalyst.....	49
FIGURE 2.9 - Magnetization curve for Fe ₃ O ₄ and the niobium nanocatalyst. Inset: Picture of the catalyst being separated from the reaction medium with the aid of a magnetic field.....	49
FIGURE 2.10 - Evaluation of the catalyst effect on Biginelli reaction.	54
FIGURE 2.11 - Evaluation of the recyclability of the niobium nanocatalyst.....	57
FIGURE 2.12 - Evaluation of the composition of the reaction medium monitored over time by GC-MS.....	59
FIGURE 3.1 - Comparison between the CO ₂ cycles of a petroleum refinery and a biorefinery.....	74

FIGURE 3.2 - General structure of lignin and its main constituents.....	77
FIGURE 3.3 - General structure of hemicellulose and its sugar constituents.	77
FIGURE 3.4 - General structure of cellulose.....	78
FIGURE 3.5 - General preparation of beta zeolite. (Reprinted with permission from ref. 24. Copyright 2011 American Chemical Society.).....	88
FIGURE 3.6 - Structure of PDDA, a polymer used for the immobilization of negatively charged species on the surface of materials.	93
FIGURE 3.7 - XRD patterns of Fe ₃ O ₄ , the zeolite NaZSM-5 and the magnetically recoverable catalyst with the zeolite in its sodic (γ -Fe ₂ O ₃ -NaZSM-5) and acid (γ -Fe ₂ O ₃ -HZSM-5) form.	94
Figure 3.9 – a) TEM image used in the construction of the b) size distribution histogram for the Fe ₃ O ₄ microspheres.	95
FIGURE 3.8 - TEM images of a) and b) Fe ₃ O ₄ microspheres and c), d) and e) the γ -Fe ₂ O ₃ -HZSM5 magnetic zeolite.	95
FIGURE 3.10 - a) HR-TEM image of magnetite spheres at 200 nm; b) HR-TEM image of γ -Fe ₂ O ₃ -HZSM5; c) HAADF image of γ -Fe ₂ O ₃ microspheres encapsulated into HZSM-5 grain; (d-h) elemental mapping of Fe, Al, O, Si and Fe/Si/Al, respectively.....	96
FIGURE 3.11 - Temperature programmed desorption of NH ₃ over Fe ₃ O ₄ -HZSM-5.....	97
FIGURE 3.12 - Infrared spectrum of pyridine.....	98
FIGURE 3.13 - Infrared spectrum of pyridine absorbed on the acidic sites of the magnetically recoverable HZSM-5 zeolite.	99
FIGURE 3.14 - ⁵⁷ Fe Mössbauer spectrum, measured at room temperature and without an external magnetic field.....	101
FIGURE 3.15 - Evaluation of reaction parameters for the conversion of FA to GVL in 2-propanol.....	104
FIGURE 3.16 - Evaluation of reaction parameters in the conversion of FA to BL in 2-butanol.	105

FIGURE 3.17 - Evaluation of the catalyst recyclability in the synthesis of a) GVL in 2-propanol and b) BL in 2-butanol.	106
FIGURE 3.18 - Evaluation of reaction composition over time. a) FA to GVL and b) FA to BL.....	107
FIGURE 3.19 - Evaluation of water addition in the catalytic conversion of FA to a) GVL and b) BL.....	108
FIGURE 4.1 - Reprinted with permission from ref. 106. Copyright 2014 American Chemical Society.	118
FIGURE 4.2 – a) and b) TEM images of DMSi, c) size distribution analysis of DMSi, d) and e) TEM images of DMSi-SA, f) SEM image of DMSi-SA and g) EDS spectrum of DMSi-SA.....	125
FIGURE 4.3 – Low angle x-ray diffractogram of DMSi-SA.	126
FIGURE 4.4 - Nitrogen adsorption/desorption isotherms of (A) DMSi and (B) DMSi-SA.	127
FIGURE 4.5 - HRTEM and chemical mapping in the sulfonic acid functionalized DMSi-SA catalyst.....	128
FIGURE 4.6 – XPS spectra of the DMSi-SA catalyst.....	129
FIGURE 4.7 – Infrared of adsorbed pyridine of the support DMSi and the catalyst DMSi-SA.	130
FIGURE 4.8 – Evaluation of reaction parameters in the conversion of furfural to 2-propyl levulinate.....	132
FIGURE 4.9 – Evaluation of a) reaction time and b) catalyst loading in the conversion of fructose to ethyl levulinate at 170 °C.....	133
FIGURE 4.10 - Evaluation of the catalyst loading in the conversion of fructose to ethyl levulinate at 120°C.....	134

List of Schemes

SCHEME 1.1 - Sharpless asymmetric dihydroxylation of β -methyl styrene catalyzed by OsO_4 in the presence of a supported chiral cinchona alkaloid derivative ligand.....	8
SCHEME 1.2 - Oxidation of benzyl alcohols promoted by a palladium complex supported on SBA-15.....	8
SCHEME 1.3 - Michael addition of 2-hydroxy-1,4-naphthoquinone to nitroalkenes catalyzed by a polystyrene-supported bifunctional squaramide organocatalyst.	9
SCHEME 1.4 - Synthesis of quinolines via Friedländer annulation catalyzed by sulfonic acid-functionalized chitosan.	10
SCHEME 1.5 - Formation of magnetite from Fe^{2+} and Fe^{3+} precursors in basic media by the co-precipitation method.....	12
SCHEME 1.6 - Synthesis of Fe_3O_4 through the thermal decomposition method.	12
SCHEME 1.7 - Synthesis of magnetite nanoparticles by the microemulsion method.....	13
SCHEME 1.8 - Preparation of magnetite microspheres by the solvothermal method.....	13
SCHEME 1.9 - Important properties associated with the catalytic activity of magnetic nanoparticles.....	17
SCHEME 1.10 - Synthesis of substituted tetrahydroisoquinolines using a copper oxide catalyst supported in magnetite nanoparticles in the presence of a DES..	20
SCHEME 1.11 - Synthesis of N-containing heterocycles derivatives catalyzed by a magnetically recoverable copper nanocatalyst via Knoevenagel condensation.	21

SCHEME 1.12 Reduction of ketones to alcohols through the Meerwein–Ponndorf–Verley transfer hydrogenation reaction and oxidation of alcohol to ketones catalyzed by a magnetically recoverable ruthenium catalyst.	22
SCHEME 1.13 - Carbonylative Sonogashira coupling employing a ruthenium nanocatalyst.....	22
SCHEME 1.14 - Morita-Bailys-Hillman reaction catalyzed by a magnetically recoverable basic catalyst.	23
SCHEME 1.15 - Asymmetric Friedel-Crafts alkylation of N-substituted pyrroles with α,β -unsaturated aldehydes using a supported MacMillan catalyst.	24
SCHEME 1.16 - (a) Halogen exchange reaction of <i>n</i> -bromooctane with KI and (b) substitution reaction of benzyl bromide with AcOK using supported crown ethers as catalysts.....	25
SCHEME 1.17 - Cycloadditions of carbon dioxide to epoxides catalyzed by magnetically recoverable ionic liquids.	25
SCHEME 1.18 - Synthesis of arylphosphonates via C–P bond formation catalyzed by a magnetically recoverable Pd complex.	26
SCHEME 2.1 - Pictorial view of the comparison between a stepwise and a multicomponent approach.....	30
SCHEME 2.2 - Examples of some of the most famous multicomponent reactions.	31
SCHEME 2.3 - Mannich reaction catalyzed by a magnetically recoverable copper catalyst prepared via direct impregnation.....	32
SCHEME 2.4 - Synthesis of substituted 1,2,3-triazoles catalyzed by a copper nanocatalyst.....	33
SCHEME 2.5 - Mannich and Hantzsch reactions catalyzed by cysteine over Fe ₃ O ₄	33
SCHEME 2.6 - Synthesis of spirioxindole derivatives 2.20 via a multicomponent reaction catalyzed by MnFe ₂ O ₄ nanoparticles.	34
SCHEME 2.7 - Biginelli reaction.	35

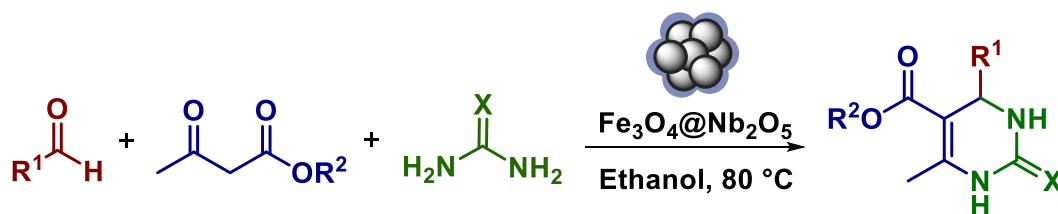
SCHEME 2.8 - Preparation of a) a Fe ₃ O ₄ -SBA-15-cysteine catalyst and b) a Fe ₃ O ₄ -OSO ₃ H catalyst.	37
SCHEME 2.9 - Examples of magnetically recoverable ionic liquids employed as catalysts on Biginelli reaction.	38
SCHEME 2.10 - Examples of magnetically recoverable metal catalysts for Biginelli reaction.	39
SCHEME 2.11 – Applications of niobium compounds in catalysis.	42
SCHEME 2.12 - Preparation of the niobium nanocatalyst.	43
SCHEME 2.13 - Evaluation of Biginelli reaction under microwave irradiation	53
SCHEME 2.14 - Scope of the reaction for the synthesis of DHPMs via Biginelli condensation.	56
SCHEME 2.15 - Possible mechanisms for Biginelli reaction.	58
SCHEME 2.16 - Proposed catalytic cycle for Biginelli reaction in the presence of the niobium nanocatalyst via the Knoevenagel mechanism.	60
SCHEME 3.1 - First-generation processes for the production of biofuels.	75
SCHEME 3.2 - Products of the acid treatment of carbohydrates derived from lignocellulosic biomass.	79
SCHEME 3.3 - Dehydration reaction mechanism for a) fructose and b) glucose.	80
SCHEME 3.4 - Conversion of furfural and 5-HMF to other platform chemicals and value-added products.	82
SCHEME 3.5 - Synthesis of GVL from furfural reported by Roman-Leshkov's group.	83
SCHEME 3.6 - Mechanism of the conversion of furfural to GVL.	85
SCHEME 3.7 - Reaction mechanism for the Meerwein-Ponndorf-Verley reduction.	86
SCHEME 3.8 - Synthesis of GVL from furfuryl alcohol reported by Rode's group.	86
SCHEME 3.9 - Synthesis of EL from furfural reported by Yuan's group.	87

SCHEME 3.10 Generation of acid sites in zeolites through thermal treatment.	89
SCHEME 3.11 - Synthesis of the magnetically recoverable HZSM-5 catalyst.	91
SCHEME 3.12 - Flowchart showing the detailed preparation of the magnetically recoverable zeolite.	92
SCHEME 3.13 - Interaction of pyridine with different acid sites on a solid acid catalyst.	98
SCHEME 3.14 Reaction pathway for the synthesis of γ -valerolactone from furfuryl alcohol.	103
SCHEME 4.1 - Sequential reduction/esterification of furfural promoted by a Pd/Al-SBA-15 catalyst.....	120
SCHEME 4.2 – Conversion of sugars using sulfonic acid-functionalized materials as catalysts.	121
SCHEME 4.3 – Conversion of glucose to levulinic acid promoted by a sulfonic acid-functionalized graphene catalyst.....	122
SCHEME 4.4 – Preparation of the catalyst comprised by sulfonic acid-functionalized dendritic mesoporous silica.....	124
SCHEME 4.5 – Conversion of furfural to 2-propyl levulinate.....	131
SCHEME 4.6 – Acid-catalyzed conversion of fructose to ethyl levulinate.	133
SCHEME 4.7 – Mechanism of the isomerization of glucose to fructose.	135

Abstract

NANOESTRUCTURED CATALYSTS FOR ORGANIC REACTIONS: DESIGN, SYNTHESIS AND APPLICATIONS

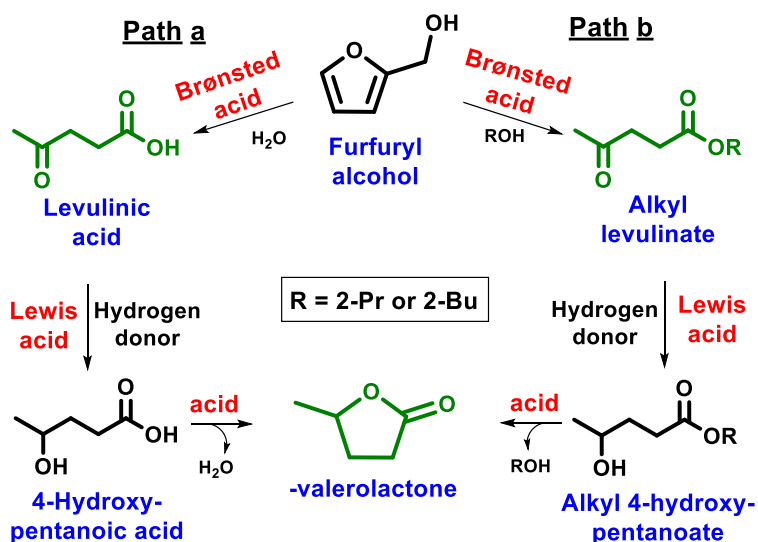
The development of more efficient and selective catalysts actively contributes for the design of safer, cleaner and less energy-demanding processes, and, therefore, catalysis is one of the cornerstones of green chemistry. In this sense, supported-heterogeneous catalysts represent a great advance in this field, especially because they overcome the difficulty in catalyst separation associated to homogeneous catalysts. In this context, this thesis is focused on the development of nanostructured materials for application in Organic Synthesis. In Chapter 1, a brief introduction regarding fundamental concepts in catalysis is presented, focusing on the synthesis and application of magnetically recoverable catalysts. Chapter 2 described the design, preparation and characterization of a new magnetically recoverable niobium nanocatalyst for application in the synthesis of 3,4-dihydropyrimidinones via Biginelli reaction (Scheme 1).



SCHEME 1 - Synthesis of 3,4-dihydropyrimidinones via Biginelli reaction promoted by a magnetically recoverable catalyst.

The catalyst (Fe₃O₄@Nb₂O₅) was prepared by coating magnetite nanoparticles with niobium oxide by using a simple wet impregnation method. The developed protocol was applicable to a wide range of aliphatic and aromatic substrates, and structurally diverse products were obtained in excellent yields. Additionally, the nanocatalyst could be easily separated from the reaction mixture with the aid of a magnetic field and reused several times without any losses in its

catalytic activity. Moreover, experimental observations provided an insight into the reaction pathway. Chapter 3 describes the synthesis and characterization of a magnetic ZSM-5 zeolite with core-shell type structure for application on the valorization of bio-derived furfuryl alcohol (Scheme 2).



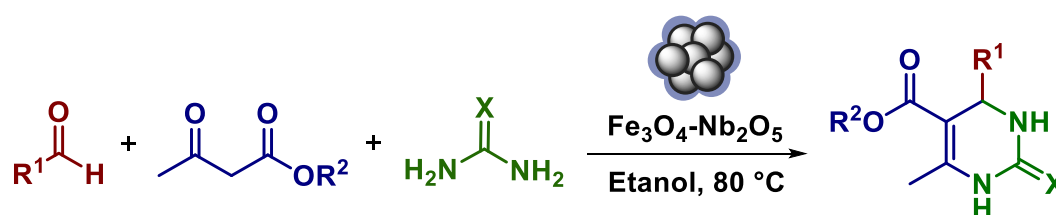
SCHEME 2 – Valorization of bio-derived furfuryl alcohol catalyzed by a magnetically recoverable zeolite.

The magnetic HZSM-5 zeolite catalyst was prepared by the encapsulation of magnetite particles in the zeolite grains using a cationic polymer followed by calcination and next, an ion exchange to obtain the zeolite in its acid form. Remarkably, the catalytic system displayed a tunable selectivity to γ -valerolactone, alkyl levulinates and even levulinic acid by simply changing the reaction conditions. Furthermore, the catalyst could be easily recovered and reused for several reaction cycles without significant losses in its catalytic activity.

Resumo

CATALISADORES NANOESTRUTURADOS PARA REAÇÕES ORGÂNICAS: DESIGN, SÍNTESE E APLICAÇÕES

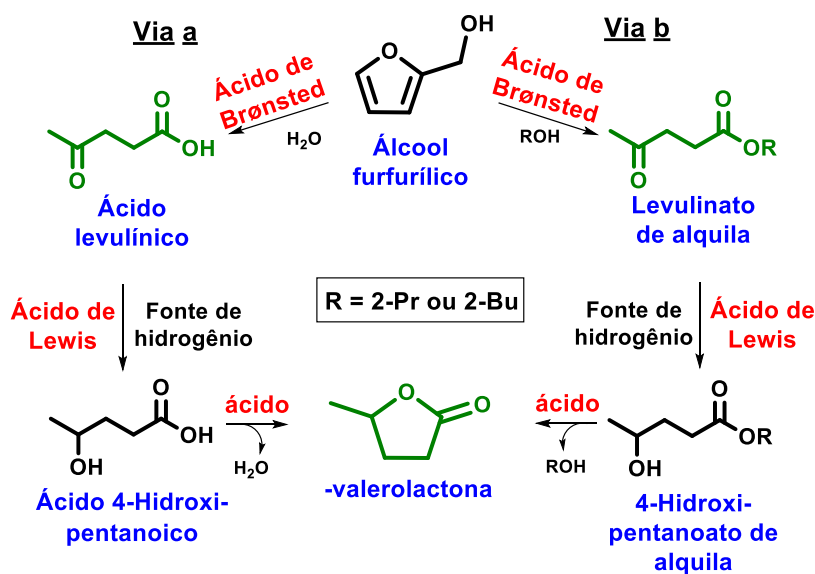
O desenvolvimento de catalisadores mais eficientes e seletivos contribui para o design de processos mais seguros, mais limpos e mais energeticamente viáveis, e, portanto, a catálise é um dos pilares da Química Verde. Neste sentido, catalisadores heterogêneos suportados representam um grande avanço nesta área, principalmente porque superam as dificuldades de separação dos catalisadores homogêneos. Neste contexto, esta tese é focada no desenvolvimento de materiais nanoestruturados para aplicação em Síntese Orgânica. No Capítulo 1 é apresentada uma breve introdução envolvendo conceitos fundamentais em catálise, com foco na síntese e aplicação de catalisadores magneticamente recuperáveis. O Capítulo 2 descreve o design, preparação e caracterização de um novo catalisador de nióbio magneticamente recuperável e sua aplicação na síntese de 1,4-dihidropirimidinonas via reação de Biginelli (Esquema 1).



ESQUEMA 1 – Síntese de 3,4-dihidropirimidinonas via reação de Biginelli promovida por um catalisador de nióbio magneticamente recuperável.

O catalisador foi preparado a partir do recobrimento de nanopartículas de magnetita com óxido de nióbio utilizando um simples método de impregnação úmida. O método desenvolvido pôde ser aplicado para uma grande quantidade de substratos alifáticos e aromáticos, e produtos com grande diversidade estrutural foram obtidos com rendimentos excelentes. Além disso, o

nanocatalisador pode ser facilmente separado do meio reacional usando um campo magnético e reutilizado várias vezes sem nenhuma perda significativa de sua atividade catalítica. Adicionalmente, observações experimentais forneceram informações sobre o mecanismo da reação. O Capítulo 3 descreve a síntese e caracterização de uma zeólita magneticamente recuperável do tipo HZSM-5 e sua aplicação na valorização do álcool furfurílico (Esquema 2).



ESQUEMA 2 – Valorização do álcool furfurílico catalisada por uma zeólita magneticamente recuperável.

O catalisador constituído pela zeólita magnética foi preparado através do encapsulamento de partículas de magnetita nos grãos da zeólita utilizando um polímero catiônico seguido de calcinação e de uma etapa de troca iônica para a obtenção da zeólita em sua forma ácida. Interessantemente, a atividade catalítica deste sistema mostrou possuir uma seletividade ajustável para γ -valerolactona, levulinatos de alquila e até mesmo ácido levulínico através da simples mudança das condições reacionais. Além disso, o catalisador pôde ser facilmente recuperado e reutilizado em vários ciclos reacionais sem perdas significativas em sua atividade catalítica.

Summary

List of Tables	ix
List of Figures	xi
List of Schemes	xv
Abstract	xix
Resumo	xxii
Chapter 1.....	3
1.1 - Homogeneous and Heterogeneous Catalysis	3
1.2 - “Semi-Heterogeneous” Catalysis.....	6
1.3 - Magnetically Recoverable Catalysts.....	10
1.3.1 - Synthesis of Magnetite Nanoparticles	11
1.3.2 - Synthesis of Magnetically Recoverable Catalysts	15
1.3.3 - Characterization of Magnetically Recoverable Catalysts	17
1.3.4 - Applications of Magnetically Recoverable Catalysts	19
Chapter 2.....	29
2.1 - Introduction.....	29
2.1.1 - Multicomponent Reactions	29
2.1.2 - Biginelli Reaction.....	35
2.1.3 - Niobium Compounds.....	40
2.2 - Aims-Objectives.....	42
2.3 - Results and Discussion	43
2.3.1 - Nanocatalysts characterization	43

2.3.2 - Evaluation of the catalytic activity of the niobium nanocatalyst on the dihydropyrimidinones synthesis via Biginelli reaction.....	50
2.4 - Conclusions.....	59
2.5 - Experimental Section.....	61
2.5.1 - General information.....	61
2.5.2 - Preparation of magnetite nanoparticles.....	61
2.5.3 - General preparation of the nanocatalysts.....	61
2.5.4 - Characterization of the nanocatalysts	62
2.5.5 - General procedure for Fe ₃ O ₄ @Nb ₂ O ₅ .nH ₂ O Biginelli reaction: Optimization of reaction conditions.....	63
2.5.6 - General procedure for Fe ₃ O ₄ @Nb ₂ O ₅ .nH ₂ O Biginelli reaction: Scope of reaction.....	63
2.5.7 - General procedure for Fe ₃ O ₄ @Nb ₂ O ₅ .nH ₂ O Biginelli reaction: Comparison of the niobium nanocatalyst efficiency with nickel and copper nanocatalysts ...	64
2.5.8 - General procedure for Fe ₃ O ₄ @Nb ₂ O ₅ .nH ₂ O Biginelli reaction: Microwave evaluation.....	64
2.5.9 - Procedure for scaling up and study of the recyclability of the Fe ₃ O ₄ @Nb ₂ O ₅ .nH ₂ O catalyst.....	65
2.5.10 - General procedure for Fe ₃ O ₄ @Nb ₂ O ₅ .nH ₂ O Biginelli reaction: Evaluation of the reactional media composition over time.	65
2.5.11 - Characterization of the dihydropyrimidinones/thiones.....	66
Chapter 3.....	73
3.1 - Introduction.....	73
3.1.1 - Conversion lignocellulose-derived compounds to value-added chemicals.....	76
3.1.2 - Zeolites as catalysts for bio-derived compounds.....	87

3.2 - Aims-Objectives.....	91
3.3 - Results and discussion.....	91
3.3.1 - Catalyst characterization.....	91
3.3.2 - Catalytic evaluation.....	102
3.4 - Conclusions.....	108
3.5 - Experimental.....	109
3.5.1 - Synthesis of Fe ₃ O ₄ microspheres.....	109
3.5.2 - Functionalization of Fe ₃ O ₄ microspheres with PDDA.....	109
3.5.3 - Synthesis of NaZSM-5 zeolite (Si/Al =14).....	109
3.5.4 - Preparation of magnetically recoverable catalyst – magnetite microspheres embedded on HZSM-5 zeolite (Fe ₃ O ₄ -HZSM-5).....	110
3.5.5 - Characterization of the support and the Fe ₃ O ₄ -HZSM-5 catalyst.....	111
3.5.6 - Catalytic evaluation.....	113
3.5.7 – Analyses of the reaction products.....	113
Chapter 4.....	116
4.1 - Introduction.....	117
4.2 - Aims-Objectives.....	123
4.3 - Results and discussion.....	123
4.5.1 - Catalyst characterization.....	123
4.5.2 - Catalytic evaluation.....	131
4.4 - Conclusions and perspectives.....	135
4.5 - Experimental.....	135
4.5.1 - Synthesis of dendritic mesoporous silica (DMSi) nanospheres.....	135
4.5.2 - Functionalization of DMSi nanospheres with sulfonic acid groups.....	136

4.5.3 - Characterization of the DMSi support and the DMSi-SA catalyst.....	136
4.5.4 - Catalytic evaluation of DMSi-SA nanospheres on furfural conversion to alkyl levulinates.....	138
4.5.5 - Catalytic evaluation of DMSi-SA nanospheres on furfural conversion to alkyl levulinates.....	139
4.5.6 - Analyses of the reaction products.....	139
References.....	141
Appendices.....	159

Chapter 1

1.

General Introduction

General overview

This chapter addresses fundamental concepts in catalysis. A brief introduction regarding homogeneous and heterogeneous catalysis is presented, followed by insights on semi-heterogeneous and magnetically recoverable catalysts. The main methods for the preparation of magnetically recoverable nanocatalysts are also described, as well as some insights into their characterization.

1.1 - Homogeneous and Heterogeneous Catalysis

Catalysis is defined as the increase in the rate of a chemical process without modification of the overall standard Gibbs energy change in the reaction caused by the use of a catalyst, a substance that provides an alternative pathway with a lower activation energy for the reaction.¹ The majority of the chemical processes in industry rely on catalysis; more than 80% of the industrial processes involve the use of a catalyst to produce fine chemicals, pharmaceuticals, polymers and other products.² Additionally, since the development of more efficient and selective catalysts actively contributes for the design of safer, cleaner and less energy-demanding processes, catalysis is one of the cornerstones of green chemistry (also called sustainable chemistry).³

1. IUPAC. Compendium of Chemical Terminology, 2nd ed. (the "Gold Book"). Compiled by McNaught, A. D. and Wilkinson, A. Blackwell Scientific Publications, Oxford, 1997.

2. (a) Bravo-Suárez, J. J.; Kidder, M. K.; Schwartz, V. Novel Materials for Catalysis and Fuels Processing. ACS Symposium Series. 1st ed. American Chemical Society, Washington-DC, 2013. (b) Hagen, J. Industrial Catalysis: A Practical Approach. 2nd ed., Hoboken, John Wiley & Sons, 2005.

3. Anastas, P. T.; Warner, J. C. Green Chemistry: Theory and Practice. 1st ed, Oxford Science Publications, Oxford, 1998.

Catalysis can be broadly divided in two types – heterogeneous and homogenous – with respect to the physical state in which the catalyst and reagents are located.

In the homogeneous catalysis, the catalyst and the reagents are in the same phase, what provides the full contact between those species. Therefore, all the catalytic sites are fairly accessible, and as a consequence, these catalysts display high activity, usually requiring low catalyst loadings. Other advantages associated with this type of catalysis include high selectivities and overall mild reaction conditions. Brønsted and Lewis acids, bases, metal salts, organometallic complexes, organocatalysts and biocatalysts are some examples of homogeneous catalysts. On the other hand, the fact the catalyst and the reagents are in the same phase is both the main advantage and disadvantage of homogeneous catalysts: in spite of the generation of highly active catalysts due to the high availability of the active sites, their homogeneous character compromises the separation from the reaction medium, and, accordingly, their reuse.⁴

In contrast, in heterogeneous catalysis the catalyst and the reagents are in different phases, what enables its easy separation from the reaction medium. However, when compared to homogeneous catalysts, the part of the catalyst that is effectively exposed to catalyze the reactions is significantly lower in heterogeneous catalysts, and, therefore, those are considerably less active than the homogeneous ones, requiring higher catalyst loadings.⁵ Table 1.1 summarizes some important features of homogeneous and heterogeneous catalysis.^{4,5}

Heterogeneous catalysts can be of two types: bulk or supported. The bulk catalysts are often metals, metal alloys or oxides, while the supported ones are constituted mainly by three parts: (1) active phase, which is the active part of

4. van Leeuwen, P.W.N.M. *Homogeneous Catalysis: Understanding the Art*. New York, Springer-Verlag, 2004.

5. Nørskov, J. K.; Studt, F.; Abild-Pedersen, F.; Bligaard, T. *Fundamental Concepts in Heterogeneous Catalysis*. Hoboken, John Wiley & Sons, 2014.

TABLE 1.1 - Comparison between homogeneous and heterogeneous catalysis.

	Homogeneous	Heterogeneous
Form	Soluble acids, bases, metal salts, organometallic complexes, organocatalysts, biocatalysts	Bulk metals or metal oxides, zeolites, supported metals or metal oxides
Active site	Well-defined, discrete molecules	Poorly defined
Activity	High	Moderate
Selectivity	High	Low
Product separation	Usually problematic	Usually easy
Catalyst recyclability	Usually problematic	Usually easy
Reaction mechanisms	Reasonably well understood	Poorly understood

the catalyst where the reactions take place, usually metals, metal alloys, oxides and complexes, (2) support, a material where the active phase is dispersed with the aim of increasing its superficial area and the mechanical resistance of the catalyst and (3) promoter, a supplementary species added to the catalyst to confer specific properties such as resistance to poisoning.

In the last decades, the surge of nanoscience has reached heterogeneous catalysis and led to great advances in this field. The appeal of it lays mainly in the fact that the decrease in the size of a particle generates a progressively larger amount exposed atoms on the surface of the material, which results in a dramatic increase in the surface area. In that way, the active sites on nano-supported materials are more available to promote the reactions when compared to the ones in a bulk solid material. In this sense, considering that catalysts supported on nanosized materials display features of both heterogeneous and homogeneous catalysts, e.g., catalyst recoverability and high accessibility of the active sites, some authors classify catalysis using these materials as “nanocatalysis”, which would be a bridge between homogeneous and

heterogeneous catalysis.⁶ However, there is no general consensus if rather nanocatalysis is in fact a new type of catalysis or merely a subtype of heterogeneous catalysis.⁷ The fact is, even with the lingering controversies related to the nanocatalysis concept, it has been a subject that has been blooming in the past decades; the first papers using the term “nanocatalyst” date back to the end of the 1990s, but only in the beginning of the 2000s that a considerable amount of reports started to appear. Figure 1.1 shows the number of papers published in this subject from the beginning of the 2000s till date (Figure 1.1).

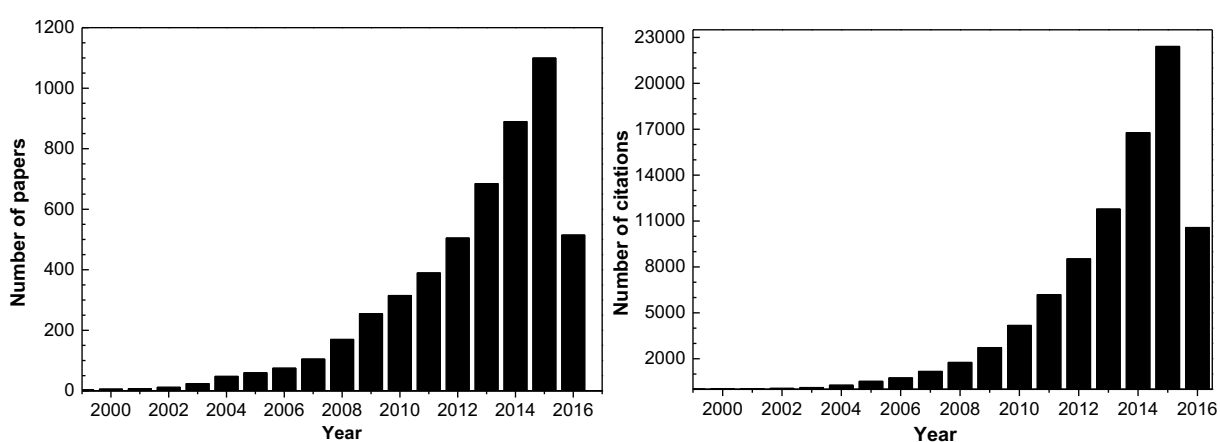


FIGURE 1.1 - Number of papers and citations published on nanocatalysts in the last years. Source: Web of Science, 2016. Search in 14/06/2016 under the term “nanocat*”.

1.2 - “Semi-Heterogeneous” Catalysis

The catalysis employing active materials supported on nanoparticles is also often called “semi-heterogeneous” or “quasi-homogeneous” catalysis. However, it is also common to consider that this type of catalysis is different from heterogeneous catalysis when the active phase is attached to the support through linkers, what would cause a part of the catalyst to be soluble on the reaction medium, promoting a more effective contact of the active phase with the reagents.

6. Astruc, D.; Lu, F.; Aranzaes, J. R. *Angew. Chem. Int. Ed.*, **44**:7852, 2005.

7. Schlögl, R.; Hamid, S. B. A. *Angew. Chem. Int. Ed.*, **43**:1628, 2004.

These catalysts are often regarded as “heterogeneous” catalysts and their general structure is depicted in Figure 1.2.

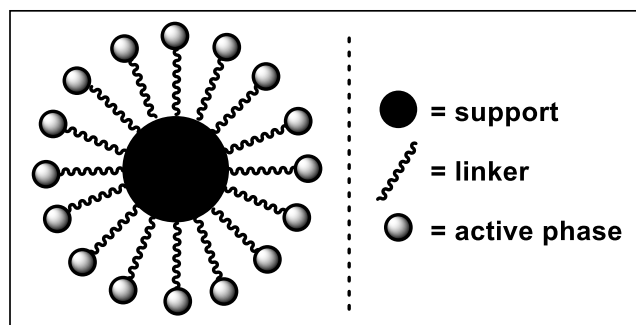


FIGURE 1.2 - General structure of a semi-heterogeneous catalyst.

An interesting feature of semi-heterogeneous catalysts is that the use of a linker allows the immobilization of different types of homogeneous catalysts, namely organic Lewis and Brønsted acid and basic catalysts, asymmetric organocatalysts, ionic liquids and biocatalysts, allowing the easy recovery of those species from the reaction medium.

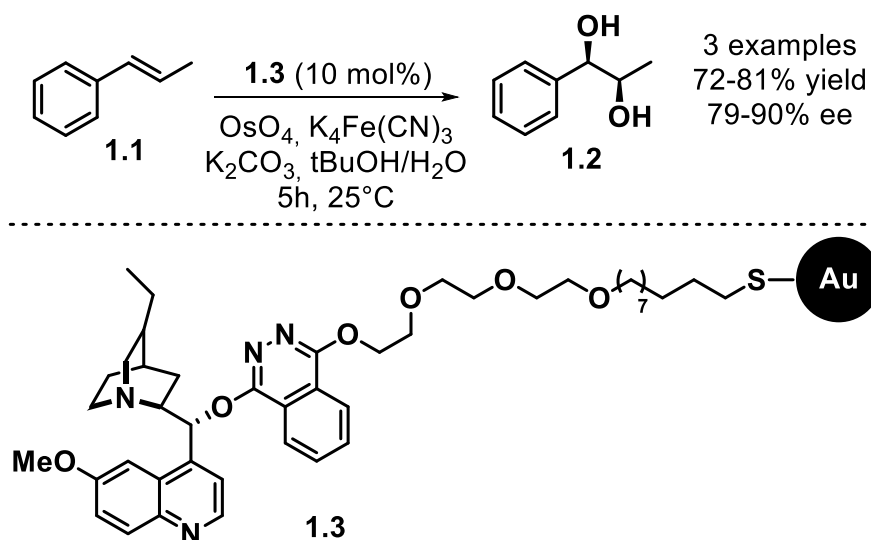
For example, the gold-supported chiral cinchona alkaloid derivative **1.3** was used as a ligand to activate osmium tetroxide and promote the Sharpless asymmetric dihydroxylation of β -methyl styrene **1.1** with high enantioselectivity (ee up to 90%).⁸ Though the material could be recycled via gel permeation chromatography and reused twice, its activity and selectivity suffered decreases in each cycle (Scheme 1.1). A similar example was reported using a dimer of a cinchona alkaloid derivative supported on SBA-15 mesoporous silica, but in this case the recyclability was considerably better, with only slight decreases in conversion and selectivity, when compared to the gold-supported ligand.⁹ More recent reports of this reaction using supported catalysts include the use of polymer-supported enzymes,¹⁰ hierarchical polyamine-silica structures with

8. Li, H.; Luk, Y.-Y.; Mrksich, M. *Langmuir*, **15**:4957, 1999.

9. Motorina, I.; Crudden, C. M. *Org. Lett.*, **3**:2325, 2001.

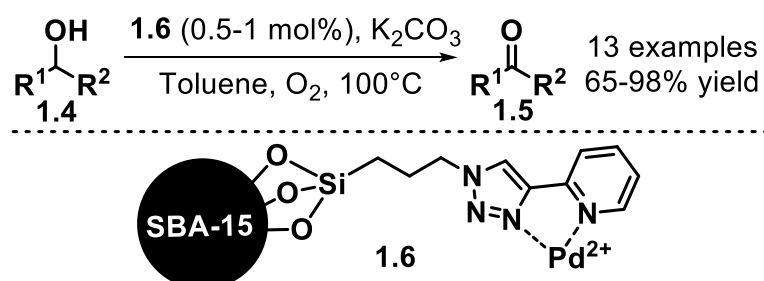
10. Konieczny, S.; Leurs, M.; Tiller, J. C. *ChemBioChem*, **16**:83, 2015.

encased osmate ions¹¹ and chiral polyoxometalate hybrid metal–organic frameworks.¹²



SCHEME 1.1 - Sharpless asymmetric dihydroxylation of β -methyl styrene catalyzed by OsO_4 in the presence of a supported chiral cinchona alkaloid derivative ligand.

Other interesting example of the use of semi-heterogeneous catalysts in organic synthesis is the oxidation of benzyl alcohols **1.4** promoted by the palladium complex supported on SBA-15 **1.6** in the presence of oxygen (Scheme 1.2).¹³ The linker was prepared by reacting a terminal azide-functionalized triethoxysilane with 2-ethynylpyridine through a click reaction, forming a triazole moiety linked to a pyridine ring which acts as a chelating ligand for the palladium ions. The catalyst could be recovered by filtration and reused for 7 reaction cycles.



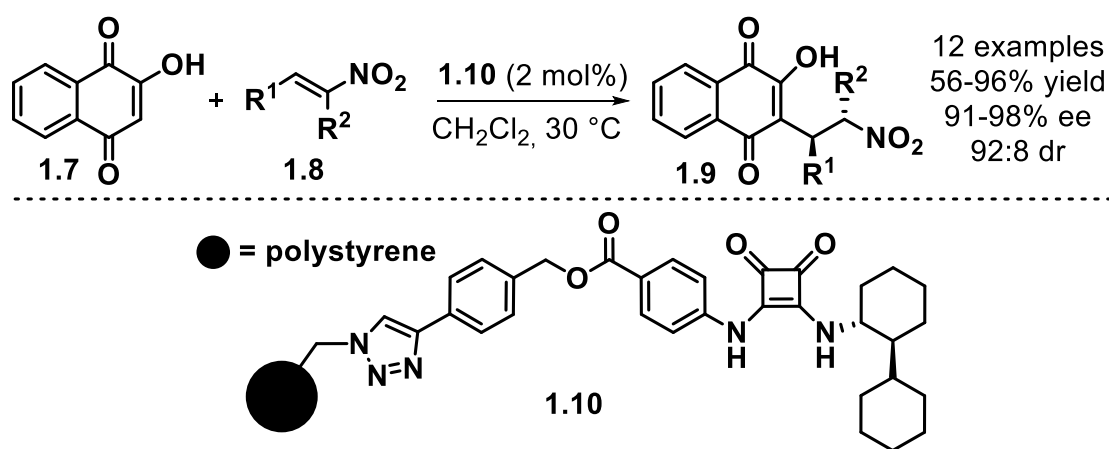
SCHEME 1.2 - Oxidation of benzyl alcohols promoted by a palladium complex supported on SBA-15.

11. Shilpa, N.; Manna, J.; Rana, R. K. *Eur. J. Inorg. Chem.*, **2015**:4965, 2015.

12. Han, Q.; He, C.; Zhao, M.; Qi, B.; Niu, J.; Duan, C. *J. Am. Chem. Soc.*, **135**:10186, 2013.

13. Zhang, G.; Wang, Y.; Wen, X.; Ding, C.; Li, Y. *Chem. Commun.*, **48**:2979, 2012.

Semi-heterogeneous catalysts have also been applied in asymmetric Michael additions. In a notable report, a polystyrene supported bifunctional squaramide organocatalyst **1.10** was used to promote the Michael addition of 2-hydroxy-1,4-naphthoquinone **1.7** to nitroalkenes **1.8** with high levels of enantioselectivity employing low catalyst loadings (Scheme 1.3). Besides that, the catalyst could be recycled for 10 cycles without significant decreases in enantioselectivity (average 96% ee) and also used under continuous flow conditions.¹⁴

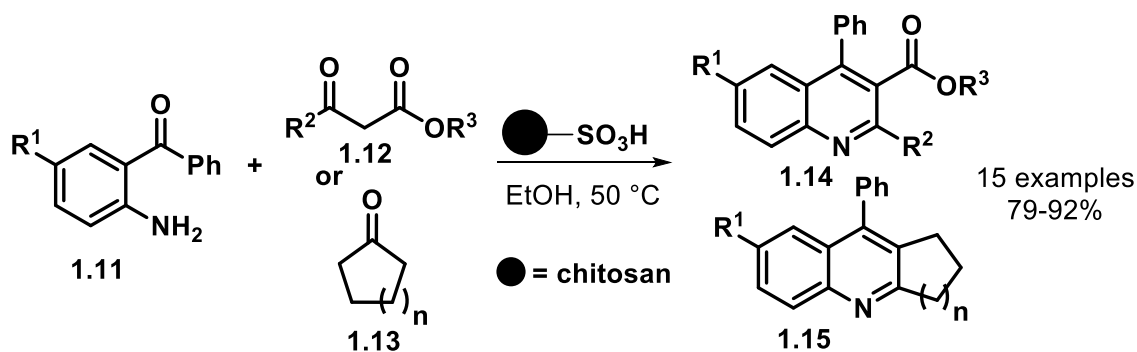


SCHEME 1.3 - Michael addition of 2-hydroxy-1,4-naphthoquinone to nitroalkenes catalyzed by a polystyrene-supported bifunctional squaramide organocatalyst.

Semi-heterogeneous catalysts can also be constituted by the support and a directly attached organic catalyst. For instance, a sulfonic acid-functionalized catalyst was prepared by simply attaching sulfonic acid to the surface of chitosan and had its catalytic activity evaluated on the synthesis of quinolones **1.14** and **1.15** via Friedländer annulation of 2-aminoarylketones **1.11** with carbonyl compounds (Scheme 1.4).¹⁵ The developed protocol could be successfully applied not only to different β -ketoesters **1.12**, but also to cyclic ketones **1.13**. The catalyst could also be recovered from the media by filtration and reused for 3 reaction cycles with only slight decreases in the isolate yield.

14. Kasaplar, P.; Rodríguez-Esrich, C.; Pericas, M. A. *Org. Lett.*, 15:3498, 2013.

15. Reddy, B. V. S.; Venkateswarlu, A.; Reddy, G. N.; Reddy, Y. V. R. *Tetrahedron Lett.*, 54:5767, 2013.



SCHEME 1.4 - Synthesis of quinolines via Friedländer annulation catalyzed by sulfonic acid-functionalized chitosan.

Though the catalysts aforementioned present several advantages when compared to the homogeneous analogous in terms of their recyclability, their recovery from the reaction medium requires filtration or centrifugation steps – additional time and energy-consuming procedures. In this context, magnetically recoverable catalysts have been pointed in the last few years as viable alternatives to overcome these separation drawbacks owing to their easy separation from the reaction media with the aid of an external magnetic field. In that way, the preparation of semi-heterogeneous catalysts supported in magnetic particles has risen as a major research area.¹⁶

1.3 - Magnetically Recoverable Catalysts

Magnetic nanoparticles such as maghemite ($\gamma\text{-Fe}_2\text{O}_3$), magnetite (Fe_3O_4) and other ferrites are amongst the most used supports for the immobilization of catalytic species; they are inexpensive, relatively chemically stable, and easy to prepare.¹⁷

16. (a) Gawande, M. B.; Branco, P. S.; Varma, R. S. *Chem. Soc. Rev.*, **42**:3371, 2013. (b) Gawande, M. B.; Monga, Y.; Zboril, R.; Sharma, R. K. *Coord. Chem. Rev.*, **288**:118, 2015. (c) Gawande, M. B.; Goswami, A.; Asefa, T.; Guo, H.; Biradar, A. V.; Peng, D.-L.; Zboril, R.; Varma, R. S. *Chem. Soc. Rev.*, **44**:7540, 2015. (d) Shylesh, S.; Schnemann, V.; Thiel, W. R. *Angew. Chem. Int. Ed.*, **49**: 3428, 2010. (e) Polshettiwar, V.; Luque, R.; Fihri, A.; Zhu, H.; Bouhrara, M.; Basset, J.-M. *Chem. Rev.*, **111**:3036, 2011.

17. (a) Rossi, L. M.; Costa, N. J. S.; Silva, F. P.; Wojcieszak, R. *Green Chem.*, **16**:290, 2014. (b) Wang, D.; Astruc, D. *Chem. Rev.*, **114**:6949, 2014.

Ferrites are ionic materials with a MFe_2O_4 chemical formula in which M represents a divalent metal. One of the most known and widely used ferrites is magnetite (Fe_3O_4), a ferromagnetic mixed iron oxide that displays a cubic inverse spinel structure and contains iron in two oxidation states (II and III). Other ferrites have also been finding several applications in catalysis in the last years, such as cobalt ($CoFe_2O_4$), copper ($CuFe_2O_4$), zinc ($ZnFe_2O_4$) and nickel ($NiFe_2O_4$) ferrites. Maghemite ($\gamma-Fe_2O_3$), on the other hand, is the product of the oxidation of magnetite under heating and is also a very popular magnetic support.

Metal nanoparticles such as Fe^0 and Co^0 can also be used as magnetic supports, but their low stability to oxidation limits their use.

1.3.1 - Synthesis of Magnetite Nanoparticles

Due to the broad application of nanosized ferrites as catalysts matrixes, great efforts have been devoted to develop methods for the synthesis of magnetic nanoparticles with controlled properties (mainly shape, size and size distribution) for application in this field. Four main approaches can be highlighted as the most employed to produce magnetic nanoparticles: co-precipitation, thermal decomposition, microemulsion and solvothermal methods.¹⁸

The co-precipitation method is one of the simplest ways to produce magnetite nanoparticles and, as a consequence, is widely used. It consists in the addition of Fe^{2+} and Fe^{3+} precursor salts to a basic aqueous solution. In this method, the size and the shape of the particles depends on several factors, such as pH, iron precursor salts and temperature. However, the size distribution of the particles synthesized by this method are not very well-controlled, and, therefore, the production of monodisperse particles is rather challenging. Also, the lack of a stabilizing agent in the surface of the synthesized nanoparticles may lead to their

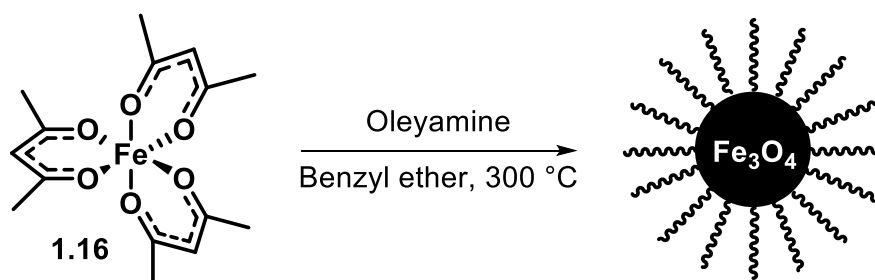
18. (a) Lu, A.-H.; Salabas, E. L.; Schüth, F. *Angew. Chem. Int. Ed.*, **46**:1222, 2007. (b) Chaudhuri, R. G.; Paria, S. *Chem. Rev.*, **112**:2373, 2012. (c) Vatta, L. L.; Sanderson, R. D.; Koch, K. R. *Pure Appl. Chem.*, **78**:1793, 2006.

agglomeration. The formation of magnetite from Fe^{2+} and Fe^{3+} precursors in basic media is showed in Scheme 1.5.



SCHEME 1.5 - Formation of magnetite from Fe^{2+} and Fe^{3+} precursors in basic media by the co-precipitation method.

The thermal decomposition method consists on the thermal decomposition of organometallic iron precursors in the presence of reducing agents under inert atmosphere. This protocol allows the synthesis of magnetic nanoparticles with a uniform shape and very narrow size distribution. The iron precursor most used currently is $\text{Fe}(\text{acac})_3$, but a wide range of precursors has been reported in the last years. The temperatures used in this process are usually in the range of 200°C to 320°C . Scheme 1.6 shows an example of the synthesis of magnetite nanoparticles through the thermal decomposition method.¹⁹ In this example, $\text{Fe}(\text{acac})_3$ **1.16** is used as iron precursor, benzyl ether as solvent and oleylamine has a dual role as a reducing agent that converts part of the Fe^{3+} to Fe^{2+} , and a stabilizing agent on the surface of the formed nanoparticles, preventing them from agglomeration.

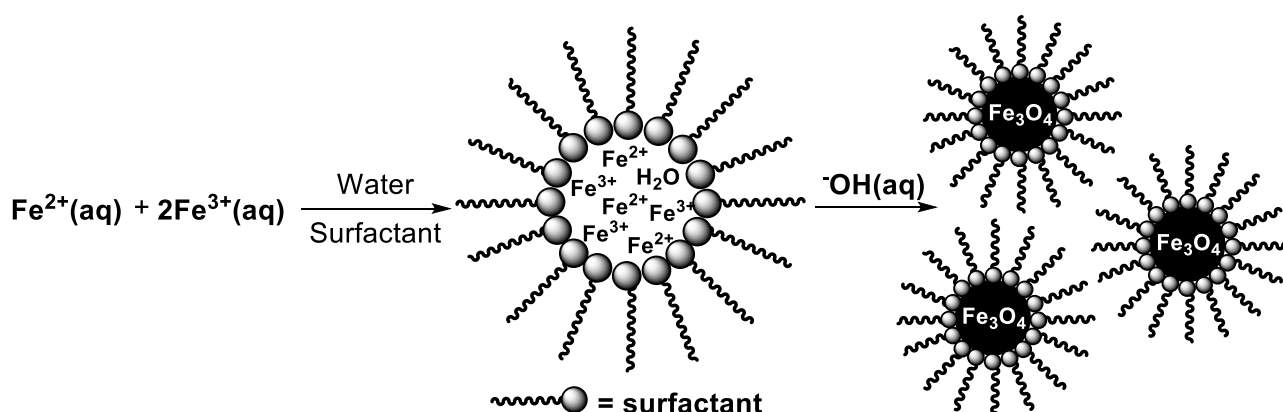


SCHEME 1.6 - Synthesis of Fe_3O_4 through the thermal decomposition method.

The microemulsion method is very similar to the co-precipitation method, but in it, the reaction to produce the magnetite nanoparticles occurs inside of aqueous droplets of a microemulsion formed by water and a surfactant. A microemulsion is a thermodynamically stable isotropic dispersion of two

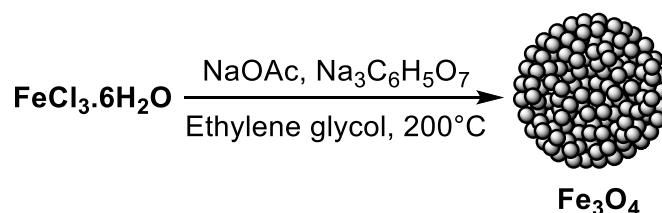
19. Xu, Z.; Shen, C.; Hou, Y.; Gao, H.; Sun, S. *Chem. Mater.*, **21**:1778, 2009.

immiscible liquids, where the microdomain of either or both liquids is stabilized by an interfacial film of surfactant molecules.²⁰ Since droplet size is very well-defined, highly monodisperse particles can be achieved by this method. The formation of magnetite from Fe^{2+} and Fe^{3+} precursors by the microemulsion method is showed in Scheme 1.6.



SCHEME 1.7 - Synthesis of magnetite nanoparticles by the microemulsion method.

In the hydrothermal method, the synthesis of the magnetite microspheres is achieved under high temperature and high pressure. This approach is operationally very simple: the reagents are placed in a sealed autoclave that is submitted to heating at pre-determined temperatures. An example of the application of this method is showed in Scheme 1.8.²¹



SCHEME 1.8 - Preparation of magnetite microspheres by the solvothermal method.

In this approach, $\text{FeCl}_3 \cdot 6\text{H}_2\text{O}$ is used as iron source, sodium acetate (NaOAc) as the alkaline source, sodium citrate ($\text{Na}_3\text{C}_6\text{H}_5\text{O}_7$) as stabilizer agent

20. Langevin, D. *Annu. Rev. Phys. Chem.*, **43**:341, 1992.

21. Liu, J.; Sun, Z.; Deng, Y.; Zou, Y.; Li, C.; Guo, X.; Xiong, L.; Gao, Y.; Li, F.; Zhao, D. *Angew. Chem. Int. Ed.*, **48**:5875, 2009.

and ethylene glycol as both high boiling point solvent and reducing agent; all the reagents are mixed, placed in a sealed autoclave and submitted to heating at 200 °C for 10 h. The magnetite is obtained in the form of microspheres with size around 200 nm that are formed by smaller nanoparticles with size around 15 nm.

In summary, all methods for the preparation of magnetite nanoparticles have their advantages and disadvantages, and the selection of a specific one depends on the final application of the material; overall, methods that generate particles with better shape and narrow size distribution are often more expensive and operationally complicated. Table 1.2 summarizes the general features of each method.

TABLE 1.2 - General features of the methods used to synthesize magnetic nanoparticles.

Preparation method	Operational conditions	Reaction temperature	Reaction time	Shape control	Size distribution
Co-precipitation	Very simple, ambient conditions	RT – 90 °C	Minutes	Not good	Relatively narrow
Thermal decomposition	Complicated, inert atmosphere and high temperatures	200 – 320 °C	Hours	Very good	Very narrow
Microemulsion	Relatively simple, ambient conditions	RT – 50 °C	Hours	Good	Narrow
Solvothermal	Simple, high pressure and temperatures	Around 200 °C	Hours	Very good	Very narrow

1.3.2 - Synthesis of Magnetically Recoverable Catalysts

Having the magnetic nanoparticles that will be used as support for the catalyst in hand, the next step is the supporting of the active phase. However, in order to be used as catalytic supports, the magnetic nanoparticles often need to have their surface coated. The coating step that precedes the immobilization of the active phase occasionally is required to avoid undesired side reactions that can be catalyzed by the exposed metals.

In this sense, several species can be used as coating agents for magnetic nanoparticles, e.g. polymers, carbon, unreactive metals and silica. Particles completely coated with capping agents form core-shell-type structures, because a shell of the capping agent is formed around the core particle. Silica is one of the most used coating agents due to its very advantageous properties such as stability in aqueous media, easy surface modification, and controllable thickness. The coating of nanoparticles with silica is usually conducted through the sol–gel process, which involves the base-catalyzed hydrolysis of tetraethyl orthosilicate (TEOS) in alcohol/water solution.²²

The supporting of the active phase can be achieved by the direct immobilization of the catalytic species directly on the nanoparticle through the hydroxyl groups on the nanoparticle surface, or can be attached through linkers.

If the active species is a metal, the direct functionalization can be attained by several methods, but the most common are coating and impregnation. In the coating technique, the surface of the material is completely covered and additionally to being the active part of the catalyst, the metal also prevents the core from promoting side reactions. In the impregnation approach, which is the most employed due to its simplicity, the catalyst is added to some parts of the support surface and pores, and catalysts produced by this method are often called “decorated”. This technique consists in the precipitation of the metal or metal

22. (a) Guerrero-Martínez, A.; Pérez-Juste, J.; Liz-Marzán, L. M. *Adv. Mater.*, **22**:1182, 2010.
(b) Jana, N. R.; Earhart, C.; Ying, J. Y. *Chem. Mater.*, **19**:5074, 2007.

oxides from a solution that contains their precursors in the presence of the support, followed by a drying process, the so-called wet impregnation. It can also be accomplished by adding very small amounts of the solvent (approximately the volume of the pores of the support) with the metal precursors to the support followed by the evaporation of the solvent and drying; this impregnation approach is known as incipient wetness impregnation or dry impregnation.

Besides coating and impregnation, the active phase can also be attached by the support through linkers, in a process often called grafting. The advantages of the use of organic linkers that bind effectively to the particles surface is that the metal is less prone to leaching and, additionally, the linkers provide better compatibility with organic solvents. Figure 1.3 summarizes the features of the different approaches for the supporting of metal species on magnetic nanoparticles.

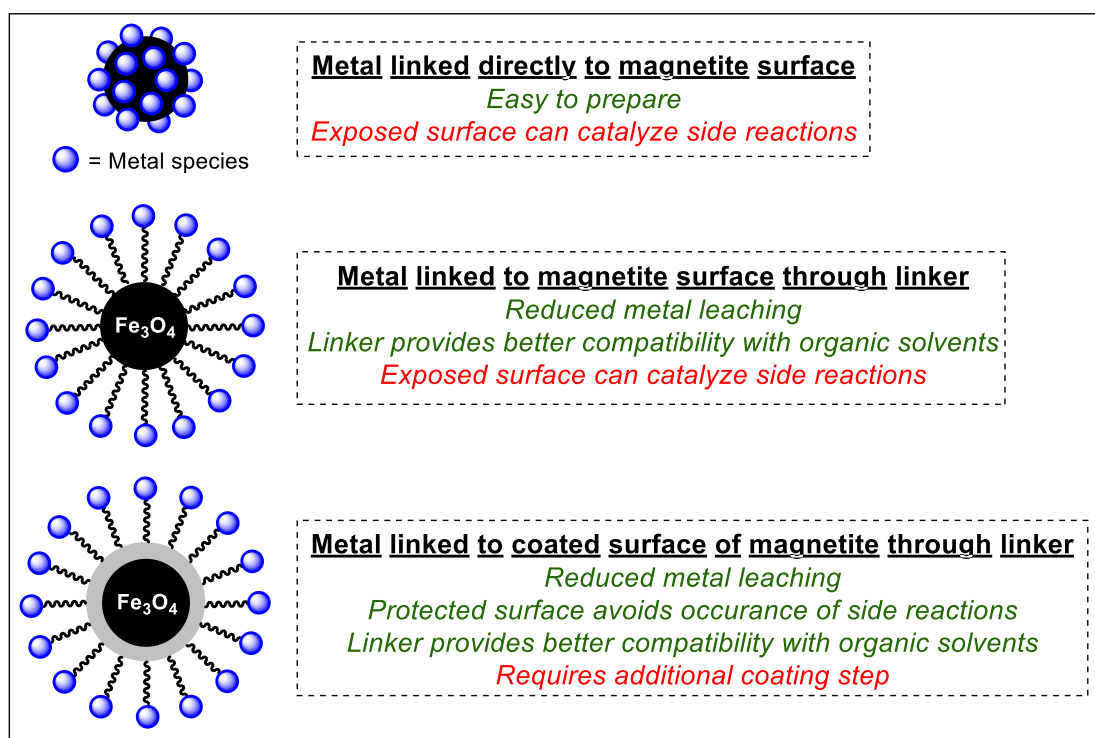


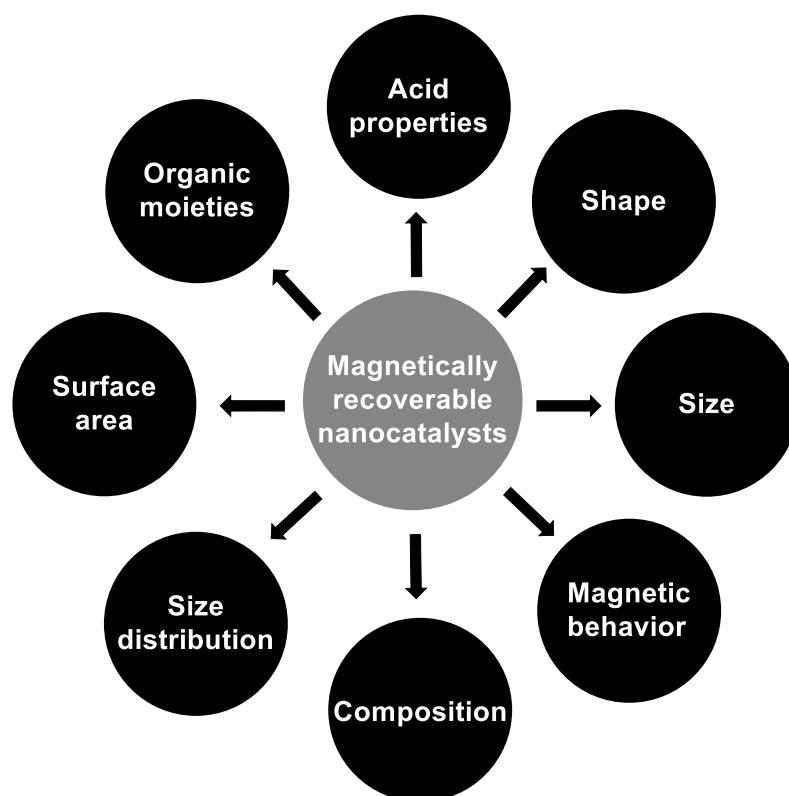
FIGURE 1.3 - General methods employed for the immobilization of metal compounds on magnetic supports.

In the case of organocatalysts, the linkers themselves may sometimes be the active phase of the catalysts, for instance, in the case of supported sulfonic

acids or supported amines. However, in the case of more intricate catalysts, usually the linker is used additionally to the organocatalysts itself. The same is valid for metal complexes and ionic liquids.

1.3.3 - Characterization of Magnetically Recoverable Catalysts

The characteristics and behavior of nanosized materials are fairly different when compared to the same material in the bulk form. In this way, after the preparation of the magnetically recoverable catalyst, a full characterization must be conducted prior to its use in order to assess parameters that will be critical to its catalytic activity.^{16,17} Scheme 1.9 shows the main properties associated with magnetic materials.



SCHEME 1.9 - Important properties associated with the catalytic activity of magnetic nanoparticles.

Since the materials used as supports for the catalysts are in the nano-range size, transmission electron microscopy (TEM) and scanning electron microscopy are required to obtain information regarding the morphology and size

distribution of the material. For more detailed information, such as structural morphology and visualization of a single particle, high resolution transmission electron microscopy (HR-TEM) can be used. X-ray diffraction (XRD) furnishes information regarding elemental composition, and also average size. Dynamic light scattering (DLS) provides interesting information on the size distribution in the sample and gas adsorption techniques regarding the surface area of the materials. For the determination of the amount of metals in the particles, inductively coupled plasma (ICP) techniques or atomic absorption can be used. However, the oxidation state of the metals can only be determined by x-ray photoelectron spectroscopy (XPS). There are also more specific techniques for determining the chemical composition of the sample relying on its magnetic properties, such as Mössbauer spectroscopy, which is about the only technique that can differentiate magnetite from maghemite with accurate certainty. For the study of the magnetic properties of magnetic nanoparticles, vibrating sample magnetometer (VSM) can be used, as well as superconducting quantum interference device (SQUID), though this technique is a very sensitive magnetometer used to measure extremely subtle magnetic fields, which is not the case of magnetic nanoparticles.

On the other hand, the characterization of the functional groups/linkers attached to the magnetic materials is considerably more challenging, since the magnetic behavior of these material precludes the use of nuclear magnetic resonance (NMR). Thus, Fourier transform infrared spectroscopy (FT-IR) seems to be one of the best techniques to characterize the organic moiety of functionalized magnetic nanoparticles. Thermogravimetric analysis (TG) and elemental analysis may provide valuable information on the account of the quantification of the organic moieties in these catalysts.

As for the acid properties of the materials, techniques such as temperature programmed desorption of ammonia (TPD-NH₃) can be used to quantify the acid site density and classify the sites regarding their strength. The

Fourier transform infrared spectroscopy of adsorbed pyridine (FTIR-Pyr) is another powerful tool to quantify and classify acid sites as Lewis or Brønsted-type. In some cases, aqueous acid-base titration can also provide help in the quantification of the acid sites.

1.3.4 - Applications of Magnetically Recoverable Catalysts

Numerous reports can be found in literature employing organocatalysts, ionic liquids, complexes and metal oxides supported on magnetic nanoparticles. Amid those, impregnated catalysts have received a lot of attention, and several metals have been used with this purpose, e.g. Pd, Ni, Co, Cu, Ce, Mo, Ru, Au, Nb, among others.²³ These nanocatalysts have been successfully applied on various organic reactions, such as Suzuki-Miyaura, Heck, Sonogashira and Hiyama reactions, alkyne–azide cycloaddition, hydrogenation of unsaturated compounds, reduction of nitroaromatics, oxidations, arylations, alkylations, epoxidation of alkenes and multicomponent one-pot synthesis of heterocycles.²⁴

A very interesting report using impregnated magnetically recoverable catalysts disclosed the use of a copper oxide catalyst supported in magnetite nanoparticles in the presence of a deep eutectic solvent for the synthesis of the substituted tetrahydroisoquinolines **1.18** (Scheme 1.10).²⁵ Deep eutectic solvents (DESs) are systems formed from a eutectic mixture of Lewis or Brønsted acids and bases which can contain a variety of anionic and/or cationic species.²⁶

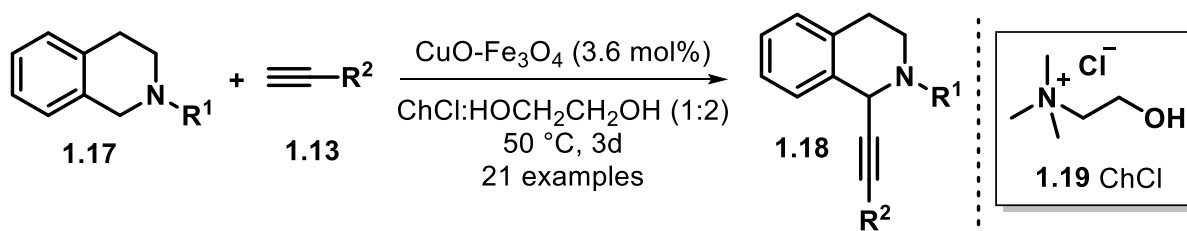
Due to their unique physicochemical properties, *e.g.* low vapor pressure and density, DESs have been widely used in organic synthesis in the last

23. Baeza, A.; Guillena, G.; Ramûn, D. J. *ChemCatChem*, **8**:49, 2016.

24. (a) Zaera, F. *Chem. Soc. Rev.*, **42**:2746, 2013. (b) McMorn, P.; Hutchings, G. J. *Chem. Soc. Rev.*, **33**:108, 2004. (c) Sheldon, R. A.; Bekkum, H. *Fine Chemicals through Heterogeneous Catalysis*, 1st ed., John Wiley & Sons, Wiley-VCH, Weinheim, New York, 2001.

25. Marset, X.; Pérez, J. M.; Ramón, D. J. *Green Chem.*, **18**:826, 2016.

26. Smith, E. L.; Abbott, A. P.; Ryder, K. S. *Chem. Rev.*, **114**:11060, 2014.



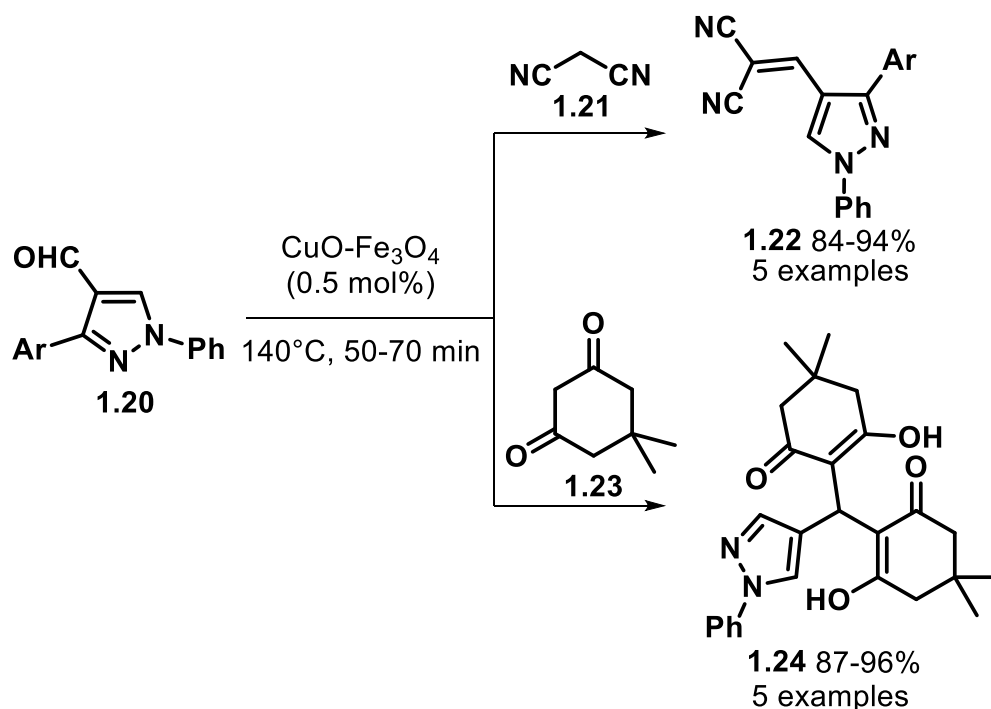
SCHEME 1.10 - Synthesis of substituted tetrahydroisoquinolines using a copper oxide catalyst supported in magnetite nanoparticles in the presence of a DES

few years and pointed as the reaction medium of the century.²⁷ In this case, a DES constituted by choline chloride (ChCl, **1.19**) and ethylene glycol was used as solvent in the cross-dehydrogenative coupling reaction between tetrahydroisoquinolines **1.17** with a broad range of pro-nucleophiles. The presence of both the copper catalyst and DES showed to be essential for the occurrence of the reaction. Interestingly, both the nanocatalyst and the DES could be recycled by extracting the products and unreacted chemicals from the reaction medium by extraction with cyclopentyl methyl ether, which is regarded as a greener solvent. The catalytic system could be reused in ten reaction cycles and the protocol could be applied to a wide range of pro-nucleophiles, namely substituted alkynes **1.13**, nitromethane, 1-methyl-1*H*-indole, diethyl phosphonate, and cyclohexanone, among others.

Another type of reaction in which magnetically recoverable copper catalysts were used is the synthesis of N-containing heterocycles derivatives (Scheme 1.11).²⁸ In this report, the pyrazole-4-carbaldehyde derivatives **1.20** reacted with malononitrile **1.21** and dimedone **1.23** via Knoevenagel condensation to afford the substitute pyrazoles **1.22** and **1.24**, respectively. In this case, only 0.5 mol% of the catalyst was required to promote the reaction, which

27. (a) Liu, P.; Hao, J.-W.; Moa, L.-P.; Zhang, Z.-H. *RSC Adv.*, **5**:48675, 2015. (b) Alonso, D. A.; Baeza, A.; Chinchilla, R.; Guillena, G.; Pastor, I. M.; Ramón, D. J. *Eur. J. Org. Chem.* **2016**:612, 2016. (c) Alonso, D. A.; Baeza, A.; Chinchilla, R.; Guillena, G.; Pastor, I. M.; Ramón, D. J. *Eur. J. Org. Chem.* **2016**:612, 2016.

28. Shelke, S. N.; Bankar, S. R.; Mhaske, G. R.; Kadam, S. S.; Murade, D. K.; Bhorkade, S. B.; Rathi, A. K.; Bundaleski, N.; Teodoro, O. M. N. D.; Zboril, R.; Varma, R. S.; Gawande, M. B. *ACS Sustainable Chem. Eng.* **2**: 1699, 2014.



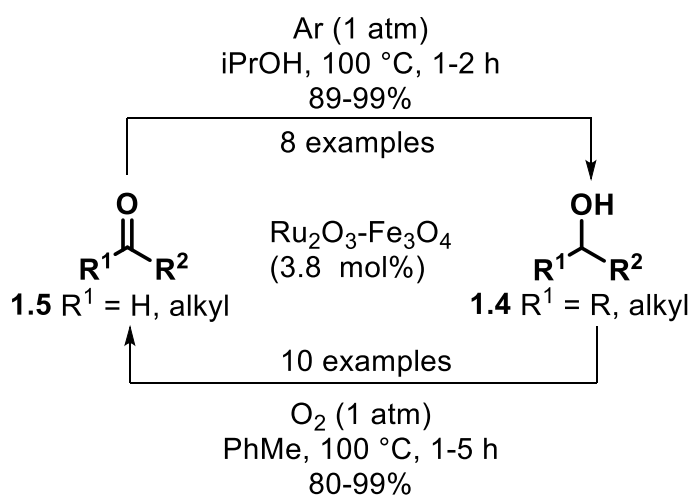
SCHEME 1.11 - Synthesis of N-containing heterocycles derivatives catalyzed by a magnetically recoverable copper nanocatalyst via Knoevenagel condensation.

proceeded in absence of solvent at 140°C . The catalyst could be reused 6 times without any significant losses in yield.

Ruthenium oxide supported on magnetite nanoparticles is another example of a magnetically recoverable catalyst successfully applied on organic synthesis. One of the examples of a reaction promoted by this catalyst is the reduction of ketones to alcohols in a Meerwein–Ponndorf–Verley transfer hydrogenation (Scheme 1.12).²⁹

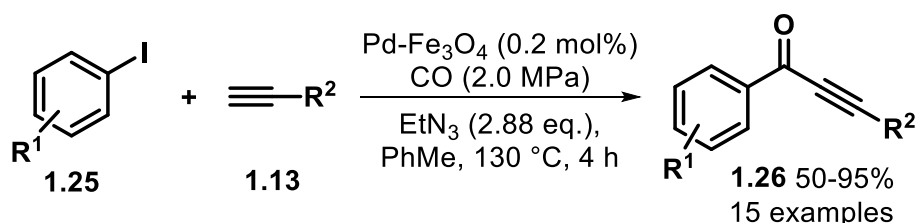
In this reaction, an alcohol is used as hydrogen source to reduce the carbonyl compound (this reaction will be further discussed in Chapter 3). Using 2-propanol as hydrogen source, the reduction of several types of carbonyl compounds was accomplished in 1-2h using the ruthenium nanocatalyst. Additionally, the oxidation of alcohols (the opposite reaction) in the presence of an oxygen atmosphere was also successfully achieved with the same catalyst, as well as the oxidation of amines to the corresponding imines or nitriles.

29. Kotani, M.; Koike, T.; Yamaguchi, K.; Mizuno, N. *Green Chem.* **8**:735, 2006.



SCHEME 1.13 Reduction of ketones to alcohols through the Meerwein–Ponndorf–Verley transfer hydrogenation reaction and oxidation of alcohol to ketones catalyzed by a magnetically recoverable ruthenium catalyst.

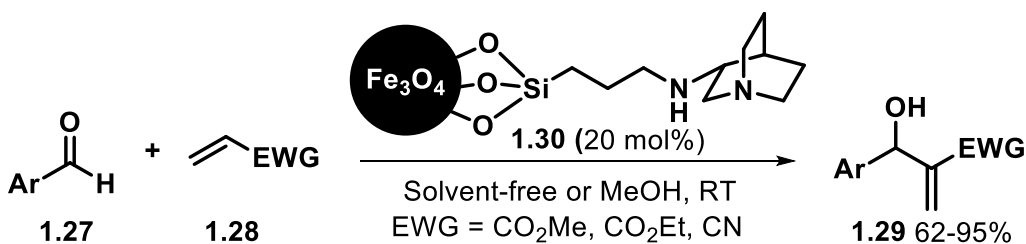
Another metal that has received considerable attention in the field of magnetically recoverable catalysts is palladium, and, therefore, several reports can be found in literature employing this catalyst. One of the seminal works describes the use of Pd⁰ nanoparticles supported on magnetite for the carbonylative Sonogashira coupling reaction of aryl iodides **1.25** with terminal alkynes **1.13** (Scheme 1.12).³⁰ The developed process could afford the corresponding products in moderate to high yields using 0.2 mol% of catalyst, which could be recycled for seven times.



SCHEME 1.12 - Carbonylative Sonogashira coupling employing a ruthenium nanocatalyst.

Organocatalysts are another class of homogeneous catalysts that has been successfully immobilized in magnetic supports. For instance, the basic catalyst **1.30** was prepared by supporting quinuclidine in magnetite nanoparticles

30. Liu, J.; Peng, X.; Sun, W.; Zhao, Y.; Xia, C. *Org. Lett.*, **10**:3933, 2008.



SCHEME 1.14 - Morita-Bailys-Hillman reaction catalyzed by a magnetically recoverable basic catalyst.

through an aminopropyl linker (Scheme 1.14).³¹

The catalyst was employed in the Morita-Bailys-Hillman reaction, which is the coupling between an activated alkene derivative **1.28** and an aldehyde **1.27** in the presence of a basic catalyst, usually DABCO (1,4-diazabicyclo[2.2.2]octane). Interestingly, the reaction with the supported catalyst proceeded in a considerably lower reaction time than the one with DABCO, affording the product in the same yield. The protocol could be applied to several substrates with moderate to high yields, and the catalyst could be used in 7 consecutive reaction runs with no loss in the yield, though the reaction time increased from 5 to 7 hours in the last reaction run.

Chiral organocatalysts are another class of catalysts that have been immobilized in magnetic supports. Several types of these catalysts have been heterogeneized using magnetic nanoparticles as support, for instance, MacMillan's, Jørgensen–Hayashi and chiral alkaloid derivatives.³² Scheme 1.15 shows an example of a MacMillan-type catalyst supported on magnetite nanoparticles **1.31** and its use in the asymmetric Friedel-Crafts alkylation of N-substituted pyrroles **1.32** with α,β -unsaturated aldehydes **1.33**.³³ The developed

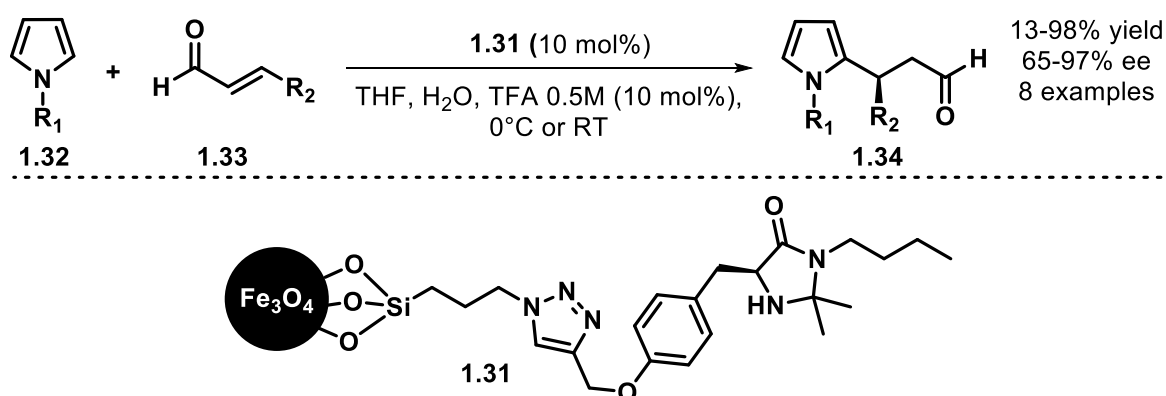
31. Luo, S.; Zheng, X.; Xu, H.; Mi, X.; Zhang, L.; Cheng, J.-P. *Adv. Synth. Catal.*, **349**:2431, 2007.

32. (a) Luo, S.; Zheng, X.; Cheng, J.-P. *Chem. Commun.*, **2008**:5719, 2008. (b) Zheng, X.; Zhang, L.; Li, J.; Luo, S.; Cheng, J.-P. *Chem. Commun.*, **47**: 12325, 2011. (c) Zeng, T.; Yang, L.; Hudson, R.; Song, G.; Moores, A. R.; Li, C.-J. *Org. Lett.*, **13**:442, 2011. (d) Gleeson, O.; Davies, G.-L.; Peschiulli, A.; Tekoriute, R.; Gun'ko, Y. K.; Connon, S. J. *Org. Biomol. Chem.*, **9**:7929, 2011. (e) Roy, S.; Pericàs, M. A. *Org. Biomol. Chem.*, **7**: 2669, 2009.

33. Riente, P.; Yadav, J.; Pericàs, M. A. *Org. Lett.*, **14**:3668, 2012.

method could be applied to a wide range of aldehydes and both methyl- and benzyl-protected pyrroles with low to high yields and moderate to high enantiomeric excesses. The recyclability studies showed that the catalysts could be reused without any drops in the enantiomeric excesses but with considerable losses in yield after the 2nd reaction run (from approximately 70% in the 2nd reaction run to 50% in the 3rd run).

Another interesting type of organocatalyst successfully employed as heterogeneized catalysts are crown ethers, which are widely use phase-transfer catalysts.³⁴

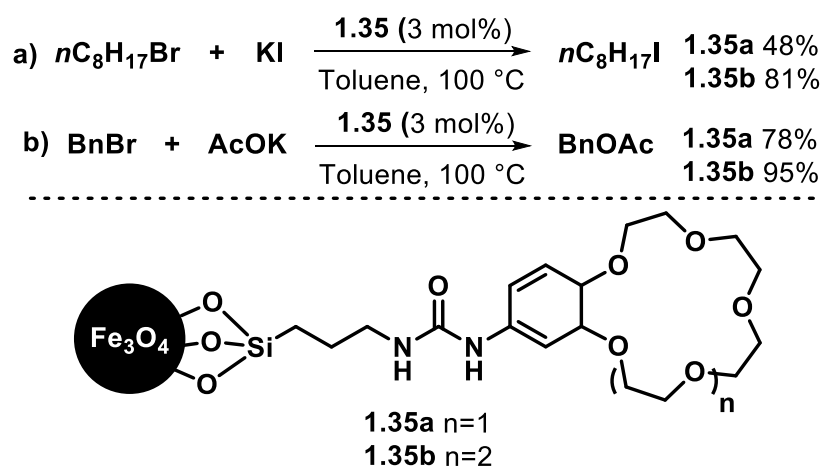


SCHEME 1.15 - Asymmetric Friedel-Crafts alkylation of N-substituted pyrroles with α,β -unsaturated aldehydes using a supported MacMillan catalyst.

The supporting of these catalysts in magnetic supports solves the toxicity and recoverability issues associated to these compounds. In an interesting report, a supported crown ether was supported on magnetite nanoparticles through an amine linker and had its catalytic activity evaluated on the halogen exchange reaction of *n*-bromooctane with KI (Scheme 1.16a) and in the substitution reaction of benzyl bromide with AcOK (Scheme 1.16b).

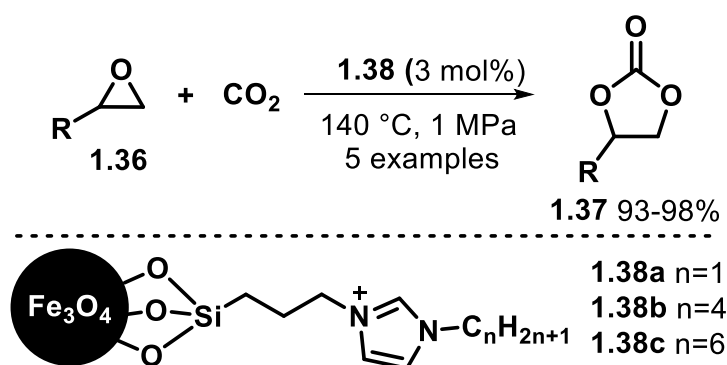
Both reactions were conducted in toluene under solid-liquid phase-transfer conditions, and catalyst **1.35b** was able to afford the products in very high yields (81 and 95%, respectively). Remarkably, the catalyst was used in 8 consecutive reaction cycles without any losses in yield.

34. Kawamura, M.; Sato, K. Chem. Commun., **2007**:3404, 2007.



SCHEME 1.16 - (a) Halogen exchange reaction of *n*-bromooctane with KI and (b) substitution reaction of benzyl bromide with AcOK using supported crown ethers as catalysts.

As for supported ionic liquids, one of the first reports in this field consists on an imidazolium ionic liquid supported on magnetite nanoparticles **1.38** via the quaternization of *N*-alkyl imidazole with 3-chloropropyl-trimethoxysilane, which was used as linker (Scheme 1.17).³⁵ Supported ionic liquids with different side alkyl side chains were synthesized (**1.38a-c**) and had their catalytic activity evaluated on the CO₂ cycloaddition reactions. The ionic liquid with the shorter alkyl chain afforded the highest yields, and, therefore, was the one chosen to evaluate the scope of the reaction. The protocol could be applied to several types

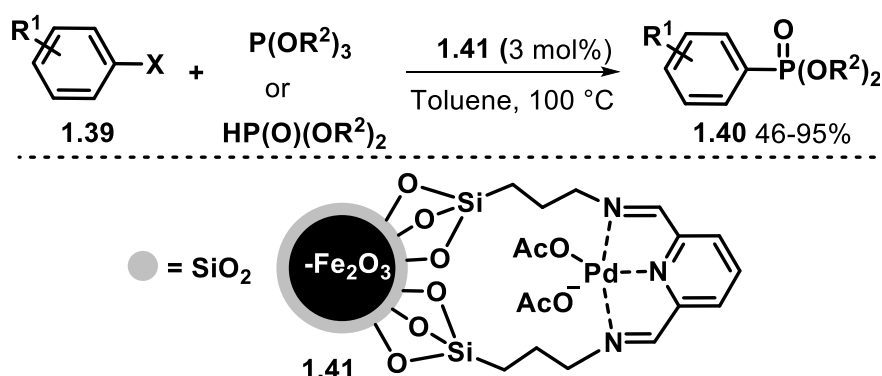


SCHEME 1.17 - Cycloadditions of carbon dioxide to epoxides catalyzed by magnetically recoverable ionic liquids.

35. Zheng, X.; Luo, S.; Zhang, L.; Cheng, J.-P. *Green Chem.*, **11**:455, 2009.

of epoxides with results comparable with that of the free ionic liquid catalysts. Recyclability studies were also conducted and showed that the catalyst could be recycled for up to 11 times.

Supported organometallic complexes have also currently become a blooming research field. This type of catalyst has been employed in several types of reactions, for instance, a Pd complex of a NNN pincer ligand supported on γ - $\text{Fe}_2\text{O}_3@ \text{SiO}_2$ **1.41** as the first magnetically recoverable heterogeneous catalyst for C–P bond forming reactions (Scheme 1.18).³⁶



SCHEME 1.18 - Synthesis of arylphosphonates via C–P bond formation catalyzed by a magnetically recoverable Pd complex.

The catalyst was used in the synthesis of arylphosphonates **1.40** via C–P bond formation by a cross-coupling reaction of different electrophilic benzenes **1.39** with phosphite esters under solvent-free conditions. The method could be successfully applied for a wide range of substrates with moderate to high yields. Besides the recyclability of the catalyst, which showed that those could be reused for 4 reaction runs without any significant loss in yield, the possibility of leached palladium species catalyzing the reaction was also studied and was ruled out.

36. Sobhani, S.; Vahidi, Z.; Zeraatkar, Z.; Khodadadi, S. RSC Adv., **5**:36552, 2015.

Chapter 2

2.

Magnetically Recyclable Niobium Nanocatalyst: Synthesis, Characterization and Application on the Multicomponent Biginelli Reaction

General overview

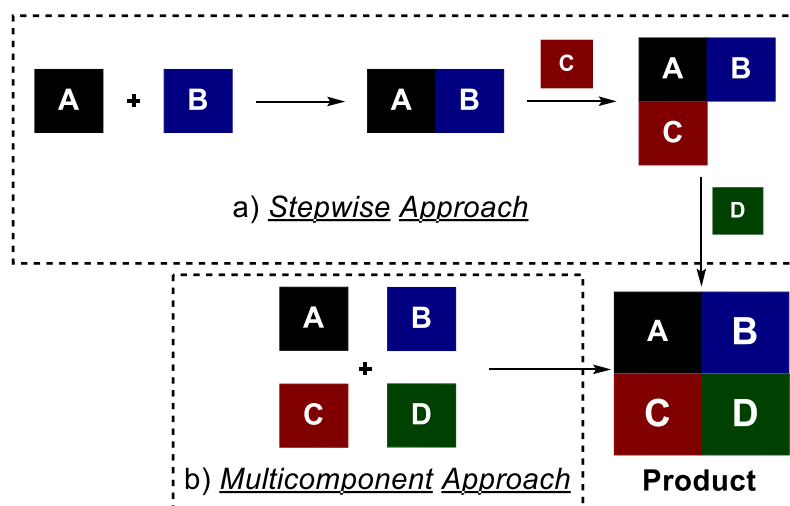
This chapter will address the design, synthesis and characterization of a new magnetically recoverable niobium nanocatalyst for application in the Biginelli multicomponent reaction. A brief introduction regarding multicomponent reactions, and more specifically, Biginelli reaction, will be presented comprising some important historical remarks as well as the latest advances concerning the development of catalysts for these reactions.

2.1 - Introduction

2.1.1 - Multicomponent Reactions

Multicomponent reactions (MCRs) are of exceptional importance in organic synthesis, especially in drug discovery processes. In such reactions, more than two reactants combine in a successive manner to afford selectively products that retain the majority of the atoms of the starting materials. Differently from a stepwise process, in which the intermediates in each step are isolated and further reacted, in MCRs all the components react in a one-pot fashion (Scheme 2.1); in that way, these processes display high atom economy, less waste production, and considerably lower time and energy consumption.³⁷

37. Cioc, R. C.; Ruijter, E.; Orru, R. V. A. *Green Chem.*, **16**:2958, 2014.



SCHEME 2.1 - Pictorial view of the comparison between a stepwise and a multicomponent approach.

Multicomponent reactions have been developed since the beginning of the 19th century, with ground-breaking reactions such as the Strecker synthesis of α -amino nitriles that can be further converted to α -aminoacids by hydrolysis (Scheme 2.2a).³⁸ Following this lead, several famous important reactions were reported for the synthesis of heterocycles, namely the Radziszewski synthesis of imidazoles (Scheme 2.2b),³⁹ the Hantzsch ester synthesis (Scheme 2.2c),⁴⁰ and a decade later, the Biginelli synthesis of 3,4-dihydropyrimidin-2(1*H*)-ones (Scheme 2.2d).⁴¹ In the 20th century, other important MCRs were disclosed, such as the Mannich reaction (Scheme 2.2e),⁴² the Bucherer-Bergs synthesis of hydantoins (Scheme 2.2f)⁴³ and later the Ugi (Scheme 2.2f)⁴⁴ and Passerini⁴⁵ (not showed in Scheme 2.2) reactions, which are among the most important reactions for the synthesis of biologically active molecules.

38. Strecker, A. Liebigs. Ann. Chem., **27**:75, 1850.

39. Radziszewski, B. Ber. Dtsch. Chem. Ges., **15**:1499, 1882.

40. Hantzsch, A. Liebigs. Ann. Chem., **215**:1, 1882.

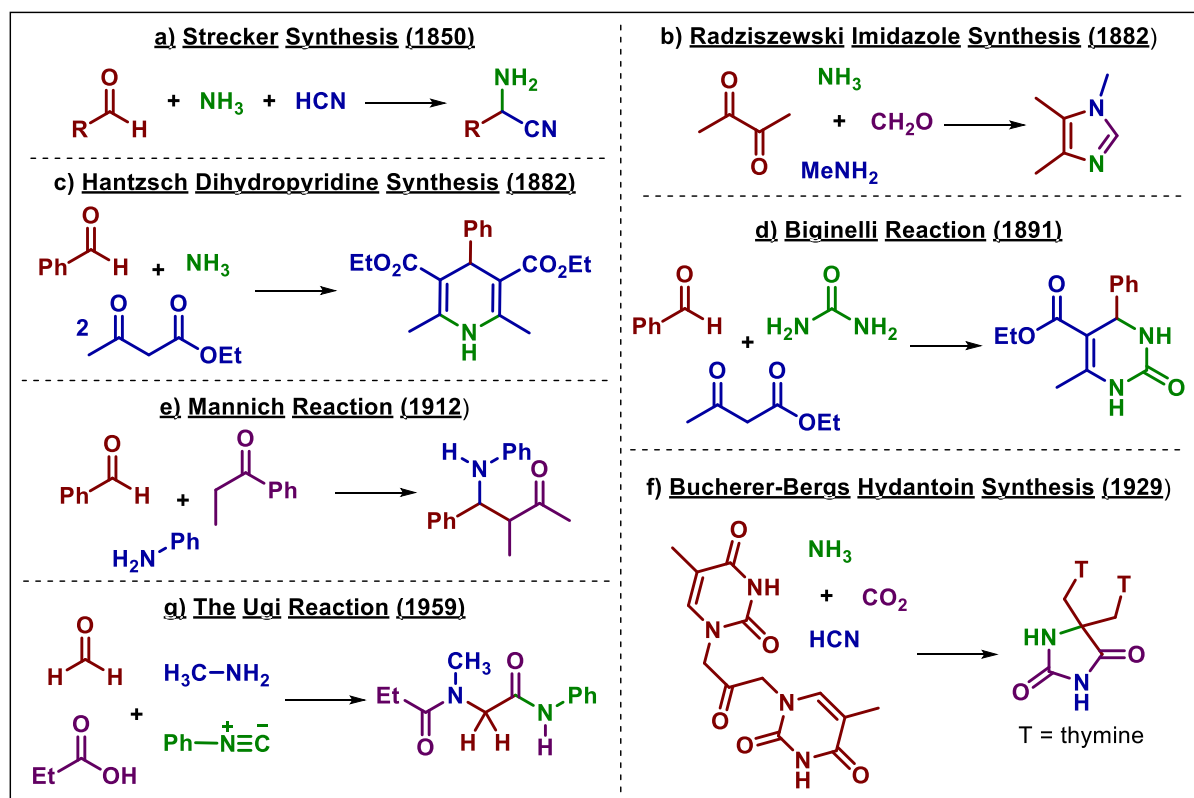
41. Biginelli, P. Chemische Berichte, **24**:1317, 1891.

42. Mannich, C.; Krosche, W. Arch. Pharm., **250**:647, 1912.

43. Bucherer, H. T.; Lieb, V. A. J. Prakt. Chem., **140**:151, 1934.

44. Ugi, I; Meyr, R.; Fetzer, U.; Steinbrückner, C. Angew. Chem. **71**:386, 1959.

45. Passerini, M.; Simone, L. Gazz. Chim. Ital. **51**:126, 1921.



SCHEME 2.2 - Examples of some of the most famous multicomponent reactions.

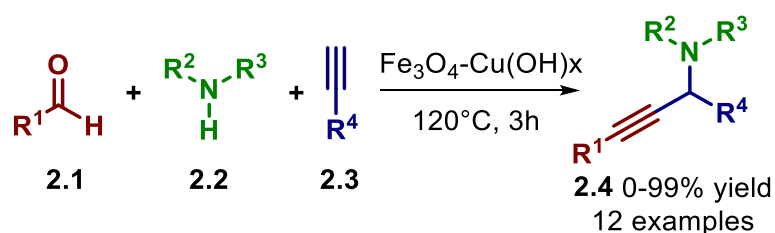
However, even with the encouraging features of MCRs and the biological importance of their products, several processes reported in the last years present disadvantages such as harsh reaction conditions, high reagent excesses, high temperatures, use of toxic solvents and expensive unrecoverable catalysts. In order to overcome these drawbacks, several groups have been reporting the development of new catalytic processes.⁴⁶ In this context, the use of magnetically recoverable catalysts has been rising as a promising alternative in this field. The magnetically recoverable catalysts used in these reactions are mainly constituted by (1) bare ferrite nanoparticles (Fe_3O_4 , $\gamma-Fe_2O_3$, $MnFe_2O_4$, $CuFe_2O_4$, $CoFe_2O_4$),⁴⁷ (2) metal oxides/hydroxides impregnated directly to the

46. (a) Ganem, B. *Acc. Chem. Res.*, **42**:463, 2009. (b) Climent, M. J.; Corma, A.; Iborra, S. *RSC Adv.*, **2**:16, 2012. (c) Biggs-Houck, J. E.; Younai, A.; Shaw, J. T. *Curr. Opin. Chem. Biol.*, **14**:371, 2010.

47. (a) Koukabi, N.; Kolvari, E.; Khazaei, A.; Zolfigol, M. A.; Shirmardi-Shaghasemic, B.; Khavasid, H. R. *Chem. Commun.*, **47**:9230, 2011. (b) Ghasemzadeh, M. A.; Safaei-Ghomi, J.; Molaei, H. *C. R. Chimie*, **15**:969, 2012. (c) Dandia, A.; Jain, A. K.; Sharma, S. *RSC Adv.*, **3**:2924, 2013. (d) Rostamnia, S.; Nuri, A.; Xin, H.; Pourjavadi, A.; Hosseini, S. H. *Tetrahedron*

surface of the magnetic nanoparticles,⁴⁸ (3) metals attached to the surface of the magnetic nanoparticles through linkers,⁴⁹ or (4) organocatalysts grafted to the magnetic support.⁵⁰

One of the first reports on the preparation of magnetically recoverable catalysts for application in multicomponent reactions was made by Yus's group in 2009,^{48a} in which a copper catalyst was developed and applied in the Mannich reaction (Scheme 2.3). The catalyst proved to be highly efficient, being able to promote the reaction with a very low loading (0.1 mol%) in a solvent-free reaction system. Several terminal alkynes **2.3** and secondary amines **2.2** were tolerated in the reaction, affording the products **2.4** in moderate to high yields (39-99%). Primary amines, though, were unreactive.



SCHEME 2.3 - Mannich reaction catalyzed by a magnetically recoverable copper catalyst prepared via direct impregnation.

Another pioneering work was reported by Varma and co-workers in 2012.^{49a} In this work, the group synthesized the magnetically recoverable copper catalyst **2.7** by supporting copper ions on magnetite using glutathione as linker (Scheme 2.4).

Lett., **54**:3344, 2013. (e) Ghahremanzadeh, R.; Rashid, Z.; Zarnani, A. H.; Naeimi, H. Appl. Catal. A-Gen., **467**:270, 2013. (f) Li, B.-L.; Zhang, M.; Hu, H.-C.; Dub, X.; Zhang, Z.-H. New J.Chem., **38**:2435, 2014.

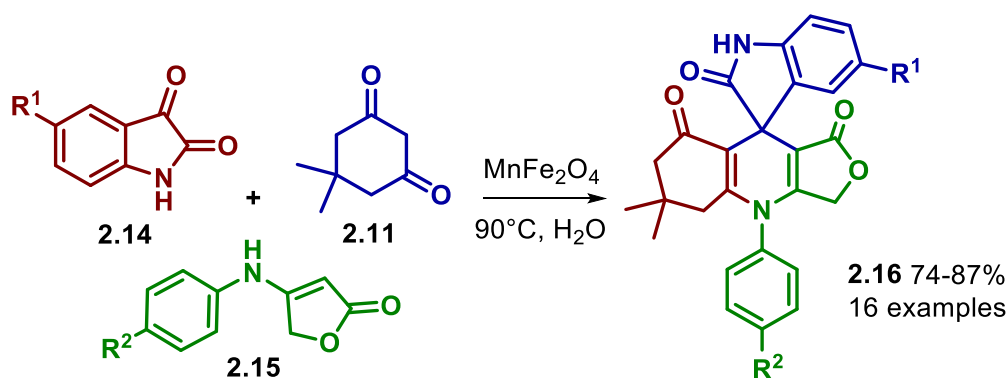
48. (a) Aliaga, M. J.; Ramón, D. J.; Yus, M. Org. Biomol. Chem., **8**: 43, 2010. (b) Gawande, M. B.; Velhinho, A.; Nogueira, I. D.; Ghumman, C. A. A.; Teodoro, O. M. N. D.; Branco, P. S. RSC Adv. **2**:6144, 2012.

49. (a) Baig, R. B. N.; Varma, R. S. Green Chem., **14**:625, 2012. (b) Xiong, X.; Cai, L.; Catal. Sci. Technol., **3**:1301, 2013. (c) Dehghani, F.; Sardarian, A. R.; Esmaeilpour, M. J. Organomet. Chem., **743**:87, 2013.

50. (a) Gawande, M. B.; Velhinho, A.; Nogueira, I. D.; Ghumman, C. A. A.; Teodoro, O. M. N. D.; Branco, P. S. RSC Advances, **2**:6144, 2012.

After the optimization of the reaction conditions for the Mannich reaction, the scope and limitations of the process were evaluated; the protocol could be successfully applied to different functionalized aldehydes **2.1** and anilines **2.8**. Aiming to further explore the potential of the newly synthesized supported-organocatalyst, the group also evaluated its application on the Hantzsch reaction (Scheme 2.5b).

Another interesting protocol was disclosed by Naeimi's group in 2013.^{47e} The group disclosed the use of bare MnFe_2O_4 nanoparticles as catalysts in the multicomponent reaction between an isatins **2.14**, dimedone **2.11** and anilinolactones **2.15** to produce the spirooxindole derivatives **2.16** (Scheme 2.6). Several isatins and anilinolactones could be employed in the reaction, affording the products in high yields.



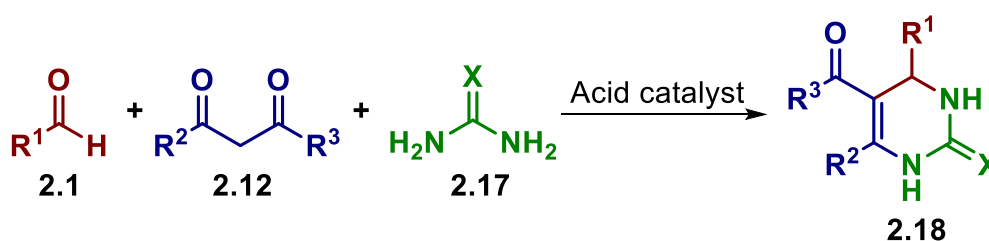
SCHEME 2.6 - Synthesis of spirooxindole derivatives **2.20** via a multicomponent reaction catalyzed by MnFe_2O_4 nanoparticles.

In all of the aforementioned examples (Schemes 2.3-2.6), the catalyst recyclability was evaluated, and in all cases, the catalysts could be recovered from the reaction medium with the aid of a magnetic field and reused for at least 4 reaction cycles.

Another multicomponent reaction that has attracted considerable interest in the last few years regarding the development of new catalysts is the Biginelli reaction, mostly due to the pronounced pharmacological activity of its products.

2.1.2 - Biginelli Reaction

The Biginelli reaction (Scheme 2.7) is a century-old reaction considered as one of the most well designed methodologies for the synthesis of dihydropyrimidinones/thiones derivatives (DHMPs) **2.18** through the acid-catalyzed condensation of a β -ketoester **2.12a**, an aldehyde **2.1** and urea/thiourea **2.17**.⁵¹



DHMPs are a very important family of compounds mostly known for their diverse pharmacological properties; these compounds may act as calcium channel modulators, antibacterial, antiviral, anti-cancer or anti-hypertensive agents. More specific examples of DHMPs compounds that display promising pharmacological activities are depicted in Scheme 2.8. Compounds **2.19** and **2.20**, for instance, are orally active antihypertensive agents, while compound **2.22** is a α_{R1} adrenoceptor-selective antagonist. Another Biginelli product that presents very interesting features is monastrol **2.21**, a rather simple product that can be synthesized through the condensation of 3-hydroxybenzaldehyde, ethyl acetoacetate and thiourea, a specific inhibitor of the the mitotic kinesin Eg5 motor protein and, therefore, a lead for the development of anticancer drugs. Some alkaloids like **2.23** inhibit the binding of HIV envelope protein gp-120 to human CD4 cells, being potential leads for AIDS therapy.⁵²

51. (a) Panda, S. S.; Khanna, P.; Khanna, L. *Curr. Org. Synth.* **16**:507, 2012. (b) Majid, M. H.; Asadi, S.; Boshra, B. M. *Molecular Diversity*, **17**:389, 2013. (c) Graaff, C.; Ruijter, E.; Orru, R. V. A. *Chem. Soc. Rev.*, **41**: 3969, 2012.

52. Kappe, C. O. *Acc. Chem. Res.*, **33**:879, 2000.

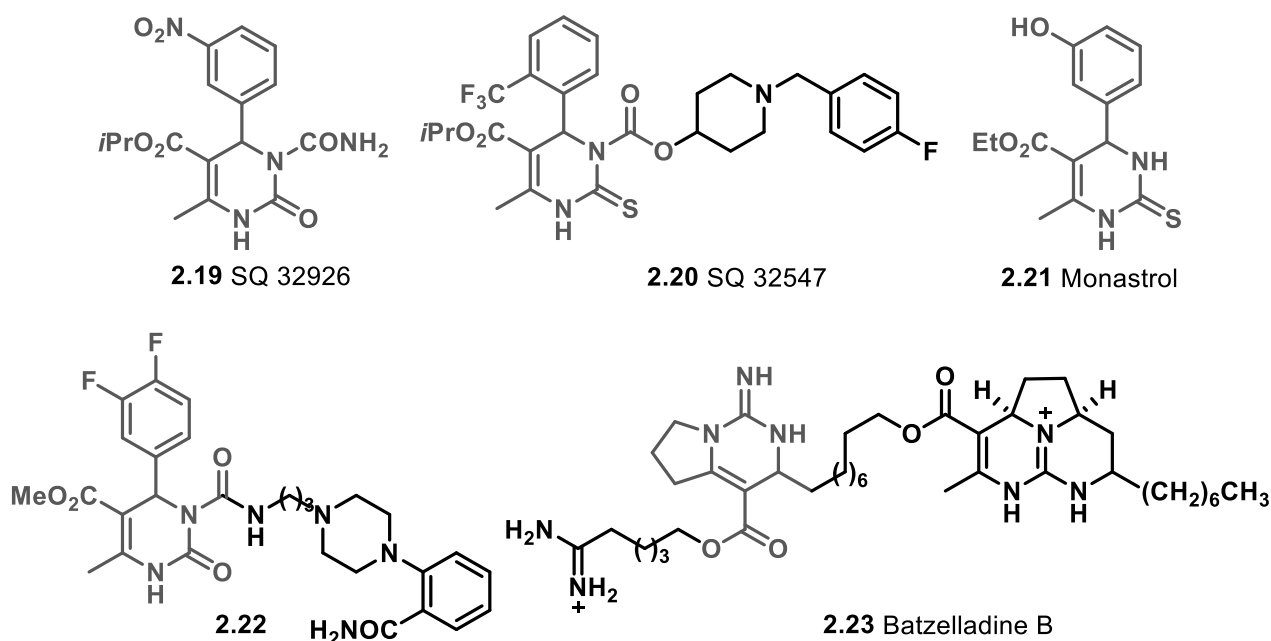


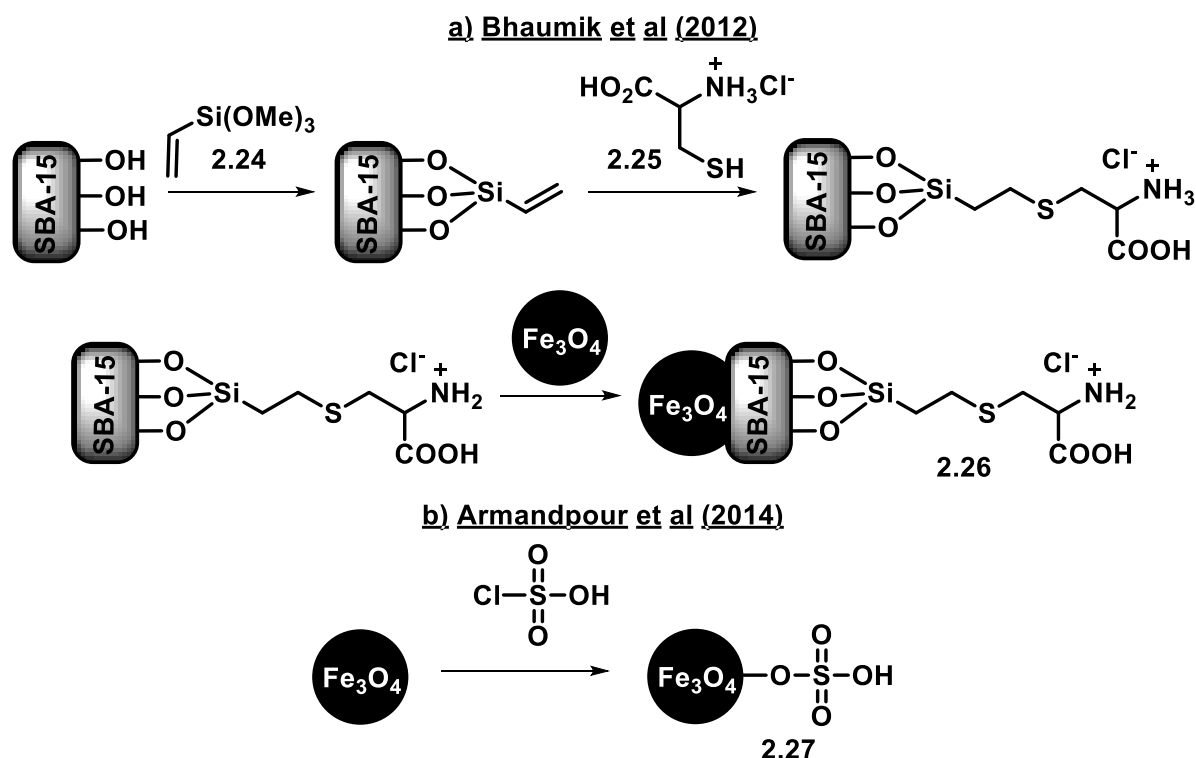
FIGURE 2.1 - Structures of DHMPs that display pharmacological activities.

The reported biological activities of DHPMs have encouraged research groups to build up wide structural diversity libraries of bioactive compounds that are active even as racemates.⁵³ Due to the vast application of DHPM derivatives, many approaches can be found in literature for their synthesis.⁵⁴ Nevertheless, most protocols present severe limitations e.g. low yields, high cost and catalyst loadings, low catalyst recovery and recyclability.

In order to surpass these limitations, several magnetically recoverable catalysts have been reported in the last few years. The reports include mainly the use of organocatalysts, ionic liquids and metal complexes/oxides supported on magnetic nanoparticles.

53. (a) Lacotte, P.; Buisson, D. A.; Ambroise, Y. *Eur. J. Med. Chem.*, **62**: 722, 2013. (b) Crespo, A.; Maatougui, A. E.; Biagini, P.; Azuaje, J.; Coelho, A.; Brea, J.; Loza, M. I.; Cadavid, M. I.; García-Mera, X.; Gutiérrez-de-Teránand, H.; Sotelo, E. *ACS Med. Chem. Lett.*, **4**:1031, 2013. 54. (a) Clark, J H.; Macquarrie, D. J.; Sherwood, J. *Chem. Eur. J.* **19**:5174, 2013. (b) Shen, Z.-L.; Xu, X.-P.; Ji, S.-J. *J. Org. Chem.* **75**:1162, 2010. (c) Nandi, G. C.; Samaiand, S.; Singh, M. S. *J. Org. Chem.*, **75**:7785, 2010. (d) Ramos, L. M.; Guido, B. C.; Nobrega, C. C.; Corrêa, J. R.; Silva, R. G.; Oliveira, H. C. B.; Gomes, A. F.; Gozzo, F. C.; Neto, B. A. *D. Chem. Eur. J.*, **19**: 4156, 2013. (e) Sharma, N.; Sharma, U. K.; Kumar, R.; Richa, Sinha, A. K. *RSC Adv.*, **2**:10648, 2012. (f) Zhu, C.; Yang, B.; Zhao, Y.; Fu, C.; Tao, L.; Wei, Y. *Polym. Chem.*, **4**:5395, 2013.

A seminal report on magnetically recoverable catalysts for Biginelli reaction was made by Bhaumik's group, in which the authors reported the synthesis of the catalyst **2.26**, assembled by Fe_3O_4 nanoparticles impregnated to a cysteine-functionalized mesoporous silica type SBA-15 (Scheme 2.8a).⁵⁵ The catalyst was prepared by the surface functionalization of SBA-15 with vinyltrimetoxysilane **2.24** followed by the grafting of cysteine **2.25** to the terminal alkene through a thiol-ene reaction; magnetite was then attached to the catalyst through an impregnation step. The catalyst could be successfully used on Biginelli reaction, and 11 examples were presented, with yields varying from 80-85% with reaction times varying from 5-12h for the differently substituted benzaldehydes. The catalyst could be reused for 7 times with no loss on the catalytic activity. Curiously, neither the reaction with the bare magnetite nor the one with SBA-15 functionalized with cysteine afforded good yields (50 and 0%, respectively), and



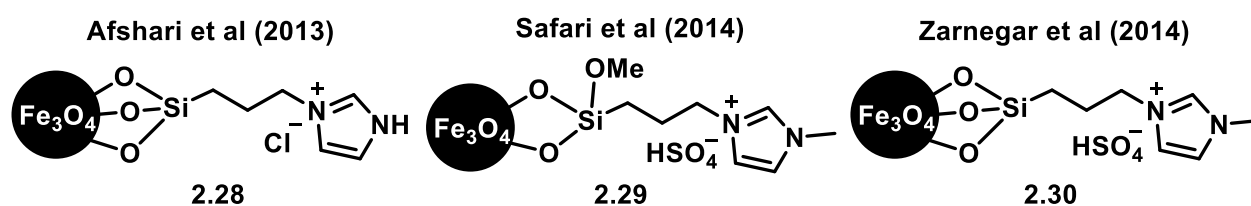
SCHEME 2.8 - Preparation of a) a Fe_3O_4 -SBA-15-cysteine catalyst and b) a Fe_3O_4 - OSO_3H catalyst.

55. Mondal, J.; Sen, T.; Bhaumik, A. Dalton Trans., **41**:6173, 2012.

the authors attributed the catalytic activity to a combination of the acidity of the components of the catalyst.

The preparation of another supported organocatalyst, the magnetically recoverable sulfonic acid organocatalyst **2.27**, was achieved by merely reacting chlorosulfonic acid with magnetite nanoparticles and reported by Armandpour's group in 2014 (Scheme 2.8b).⁵⁶ The group accomplished the synthesis of 21 compounds with yields ranging from 69 to 95% in 3 hours, though only aromatic aldehydes were evaluated. Additionally, a high catalyst loading was necessary in order to promote the reaction.

Supported-ionic liquids also proved to be good catalysts for Biginelli reaction and those could be prepared by the immobilization of alkoxy-silane-functionalized ionic liquids directly to the surface of bare magnetite nanoparticles; some examples (**2.28** – **2.30**) reported in the last few years employing this approach are depicted in Scheme 2.9.⁵⁷ In the case of all three catalysts, the products could be achieved in high yields and low reaction times (30 min – 1h), though high catalyst loadings are required and only aromatic aldehydes are tolerated.



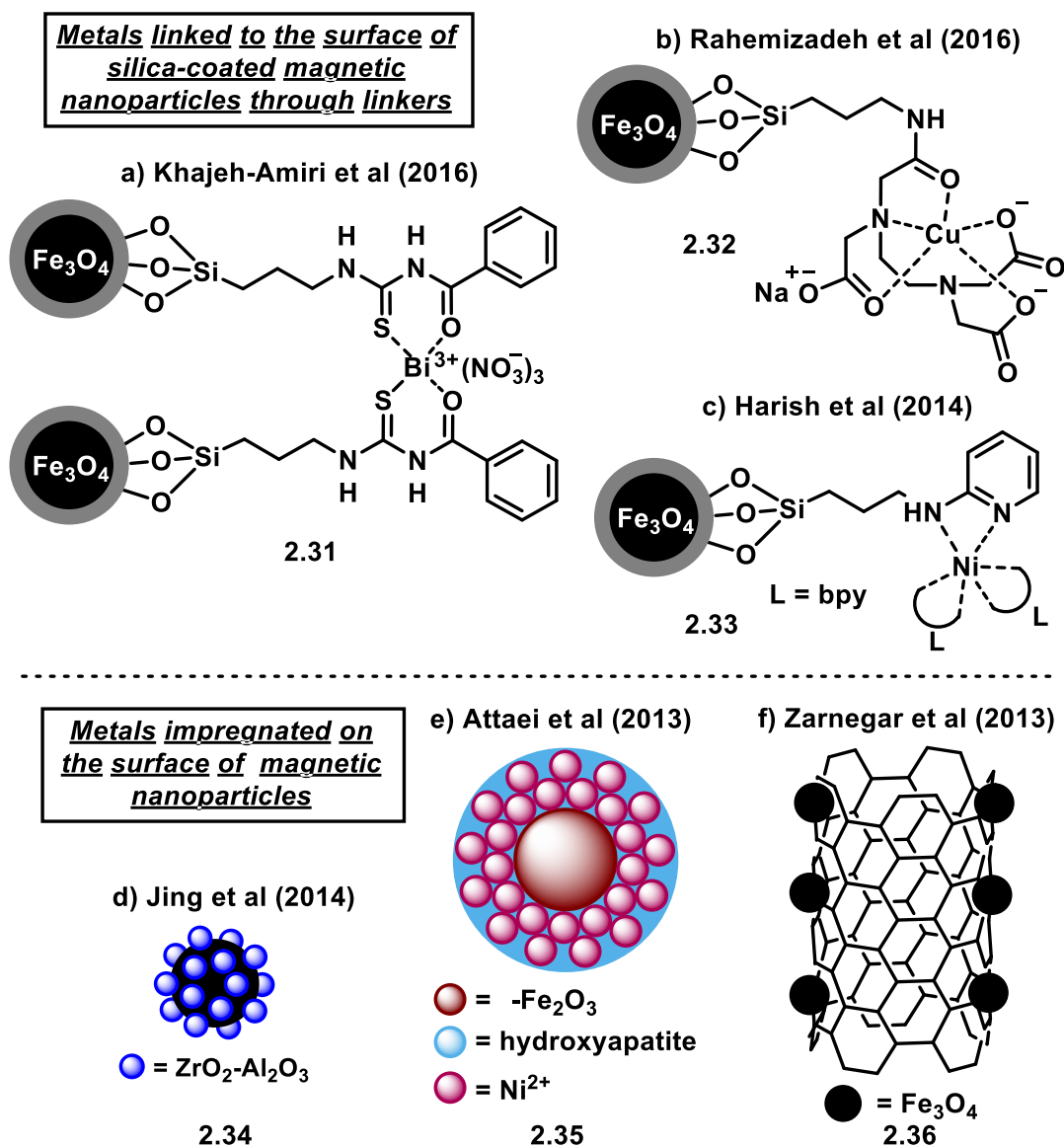
SCHEME 2.9 - Examples of magnetically recoverable ionic liquids employed as catalysts on Biginelli reaction.

Another class of magnetically recoverable catalysts highly employed in Biginelli reaction are supported metals. In this case, the immobilization of the active phase is performed either on the surface of silica-coated magnetic

56. Kolvari, E.; Koukabi, N.; Armandpour, O. *Tetrahedron* **70**:1383, 2014.

57. (a) Nazari, S.; Saadat, S.; Fard, P. K.; Gorjizadeh, M.; Nezhad, E. R.; Afshari, M. *Monatsh Chem* **144**:1877, 2013. (b) Zarnegar, Z.; Safari, J. J. *Nanopart Res.*, **16**:2509, 2014. (c) Safari, J.; Zarnegar, Z. *New J.Chem.*, **38**:358, 2014.

nanoparticles through linkers, forming complexes (2.31 – 2.33, Scheme 2.10) or using bare magnetite nanoparticles as support via impregnation (2.34 and 2.35, Scheme 2.10). Another interesting example of magnetically recoverable metal catalyst for Biginelli reaction is constituted by magnetite nanoparticles supported over carbon nanotubes 2.36.⁵⁸ As in the case of supported ionic liquids, most of



SCHEME 2.10 - Examples of magnetically recoverable metal catalysts for Biginelli reaction.

58. (a) Girija, D.; Naik, H. S. B.; Kumar, B. V.; Sudhamani, C. N.; Harish, K. N. Arab. J. Chem. doi:10.1016/j.arabjc.2014.08.008. (b) Mobinikhaledi, A.; Foroughifar, N.; Khajeh-Amiri, A. *Reac Kinet Mech Cat* **17**:59, 2016. (c) Sheykhani, M.; Yahyazadeh, A.; Rahemizadeh, Z. *RSC Adv.*, **6**:34553, 2016. (d) Safari, J.; Zarnegar, Z. *RSC Advances*, **3**:17962, 2013. (e) Wang, A.; Liu, X.; Su, Z.; Jing, H. *Catal. Sci. Technol.*, **4**:71, 2014. (f) Nezhad, E. R.; Abbasi, Z.; Moghaddam, M. R.; Attaei, M. A. *Iran. Chem. Commun.*, **1**:35, 2013.

these protocols involve the use of high catalyst loadings and all of them are exclusively applicable for aromatic aldehydes.

2.1.3 Niobium Compounds

Since late years, niobium compounds are known on account of their marked features when employed as supports for catalysts in a wide range of reactions, mostly in catalytic oxidations.⁵⁹

Even though there are a few differences in physicochemical properties between Nb and its neighbors in the periodic table (V, Mo, Zr), it is interesting to notice that the catalytic behavior and high acidity of niobium compounds are quite different from those displayed by the compounds of its surrounding elements. In fact, niobium-based catalysts display high acidity on their surface, exhibiting high activity and selectivity, even when water is present in the reaction media.⁶⁰

The niobium compounds that find most applications in catalysis are niobium(V) pentoxide (Nb_2O_5) and chloride (NbCl_5). Niobium pentoxide, particularly, has been widely applied in numerous reactions, namely dehydration of alcohols, oxidations, esterification, alkylations, isomerizations, hydrogenolysis and metathesis, primarily as catalytic support or a promoter. Hydrated niobium oxide ($\text{Nb}_2\text{O}_5 \cdot n\text{H}_2\text{O}$), also known as niobic acid, displays a high acid strength and

59. (a) Nowak, I.; Ziolk, M. *Chem. Rev.*, **99**: 3603, 1999. (b) García-Sancho, C.; Sádaba, I.; Moreno-Tost, R.; Mérida-Robles, J.; Santamaría-González, J.; López-Granados, M.; Maireles-Torres, P. *ChemSusChem*, **6**:635, 2013. (c) Ekhsan, J. M.; Lee, S. L.; Nur, H. *Appl. Catal. A-Gen.*, **471**:142, 2014. (d) Tiozzo, C.; Bisio, C.; Carniatoand, F.; Guidottia, M. *Catal. Today* **235**:49, 2014. (e) Chagas, P.; Oliveira, H. S.; Mambrini, R.; Hyaric, M. L.; Almeida, M. V.; Oliveira, L. C. A. *Appl. Catal. A-Gen.* **454**:88, 2013.

60. (a) Marin, M. L.; Hallett-Tapley, G. L.; Impellizzeri, S.; Fasciani, C.; Simoncelli, S.; Netto-Ferreira, J. C.; Scaiano, J. C. *Catal. Sci. Technol.*, **4**: 3044, 2014. (b) Ushikubo, T.; Iizuka, T.; Hattori, H.; Tanabe, K. *Catal. Today* **16**:291, 1993. (c) Armaroli, T.; Busca, G.; Carlini, C.; Giuttari, M.; Gallettib, A. M. R.; Sbrana, G. J. *Mol. Cat. A-Chem.* **151**: 233, 2000. (d) K. Tanabe, *Mater. Chem. Phys.* 1987, **17**, 217.

possesses both Lewis acid sites and Brønsted acid sites. The Lewis acid sites increase with increasing temperatures up to 500 °C (T and TT phases in the diagram depicted in Figure 2.2) and then decrease at higher temperatures (M and B phases). Brønsted acid sites are most abundant at temperatures up to 200 °C, when it is present as an amorphous compound, and decrease at higher temperatures.⁵⁹

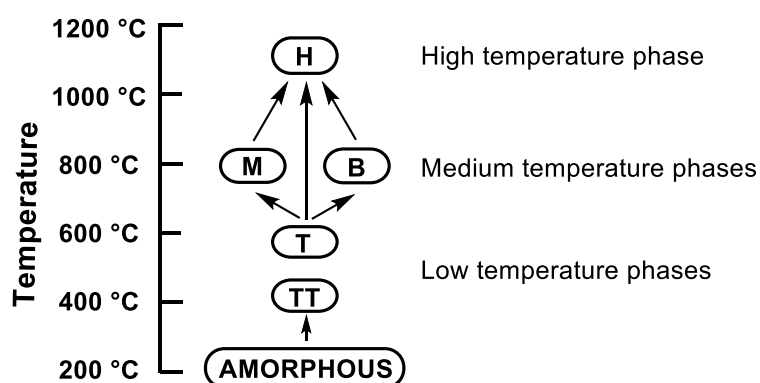
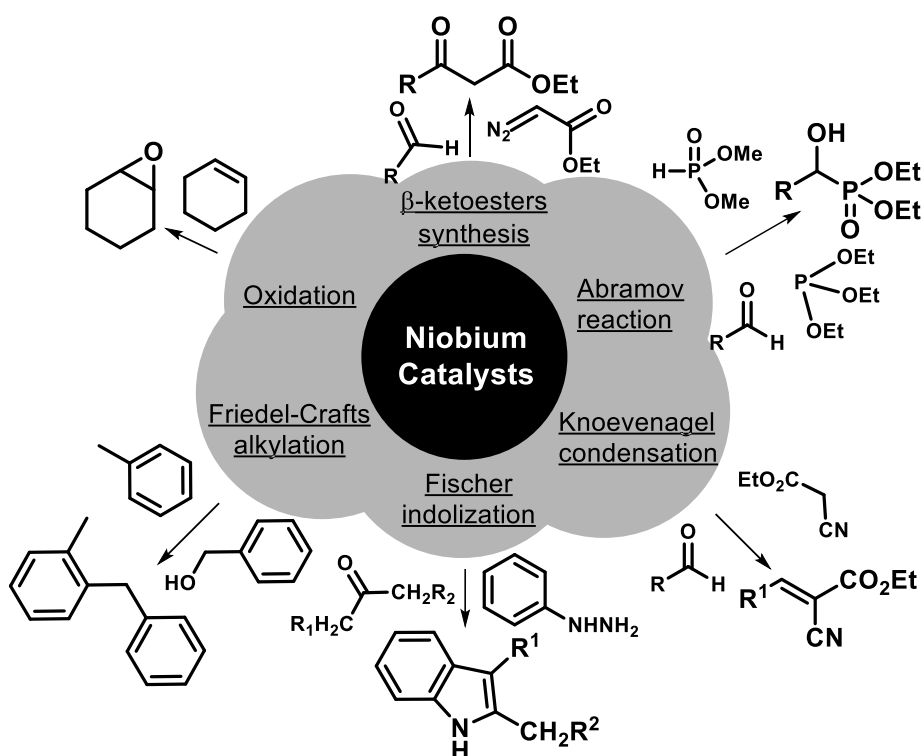


FIGURE 2.2 - Diagram showing the polymorphism of niobium oxides at different temperatures.

On the other hand, niobium chloride displays considerable applications in Organic Synthesis in reactions like Fischer indolization, synthesis of β -mercapto compounds, β -keto esters, Knoevenagel condensation, Friedel-Crafts acylation, Diels-Alder and Biginelli reaction.⁶¹ Scheme 2.11 summarizes the applications of niobium compounds in catalysis.

In spite of its promising reactivity, niobium chloride presents some disadvantages in its use, such as its low stability in the presence of moisture; its contact with water leads to hydrolysis, forming hydrochloric acid. In that way, the supporting of niobium compounds in solid supports for application in organic synthesis is highly desirable.

61. Arpini, B. H.; Bartolomeu, A. A.; Andrade, C. K. Z.; Silva-Filho, L. C.; Lacerda, V. *Curr. Org. Synth.*, **12**:570, 2015.



SCHEME 2.11 – Applications of niobium compounds in catalysis.

2.2 Aims-Objectives

Considering the exceptional chemical properties of niobium compounds, their relatively low prices, high availability in earth crust and the low application of supported niobium compounds in Organic Synthesis, the aim of the work described in this chapter was the development of a new magnetically recoverable niobium catalyst for application on Biginelli reaction. Specific objectives of this work include:

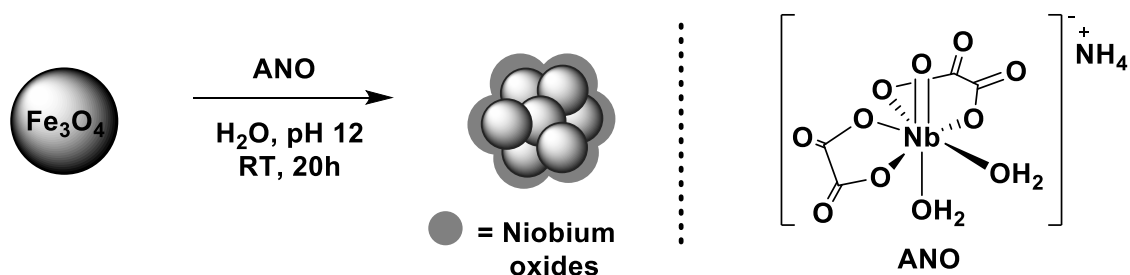
- ✓ Synthesis of a catalyst constituted by Fe_3O_4 as support and Nb_2O_5 as active phase;
- ✓ Full characterization of the catalyst;
- ✓ Evaluation of the catalytic activity of the newly developed catalyst on Biginelli reaction;

- ✓ Comparison of the catalytic activity of the niobium nanocatalyst with other known catalysts;
- ✓ Evaluation of the recyclability of catalyst.

2.3 - Results and Discussion

2.3.1 - Nanocatalysts characterization

The magnetite nanoparticles used as a solid support for the catalyst were prepared by the co-precipitation method using urea as a pH-controlling agent under ultrasound irradiation. This method was chosen because it is scalable and can be carried out under ambient conditions. The magnetite-niobium oxide nanocatalyst ($\text{Fe}_3\text{O}_4@\text{Nb}_2\text{O}_5$) was synthesized through a simple wet impregnation method using ammonium niobate oxalate hydrate (ANO, Scheme 2.12), $\text{C}_4\text{H}_4\text{NNbO}_9 \cdot 3\text{H}_2\text{O}$) as the niobium source (Scheme 2.12). The hydrolysis of the niobium precursor in alkaline media leads to the aggregation of niobium hydroxides that condensate over the surface of Fe_3O_4 nanoparticles giving off water and forming the Nb_2O_5 layer. For comparison purposes, copper and nickel nanocatalyst were also prepared through the same method using $\text{CuCl}_2 \cdot 2\text{H}_2\text{O}$ and $\text{Ni}(\text{NO}_3)_2 \cdot 2\text{H}_2\text{O}$ as copper and nickel sources, respectively.



SCHEME 2.12 - Preparation of the niobium nanocatalyst.

Both the support and the final nanocatalyst were fully characterized by X-ray diffraction (XRD), inductive coupled plasma-optical emission spectroscopy (ICP-OES), High Resolution Transmission Electron Microscopy

(HRTEM), Scanning Transmission Electron Microscopy (STEM), and temperature programmed desorption of ammonia (NH₃-TPD). The copper and nickel nanocatalysts were characterized through XRD and ICP measurements.

The X-ray powder diffraction (XRD) measurements were conducted to confirm the magnetite crystallographic phase and to calculate the average size of crystallites by the Debye-Scherrer equation (Equation 2.1):

$$D_{hkl} = \frac{K\lambda}{\beta \cos(\theta)} \quad \text{Equation 2.1}$$

In this equation, D is the average crystallite size of the crystallite, K is a constant related to the shape of the particles (K = 0.94 for a sphere-shaped particle), λ is the wavelength of the X-ray radiation (in this case, CuK α λ = 1.54056 Å), θ is the diffraction angle of the peak of choice and $\beta(2\theta)$ is the full width at half maximum (FWHM) of the peak of choice. The XRD diffractograms for the niobium nanocatalyst and the Fe₃O₄ nanoparticles used as support are showed in Figure 2.3.

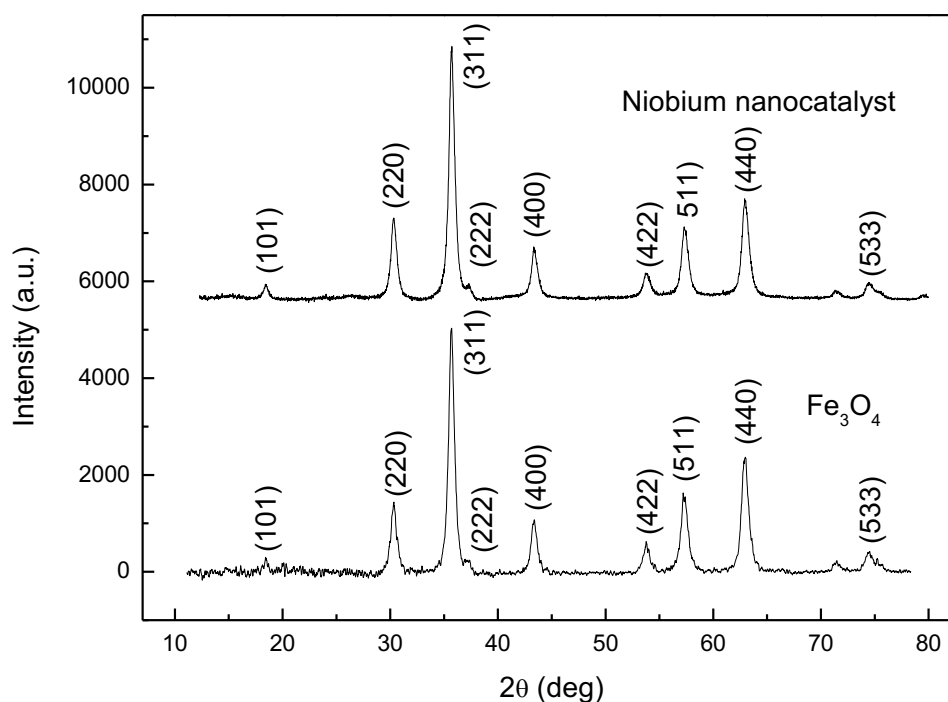


FIGURE 2.3 - X-ray diffractogram for Fe₃O₄ and the niobium nanocatalyst.

The diffractogram for the support showed the characteristic peaks of the inverted spinel structure, characteristic of magnetite, while the diffractogram for $\text{Fe}_3\text{O}_4@ \text{Nb}_2\text{O}_5$ showed only the diffraction peaks of magnetite, what was already expected, considering the amorphous character of $\text{Nb}_2\text{O}_5 \cdot n\text{H}_2\text{O}$.⁵⁴ The exact amount of niobium on the nanocatalyst was determined by ICP-OES and it was found to be 6.5 wt%. The calculated average size was 17 nm.

Analogous copper and nickel nanocatalysts were synthesized employing the same method in order to have their catalytic activity compared with that of niobium; these catalysts were characterized by XRD and ICP-OES. Their diffractogram (Figure 2.4) also showed only characteristic peaks of the Fe_3O_4 nanoparticles. The non-appearance of the peaks related to copper and nickel oxides may be related to their relatively low amount and high dispersion in the catalyst. The amount of copper and nickel impregnated to the nanocatalysts were determined by ICP-OES and it was found to be 8.4% for both copper and nickel nanocatalysts.

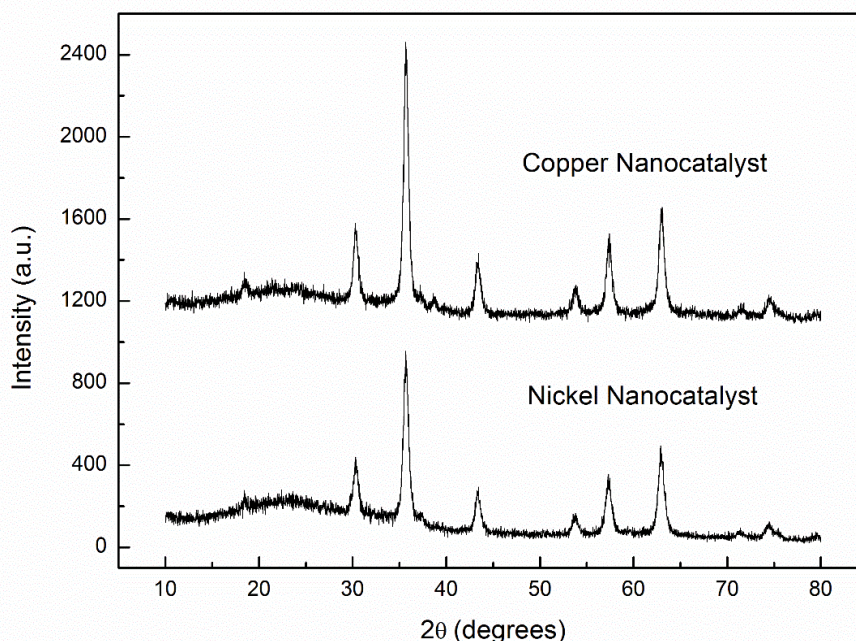


FIGURE 2.4 - X-ray diffractogram for the copper and nickel nanocatalysts.

The TEM images of the nanocatalyst (Figure 2.5a) showed that the particles exhibited equiaxial morphology and are within the nanorange sizes (15-

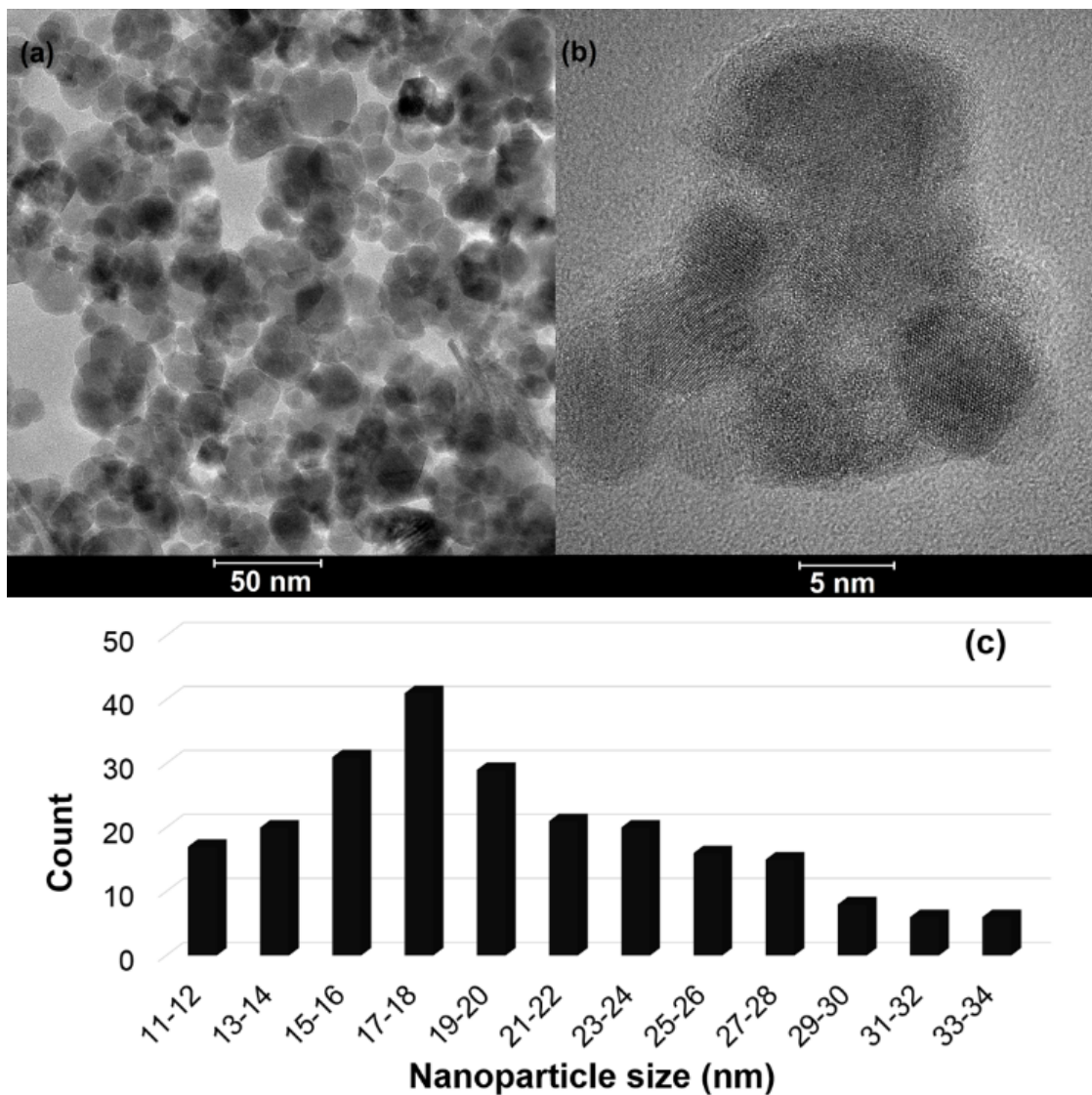


FIGURE 2.5 - (a) TEM image, (b) HRTEM image and (c) particle size distribution analysis for the niobium nanocatalyst.

40 nm), with some tendency to clustering. The particle count (Figure 2.4c) showed that in spite of the main particle size being around 17-18 nm, which corroborates with the XRD calculations, the particles are not monodisperse, that is, they are present in the sample in a wide range of sizes. Moreover, a layer around a small cluster of nanoparticles can be seen in Figure 2.5b. To comprehend the formation of this layer around the nanoparticles and to evaluate the incorporation of Nb_2O_5 into the Fe_3O_4 nanoparticle surface, a STEM analysis was performed. Figure 2.6a shows the details of the bright-field STEM image and Figure 2.6b, the line along which the energy-dispersive X-ray spectroscopy (EDS) line profiles of the niobium nanocatalyst were recorded. The EDS line profile shows the niobium and

iron composition along the line featured in Figure 2.6a, and it is noticeable that the niobium composition is constant along the entire line. The iron composition is higher in the center of the nanoparticles cluster and lower at the edges: from 0 to 15 nm, at the left edge of the sample, the iron composition is constant and near to zero, while in the center, from 16 nm to 125 nm, it is considerably higher; at the right edge of the sample, from 126 to 140 nm, the iron composition goes back to zero.

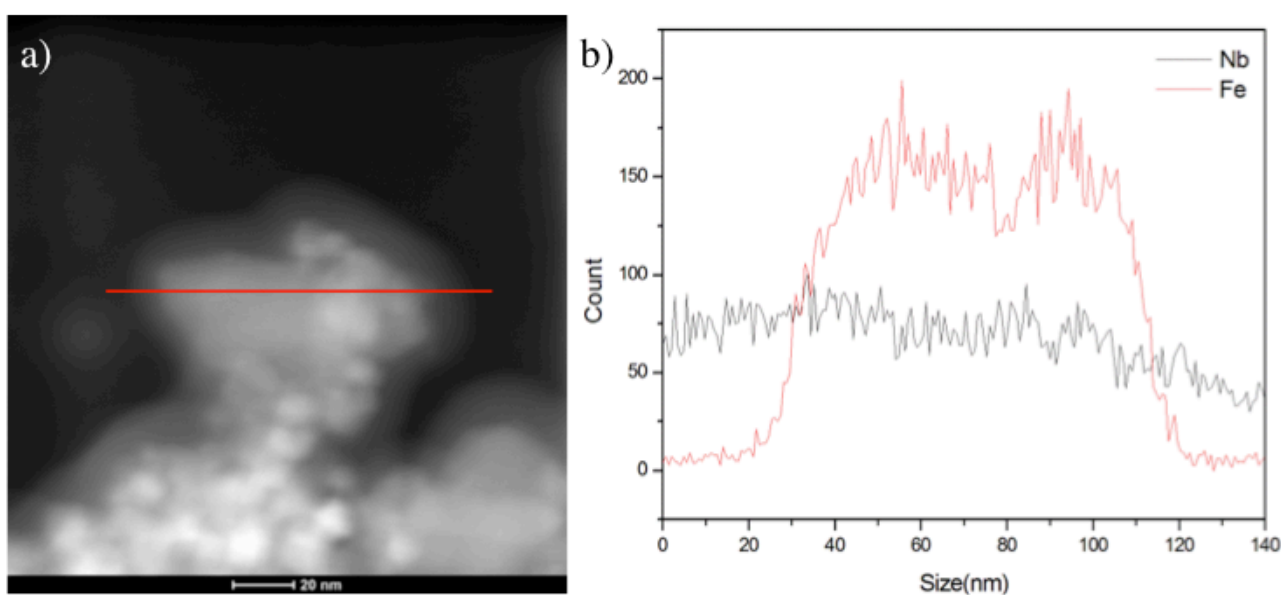


FIGURE 2.6 - (a) BF-STEM image showing the amorphous Nb_2O_5 on the magnetite surface and (b) EDS line profile.

These results suggest that the Nb_2O_5 fully coats the nanoparticles cluster, forming a 15 nm layer around it. The EDS results are fairly interesting, because the formation of a full layer of Nb_2O_5 around the magnetite support eliminates any possibility of iron oxides participating on the catalytic reactions. EDS elemental maps were also acquired in low magnification to certify the homogeneity of the niobium oxide on the magnetite surface (Figure 2.7).

The EDS elemental maps also showed that the surface of the nanocatalyst is rich in niobium, and the combine results of Electron Microscopy suggest strongly that it forms a well-defined layer around the magnetite, establishing a core-shell structure.

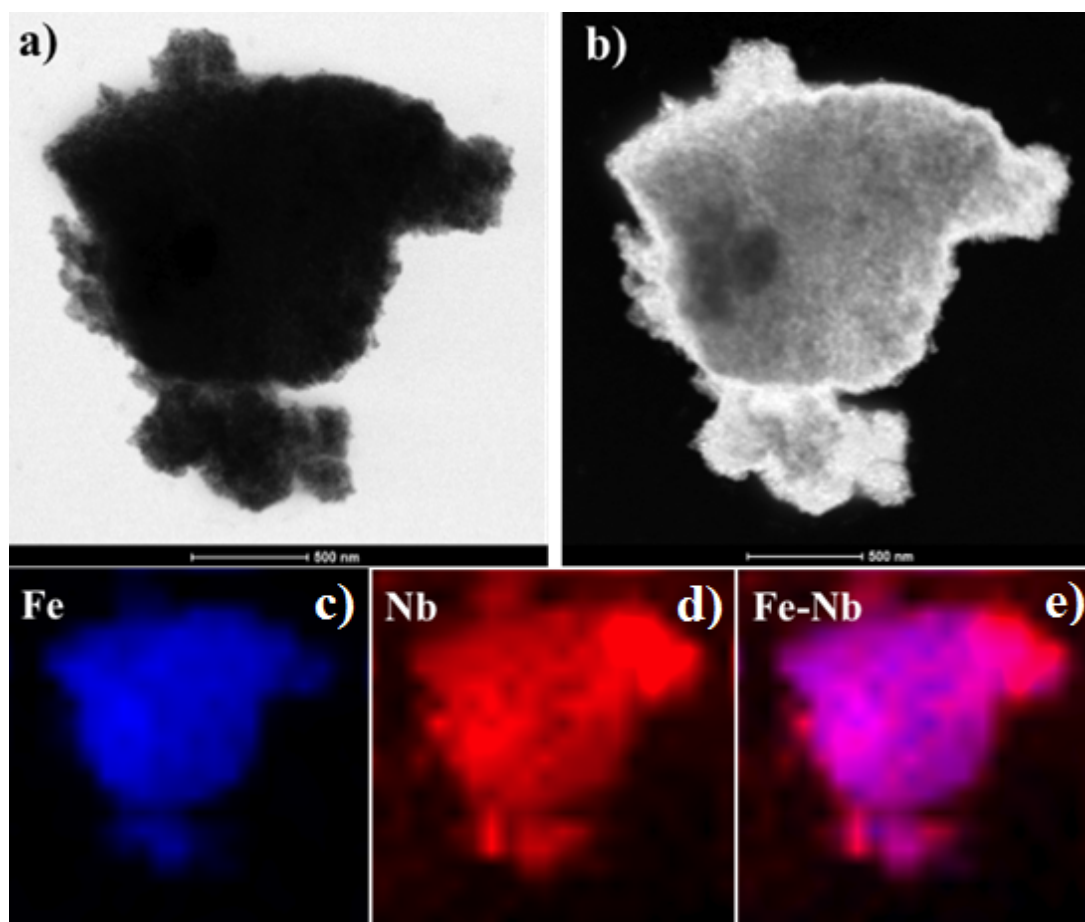


FIGURE 2.7 - EDS elemental maps for $\text{Fe}_3\text{O}_4@\text{Nb}_2\text{O}_5$. a) BF-STEM image, b) DF-STEM image, c) Fe map, d) Nb map and e) Fe + Nb map.

Aiming to study the total acid site density of the catalyst, NH_3 -TPD (Temperature Programmed Desorption of Ammonia) measurements were performed and afforded an insight on the effect of the $\text{Nb}_2\text{O}_5 \cdot n\text{H}_2\text{O}$ shell, also known as niobic acid, on the acidity of nanocatalyst (Figure 2.8).

In this technique, the sample is initially treated with ammonia, that will be adsorbed on the acid sites of the material; the material is next submitted to a programmed increase of the temperature, what will cause the ammonia molecules to desorb from the acid sites. The amount of ammonia desorbed from the sample is then plotted against the temperature, and the integration of the area under this curve is correspondent to the amount of total desorbed ammonia, and consequently, the total amount of acid sites. The results of this technique allowed to determine that the acidity of the nanocatalyst is at least 13 times higher than

that observed magnetite nanoparticles. The acidity of the magnetite support was $6.4 \mu\text{mol}_{\text{NH}_3} \text{g}^{-1}$, while for the $\text{Fe}_3\text{O}_4@\text{Nb}_2\text{O}_5$ it was $84.9 \mu\text{mol}_{\text{NH}_3} \text{g}^{-1}$.

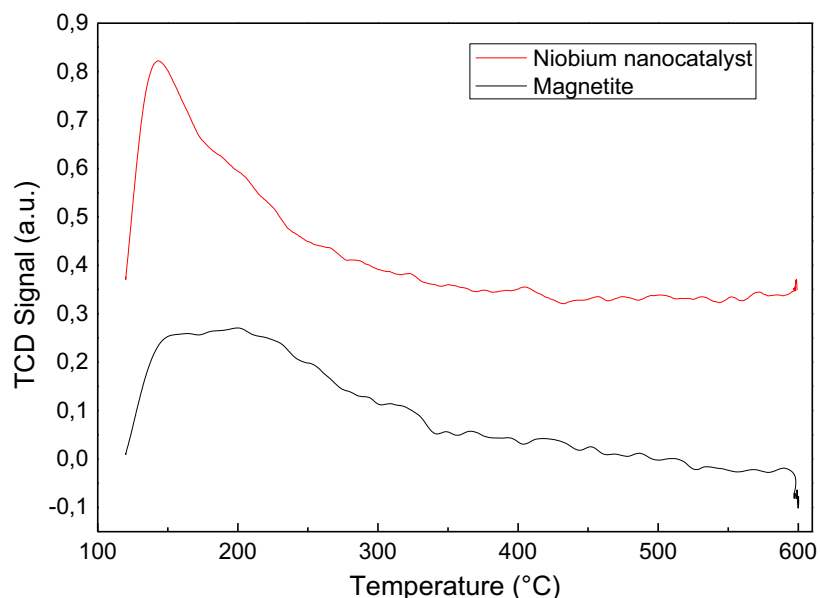


FIGURE 2.8 - NH_3 -TPD curve for Fe_3O_4 and the niobium nanocatalyst.

In order to evaluate the effect of the niobium oxide shell on the magnetic properties of this material, SQUID measurements were conducted. The magnetization curve for both the magnetite sample and the niobium nanocatalyst is showed in Figure 2.9.

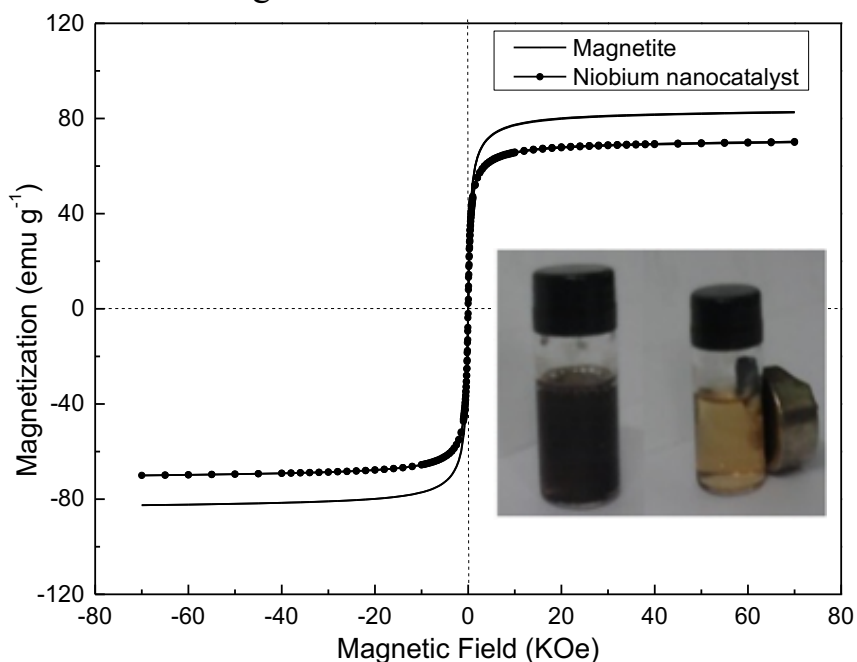


FIGURE 2.9 - Magnetization curve for Fe_3O_4 and the niobium nanocatalyst. Inset: Picture of the catalyst being separated from the reaction medium with the aid of a magnetic field.

The saturation magnetization for the magnetite sample was 82 emu g⁻¹, while for the niobium nanocatalyst 70 emu g⁻¹, showing that the functionalization of magnetite with niobium species do not affect considerably its magnetic behavior.

With the full characterization of the catalyst in hand, the next step was the evaluation of its catalytic activity on Biginelli reaction.

2.3.2 - Evaluation of the catalytic activity of the niobium nanocatalyst on the dihydropyrimidinones synthesis via Biginelli reaction

The catalytic activity of the niobium nanocatalyst was evaluated in the synthesis of dihydropyrimidines via Biginelli reaction. As follows, the multicomponent reaction between benzaldehyde, ethyl acetoacetate and urea was chosen as a model reaction in the search for the optimal conditions. Bearing this in mind, different benign solvents and catalysts were studied, as well as the catalyst loading (Table 2.1).

The search for the optimal conditions for Biginelli reaction employing the newly developed niobium nanocatalyst started by studying the catalyst loading. In order to understand how this parameter could have an effect on the reaction, three reactions were performed using ethanol as solvent at 80°C (entries 1-3). The yields of these three reactions allowed us to conclude that the catalyst loading has great effect in the reaction outcome and, surprisingly, when a high catalyst loading was examined (10 mol%, entry 1) no product formation was observed, while small loadings (1 mol% and 0.1 mol%, entries 2 and 3, respectively) gave rise to the product in excellent yields. The explanation for the failure on the product formation using high catalyst loadings may lie on the strong adsorption properties of niobium, which somehow could interact with urea, keeping this component from reacting. This hypothesis was not thoroughly studied, but the isolation of the Knoevenagel intermediate as the single product of

the reactions performed with high catalyst loadings strongly suggests that niobium might be in fact withdrawing the urea component from the reaction.

TABLE 2.1 - Optimization of the reaction conditions for the synthesis of DHPMs via Biginelli reaction.

Entry ^a	Catalyst	Catalyst loading (mol %)	Solvent	Yield (%) ^b
1	Fe ₃ O ₄ -Nb ₂ O ₅	10	Ethanol	0
2	Fe ₃ O ₄ -Nb ₂ O ₅	1	Ethanol	99
3	Fe ₃ O ₄ -Nb ₂ O ₅	0.1	Ethanol	99
4	Fe ₃ O ₄ -Nb ₂ O ₅	0.1	Water	20
5	Fe ₃ O ₄ -Nb ₂ O ₅	0.1	Glycerol	52
6	Fe ₃ O ₄ -Nb ₂ O ₅	0.1	PEG 400	39
7	Fe ₃ O ₄ -Nb ₂ O ₅	0.1	-	98 ^c
8	Nb ₂ O ₅	0.1	Ethanol	24
9	Fe ₃ O ₄	0.1	Ethanol	60
10	-	-	Ethanol	54

^aUnless otherwise specified, all the reactions were performed in the presence of benzaldehyde (1.0 equiv.), ethyl acetoacetate (1.0 equiv.), urea (1.5 equiv.) and catalyst (0.1 mol%) in 500μL of ethanol at 80°C in a closed vial for 12h. ^b Isolated yields. ^cReaction performed solvent-free with a molar ratio of 1:2:2 benzaldehyde:ethyl acetoacetate:urea at 80°C for 2h.

Moving forward to the investigation of the solvent influence on this catalytic system, five reactions were performed using 0.1 mol% of the niobium nanocatalyst in the presence of environmentally benign solvents such as water, glycerol, PEG 400 and ethanol (entries 3-6) or without any solvent (entry 7). The best solvent for this reaction protocol turned out to be ethanol (entry 3), in which the desired product was isolated with 99% yield. The reaction performed in water afforded a low yield (entry 4), what can be a result of the low solubility of the chemicals in this high polarity solvent, while similar complications were observed for glycerol (entry 5). When PEG 400 was used as solvent, the separation of the desired DHPMs from the reaction media was compromised, and that caused an

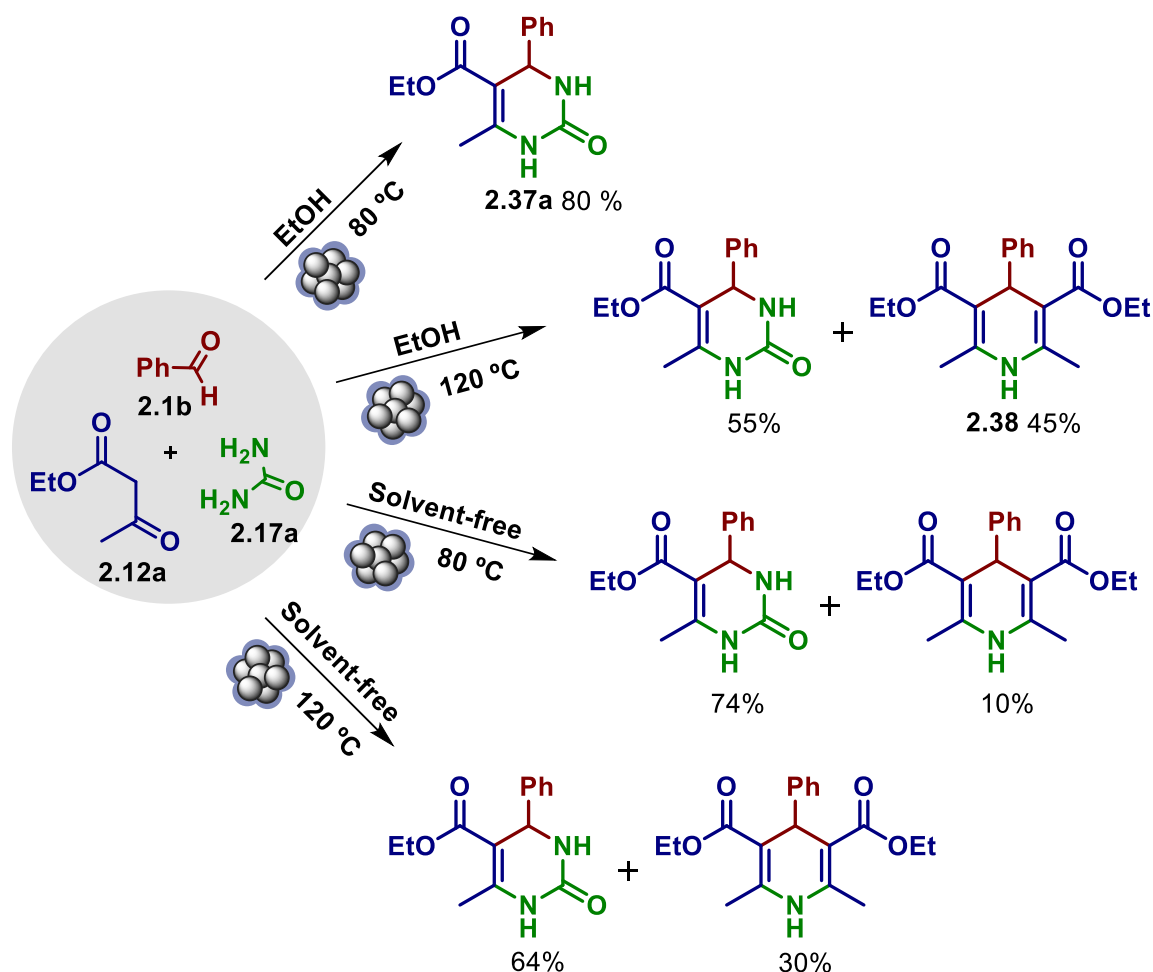
erosion in the chemical yield to 39% (entry 6). When the model reaction was performed without any solvent (entry 7), a high yield was obtained and the reaction was finished after 2 hours with 98% yield of the Biginelli product. However, when the solvent-free approach was applied to the multicomponent reaction employing other substituted benzaldehydes the reaction did not proceed well, probably due to the physical state and low solubility of the aldehydes in the other components of the reaction. The limitations of the solvent-free Biginelli reaction have already been discussed by other research groups.⁶²

Aiming to examine the importance of supporting the active part catalyst on magnetite nanoparticles, the reaction with the bulk Nb₂O₅ (entry 8) as catalyst, with the bare Fe₃O₄ nanoparticles (entry 9), and finally, without the presence of catalyst (entry 10) were performed. The reaction performed in the optimized reaction conditions without catalyst (entry 10) and with the bare magnetite nanoparticles (entry 5) produced similar moderate yields, while the reaction performed with the bulk Nb₂O₅ as catalyst (entry 8) interestingly produced a lower yield. These outcomes prove that the catalytic activity indeed derives from the highly acidic niobium species on the surface of the nanocatalyst and, furthermore, that it is greatly enhanced by the increase of the surface area of the catalyst, a consequence of supporting of the active phase in a nanosized material.

The feasibility of the Biginelli reaction in the absence of a catalyst is a hotly debated subject; while some authors report that the reaction may be conducted in the absence of a catalyst, the methods presented in these reports present severe disadvantages such as long reaction times, low yields and subtract-dependent results. Besides that, it has been already proven the catalyst plays a leading role in the selection of the reaction pathway (the mechanism of the Biginelli reaction will be further discussed in the following pages).⁶²

62. Alvim, H. G. O.; Lima, T. B.; Oliveira, A. L.; Oliveira, H. C. B.; Silva, F. M.; Gozzo, F. C.; Souza, R. Y.; Silva, W. A.; Neto, B. A. D. *J. Org. Chem.*, **79**:3383, 2014.

In order to study the effect of microwave irradiation (MW) over this catalytic system, four experiments were carried out at 80°C and 120°C employing ethanol as solvent or using a solvent-free system. The results of these experiments (Scheme 2.13) allowed us to conclude that MW irradiation do not have a pronounced effect on the reaction performance in the presence of solvent, which is in accordance with previous studies by Kappe and co-workers.⁶³



SCHEME 2.13 - Evaluation of Biginelli reaction under microwave irradiation

As depicted in Scheme 2.13, the reaction performed in the presence of ethanol at 80°C afforded an 80% yield after 2 h, whereas the Knoevenagel adduct was isolated as a by-product. Even after longer reaction times (4 h) at the same conditions, the reaction did not achieve completion, and the isolated yield

63. Stadlera, A.; Kappe, C.O. *J. Chem. Soc. Perkin Trans. 2*:1363, 2000.

of DHMP **2.37a** was slightly higher (86%). When the temperature was raised up to 120°C, the Knoevenagel adduct was completely consumed after 30 minutes, however, a known by-product was observed – the 1,4-dihydropyridine (DHP) **2.38** also known as the Hantzsch ester; the DHP product is formed through the condensation of benzaldehyde, two equivalents of the β -ketoester and ammonia, which is produced *in situ* by the decomposition of the urea component, a common side reaction that takes place in the presence of water at temperatures above 90°C. Under this reaction conditions, the DHP product was formed in 35% yield, while the yield of DHPMs product was 55%. When the reaction was conducted in solvent-free conditions, the yield at 80°C was 10% superior to the yield at 120°C, and in both cases, the Hantzsch ester was isolated as a by-product.

With the optimized reaction conditions in hand, the next step was the comprehension of how other analogous magnetically recoverable-transition metal catalysts could possibly affect the reaction. To accomplish that, the efficiency of the niobium nanocatalyst was compared to the already known copper and nickel nanocatalysts in the optimized reaction conditions (Figure 2.10). These results indicate that both the nature and loading of the nanocatalyst have a strong influence in the yields of the Biginelli product.

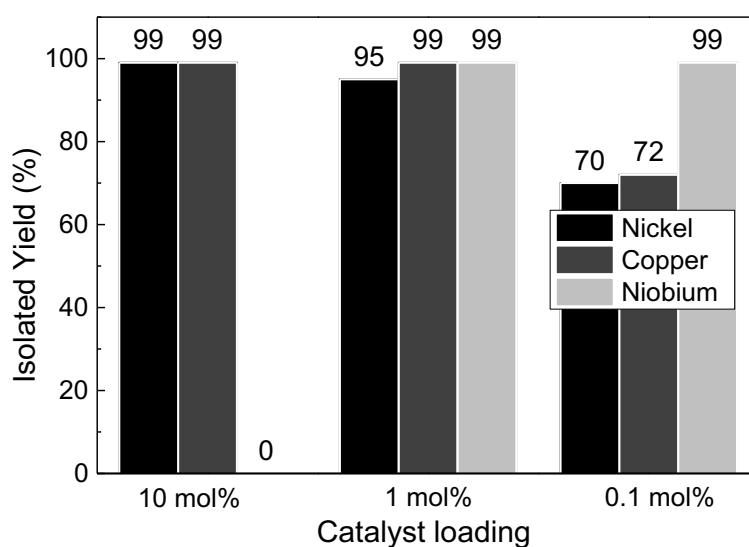
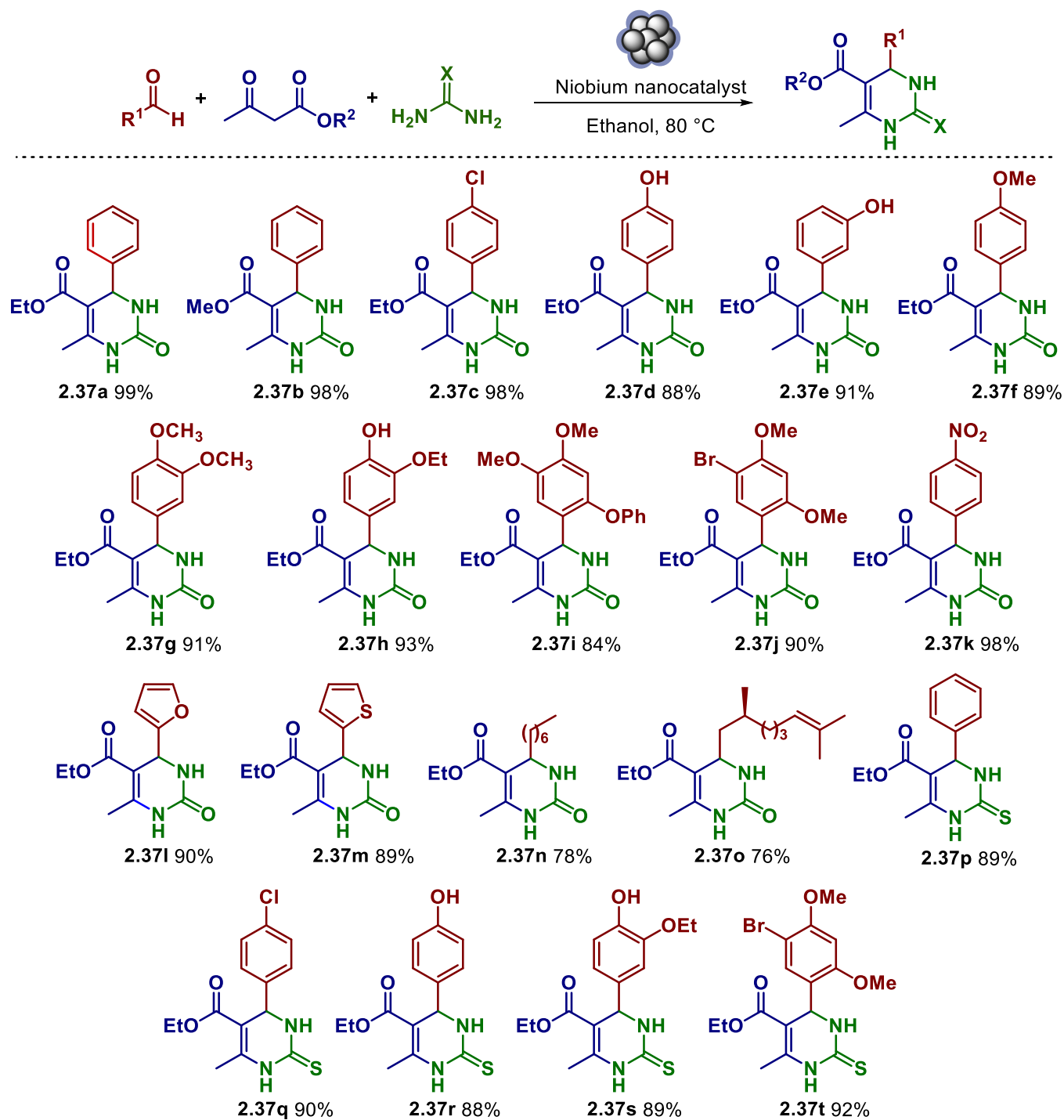


FIGURE 2.10 - Evaluation of the catalyst effect on Biginelli reaction.

As showed in Figure 2.10, when the three nanocatalysts were evaluated in a 10 mol% loading, the niobium nanocatalyst afforded no product, being the Knoevenagel intermediate the only isolated product with 93% yield, while copper and nickel nanocatalysts produced high DHMPs yields (99% for both). When the catalyst amount was dropped to 1 mol% all three nanocatalysts afforded good yields, that being 99 % for both copper and niobium nanocatalysts and 95% for nickel. At 0.1 mol% nanocatalyst loading, only the niobium nanocatalyst promoted a full conversion, whereas the nickel and copper nanocatalysts exhibited diminished performance, yielding the product in only 70 and 72%, respectively.

Having explored all major aspects surrounding Biginelli reaction employing the newly developed niobium nanocatalyst, the scope and limitations of the reaction were investigated (Scheme 2.14). Employing optimized conditions, ethanol was used as an environmentally benign solvent at 80 °C, with the niobium nanocatalyst being added in a very small loading (0.1 mol%). Remarkably, the formation of the DHMPs products did not seem to be not affected considerably by steric and electronic effects in the aryl moiety of the aldehydes, since both substrates having one or more electron donating or withdrawing groups led to the formation of products **2.37a-m**, with yields in the range of 78–95%. When aliphatic aldehydes were employed (products **2.37n** and **2.37o**), the yields were slightly diminished from excellent to good yields (78% and 76%, respectively). Likewise, the use of urea or thiourea did not have a significant effect on the yields, that were achieved in the range of 83-92% (products **2.37p-t**).

After successfully evaluating the scope of the Biginelli reaction using the new niobium catalytic system, the recyclability of the nanocatalyst and scaling up of the reaction were the focus of study (Figure 2.11). To accomplish that, the reactions were performed in a 10 mmol scale in optimized conditions; when the



SCHEME 2.14 - Scope of the reaction for the synthesis of DHPMs via Biginelli condensation.

reactions achieved completion, the nanocatalyst was retrieved from the media with the aid of a magnet, washed with ethanol, dried under vacuum and reused.

As depicted in Figure 7, in the first run the components were quantitatively converted to the desired product (>99% isolated yield). In the

subsequent runs, the conversion to the DHPMs products was almost complete and the isolated yields only started to decrease after the 7th run.

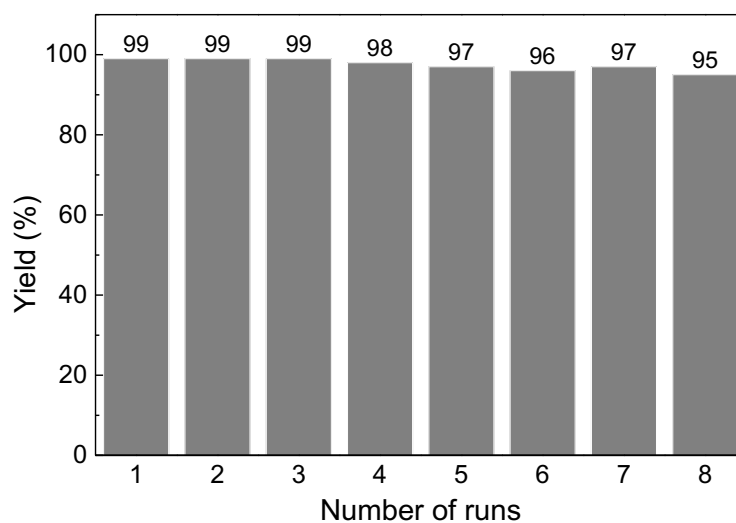


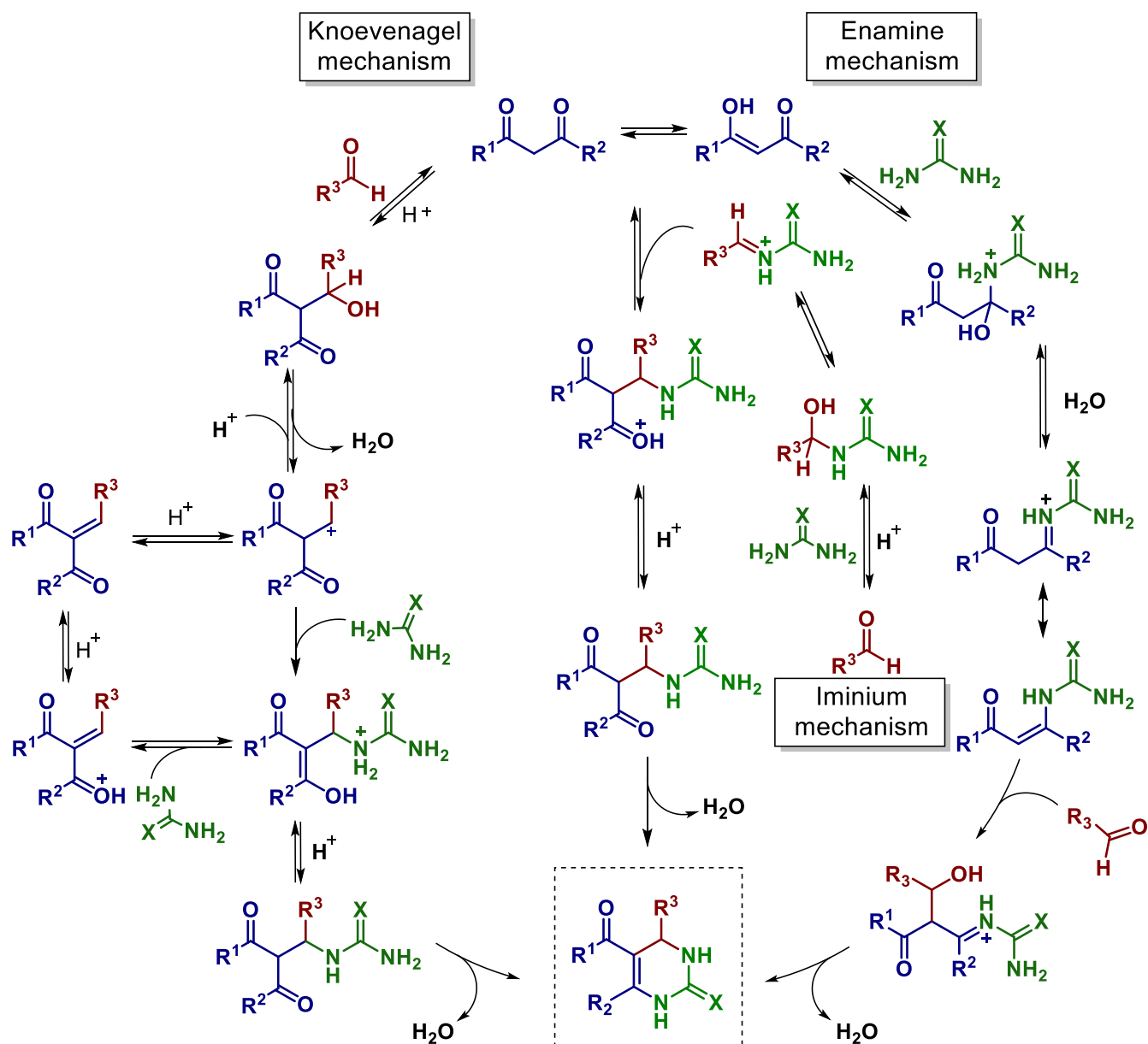
FIGURE 2.11 - Evaluation of the recyclability of the niobium nanocatalyst.

Therefore, besides presenting the advantage of the use in remarkably low loadings, the recyclability studies for $\text{Fe}_3\text{O}_4\text{-Nb}_2\text{O}_5$ showed that this catalyst could be used several times without significant loss of the catalytic activity.

The mechanism of the Biginelli reaction is still a controversial subject, but it is already known that the reaction that leads to the DHPM product can happen through three different pathways,⁶⁴ in which the process starts by the formation of three possible intermediates: Knoevenagel, iminium or enamine (Scheme 2.15).

Aiming to have an experimental insight on the reaction mechanism in the presence of the niobium nanocatalyst, an experiment in optimized reaction conditions was conducted in which the composition of the reaction medium was monitored over time by the injection in a GC-MS of aliquots withdrawn from the reaction media in regular intervals of time (Figure 2.12).

64. (a) Kappe, C. O. *J. Org. Chem.*, **62**:7201, 1997. (b) Sweet, F.; Fissekis, J. D. *J. Am. Chem. Soc.*, **95**:8741, 1973. (c) Souza, R. O. M. A.; Penha, E. T.; Milagre, H. M. S.; Garden, S. J.; Esteves, P. M.; Eberlin, M. N.; Antunes, O. A. C. *Chem. Eur. J.*, **15**: 9799, 2009.



SCHEME 2.15 - Possible mechanisms for Biginelli reaction.

As showed in Figure 2.12, the concentration on the initial GC-MS injection (30 min) was around 70% for the Knoevenagel adduct and 30% for the Biginelli product. With the proceeding of the reaction, the intermediate concentration rapidly decreased while the Biginelli product concentration increased. This profile suggests that the reaction evaluated in the optimized reactions conditions occurs via the Knoevenagel intermediate mechanism.

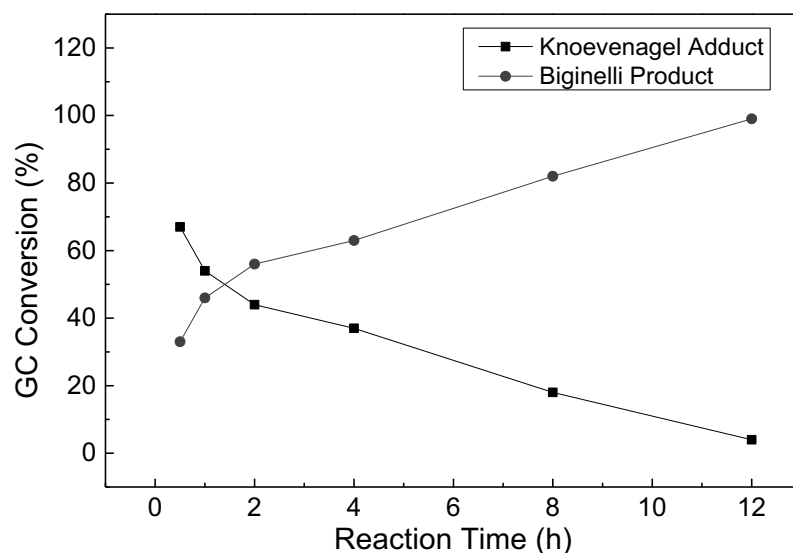
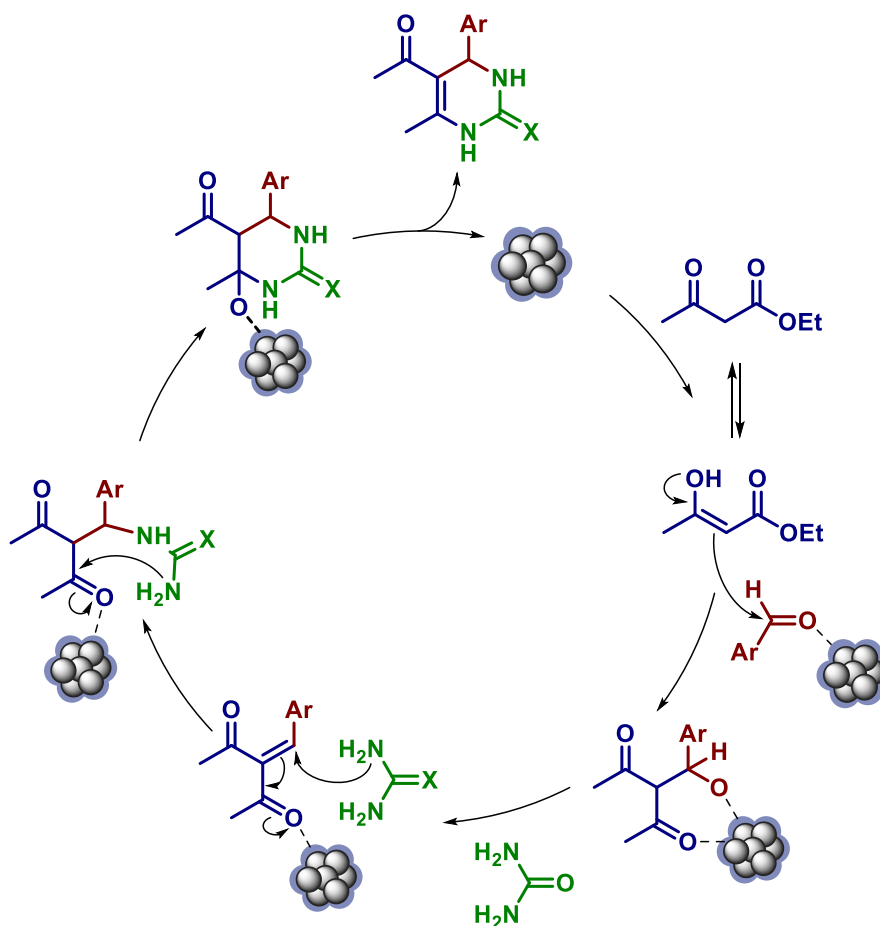


FIGURE 2.12 - Evaluation of the composition of the reaction medium monitored over time by GC-MS.

Based on the experimental observations, and on the assumption that the reaction occurs via a Knoevenagel intermediate, a catalytic cycle was proposed (Scheme 2.16). In the proposed reaction mechanism, the reaction starts with the Knoevenagel condensation between the β -ketoester and the aldehyde, forming an α,β -conjugated ketone that is attacked by an amino group of a urea or thiourea molecule. Next, the intramolecular attack of the remaining amino group of the urea moiety on the neighboring carbonyl group followed by the elimination of a water molecule gives rise to the Biginelli product.

2.4 - Conclusions

In summary, a highly efficient magnetically recoverable niobium nanocatalyst was prepared from inexpensive precursors magnetite and ammonium niobate(V) oxalate hydrate and fully characterized. This novel niobium nanocatalyst has showed great advantages when compared to nickel and copper analogous, especially on the amount of catalyst required in the reaction. When used in acid demanding multicomponent Biginelli reaction, it proved to be very effective, providing the respective DHMP products in good to excellent yields,



SCHEME 2.16 - Proposed catalytic cycle for Biginelli reaction in the presence of the niobium nanocatalyst via the Knoevenagel mechanism.

using a very low catalyst loading (0.1 mol%) under benign reaction conditions. Moreover, due to its magnetic character, the catalyst could be easily recovered and reused several times without any loss on its catalytic activity. Its robustness, magnetically recoverable nature and highly efficiency are the very notable features of this nanocatalyst. The work described in this chapter generated a manuscript that was published in 2014 in the journal *ChemCatChem*.⁶⁵

65. Lima, C. G. S.; Silva, S.; Gonçalves, R. H.; Leite, E. R.; Schwab, R. S.; Corrêa, A. G.; Paixão, M. W. *ChemCatChem*, **6**:3455, 2014.

2.5 - Experimental Section

2.5.1 - General information

All solvents were dried and distilled prior to use by standard procedures. Reagents were purchased at the highest commercial quality and used without further purification, unless otherwise stated. Flash column chromatography was carried out using silica gel 60 (230–400 mesh), and analytical thin-layer chromatography (TLC) was performed using silica gel aluminum sheets. ^1H NMR and ^{13}C NMR spectra were recorded at 400 MHz for ^1H and 100 MHz for ^{13}C , respectively using DMSO- d_6 as solvents. Chemical shifts (δ) are reported in parts per million relative to tetramethylsilane (TMS), and coupling constants (J) are reported in hertz.

2.5.2 - Preparation of magnetite nanoparticles

$\text{FeCl}_3 \cdot 6\text{H}_2\text{O}$ (5.4 g, 33 mmol) and urea (3.6 g, 60 mmol) were dissolved in water. The mixture was stirred at 90°C for 2 h. After cooling to room temperature, $\text{FeCl}_2 \cdot 4\text{H}_2\text{O}$ (2.0 g, 15 mmol) was added to the solution and the pH was adjusted to 10 using NaOH 0.1 mol L $^{-1}$ solution. The obtained hydroxides were treated by ultrasound bath for 30 min. After ageing for 12 h, the fine black powder (Fe_3O_4) was washed several times with distilled water and the aid of a magnet. The washing process was repeated until the pH of the suspension became neutral. The obtained solid was washed once with ethanol and dried under vacuum.

2.5.3 - General preparation of the nanocatalysts

The nanocatalysts were prepared by the wet impregnation method, where magnetite (2 g) was dispersed in water followed by the addition of the metal oxide precursor salt ($\text{C}_4\text{H}_4\text{NNbO}_9 \cdot 3\text{H}_2\text{O}$, $\text{CuCl}_2 \cdot 2\text{H}_2\text{O}$ or $\text{Ni}(\text{NO}_3)_2 \cdot 2\text{H}_2\text{O}$ for niobium, copper and nickel nanocatalyst, respectively, to obtain 10% wt%). After

stirring for 1 h at room temperature, the pH was adjusted to 12 with NaOH 1 mol L⁻¹. After stirring for 20 h at room temperature, the nanocatalysts were washed with distilled water and the aid of a magnet. The washing process was repeated until the pH of the suspension became neutral. The obtained solid was washed once with ethanol and dried under vacuum.

2.5.4 - Characterization of the nanocatalysts

Powder XRD was performed in a Rigaku D/MAX, 2500 PC diffractometer, with a rotary anode operating at 150 kV and 40 mA using CuK α radiation. TEM/HRTEM and STEM/energy dispersive x-ray spectroscopy (EDS) characterization images were obtained with a TECNAI F20 X-Twin, operating at 200 kV. For the EDS map, a spot size of 1.5 nm was used. ICP-OES measurements were conducted in a Thermo Fisher Scientific, iCAP 6300 Duo, with a CID (Charge Injection Device). For this measurement, the standards for the calibration curve were prepared by dilution of a SpecSol® standard in ultra-pure nitric acid solution. The gas utilized to form the plasma was argon 5.0 and the measurement was conducted at a 309.418 nm wavelength. function of applied magnetic field at 298 K.

TPD measurements were conducted in a Micromeritics Autochem II 2920 Chemisorption Analyzer equipment with a TCD (Thermal Conductivity Detector) detector. For this, 0.05 g of the sample were pre-treated thermally under 30 mL.min⁻¹ helium flow at a heating rate of 10 °C min⁻¹ until 600 °C and kept at this temperature for 30 minutes. After this period, the reactor was cooled to 120°C, and the He flow was kept for 60 minutes. Next, the adsorption of ammonia was performed through the passing of a 15% mixture of NH₃ in He for 30 minutes over the sample. After saturation, the sample was purged with He for 1 hour to remove the excess of ammonia. Finally, the temperature desorption was initiated under a 30 mL min⁻¹ He flow in a 15°C min⁻¹ heating rate until 600°C. To quantify

the acid sites, the area under the curve of the graph of TCD signal x temperature was calculated.

2.5.5 - General procedure for $\text{Fe}_3\text{O}_4@\text{Nb}_2\text{O}_5.n\text{H}_2\text{O}$ Biginelli reaction: Optimization of reaction conditions

A mixture of benzaldehyde (106 μL , 1 mmol), ethyl acetoacetate (130 μL , 1 mmol) and urea (85mg, 1.5 mmol), 500 μL of solvent and the appropriated amount of each catalyst (niobium nanocatalyst, magnetite, bulk niobium oxide) was stirred in a 10 mL closed test tube at 80 °C for 12h. For the solvent-free reaction, 106 μL of benzaldehyde (1 mmol), 260 μL of ethyl acetoacetate (2 mmol), 120 mg of urea (2 mmol), 1.4 mg of the niobium nanocatalyst (0.1 mol %) were stirred in a 10 mL closed test tube at 80 °C for 2h. After cooling to room temperature, the catalyst was separated from the reaction media with the aid of a magnet in the case of magnetite or by filtration, in the case of bulk niobium oxide, and washed with ethanol several times. The combined organic layers were concentrated and purified by flash column chromatography using hexane/ethyl acetate as eluent.

2.5.6 - General procedure for $\text{Fe}_3\text{O}_4@\text{Nb}_2\text{O}_5.n\text{H}_2\text{O}$ Biginelli reaction: Scope of reaction

A mixture of aldehyde (1 mmol), acetoacetate (1 mmol) and urea/thiourea (1.5 mmol), 500 μL of ethanol and niobium nanocatalyst (1.5 mg, 0,1 mol%) was stirred in a 10 mL closed test tube at 80 °C for 12h. After cooling to room temperature, the catalyst was separated from the reaction media with the aid of a magnet and washed with ethanol several times. The combined organic layers were concentrated and purified by flash column chromatography using hexane/ethyl acetate as eluent.

2.5.7 - General procedure for $\text{Fe}_3\text{O}_4@\text{Nb}_2\text{O}_5.n\text{H}_2\text{O}$ Biginelli reaction: Comparison of the niobium nanocatalyst efficiency with nickel and copper nanocatalysts

The amount of nanocatalyst employed in each reaction was calculated considering the loading of the metal on the magnetite nanoparticles determined by ICP-OES in the case of niobium nanocatalyst, and atomic absorption for nickel and copper. Table 2.2 shows the quantities weighted of each catalyst employed in the catalyst evaluation reactions.

For all reactions, a mixture of aldehyde (1 mmol), acetoacetate (1 mmol) and urea/thiourea (1.5 mmol), 500 μL of ethanol and the appropriated amount of catalyst was stirred in a 10 mL closed test tube at 80 °C for 12h. After cooling to room temperature, the catalyst was separated from the reaction media with the aid of a magnet and washed with ethanol several times. The combined organic layers were concentrated and purified by flash column chromatography using hexane/ethyl acetate as eluent.

TABLE 2.2 Amount of each nanocatalyst employed in the catalyst evaluation reactions.

Nanocatalyst	$m_{\text{nanocatalyst}}$ (mg)		
	0.1 mol %	1 mol %	10 mol %
Niobium	1.4	14	140
Nickel	1	10	100
Copper	1	10	100

2.5.8 - General procedure for $\text{Fe}_3\text{O}_4@\text{Nb}_2\text{O}_5.n\text{H}_2\text{O}$ Biginelli reaction: Microwave evaluation

A mixture of aldehyde (1 mmol), acetoacetate (1 mmol) and urea/thiourea (1.5 mmol), 500 μL of ethanol (or no solvent, in the case of the solvent-free reaction) and niobium nanocatalyst (1.5 mg, 0,1 mol%) was stirred in a 10 mL

microwave tube at 80 °C under 300W microwave irradiation in a CEM Discover Microwave Reactor. From 10 to 10 minutes, the formation of the product was evaluated through TLC. When the suitable time of reaction was determined, the reaction was repeated, the catalyst was separated from the reaction media with the aid of a magnet and washed with ethanol several times. The combined organic layers were concentrated and purified by flash column chromatography.

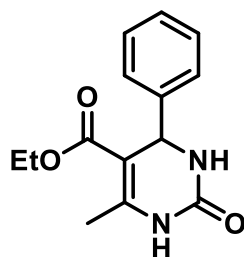
2.5.9 - Procedure for scaling up and study of the recyclability of the $\text{Fe}_3\text{O}_4@\text{Nb}_2\text{O}_5.n\text{H}_2\text{O}$ catalyst

A mixture of benzaldehyde (1.06 mL, 10 mmol), ethyl acetoacetate (1.3 mL, 10 mmol) and urea (850mg, 15 mmol), 5 mL of solvent and 14 mg (0.1 mol %) of the niobium nanocatalyst was stirred in a 10 mL round-bottom flask at 80 °C for 12h. After cooling to room temperature, the catalyst was separated from the reaction media with the aid of a magnet and washed with ethanol several times. The combined organic layers were concentrated and purified by flash column chromatography. The niobium nanocatalyst was dried and reused for 7 subsequent runs.

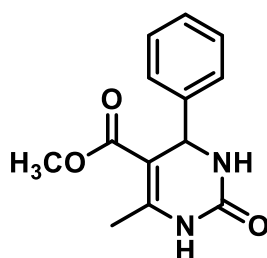
2.5.10 - General procedure for $\text{Fe}_3\text{O}_4@\text{Nb}_2\text{O}_5.n\text{H}_2\text{O}$ Biginelli reaction: Evaluation of the reactional media composition over time.

A mixture of benzaldehyde (106 μL , 1 mmol), ethyl acetoacetate (130 μL , mmol) and urea (85mg, 1.5 mmol), 500 μL of solvent and 1.4 mg of the niobium nanocatalyst was stirred in a 10 mL closed test tube at 80 °C. Aliquots of 1 μL were withdrawn from the reaction media at regular reaction times and injected on a Shimadzu GCMS-QP2010S Gas Chromatograph coupled to a MS detector. The area of the peaks on the chromatograms corresponding to the Knoevenagel intermediate and the Biginelli product were calculated and the composition of the reaction media was plotted against time.

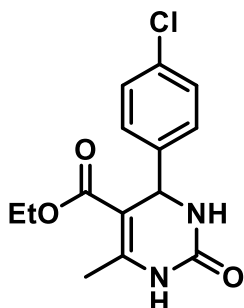
2.5.11 - Characterization of the dihydropyrimidinones/thiones



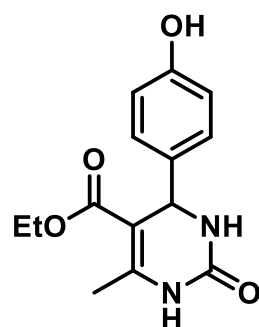
Ethyl 6-methyl-2-oxo-4-phenyl-1,2,3,4-tetrahydropyrimidine-5-carboxylate (2.46). Yield: 99%. ^1H NMR (400 MHz, DMSO) δ 9.19 (s, 1H), 7.74 (s, 1H), 7.37 – 7.19 (m, 5H), 5.15 (d, $J = 3.3$ Hz, 1H), 3.99 (q, $J = 7.1$ Hz, 2H), 2.28 (s, 1H), 1.10 (t, $J = 7.1$ Hz, 3H). ^{13}C -NMR (DMSO, 100 MHz) δ (ppm): 165.30, 152.09, 148.32, 144.83, 128.35, 127.22, 126.21, 99.22, 59.14, 53.92, 17.74, 14.04.



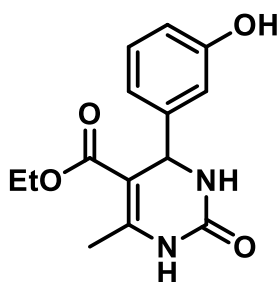
Methyl 6-methyl-2-oxo-4-phenyl-1,2,3,4-tetrahydropyrimidine-5-carboxylate (2.48). Yield: 98%. ^1H NMR (400 MHz, DMSO) δ 9.24 (s, 1H), 7.77 (s, 1H), 7.29 (m, 5H), 5.17 (d, $J = 3.3$ Hz, 1H), 3.53 (s, 3H), 2.26 (s, 3H). ^{13}C NMR (100 MHz, DMSO) δ 165.81, 152.19, 148.61, 144.64, 128.41, 127.25, 126.14, 99.01, 53.79, 50.73, 17.79.



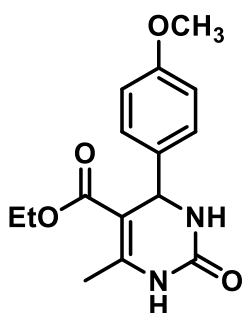
Ethyl 4-(4-chlorophenyl)-6-methyl-2-oxo-1,2,3,4-tetrahydropyrimidine-5-carboxylate (2.49). Yield: 98%. ^1H NMR (400 MHz, DMSO) δ 9.24 (s, 1H), 7.76 (s, 1H), 7.39 (d, $J = 8.4$ Hz, 2H), 7.24 (d, $J = 8.4$ Hz, 2H), 5.14 (d, $J = 3.3$ Hz, 1H), 3.98 (q, $J = 7.1$ Hz, 1H), 2.25 (s, 3H), 1.09 (t, $J = 7.1$ Hz, 3H). ^{13}C NMR (100 MHz, DMSO) δ 165.17, 151.89, 148.69, 143.76, 131.74, 128.36, 128.15, 98.78, 59.22, 53.37, 17.76, 14.03.



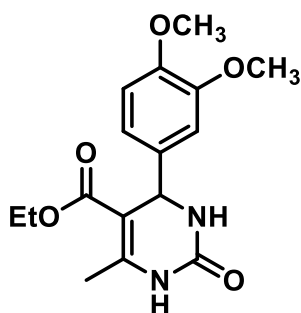
Ethyl 4-(4-hydroxyphenyl)-6-methyl-2-oxo-1,2,3,4-tetrahydropyrimidine-5-carboxylate (2.50). Yield: 88%. ^1H NMR (400 MHz, DMSO) δ 9.32 (s, 1H), 9.11 (s, 1H), 7.62 (s, 1H), 7.03 (d, $J = 8.3$ Hz, 2H), 6.69 (d, $J = 8.3$ Hz, 2H), 5.05 (d, $J = 2.5$ Hz, 1H), 3.97 (q, $J = 7.0$ Hz, 2H), 2.20 (d, $J = 2.8$ Hz, 3H), 1.09 (t, $J = 7.0$ Hz, 3H). ^{13}C NMR (100 MHz, DMSO) δ 165.39, 156.51, 152.17, 147.69, 135.40, 127.37, 114.94, 99.72, 59.07, 53.41, 17.70, 14.05.



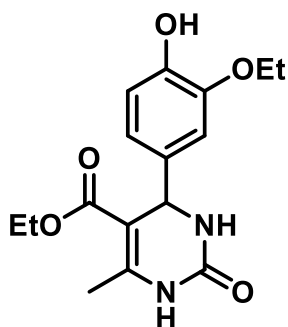
Ethyl 4-(3-hydroxyphenyl)-6-methyl-2-oxo-1,2,3,4-tetrahydropyrimidine-5-carboxylate (2.51). Yield: 91%. ^1H NMR (400 MHz, DMSO) δ 9.37 (s, 1H), 9.15 (s, 1H), 7.68 (s, 1H), 7.09 (t, $J = 8.0$ Hz, 1H), 6.71 – 6.58 (m, 3H), 5.06 (d, $J = 3.3$ Hz, 1H), 4.00 (q, $J = 7.1$ Hz, 2H), 2.23 (s, 3H), 1.12 (t, $J = 7.1$ Hz, 3H). ^{13}C NMR (101 MHz, DMSO) δ 165.36, 157.29, 152.18, 148.05, 146.21, 129.25, 116.84, 114.12, 113.03, 99.34, 59.16, 53.76, 17.72, 14.06.



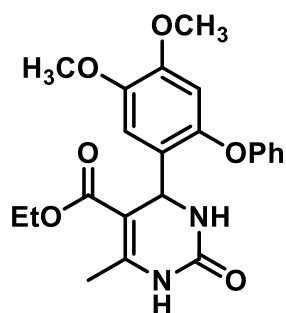
Ethyl 4-(4-methoxyphenyl)-6-methyl-2-oxo-1,2,3,4-tetrahydropyrimidine-5-carboxylate (2.52). Yield: 89%. ^1H NMR (400 MHz, DMSO) δ 9.16 (s, 1 H), 7.68 (s, 1 H), 7.15 (d, $J = 8.2$ Hz, 2 H), 6.88 (d, $J = 8.2$ Hz, 2 H), 5.09 (s, 1 H), 3.98 (q, $J = 6.8$ Hz, 2 H), 3.72 (s, 3 H), 3.38 (s, 3 H), 2.24 (s, 3 H), 1.10 (t, $J = 6.9$ Hz, 3 H). ^{13}C NMR (100 MHz, DMSO) δ 165.36, 159.83, 158.42, 152.25, 147.96, 137.00, 127.38, 113.66, 99.56, 59.13, 55.01, 53.30, 17.70, 14.06.



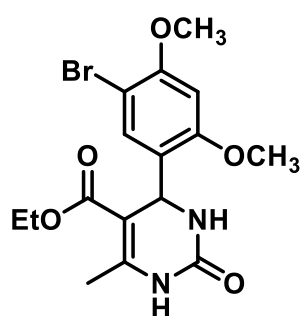
Ethyl 4-(3,4-dimethoxyphenyl)-6-methyl-2-oxo-1,2,3,4-tetrahydropyrimidine-5-carboxylate (2.53). Yield: 91%. ^1H NMR (400 MHz, DMSO) δ 9.12 (s, 1H), 7.26 (s, 1H), 6.92 (d, $J = 8.9$ Hz, 1H), 6.81 (dd, $J = 8.9, 3.1$ Hz, 1H), 6.59 (d, $J = 3.1$ Hz, 1H), 5.44 (d, $J = 3.0$ Hz, 1H), 4.12 – 3.88 (m, 2H), 3.74 (s, 3H), 3.66 (s, 3H), 2.27 (s, 3H), 1.05 (t, $J = 7.1$ Hz, 3H). ^{13}C NMR (100 MHz, DMSO) 165.28, 152.86, 152.09, 150.70, 148.78, 132.80, 114.00, 112.13, 111.95, 97.54, 58.98, 55.88, 49.09, 17.64, 14.00.



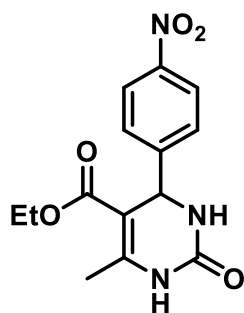
Ethyl 4-(3-ethoxy-4-hydroxyphenyl)-6-methyl-2-oxo-1,2,3,4-tetrahydropyrimidine-5-carboxylate (2.54). Yield: 93%. ^1H NMR (400 MHz, DMSO) δ 9.10 (s, 1H), 8.82 (s, 1H), 7.61 (s, 1H), 6.77 (d, $J = 2.0$ Hz, 1H), 6.70 (d, $J = 8.1$ Hz, 1H), 6.60 (dd, $J = 8.2, 2.0$ Hz, 1H), 5.03 (d, $J = 3.2$ Hz, 1H), 4.04 – 3.88 (m, 4H), 2.23 (s, 3H), 1.31 (t, $J = 7.0$ Hz, 3H), 1.11 (t, $J = 7.1$ Hz, 3H). ^{13}C NMR (100 MHz, DMSO) δ 165.42, 152.20, 147.81, 146.26, 146.08, 135.86, 118.39, 115.33, 112.28, 99.56, 63.88, 59.08, 53.47, 17.68, 14.73, 14.10.



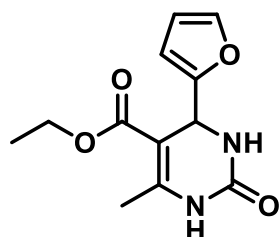
Ethyl 4-(4,5-dimethoxy-2-phenoxyphenyl)-6-methyl-2-oxo-1,2,3,4-tetrahydropyrimidine-5-carboxylate (2.55). Yield: 84%. ^1H NMR (400 MHz, DMSO) δ 9.05 (s, 1H), 7.56 – 7.27 (m, 5H), 7.22 (s, 1H), 6.72 (s, 1H), 6.66 (s, 1H), 5.53 (s, 1H), 5.13 (q, J = 12.2 Hz, 2H), 3.90 (dd, J = 6.9, 4.4 Hz, 2H), 3.72 (s, 3H), 3.62 (s, 3H), 2.25 (s, 3H), 1.00 (t, J = 7.0 Hz, 3H). ^{13}C NMR (100 MHz, DMSO) δ 165.33, 151.96, 149.80, 148.98, 148.29, 142.49, 137.62, 128.30, 127.58, 127.38, 124.17, 112.73, 99.88, 98.08, 70.25, 58.90, 56.49, 55.75, 48.97, 17.64, 14.00.



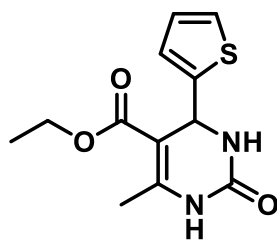
Ethyl 4-(5-bromo-2,4-dimethoxyphenyl)-6-methyl-2-oxo-1,2,3,4-tetrahydropyrimidine-5-carboxylate (2.56). Yield: 90%. ^1H NMR (400 MHz, DMSO) δ 9.13 (s, 1H), 7.31 (s, 1H), 7.09 (s, 1H), 6.74 (s, 1H), 5.36 (d, J = 2.8 Hz, 1H), 3.92 (q, J = 7.1 Hz, 2H), 3.86 (s, 3H), 3.83 (s, 3H), 2.26 (s, 3H), 2.08 (s, 1H), 1.05 (t, J = 7.1 Hz, 3H). ^{13}C NMR (100 MHz, DMSO) δ 165.20, 157.24, 155.54, 151.96, 148.78, 130.82, 125.66, 99.91, 97.85, 97.25, 59.00, 56.35, 55.92, 48.96, 17.67, 13.96.



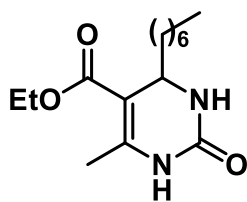
Ethyl 6-methyl-4-(4-nitrophenyl)-2-oxo-1,2,3,4-tetrahydropyrimidine-5-carboxylate (2.57). Yield: 98%. ^1H NMR (400 MHz, DMSO) δ 9.36 (s, 1H), 8.22 (d, J = 8.6 Hz, 2H), 7.90 (s, 1H), 7.51 (d, J = 8.6 Hz, 2H), 5.28 (d, J = 3.0 Hz, 1H), 3.99 (q, J = 7.0 Hz, 2H), 2.27 (s, 3H), 1.10 (t, J = 7.1 Hz, 3H). ^{13}C NMR (100 MHz, DMSO) δ 165.02, 151.96, 151.72, 149.35, 146.68, 127.62, 123.79, 98.14, 59.35, 53.64, 17.83, 14.00.



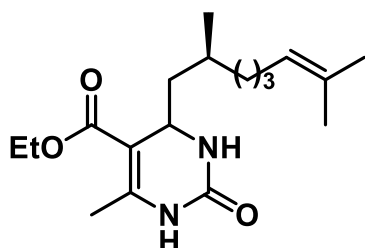
Ethyl 4-(furan-2-yl)-6-methyl-2-oxo-1,2,3,4-tetrahydropyrimidine-5-carboxylate (2.58). Yield: 90%. ^1H NMR (400 MHz, DMSO) δ 9.23 (s, 1H), 7.75 (s, 1H), 7.55 (dd, J = 1.8, 0.8 Hz, 1H), 6.35 (dd, J = 3.2, 1.8 Hz, 1H), 6.09 (d, J = 3.2 Hz, 1H), 5.20 (d, J = 3.4 Hz, 1H), 4.09 – 3.97 (m, 2H), 2.23 (s, 3H), 1.13 (t, J = 7.1 Hz, 3H). ^{13}C NMR (100 MHz, DMSO) δ 164.97, 155.90, 152.36, 149.31, 142.10, 110.30, 105.23, 96.71, 59.18, 47.67, 17.68, 14.11.



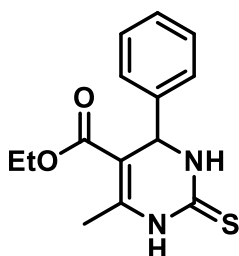
Ethyl 6-methyl-2-oxo-4-(thiophen-2-yl)-1,2,3,4-tetrahydropyrimidine-5-carboxylate (2.59). Yield: 89%. ^1H NMR (400 MHz, DMSO) δ 9.31 (s, 1H), 7.90 (s, 1H), 7.35 (dd, $J = 5.0, 1.3$ Hz, 1H), 6.94 (dd, $J = 5.0, 3.5$ Hz, 1H), 6.89 (d, $J = 3.1$ Hz, 1H), 5.41 (d, $J = 3.6$ Hz, 1H), 4.11 – 4.01 (m, 2H), 2.22 (s, 3H), 1.17 (t, $J = 7.1$ Hz, 3H). ^{13}C NMR (100 MHz, DMSO) δ 165.00, 152.21, 148.74, 148.62, 126.64, 124.60, 123.48, 99.75, 59.33, 49.30, 17.63, 14.11.



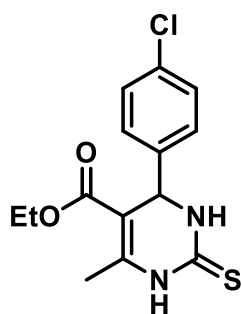
Ethyl 4-heptyl-6-methyl-2-oxo-1,2,3,4-tetrahydropyrimidine-5-carboxylate (2.60). Yield: 78%. ^1H NMR (400 MHz, DMSO) δ 8.92 (s, 1H), 7.32 (s, 1H), 4.12 – 4.00 (m, 3H), 2.16 (s, 3H), 1.38 (s, 2H), 1.28 – 1.15 (m, 13H), 0.85 (t, $J = 6.7$ Hz, 3H). ^{13}C NMR (100 MHz, DMSO) δ 165.42, 152.75, 148.22, 99.38, 58.99, 49.99, 36.63, 31.16, 28.69, 28.59, 23.61, 22.04, 17.65, 14.16, 13.90.



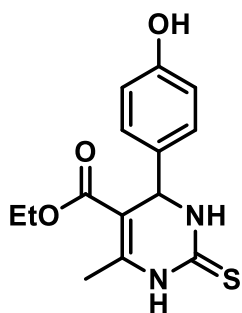
Ethyl 4-((S)-2,7-dimethyloct-6-en-1-yl)-6-methyl-2-oxo-1,2,3,4-tetrahydropyrimidine-5-carboxylate (2.61). Yield: 76%. ^1H NMR (400 MHz, DMSO) δ 8.95 (d, $J = 5.4$ Hz, 1H), 7.41 (s, 1H), 5.13 – 5.02 (m, 1H), 4.10 – 4.01 (m, 3H), 2.16 (s, 3H), 2.00 – 1.86 (m, 2H), 1.68 – 0.95 (m, 17H), 0.85 (d, $J = 6.5$ Hz, 3H). ^{13}C NMR (100 MHz, DMSO) δ 165.33, 165.22, 152.80, 152.64, 148.21, 130.44, 130.27, 124.73, 124.48, 100.31, 59.01, 48.09, 47.95, 44.06, 43.65, 37.56, 35.46, 27.35, 26.97, 25.49, 25.45, 24.91, 24.44, 20.51, 18.74, 17.64, 17.59, 17.46, 14.13.



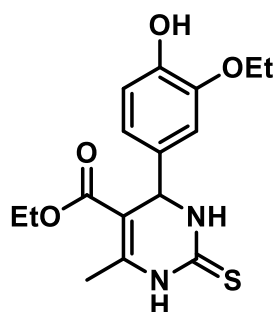
Ethyl 6-methyl-4-phenyl-2-thioxo-1,2,3,4-tetrahydropyrimidine-5-carboxylate (2.62). Yield: 89%. ^1H NMR (400 MHz, DMSO) δ 9.19 (s, 1H), 7.74 (s, 1H), 7.35 – 7.21 (m, 5H), 5.14 (d, $J = 2.7$ Hz, 1H), 3.98 (q, $J = 7.1$ Hz, 2H), 2.25 (s, 3H), 1.09 (t, $J = 7.1$ Hz, 3H). ^{13}C NMR (100 MHz, DMSO) δ 174.20, 165.10, 145.00, 143.46, 128.53, 127.65, 126.35, 100.68, 59.56, 54.00, 17.12, 13.97.



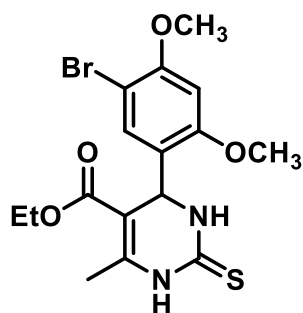
Ethyl 4-(4-chlorophenyl)-6-methyl-2-thioxo-1,2,3,4-tetrahydropyrimidine-5-carboxylate (2.63). Yield: 90%. ^1H NMR (400 MHz, DMSO) δ 10.38 (s, 1H), 9.67 (s, 1H), 7.42 (d, $J = 8.5$ Hz, 2H), 7.23 (d, $J = 8.5$ Hz, 2H), 5.17 (d, $J = 3.7$ Hz, 1H), 4.01 (q, $J = 7.0$ Hz, 2H), 2.29 (s, 3H), 1.09 (t, $J = 7.0$ Hz, 3H). ^{13}C NMR (100 MHz, DMSO) δ 174.22, 164.96, 145.34, 142.34, 132.23, 128.55, 128.28, 100.26, 59.62, 53.41, 17.14, 13.96.



Ethyl 4-(4-hydroxyphenyl)-6-methyl-2-thioxo-1,2,3,4-tetrahydropyrimidine-5-carboxylate (2.64). Yield: 88%. ^1H NMR (400 MHz, DMSO) δ 10.25 (s, 1H), 9.55 (s, 1H), 9.43 (s, 1H), 7.01 (d, $J = 4.6$ Hz, 2H), 6.71 (d, $J = 8.6$ Hz, 2H), 5.07 (d, $J = 3.7$ Hz, 1H), 4.00 (q, $J = 7.1$ Hz, 2H), 2.28 (s, 3H), 1.10 (t, $J = 7.1$ Hz, 3H). ^{13}C NMR (100 MHz, DMSO) δ 173.83, 165.17, 156.86, 144.47, 134.07, 127.61, 115.10, 101.07, 59.46, 53.52, 17.08, 13.99.



Ethyl 4-(3-ethoxy-4-hydroxyphenyl)-6-methyl-2-thioxo-1,2,3,4-tetrahydropyrimidine-5-carboxylate (2.66). Yield: 89%. ^1H NMR (400 MHz, DMSO) δ 10.25 (s, 1H), 9.55 (s, 1H), 8.93 (s, 1H), 6.66 (m, 3H), 5.06 (d, $J = 3.6$ Hz, 1H), 4.09 – 3.92 (m, 5H), 2.27 (s, 3H), 1.32 (t, $J = 7.0$ Hz, 3H), 1.11 (t, $J = 7.1$ Hz, 3H). ^{13}C NMR (100 MHz, DMSO) δ 173.94, 165.13, 146.42, 144.52, 134.47, 118.61, 115.44, 112.27, 101.00, 63.86, 59.49, 53.60, 17.06, 14.69, 14.03.



Ethyl 4-(5-bromo-2,4-dimethoxyphenyl)-6-methyl-2-thioxo-1,2,3,4-tetrahydropyrimidine-5-carboxylate (2.67). Yield: 92%. ^1H NMR (400 MHz, DMSO) δ 10.25 (s, 1H), 9.25 (s, 1H), 7.10 (s, 1H), 6.76 (s, 1H), 5.36 (d, $J = 2.9$ Hz, 1H), 3.96 (q, $J = 7.0$ Hz, 2H), 3.88 (s, 3H), 3.84 (s, 3H), 2.28 (s, 3H), 1.08 (t, $J = 7.0$ Hz, 3H). ^{13}C NMR (100 MHz, DMSO) δ 174.02, 165.04, 157.47, 155.88, 145.09, 131.41, 124.48, 99.96, 98.99, 97.88, 59.38, 56.38, 56.02, 49.46, 16.98, 13.89.

Chapter 3

3.

Magnetic ZSM-5 zeolite: synthesis, characterization and application on the valorization of furfuryl alcohol to γ -valerolactone, alkyl levulinates or levulinic acid

General overview

This chapter will address the design, synthesis and characterization of a magnetically recoverable zeolite catalyst for application in the valorization of bio-derived furfuryl alcohol. A brief introduction regarding the valorization of bio-derived compounds will be presented, comprising latest advances concerning the development of catalysts for these reactions.

3.1 - Introduction

Crude oil is currently the major source for the production of energy/fuels and chemicals used to produce plastics and other essential materials. However, petroleum is considered a non-renewable source, and as its supply diminishes, its prices have risen, depending not only on worldwide supply/demand, but also on political and economic situations. Besides that, other problems associated with the use of fossil fuels include the increase in the emission of greenhouse gases such as CO₂, CH₄, N₂O.⁶⁶

In this context, the increasing worldwide demand for transportation fuels and starting materials for the production of fine chemicals has turned biomass into a promising feedstock in the last decades since it represents a

66. Speight, J. G. *An Introduction to Petroleum Technology, Economics, and Politics*, 1st ed., Hoboken, John Wiley & Sons, 2011.

multiple source alternative when compared to petroleum as a single source.⁶⁷ Furthermore, the utilization of biomass contributes to the mitigation of greenhouse gases through cycles of regrowth of the biomass source and production of CO₂ by combustion (Figure 3.1).⁶⁸

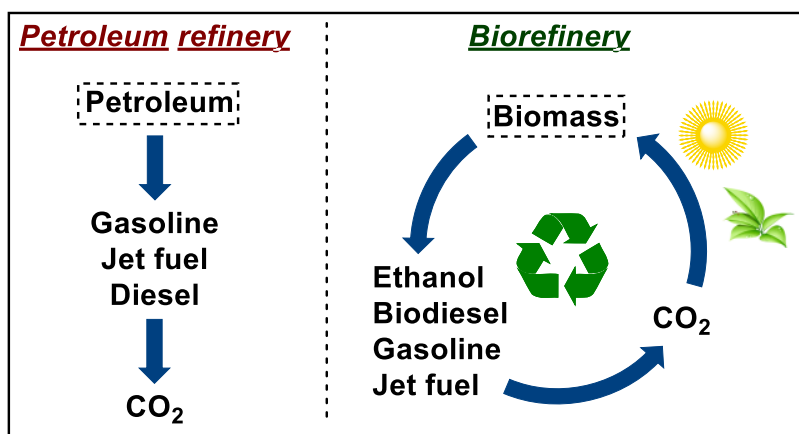


FIGURE 3.1 - Comparison between the CO₂ cycles of a petroleum refinery and a biorefinery.

Considering the source from which biomass is derived, it can be classified as 1) starchy feedstocks, namely corn, beets, and sugar cane, 2) triglyceride feedstocks, such as soybean, algae, jatropha and other types of crop oils, and lignocellulosic feedstocks.⁶⁹ Lignocellulosic biomass is by far the most abundant feedstock, and it is present in all types of biomass since it contributes to the structural integrity of all plants.

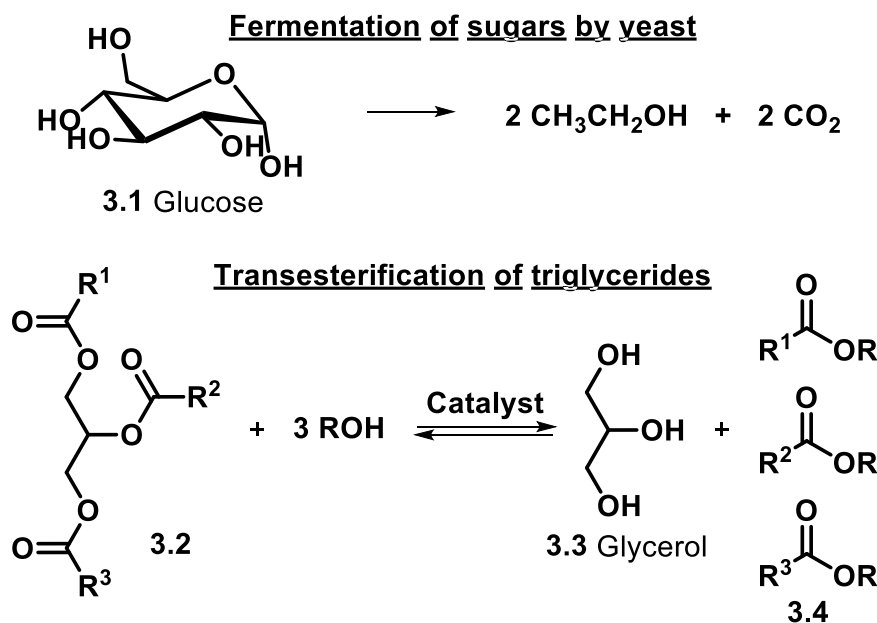
The starchy and triglyceride feedstocks can be converted to fuels and chemicals through the so-called first-generation processes, which include the direct fermentation of the sugars present in the starchy feedstocks to produce ethanol and the transesterification of triglycerides to produce biodiesel (Scheme

67. (a) Cortright, R. D.; Davda, R. R.; Dumesic, J. A. *Nature*, **418**:964, 2002. (b) Huber, G. W.; Chheda, J. N.; Barrett, C. J.; Dumesic, J. A. *Science*, **308**:1446, 2005. (c) Román-Leshkov, Y.; Barrett, C. J.; Liu, Z. Y.; Dumesic, J. A. *Nature*, **447**:982, 2007. (d) Chheda, J. N.; Huber, G. W.; Dumesic, J. A. *Angew. Chem. Int. Ed.*, **46**:7164, 2007 (e) Serrano-Ruiz, J. C.; Luque, R.; Sepúlveda-Escribano, A.; *Chem. Soc. Rev.*, **40**:5266, 2011. (f) Climent, M. J.; Corma, A.; Iborra, S. *Green Chem.*, **16**:516, 2014.

68. Alonso, D. M.; Bond, J. Q.; Dumesic, J. A. *Green Chem.*, **12**:1493, 2010.

69. Lee, J. W. *Advanced Biofuels and Bioproducts*, 1st ed, New York, Springer-Verlag, 2013.

3.1). However, since most of these feedstocks are edible, they have generated a “food *versus* fuel” issue, where the production of biofuels has been claimed to divert crops away from food in order to produce fuels.



SCHEME 3.1 - First-generation processes for the production of biofuels.

Besides fuels, first-generation chemicals and materials can be produced from sugars/starch, and those include polymers (polylactic acid, PLA) and chemical building blocks (succinic acid and 1,3-propanediol). On the other hand, first-generation chemicals from vegetable oils are basically fatty acids and their esters.

As aforementioned, lignocellulosic biomass is highly abundant due to its presence in all kinds of plants. Moreover, it is non-edible, and, therefore, does not aggravate “food versus fuel” issues. In this way, it has been used to produce second-generation fuels, mainly through the initial biochemical hydrolysis of the polysaccharides in the biomass, followed by the fermentation of its sugars into ethanol.⁷⁰ Other types of conversion are also possible, such as fast-pyrolysis, a thermochemical process that produces bio-oil, which is a mixture of

70. Wertz, J.-L.; Bédoué, O. *Lignocellulosic Biorefineries*, 1st ed, Lausanne, EPFL Press, 2013.

hydroxyaldehydes, hydroxyketones, sugars and dehydrosugars, carboxylic acids and phenolic compounds.⁷¹

In spite of second-generation ethanol being certainly the most popular compound produced from lignocellulosic biomass, a great effort has been dedicated in the last decades to the separation of lignocellulosic biomass in its different fractions and conversion of those to highly valuable chemical compounds known as platform chemicals.

3.1.1 - Conversion lignocellulose-derived compounds to value-added chemicals

Lignocellulosic biomass is defined as non-edible plant materials constituted primarily of cellulose, hemicelluloses, and lignin. Several types of plant materials composed by lignocellulosic biomass can be used to produce fuels and value-added chemicals, namely, agricultural waste (straw, corn stovers and cobs, bagasse, molasses), forestry wastes (wood chips), fractions of urban and industrial paper wastes and fast-growing energy crops (miscanthus, switchgrass, short-rotation poplar or willow coppice).⁷⁰

Lignins are the minor constituents of lignocellulosic biomass, being present in 10-25% in its dry weight and it has the main function of furnishing structural rigidity to plants; it can be separated from biomass through depolymerization/solubilization in alkaline alcoholic solutions.⁷² This fraction is a polymer with a structure like **3.8** composed by methoxylated phenylpropane moieties such as coumaryl, coniferyl and sinapyl alcohols (**3.9**, **3.10** and **3.11**, respectively, in Figure 3.2).

71. Mohan, D.; Pittman Jr., C. U.; Steele, P. H. *Energy & Fuels*, **20**:848, 2006.

72. (a) Mosier, N.; Wyman, C. E.; Dale, B. E.; Elander, R. T.; Lee, Y. Y.; Holtzapple, M.; Ladisch, M. R. *Bioresour. Technol.*, **96**:673, 2005. (b) Chakar, F. S.; Ragauskas, A. J. *Ind. Crops Prod.*, **20**:131, 2004.

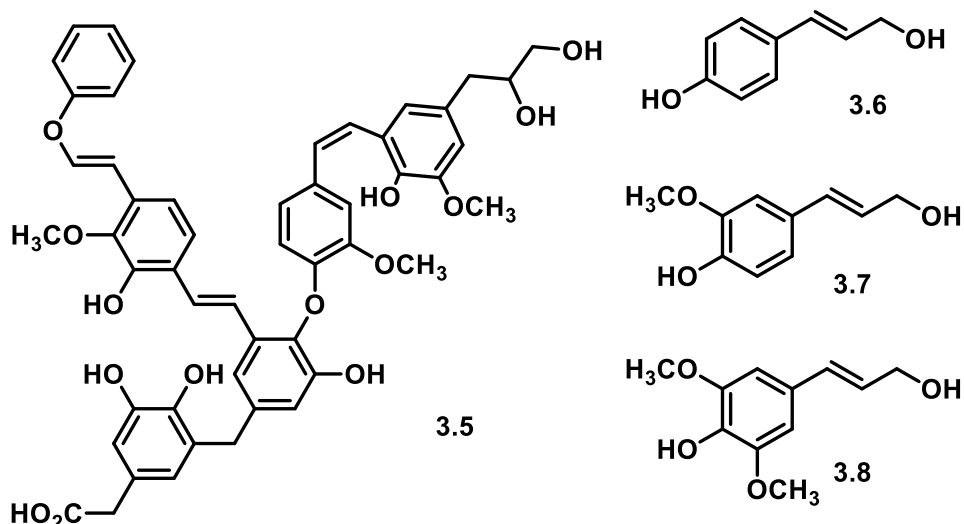


FIGURE 3.2 - General structure of lignin and its main constituents.

Notwithstanding recent developments in this field,⁷³ the conversion of lignins to value-added compounds still remains challenging and, therefore, the main final destination of these compounds is fast-pyrolysis in order to produce bio-oil.

The second most abundant fraction of lignocellulosic biomass is hemicellulose, being present in 25-35% in its dry weigh. Hemicellulose is a polymer comprised mainly by the pentose D-xylose, but other sugar monomers such as the pentose L-arabinose, and the hexoses D-galactose, D-glucose and D-mannose are also present as minor constituents (Figure 3.3).

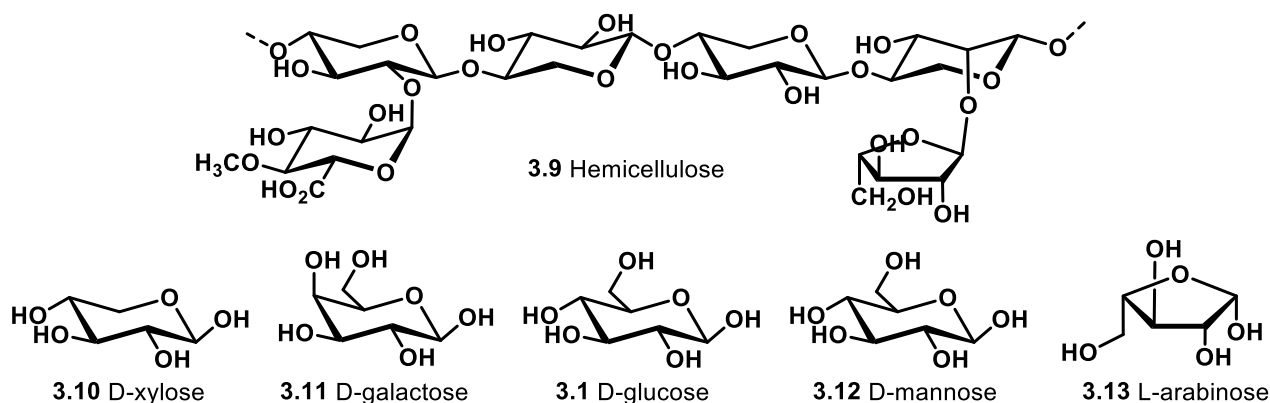


FIGURE 3.3 - General structure of hemicellulose and its sugar constituents.

73. (a) Thakur, V. K.; Thakur, M. K.; Raghavan, P.; Kessler, M. R. *ACS Sustainable Chem. Eng.* **2**:1072, 2014. (b) Azadi, P.; Inderwildi, O. R.; Farnood, R.; King, D. A. *Renew. Sust. Energ. Rev.* **21**:506, 2013.

Hemicellulose can be extracted from lignocellulosic biomass employing physical methods or a combination of physical and chemical methods. Once separated from the other fractions of lignocellulosic biomass, it can be easily hydrolyzed to its monomers in diluted acidic media, generating xylose as the main product.

Cellulose is the major constituent of lignocellulose, being present in 40-50% of its dry weight. It is a polymer of glucose units linked via β -glycosidic bonds, what confers a relative rigid crystallinity to the overall structure, which causes its hydrolysis to be considerably more difficult when compared to hemicellulose (Figure 3.4). High yields (up to 90%) in the hydrolysis of cellulose to its glucose monomers can be attained via biocatalysis after biomass pretreatment.⁷⁴ The hydrolysis of this polymer using strong acids such as sulfuric acid is usually problematic, since dehydration and polymerization products may be generated in the process.

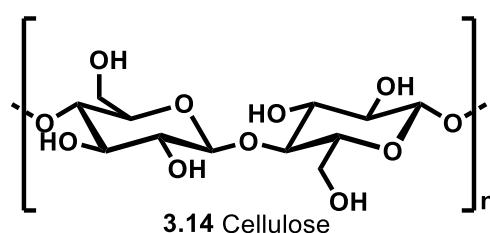


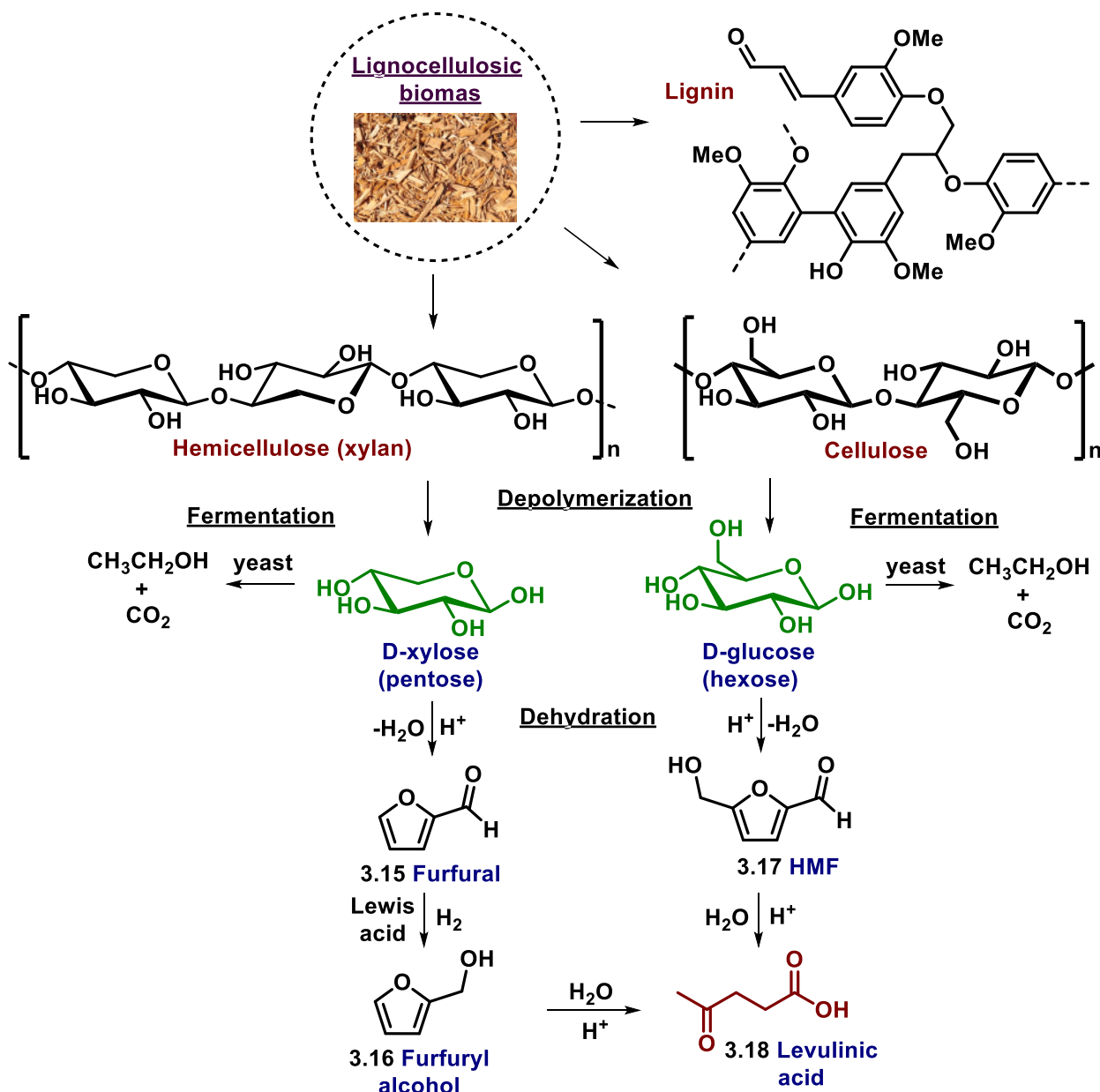
FIGURE 3.4 - General structure of cellulose.

Once the monomer sugars D-xylose and D-glucose are produced via hydrolysis from hemicellulose and cellulose, respectively, they may be submitted to fermentation to produce second-generation ethanol. However, the energetics of xylose fermentation are seemingly less favorable than those for glucose, a result of differences in the formation of the key precursor intermediates for the fermentation of these two sugars.⁷⁵

74. (a) Wyman, C. E.; Dale, B. E.; Elander, R. T.; Holtzapple, M; Ladisch, M. R., Lee, Y. Y. *Bioresour. Technol.*, **96**:2026, 2005. (b) Lloyd, T. A.; Wyman, C. E.; *Bioresour. Technol.*, **96**:1967, 2005.

75. Martin, A. M. *Bioconversion of Waste Materials to Industrial Products*, 1st ed, New York, Springer-Verlag, 1998.

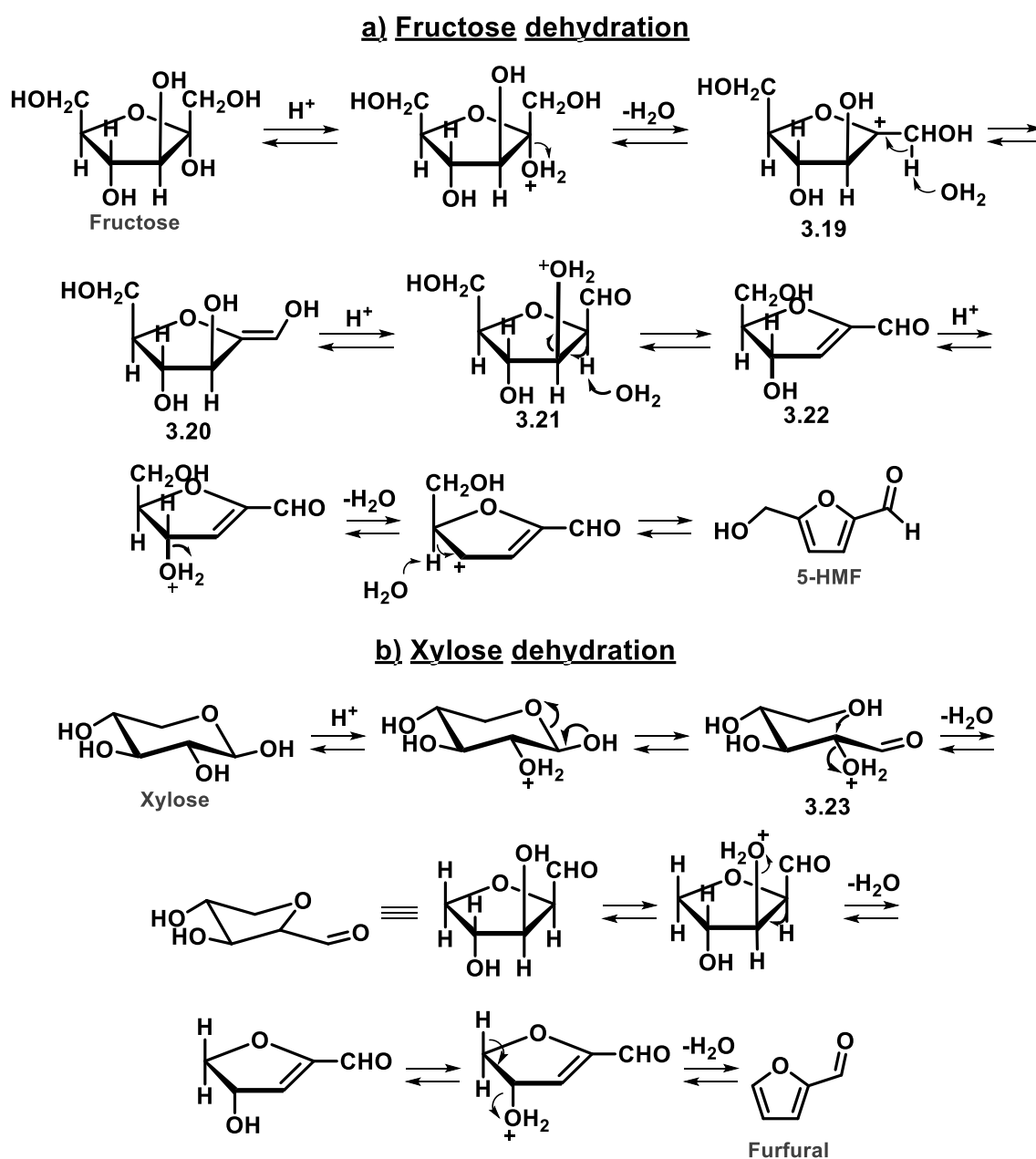
Besides fermentation, sugars from lignocellulosic biomass can also react in acid media to afford dehydration products – furfural (Fur) from xylose and 5-hydroxymethylfurfural (5-HMF) from glucose. 5-HMF may further react in acid media, generating levulinic acid (LA) and formic acid in the presence of water, while the conversion of Fur to LA requires a hydrogenation step in order to convert the aldehyde to alcohol, which undergoes hydrolysis (Scheme 3.2).⁷⁶



SCHEME 3.2 - Products of the acid treatment of carbohydrates derived from lignocellulosic biomass.

76. (a) Wang, T.; Nolte, M. W.; Shanks, B. H. *Green Chem.*, **16**:548, 2014. (b) Chheda, J. N.; Dumesic, J. A. *Catal. Today*, **123**:59, 2007.

The dehydration of fructose (Scheme 3.3a) and xylose (Scheme 3.3b) involves a series of steps. Fructose dehydration starts with the elimination of a water molecule from the anomeric carbon after protonation, giving intermediate **3.19**, and the enol **3.20** after an E1 elimination reaction. After tautomerization and another protonation step, aldehyde **3.21** is formed. The elimination of another water molecule from carbon 3 and a proton from carbon 4 originates the product. On the other hand, xylose dehydration starts in its protonated open aldose form **3.23** with the elimination of a water molecule from



SCHEME 3.3 - Dehydration reaction mechanism for a) fructose and b) glucose.

carbon 2 after protonation. Next, the elimination of two additional water molecules affords the product.

Compounds such as furfural, furfuryl alcohol, 5-HMF and levulinic acid are currently known as platform chemicals, i.e., compounds that are used as building blocks for highly valuable chemical compounds and fuels (Scheme 3.4).⁶⁸

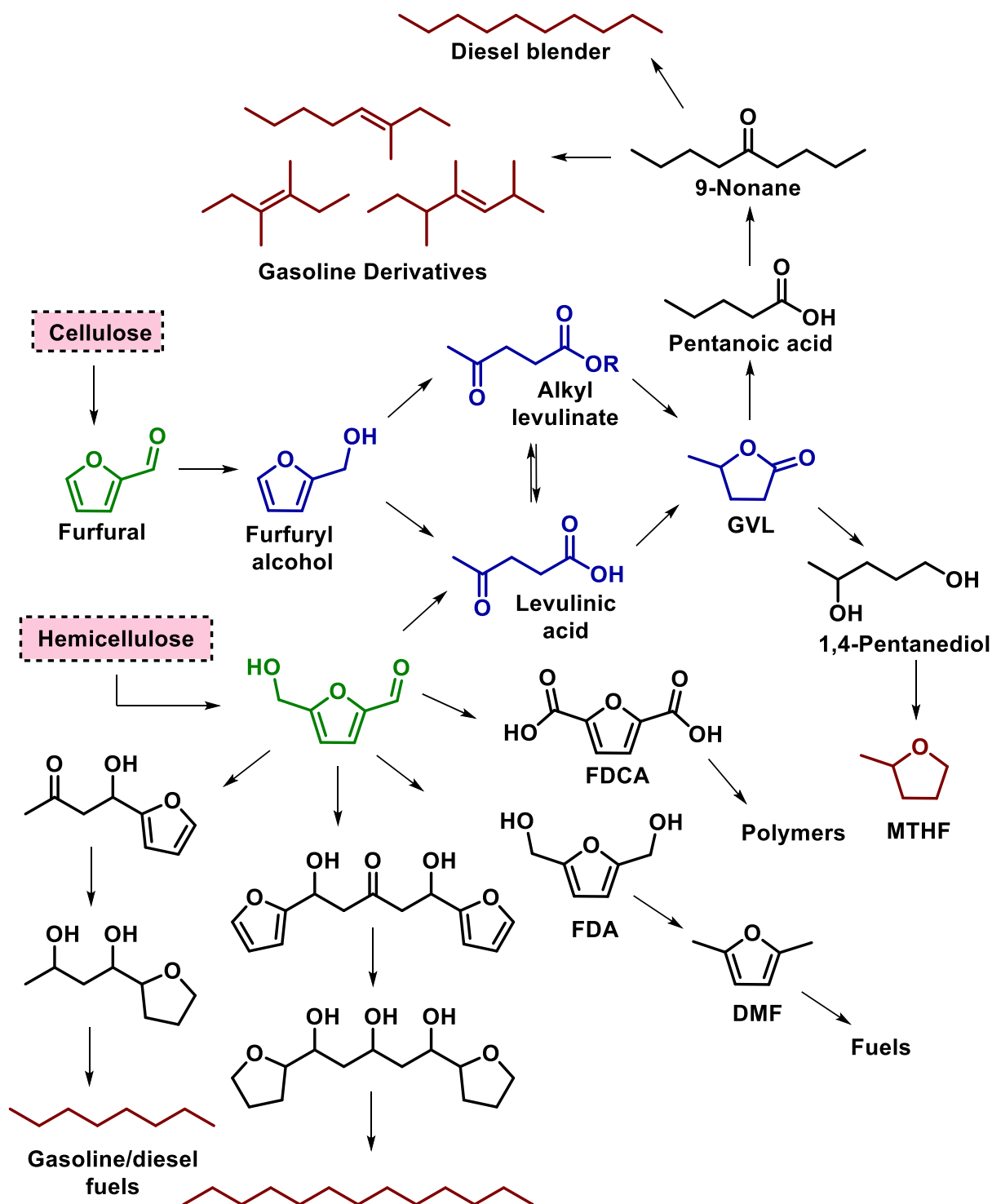
In this context, a molecule that has been the target of considerable research is levulinic acid (LA), since it can be converted to compounds that are precursors to several products used in personal care, in the pharmaceutical industry, and as a fragrance and flavoring agent. Interestingly, LA can be synthesized from furfural (which is produced from a pentose) in a process that has furfuryl alcohol as an intermediate, and also from 5-HMF (which is produced from hexoses).⁷⁷

Likewise, the esters of LA (alkyl levulinates, AL) also find several important direct applications, namely as green solvent, food additive, polymerization additive, perfume, flavoring and fuel formulations. Among these applications, the latter has been pointed as very promising, since AL can be used as additives in gasoline, diesel or even in biofuels and present the advantage of leading to a cleaner combustion and consequently, decreasing the gaseous emissions such as NO_x when compared to conventional additives.⁷⁸

An important compound produced from LA or its esters is γ -valerolactone (GVL), a cyclic compound soluble in water and that presents very low toxicity. GVL finds a variety of direct uses, particularly as solvent, food additive and in the production of perfumes. Furthermore, GVL behaves similarly to ethanol in mixtures with petroleum derivatives, although it has a lower vapor pressure, which improves combustion and makes it a valuable fuel additive.

77. (a) Rackemann, D. W.; Doherty, W. O. S. *Biofuels, Bioprod. Bioref.* **5**:198, 2011. (b) Leonard, R. H. *Ind. Eng. Chem.*, **48**:1330, 1956. (c) Timokhin, B. V.; Baransky, V A.; Eliseeva, G. D. *Russ. Chem. Rev.*, **68**:73, 1999.

78. Démolis, A.; Essayem, N.; Rataboul, F. *ACS Sustainable Chem. Eng.*, **2**:1338, 2014.



SCHEME 3.4 - Conversion of furfural and 5-HMF to other platform chemicals and value-added products.

Additionally, it has been also showing to be a very promising precursor to fuels.⁷⁹ 5-HMF is another example of a compound easily produced from lignocellulosic

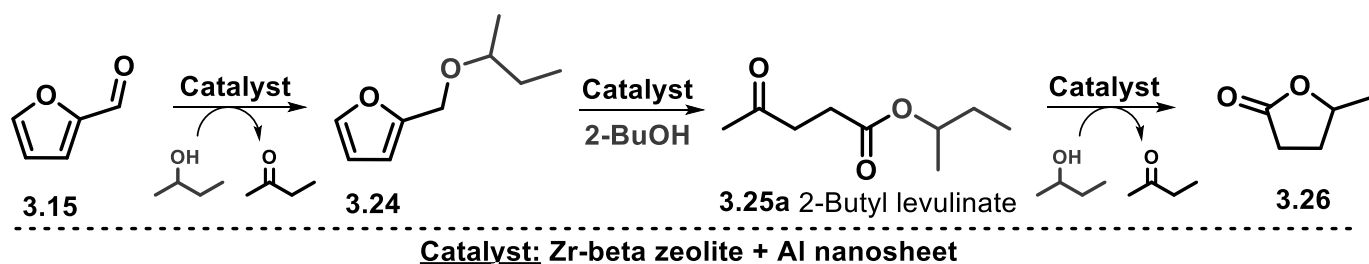
79. Alonso, D. M.; Wettstein, S. G.; Dumesic, J. A. *Green Chem.*, **15**:584, 2013.

biomass that can be converted to a wide range of molecules that are precursors to polymers, solvents and fuels.⁸⁰

Taking these factors into account, the development of alternative sustainable routes for the production of these scaffolds is of great interest. For instance, the most common method for the production of GVL still consists in the stepwise hydrogenation of levulinic acid or its esters in the presence of Lewis acids followed by cyclization, while levulinic esters are mainly produced from the esterification of levulinic acid using mineral acids as catalysts. In order to overcome these drawbacks, several groups have been reporting new and greener approaches for the synthesis of these compounds.

In this sense, several catalysts have been reported for the conversion of Fur or furfuryl alcohol (FA) to AL and/or GVL, such as sulfonic acid functionalized materials, ion-exchanged resins, Cu-Fe, Ru/C, Ru/graphite, RuCl₃-PPh₃, ZrO₂, MgO, Al₂O₃, CeZrO₄.⁸¹

A very interesting work was disclosed by Roman-Leshkov's group, which reported a pioneering domino approach for the synthesis of GVL directly from furfural (Scheme 3.5).⁸²



SCHEME 3.5 - Synthesis of GVL from furfural reported by Roman-Leshkov's group.

80. Rosatella, A. A.; Simeonov, S. P.; Frade, R. F. M.; Afonso, C. A. M. *Green Chem.*, **13**:754, 2011.

81. (a) Lange, J. P.; van de Graaf, W.D.; Haan, R. J. *ChemSusChem*, **2**:437, 2009. (b) Yan, K.; Chen, A. *Fuel*, **115**:101, 2014. (c) Kijeński, J.; Winiarek, P.; Paryjczak, T.; Lewicki, A.; Mikołajska, A. *Appl. Catal. A:Gen.*, **233**:171, 2002. (d) Jae, J.; Zheng, W.; Lobo, R. F.; Vlachos, D. G. *ChemSusChem*, **6**:1158, 2013. (e) Panagiotopoulou, P.; Martin, N.; Vlachos, D. G. *J. Mol. Catal. A-Chem.*, **392**:223, 2014. (f) Chia, M.; Dumesic, J. A. *Chem. Commun.*, **47**:12233, 2011.

82. Bui, L.; Luo, H.; Gunther, W. R.; Román-Leshkov, W. *Angew. Chem.* **125**:8180, 2013.

The use of Fur as a starting material for the production of GVL is highly desirable, since its production from lignocellulosic biomass can be achieved in a few steps. Some other starting materials, namely levulinic acid and its esters, can be easily hydrogenated and cyclized to afford GVL, and, as such, several catalysts have been reported for this transformation;⁸³ however, the production of LA and AL from lignocellulosic biomass requires several additional steps when compared to furfural or furfuryl alcohol.

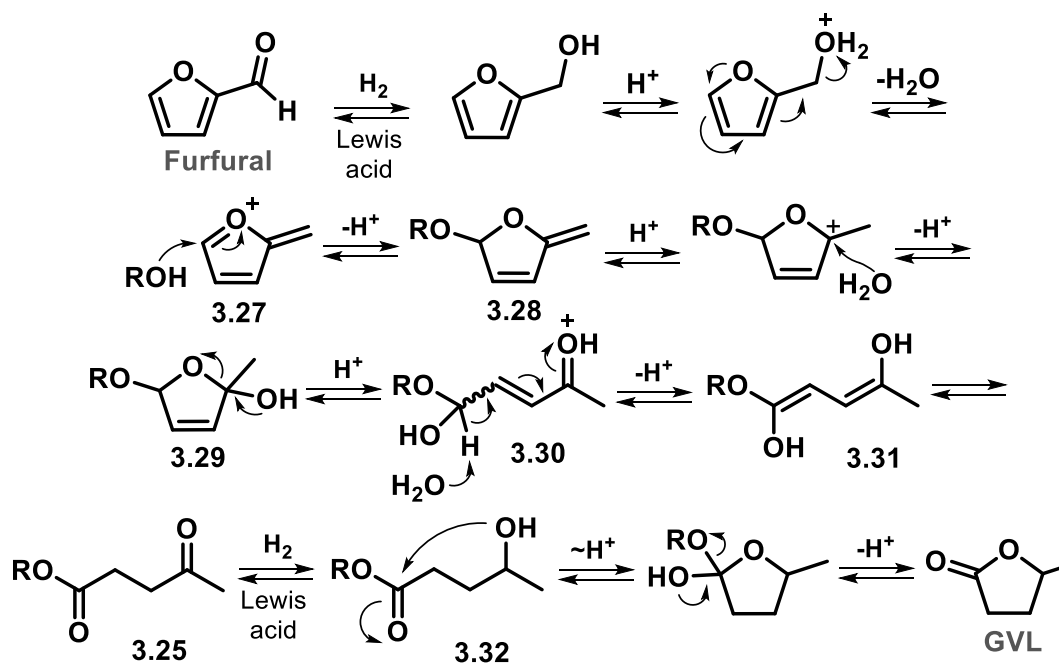
In order to achieve all reaction steps in a single-pot, a combination of catalysts was used, since the transformations require both Brønsted and Lewis acid catalysts. In that way, the group studied a variety of catalysts, and the highest yield of GVL (68%) was achieved by the use of a combination of Zr-beta zeolite (Lewis acid catalyst) and an Al-nanosheet (Brønsted acid catalyst). A great feature of this work was the use of secondary alcohols as hydrogen donors in the reduction steps, which eliminates the need of working with molecular hydrogen.

Though the conversion of bio-derived compounds to valerolactone is currently a hot topic in literature, the mechanism of this transformation is scarcely reported.⁸⁴ However, mechanistic studies suggest that the transformation occurs via a series of steps that start with the conversion of furfural to furfuryl alcohol (Scheme 3.6). Next, the elimination of a water molecule leads to the formation of a stabilized carbocation intermediate **3.27**, which undergoes a nucleophilic attack by an alcohol molecule, giving intermediate **3.28**. Next, the protonation of **3.28** followed by the attack of a water molecule leads to cyclic enol **3.29**. Next, the acid-catalyzed ring-opening reaction of **3.29** gives the protonated α,β -unsaturated enone **3.30**, which after deprotonation affords conjugated enol **3.31**. Finally, the

83. (a) Yan, Z.; Lin, L.; Liu, S. *Energ. Fuel.*, **23**:3853, 2009. (b) Galletti, A. M. R.; Antonetti, C.; De Luise, V.; Martinelli, M. *Green Chem.*, **14**:688, 694. (c) Upare, P. P.; Lee, J.-M.; Hwang, D. W.; Halligudi, S. B.; Hwang, Y. K.; Chang, J.-S. *J. Ind. Eng. Chem.*, **17**:287, 287. (d) Hengne, A. M.; Rode, C. V. *Green Chem.*, **14**:1064, 2012. (e) Wettstein, S. G.; Bond, J. Q.; Alonso, D. M.; Pham, H. N.; Datsy, A. K.; Dumesic, J. A. *Appl. Catal. B-Environ.*, **117-118**:321, 2012. (f) Li, W.; Xie, J.-H.; Lina, H.; Zhou, Q.-L. *Green Chem.*, **14**:2388, 2012. (g) Deng, L.; Zhao, Y.; Li, J.; Fu, Y.; Liao, B.; Guo, Q.-X. *ChemSusChem*, **3**:1172, 2010.

84. Horvat, J.; Klaić, B.; Metelko, B.; Šunjić, V. *Tetrahedron Lett.*, **26**:2111, 1985.

tautomerization of **3.31** gives the ester product **3.25**. The final steps of the reaction involve the reduction of the carbonyl group in compound **3.32** followed by cyclization and elimination of an alcohol molecule, giving rise to GVL as the final product.

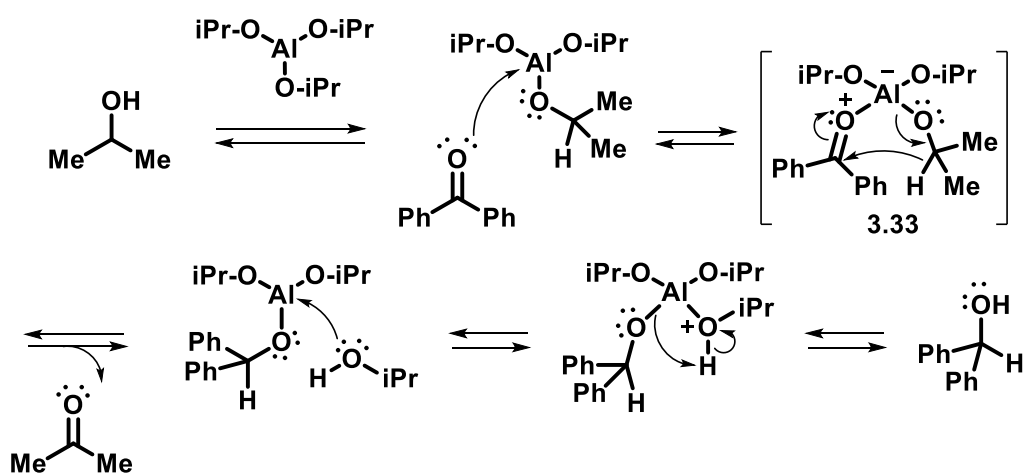


SCHEME 3.6 - Mechanism of the conversion of furfural to GVL.

The hydrogenation method in the aforementioned protocol consists on a transfer hydrogenation reaction, also known as Meerwein-Ponndorf-Verley (MPV) reduction (Scheme 3.7), and it has been widely used in the last few years in the conversion of bio-derived compounds.⁸⁵

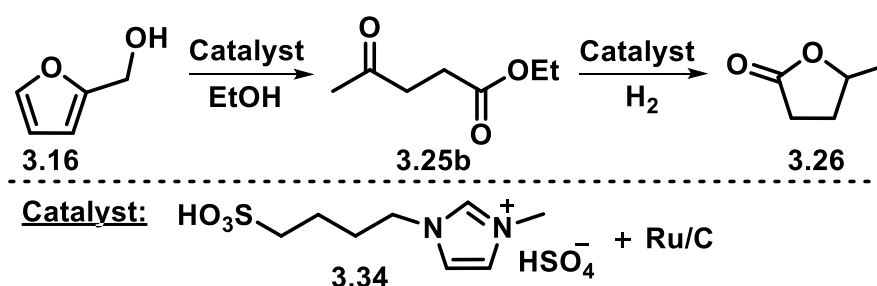
In this reaction, a secondary alcohol donates hydrogen through the coordination with a Lewis acid catalyst (being aluminum isopropoxide the traditional one), proceeding via a six-membered transition state **3.33**. A ketone, the oxidized form of the hydrogen donor, is also a product of the reaction; the oxidation reaction of the hydrogen donor to the ketone is known as Oppenauer oxidation (Scheme 3.7).

85. (a) Gilkey, M. J.; Xu, B. *ACS Catal.*, **6**:1420, 2016. (b) Wang, D.; Astruc, D. *Chem. Rev.*, **115**:6621, 2015.



SCHEME 3.7 - Reaction mechanism for the Meerwein-Ponndorf-Verley reduction.

Another interesting protocol for the synthesis of GVL was reported by Rode's group, which employed furfuryl alcohol as starting material and a combination of the acidic ionic liquid **3.34** and ruthenium supported on carbon as Lewis acid catalyst (Scheme 3.8). In this case, the reduction step was accomplished employing molecular hydrogen.⁸⁶

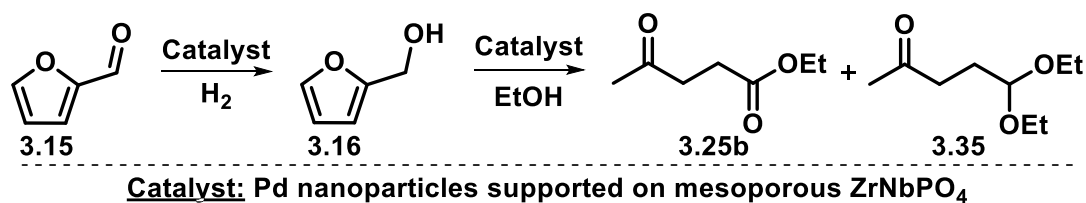


SCHEME 3.8 - Synthesis of GVL from furfuryl alcohol reported by Rode's group.

Yuan's group also reported a standout method for the synthesis of ethyl levulinate (EL) from furfural (Scheme 3.9).⁸⁷ Nanoparticles of palladium supported on a mesoporous zirconium niobium mixed phosphate synthesized by a sol-gel approach were used as catalyst in ethanol using molecular hydrogen for the reduction step. Additionally, selectivities up to 76% to ethyl levulinate were

86. Hengne, A. M.; Kamble, S. B.; Rode, C. V. *Green Chem.*, **15**:2540, 2013.

87. Chen, B.; Li, F.; Huang, Z.; Lu, T.; Yuan, Y.; Yuan, G. *ChemSusChem*, **7**:202, 2014.



SCHEME 3.9 - Synthesis of EL from furfural reported by Yuan's group.

achieved, with 5,5-diethoxypentan-2-one (DPO) **3.35** being detected as a byproduct. The recyclability of the catalyst was also evaluated in a five-run test, without expressive losses in the yield of the ester products.

Additional methods have been reported using carbohydrates as substrates for GVL production.⁸⁸ In spite of these developments for the valorization of biomass-derived compounds, there are some lingering drawbacks such as the use of high temperatures, high pressures and the requirement of noble metal or cooperative catalysts (both a Brønsted and a Lewis acid catalyst), which may compromise the recovery and reuse of these materials at the end of the reaction.

3.1.2 - Zeolites as catalysts for bio-derived compounds

Zeolites are crystalline, microporous three-dimensional aluminosilicates, comprised of corner-sharing TO₄ tetrahedra, in which T can be Si or Al. The framework of these materials contains open cavities in the form of channels and cages that can be occupied by H₂O molecules and extra-framework cations (K⁺, Na⁺, Ca²⁺) that are commonly exchangeable. Interestingly, since the

88. (a) Deng, L.; Li, J.; Lai, D. M.; Fu, Y.; Guo, Q. X. *Angew. Chem. Int. Ed.*, **48**:6529, 2009. (b) Du, X.-L.; He, L.; Zhao, S.; Liu, Y.-M.; Cao, Y.; He, H.-Y.; Fan, K.-N. *Angew. Chemie*, **123**:7961, 2011. (c) Qi, L.; Horváth, I. *TACS Catal.*, **2**:2247, 2012. (d) Yuan, J.; Li, S.; Yu, L.; Liu, Y.; Cao, Y.; He, H.; Fan, K.-N. *Energy Environ. Sci.*, **6**:3308, 2013 (e) Cui, J.; Tan, J.; Deng, T.; Cui, X.; Zheng, H.; Zhu, Y.; Li, Y. *Green Chem.*, **17**:3084, 2015. (f) Zhou, H.; Song, J.; Kang, X.; Hu, J.; Yang, Y.; Fan, H.; Meng, Q.; Han, B. *RSC Adv.*, **5**:15267, 2015.

channels in the zeolite structure are large enough to allow the passage of guest species, these materials are known as molecular sieves.⁸⁹

There are several methods for the preparation of zeolites, which basically consist on the hydrolysis of Al and Si precursors in basic media in the presence of organic templates. Depending on the Si/Al ratio, on the employed organic template and in the temperature of synthesis, different zeolites can be prepared. Figure 3.5 shows the general preparation of a beta zeolite.⁹⁰

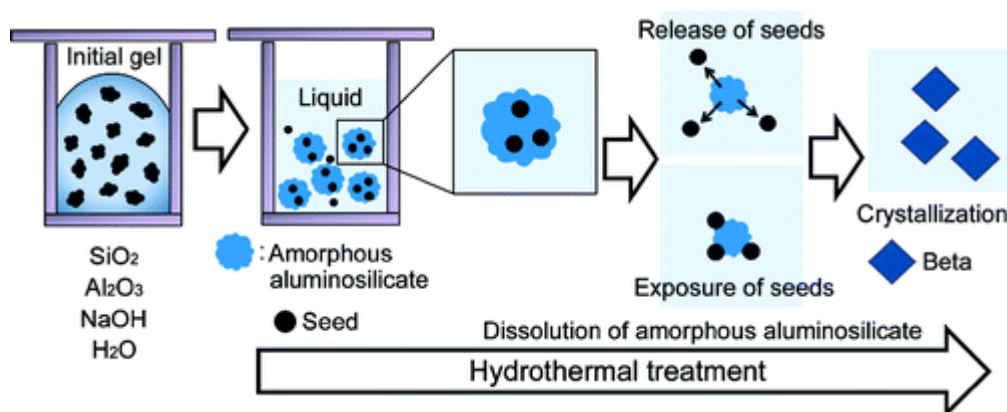


FIGURE 3.5 - General preparation of beta zeolite. (Reprinted with permission from ref. 24. Copyright 2011 American Chemical Society.)

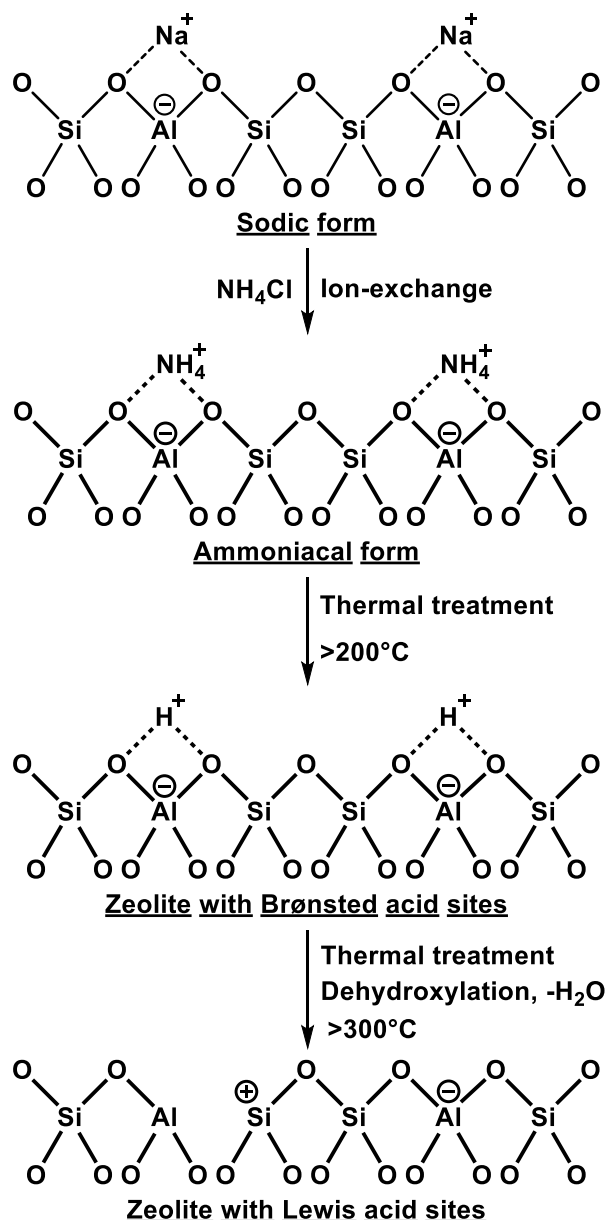
In the process of preparation of the zeolite, the precursors initially hydrolyze in basic media, forming SiO_2 and Al_2O_3 particles, establishing a gel. Next, when submitted to a hydrothermal treatment, the gel is converted to small crystalline particles of aluminosilicates that act as seeds embedded in an amorphous aluminosilicate phase that is further solubilized in the medium. In the final step, the aluminosilicates seeds condensate, forming the crystalline zeolitic material.

89. (a) Auerbach, S. M.; Carrado, K. A.; Dutta, P. K. Handbook of Zeolite Science and Technology, Boca Raton, CRC Press, 2003. (b) Xu, R.; Pang, W.; Yu, J.; Huo, Q.; Chen, J. Chemistry of Zeolites and Related Porous Materials: Synthesis and Structure, 1st ed, Hoboken, John Wiley & Sons, 2007. (c) Cejka, J.; Corma, A.; Zones, S. Zeolites and Catalysis: Synthesis, Reactions and Applications, 1st ed, John Wiley & Sons, 2010.

90. Kamimura, Y.; Tanahashi, S.; Itabashi, K.; Sugawara, A.; Wakihara, T.; Shimojima, A.; Okubo, Tatsuya. J. Phys. Chem. C, **115**:744, 2011.

A very interesting feature of zeolitic materials are their tunable acidity, which is dependent on the method of preparation, form of the material, temperature of dehydration and Si/Al ratio.⁹¹

Interestingly, different temperatures of calcination may completely change the nature of the acid sites in the zeolite framework, as showed in Scheme 3.10.



SCHEME 3.10 Generation of acid sites in zeolites through thermal treatment.

91. (a) Yu, Z.; Li, S.; Wang, Q.; Zheng, A.; Jun, X.; Chen, L.; Deng, F. J. Phys. Chem. C, **115**:22320, 2011. (b) Lonyi, F.; Valyon, J. Micropor. Mesopor. Mater., **47**:293, 2001. (c) Coster, D.; Blumenfeld, A. L.; Fripiat, J. J. J. Phys. Chem., **98**:6201, 1994. (d) Chukin, G. D.; Kulikov, A. S.; Sergienko, S. A. React. Kinet. Catal. L, **27**:287, 1985.

The zeolite is usually prepared in its sodic form, which presents few superficial acid sites; it may be further converted to its ammoniacal form through a simple ion exchange procedure that followed by a thermal treatment in temperatures between 200 and 300 °C generate the acid form of the material, releasing ammonia in the process. It is important to highlight that the acid sites generated at 200-300°C are Brønsted-type acid sites. If Lewis acid sites are desirable in the zeolite, those can be generated through the calcination at temperatures above 300°C, which leads to the dehydration of the material, generating coordinatively unsaturated Al and Si atoms, as which act as strong Lewis acids (Scheme 3.10).

Due to their tunable properties, especially acidity and pore size, zeolites are among the most efficient catalysts for the conversion of bio-derived compounds. Some groups have reported, for instance, highly selective conversions of methyl levulinate to GVL (selectivity up to 97%) using zeolites as catalysts, by doping these structures with metals or combining them with other supported metal catalysts.⁹² Cao and co-workers have disclosed the use of the HZSM-5 (Si/Al=25) zeolite in the FA conversion to etherification products, achieving moderate to high selectivities.⁹³ HZSM-5 zeolites were also reported to promote successfully the conversion of FA to LA in biphasic systems.⁹⁴

Although these materials are highly active catalysts, tedious and high-power consumption processes such as centrifugation or filtration steps are required for their separation from the reaction medium. To overcome this limitation, magnetically recoverable zeolites provide a sustainable alternative, being easily recovered from the reaction medium by simply applying an external magnetic field.

92. (a) Nadgeri, J. M.; Hiyoshi, N.; Yamaguchi, A.; Sato, O.; Shirai, M. *Appl. Catal. A-Gen.*, **470**:215, 2014. (b) Luo, H. Y.; Consoli, D. F.; Gunther, W. R.; Román-Leshkov, Y. *J. Catal.*, **320**:198, 2014. (c) Wang, J.; Jaenicke, S.; Chuah, G.-K. *RSC Adv.*, **4**:13481, 2014.

93. Cao, Q.; Guan, J.; Peng, G.; Hou, T.; Zhou, J.; Mu, X. *Catal. Commun.*, **58**:76, 2015.

94. Mellmer, M. A.; Gallo, J. M. R.; Alonso, D. M.; Dumesic, J. A. *ACS Catal.*, **5**:3354, 2015.

3.2 - Aims-Objectives

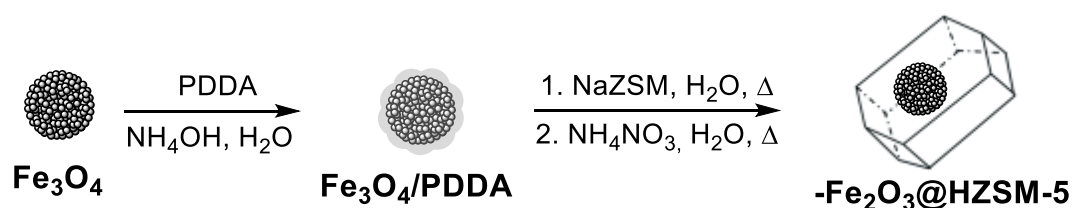
As discussed, zeolites display remarkable properties, especially in what regards the conversion of bio-derived compounds. Additionally, there is a growing concern related to the development of more environmentally benign processes for the valorization of bio-derived compounds. Considering these facts, the aim of the work described in this chapter was the preparation of a magnetically recoverable zeolite catalyst that displays both Brønsted and Lewis acid sites. That feature allows the direct domino conversion of furfuryl alcohol to GVL mediated by a single catalyst. Specific objectives of this work include:

- ✓ Synthesis of a catalyst constituted by Fe_3O_4 as support and HZSM-5 zeolite as active phase;
- ✓ Full characterization of the catalyst;
- ✓ Evaluation of the catalytic activity of this material on the conversion of furfuryl alcohol to GVL;
- ✓ Evaluation of the possibility of generating other highly valuable platform chemicals by the fine tuning of the catalytic system;
- ✓ Evaluation of the recyclability of catalyst.

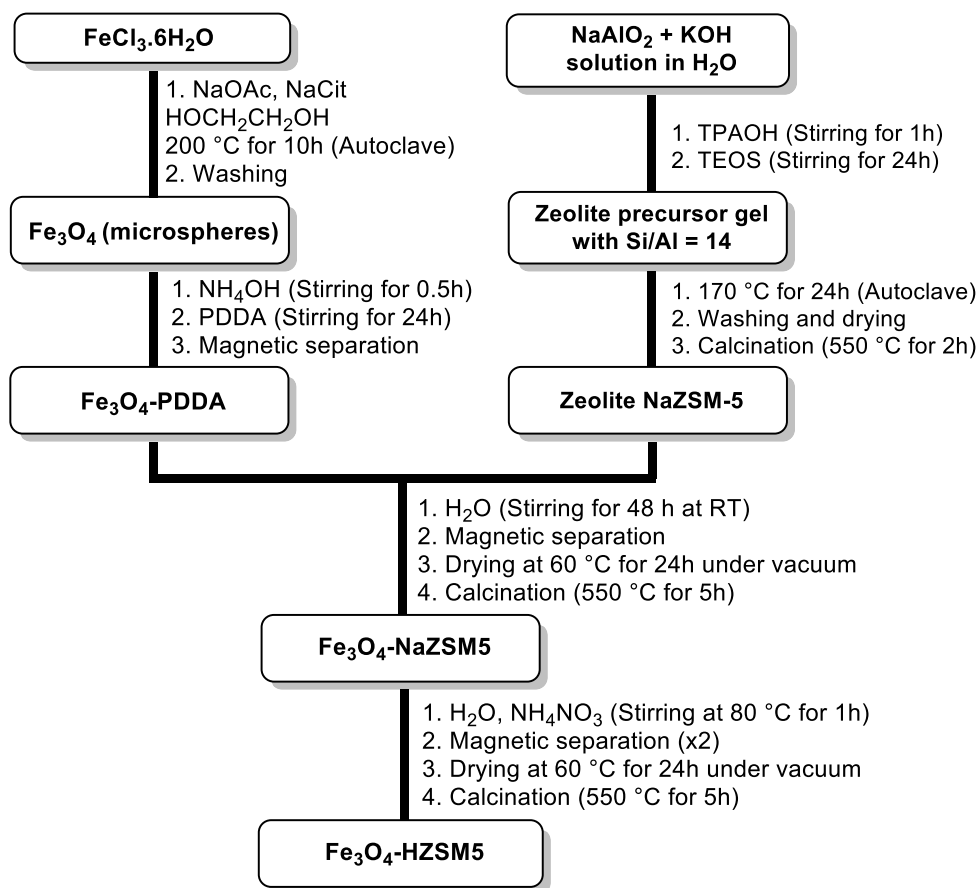
3.3 - Results and discussion

3.3.1 - Catalyst characterization

The overall method for the preparation of the magnetically recoverable catalyst is depicted in Scheme 3.11, while a detailed flowchart with the procedure is showed in Scheme 3.12.



SCHEME 3.11 - Synthesis of the magnetically recoverable HZSM-5 catalyst.

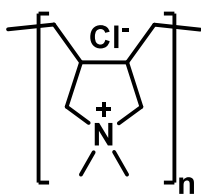


SCHEME 3.12 - Flowchart showing the detailed preparation of the magnetically recoverable zeolite.

The preparation of the catalyst was initiated by the synthesis of the magnetite microspheres used as support employing a solvothermal approach having $\text{FeCl}_3 \cdot 6\text{H}_2\text{O}$ as the iron source, ethylene glycol as solvent and reducing agent, sodium acetate as alkali source and sodium citrate as a stabilizing agent.²¹ In this case, the solvothermal method was chosen because it affords particles with good morphology using relatively inexpensive starting materials, although relatively high temperatures are required.

The support was next functionalized with Poly(diallyldimethylammonium chloride) (3.36, Figure 3.6); a cationic polymer that is able to interact with the negatively charged moieties of the zeolite framework.⁹⁵

95. Lv, Q.; Li, G.; Lu, H.; Cai, W.; Huang, H.; Cheng, C. **203**:202, 2015.



3.36 PDDA

FIGURE 3.6 - Structure of PDDA, a polymer used for the immobilization of negatively charged species on the surface of materials.

For the zeolite's preparation ($\text{Si}/\text{Al} = 14$), sodium aluminate, tetraethyl orthosilicate and potassium hydroxide were used as alumina, silica and alkali source, respectively, while tetrapropylammonium hydroxide was employed as the organic template. After the zeolite was obtained in its sodic form, it was immobilized on the magnetite microspheres, submitted to calcination to remove the PDDA polymer followed by an ion exchange to transform the zeolite from its sodic (NaZSM-5) to the ammoniacal form ($\text{NH}_4\text{ZSM-5}$); finally, a thermal treatment converted the zeolite to its acid form (HZSM-5) and the magnetite microspheres to maghemite ($\gamma\text{-Fe}_2\text{O}_3$).

The ensuing magnetically recoverable catalyst was thoroughly characterized using several techniques such as XRD, TEM, HAADF-STEM chemical mapping and Mössbauer spectroscopy. XRD studies of the Fe_3O_4 microspheres confirmed the presence of diffraction peaks related to the cubic structure spinel type. Moreover, the average crystallite size, calculated by Scherrer's equation, was 16 nm, which is the average size of the individual nanoparticles that constitute the microspheres (Figure 3.7).

The XRD pattern of the pure zeolite NaZSM-5 (green diffractogram in Figure 3.7) displayed its characteristic peaks, as well as a peak related to the presence of silica in quartz phase in $2\theta = 21^\circ$. However, during the immobilization step under a relatively basic media, the quartz phase is dissolved and, therefore, does not appear in the final catalyst (red diffractogram in Figure 3.7).

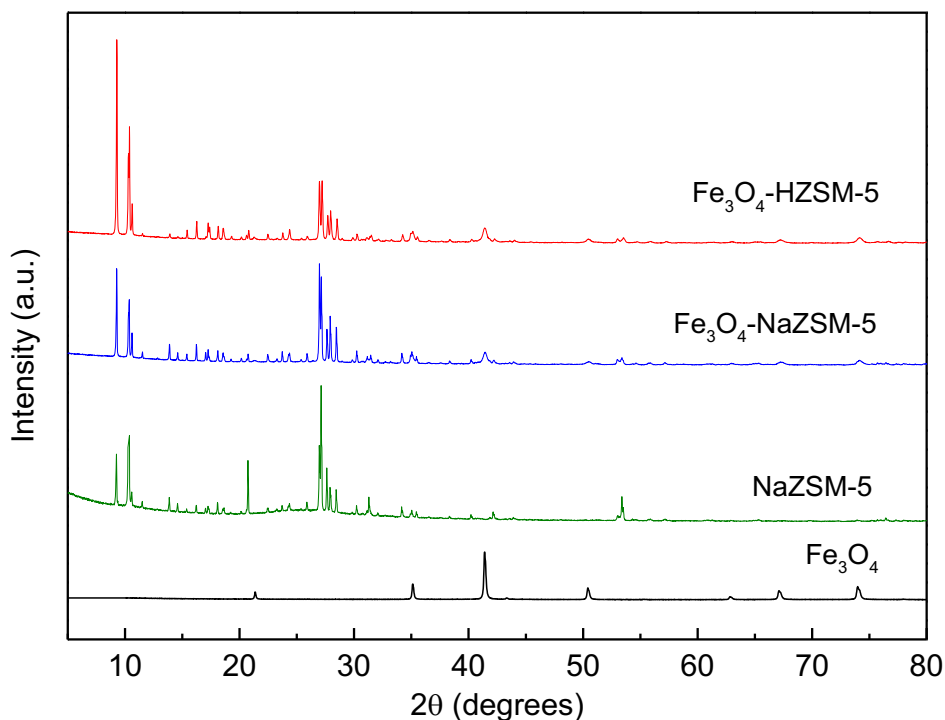


FIGURE 3.7 - XRD patterns of Fe_3O_4 , the zeolite NaZSM-5 and the magnetically recoverable catalyst with the zeolite in its sodic ($\gamma\text{-Fe}_2\text{O}_3\text{-NaZSM-5}$) and acid ($\gamma\text{-Fe}_2\text{O}_3\text{-HZSM-5}$) form.

Next, the morphological characterization was conducted for both the Fe_3O_4 microspheres and the magnetic ZSM-5 zeolite catalyst using TEM (Figure 3.8).

Indeed, Figures 3.8a and 3.8b show small Fe_3O_4 nanoparticles arranged in microspheres with sizes ranging from 100 to 290 nm and a mean size around 170 nm. A detailed particle count of the Fe_3O_4 is depicted in Figure 3.9. The images in Figures 3.8c, 3.8d and 3.8e show a thick shell of zeolite HZSM-5 of approximately 45 nm surrounding the magnetic microspheres in a core-shell type structure, although some of the zeolite grains do not display any magnetic core due to the high amount of zeolite on the material.

The HRTEM images of the pure magnetite (Figure 3.10a) show the presence of microspheres of around 160 nm of diameter while the images of the magnetic zeolite (Figure 3.10b and 3.10c) show the presence of a large HZSM-5 grain, with size around 600 nm, encapsulating the magnetic microspheres, as

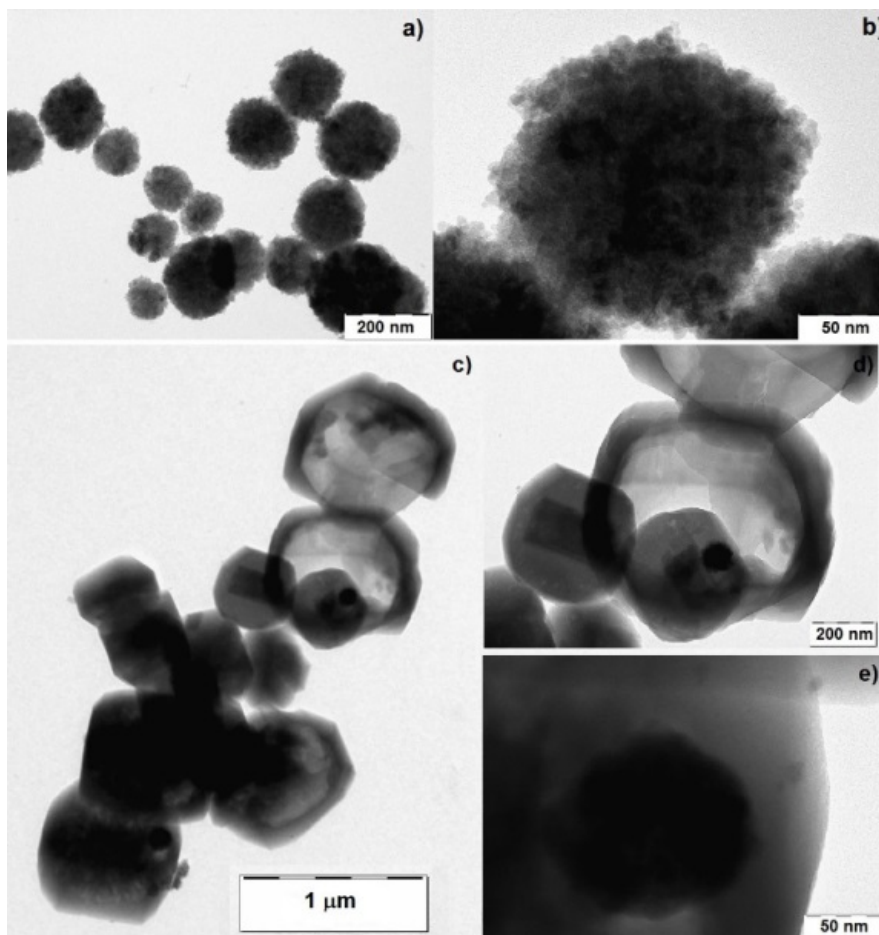


FIGURE 3.9 - TEM images of a) and b) Fe_3O_4 microspheres and c), d) and e) the $\gamma\text{-Fe}_2\text{O}_3\text{-HZSM5}$ magnetic zeolite.

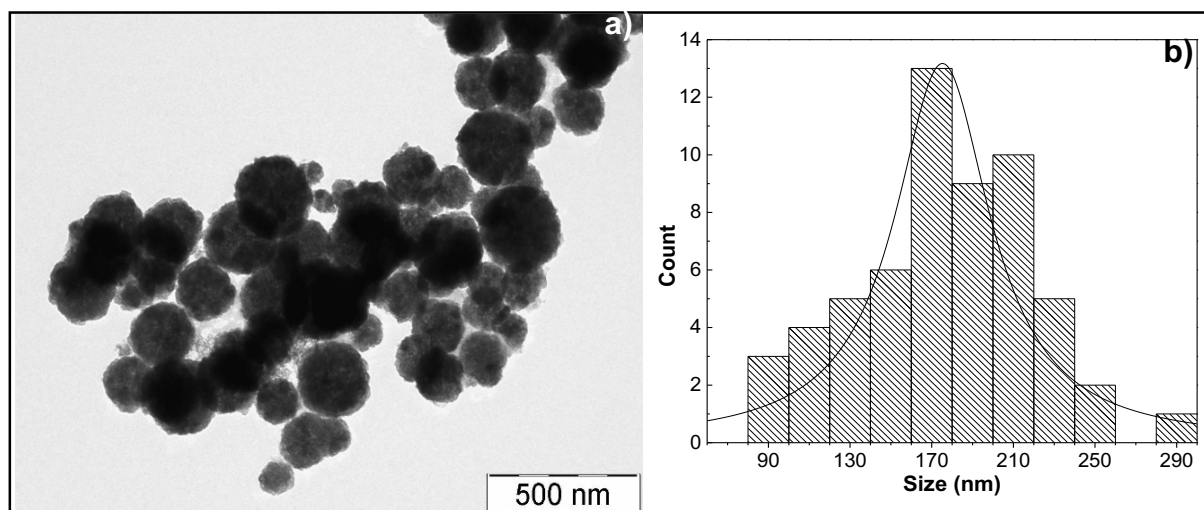


Figure 3.8 – a) TEM image used in the construction of the b) size distribution histogram for the Fe_3O_4 microspheres.

evidenced by the elemental mapping of Fe, Al, Si and Fe/Al/Si (Figure 3.10d-f, respectively). Furthermore, it is noteworthy that even the magnetic microspheres

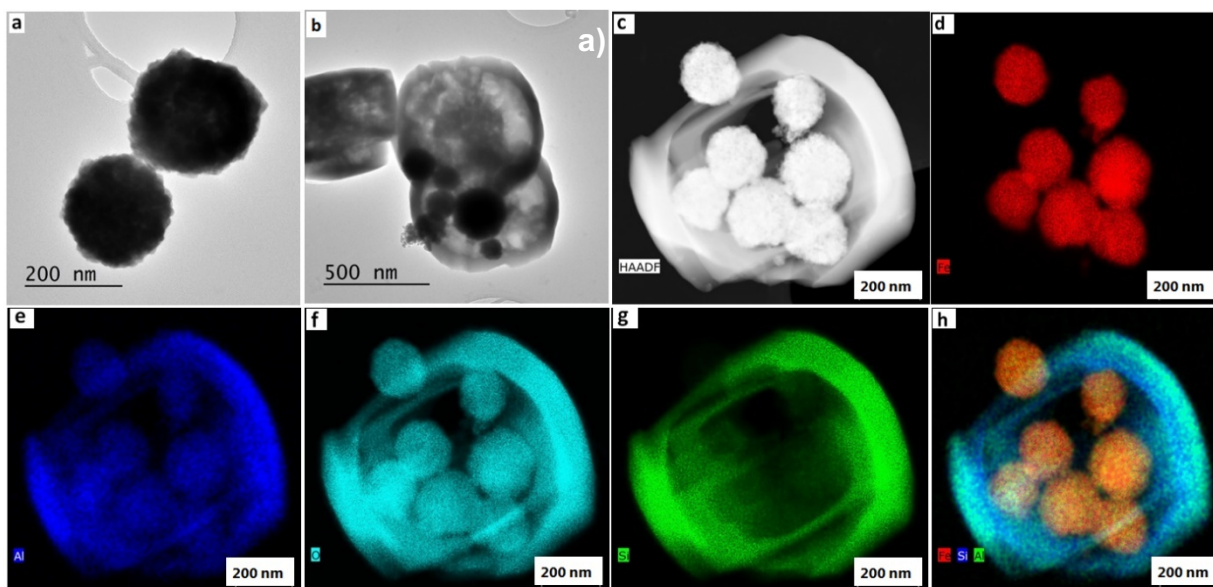


FIGURE 3.10 - a) HR-TEM image of magnetite spheres at 200 nm; b) HR-TEM image of $\gamma\text{-Fe}_2\text{O}_3\text{-HZSM5}$; c) HAADF image of $\gamma\text{-Fe}_2\text{O}_3$ microspheres encapsulated into HZSM-5 grain; (d-h) elemental mapping of Fe, Al, O, Si and Fe/Si/Al, respectively.

outside of the large zeolite particles display a layer of Si and Al atoms, suggesting the coating with the HZSM-5 zeolite.

In order to have a better insight on the total acid site density of the catalyst, a temperature-programmed desorption of NH_3 (TPD- NH_3) analysis was conducted. The high acidity value ($1840 \mu\text{mol g}^{-1}$) obtained for this material is related to the high amount of aluminum present in the zeolite; the Si/Al ratio determined by XRF was around 12 (theoretical ratio being Si/Al = 14).

The TPD- NH_3 desorption curve revealed the presence of two different types of acid sites, with one desorption peak around 207°C , which represents the weak acid sites, and another in 355°C , related to moderate to strong acid sites (Figure 3.11).

With the aim to comprehend the nature of these acid sites, a FTIR spectroscopy analysis of adsorbed pyridine was conducted, determining qualitatively the presence of Lewis and Brønsted acid sites in the sample.

The FTIR spectroscopy of adsorbed molecules is one of the most common methods for determining the nature of the surface functional groups in solid materials. Considering that the infrared spectra of a molecule reflects its

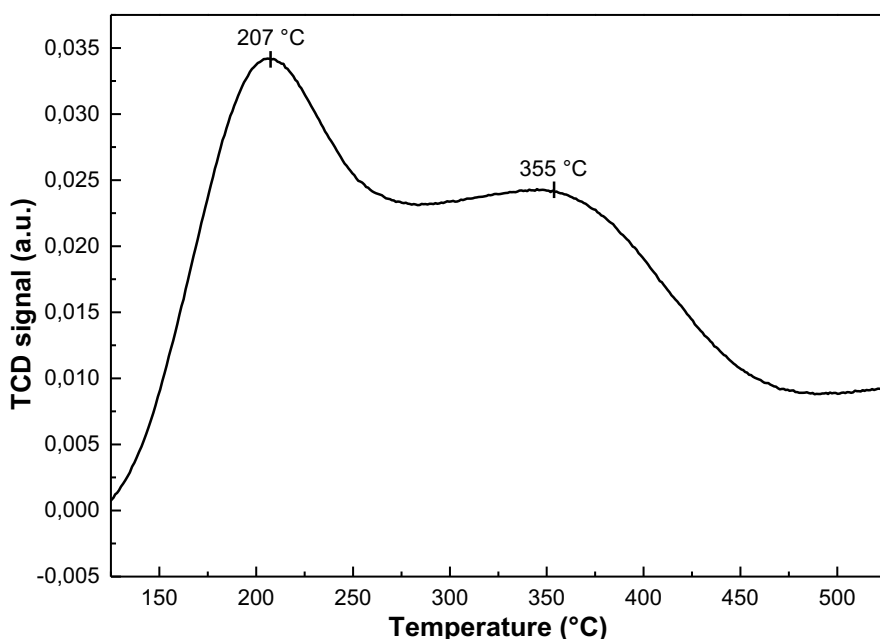


FIGURE 3.11 - Temperature programmed desorption of NH₃ over Fe₃O₄-HZSM-5.

overall structure as well as specific features of determined functional groups, when a probe molecule gets in contact with a solid surface, the formation of adsorption complexes will cause some specific bands to shift, affording various types of information.

Pyridine, for instance, has showed to be an exceptional probe for the determination of acid sites in solid acids, since its ring vibration modes are very sensitive to their environment and can be used to differentiate Lewis and Brønsted acid sites.⁹⁶ Figure 3.12 shows the characteristic infrared spectrum for pyridine; it is possible to distinguish two different regions in it, one regarding the stretching of C-H bonds (1800-3100 cm⁻¹) and other regarding the stretching of the C-C bonds in the aromatic ring (400-1800 cm⁻¹), and more specifically, a region with very well define bands in the region of 1400-1700 cm⁻¹ (C_{2v} group symmetry).

96. (a) Hattori, H.; Ono, Y. *Solid Acid Catalysis: From Fundamentals to Applications*, 1st ed., Boca Raton, CRC Press, 2015. (b) Bhatia, S. *Zeolite Catalysts: Principles and Applications*, Boca Raton, CRC Press, 1989. (c) Lercher, J. A.; Grundling, C.; Eder-Mirth, G. *Catal. Today*, **27**:353, 1996.

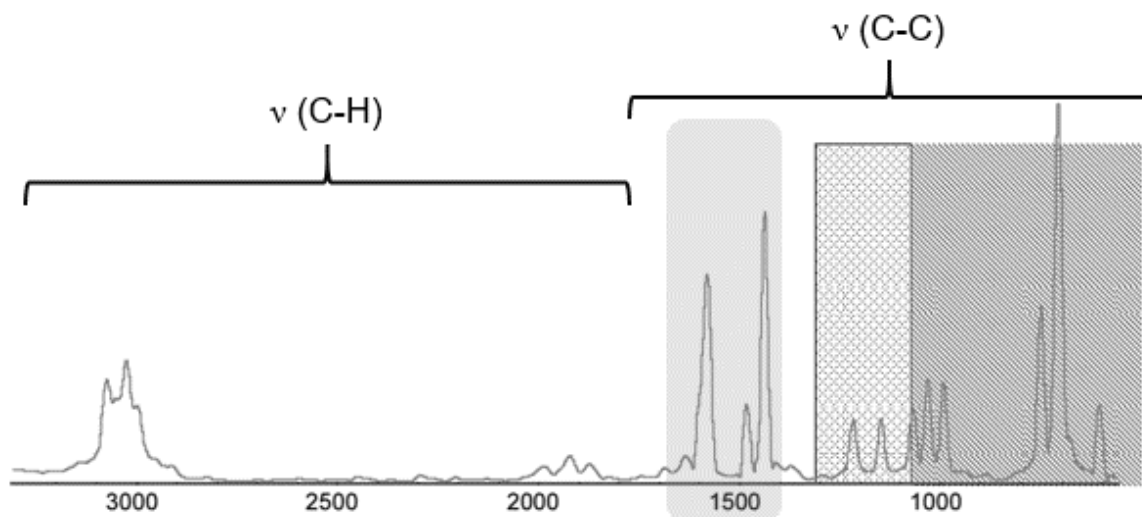
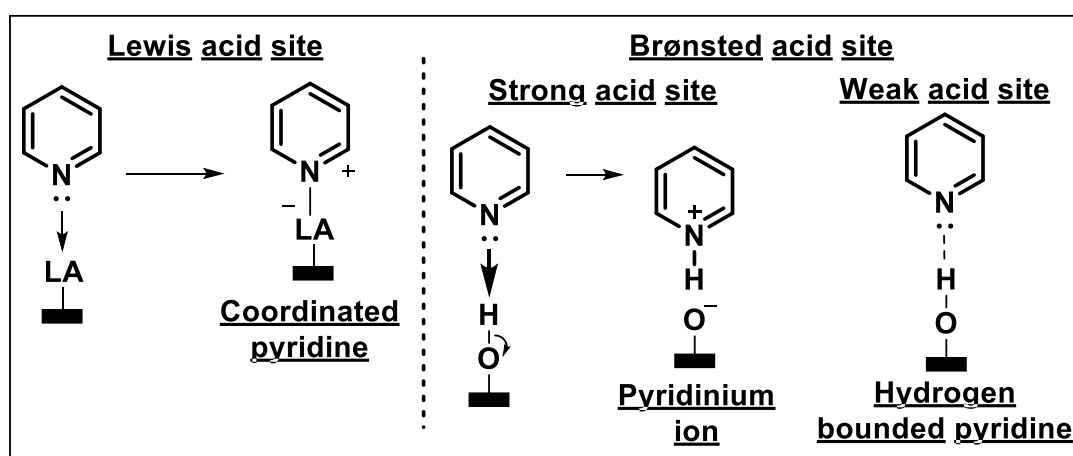


FIGURE 3.12 - Infrared spectrum of pyridine.

When pyridine is absorbed over an acid solid surface, it may interact with it in three different ways: (1) if the acid site is of Lewis type, a coordination complex will be formed, while if the site is of Brønsted type, (2) the pyridinium ion is formed through the protonation of pyridine by strong acid sites, or (3) pyridine interacts with weak acid sites through hydrogen bonding (Scheme 3.13).

Interestingly, in spite of all the infrared bands in the evaluated region being due to the stretching of C-C bonds in the aromatic ring, it is possible to distinguish between the different species formed since the interaction with each type of acid site will cause a different effect in the bonds on the aromatic ring, and, therefore, displaying bands with different wavenumbers.



SCHEME 3.13 - Interaction of pyridine with different acid sites on a solid acid catalyst.

In this way, the presence of Brønsted and Lewis acid sites in the sample was confirmed by analyzing the infrared spectra of absorbed pyridine of the prepared catalyst (Figure 3.13). The position of the bands in the infrared spectra of pyridine absorbed over the magnetically recoverable zeolite catalyst are listed in Table 3.1 with their respective assignments and the types of acid site to which they are referred to.

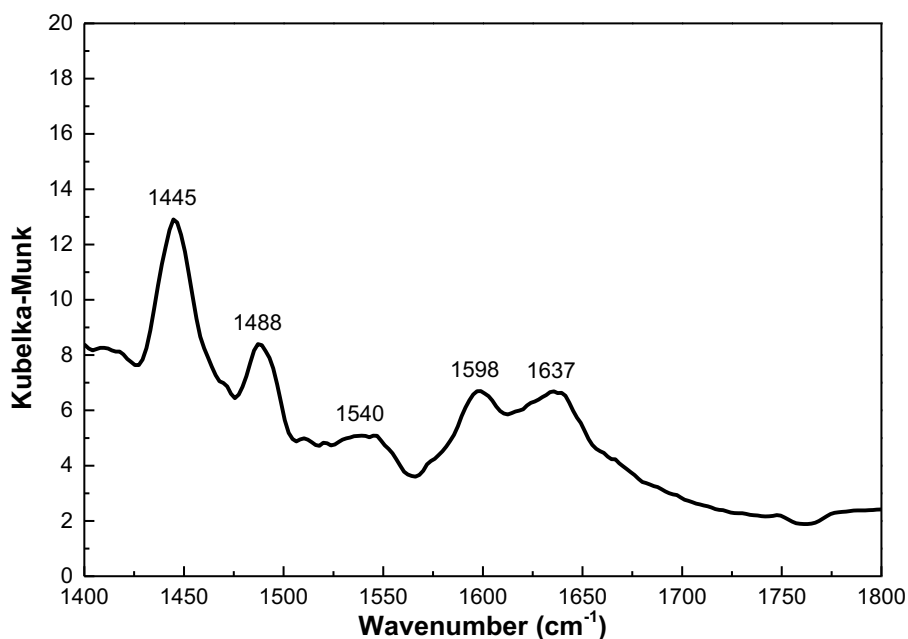


FIGURE 3.13 - Infrared spectrum of pyridine absorbed on the acidic sites of the magnetically recoverable HZSM-5 zeolite.

TABLE 3.1 - Position of the bands in the infrared spectra of pyridine absorbed over the magnetically recoverable zeolite catalyst.

Band	Wavenumber (cm ⁻¹)	Assignment	Type of acid site
1	1445	Coordinated pyr	Lewis
2	1488	2-type interaction	Lewis and Brønsted
3	1540	Pyridinium ion	Brønsted
4	1598	Coordinated pyr	Lewis
5	1637	Pyridinium ion	Brønsted

As showed in Figure 3.13 and Table 3.1, the catalyst displays both Lewis and Brønsted acid types. The band in 1445 cm⁻¹ is correspondent solely to Lewis acid sites, while the one in 1488 cm⁻¹ corresponds to both Lewis and

Brønsted acid sites. The other three bands present in the spectrum are assigned to Brønsted acid sites, being the ones in 1540 cm^{-1} and 1637 cm^{-1} ascribed to the stretching of C-C bonds in the aromatic ring of the pyridinium ion, which implies the presence of strong Brønsted acid sites.⁹⁷

In order to get a deeper insight into the chemical nature of the sample in terms of iron-containing phases, ^{57}Fe Mössbauer spectroscopy was employed. Mössbauer spectroscopy is one of the most consolidated techniques for the differentiation between magnetite and maghemite; it is a very useful technique used to study nuclear structure through the absorption and re-emission of gamma rays, using a combination of the Mössbauer effect and Doppler shifts to probe the hyperfine transitions between the excited and ground states of a determined nucleus. Though many isotopes can be analyzed by this technique, ^{57}Fe is by far the most studied.⁹⁸

The ^{57}Fe Mössbauer spectrum of the magnetic zeolite, recorded at room temperature, is showed in Figure 3.14 and the values of the Mössbauer hyperfine parameters, derived upon spectrum fitting, are listed in Table 3.2.

The analysis of the room-temperature ^{57}Fe Mössbauer spectrum identified three spectral components, i.e., the two sextets and one doublet (see Figure 3.14 and Table 3.2). The isomer shift value of the sextet with the dominant spectral area falls within the range expected for Fe^{3+} ions with high-spin state (i.e., $S = 5/2$) in both tetrahedral and octahedral coordination. If present alone without any other spectral components, the spectrum would resemble features typical for $\gamma\text{-Fe}_2\text{O}_3$, i.e., one sextet with the values of the Mössbauer hyperfine parameters

97. (a) Jin, F.; Li, Y. *Catal. Today*, **145**:101, 2009. (b) Buzzoni, R.; Bordiga, S.; Ricchiardi, G.; Lamberti, C.; Zecchina, A. *Langmuir*, **12**:930, 1996.

98. (a) Yoshida, Y.; Langouche, G. *Mössbauer Spectroscopy*, 1st ed, New York, Springer-Verlag, 2013. (b) Sharma, V. K.; Klingelhöfer, G.; Nishida, T. *Mössbauer Spectroscopy: Applications in Chemistry, Biology, and Nanotechnology*, 1st ed, Hoboken, John Wiley & Sons, 2013.

averaged over both the tetrahedral and octahedral sites in the γ -Fe₂O₃ crystal structure.⁹⁹

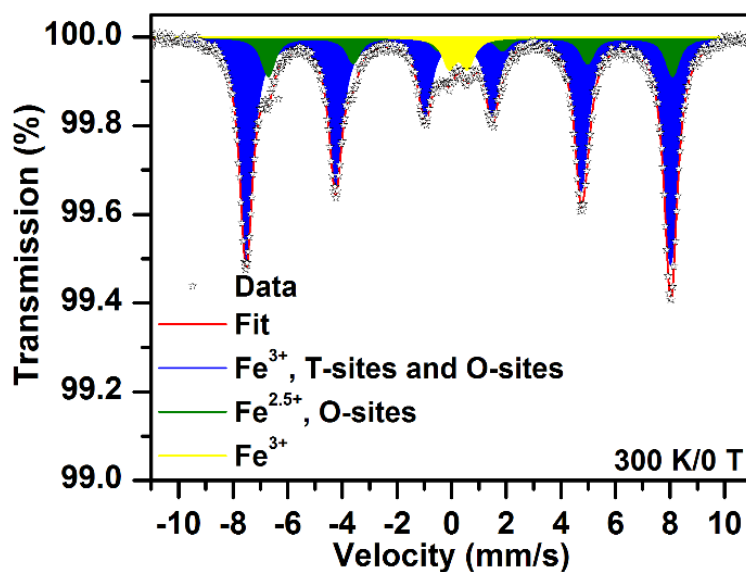


FIGURE 3.14 - ⁵⁷Fe Mössbauer spectrum, measured at room temperature and without an external magnetic field.

TABLE 3.2 - Values of the Mössbauer hyperfine parameters, derived from the least-square fitting of the room-temperature ⁵⁷Fe Mössbauer spectrum, where δ is the isomer shift, ΔE_Q is the quadrupole splitting, B_{hf} is the hyperfine magnetic field, and RA is the relative spectral area of individual spectral components identified during fitting. T-sites denote the tetrahedral cation sites in the crystal structure of Fe₃O₄ (of inverse spinel type) and O-sites stand for the octahedral cation sites in the crystal structure of Fe₃O₄.

Component	$\delta \pm 0.01$ (mm/s)	$\Delta E_Q \pm 0.01$ (mm/s)	$B_{\text{hf}} \pm 0.3$ (T)	RA ± 1 (%)	Assignment
Sextet	0.29	0.00	48.3	81	Fe ³⁺ , T-sites and O-sites
Sextet	0.69	0.00	45.8	14	Fe ^{2.5+} , O-sites
Doublet	0.31	0.69	-----	5	Fe ³⁺

The emergence of the second sextet with the minor spectral area implies non-stoichiometric nature of γ -Fe₂O₃; the values of the isomer shift and hyperfine magnetic field correspond to those reported for Fe²⁺ and Fe³⁺ ions with electron hopping between them typically occurring in the octahedral sites of the

99. Tucek, J.; Zboril, R.; Petridis, D. J. Nanosci. Nanotechnol., 6:926, 2006.

Fe_3O_4 crystal structure above the Verwey transition temperature (≈ 120 K).¹⁰⁰ Thus, in the octahedral sites, two cases can be distinguished, i.e., Fe^{3+} ion with Fe^{2+} ion as the nearest neighbor, and Fe^{3+} ion having another Fe^{3+} ion as the nearest neighbor. If an Fe^{2+} ion is located next to an Fe^{3+} ion in the octahedral sites of the Fe_3O_4 crystal structure, electron hopping is favored with a relaxation time faster than the characteristic measuring time of the Mössbauer spectroscopy ($\approx 10^{-8}$ s); the valence state is averaged as 2.5+ and is witnessed by a value of the isomer shift (≈ 0.65 mm/s at room temperature) between that for Fe^{2+} (≈ 0.90 mm/s) and Fe^{3+} (≈ 0.40 mm/s) in the respective cation coordination. If an Fe^{3+} ion is situated next to another Fe^{3+} ion in the octahedral sites of the $\gamma\text{-Fe}_2\text{O}_3$ crystal structure, electron hopping does not occur and the values of the Mössbauer hyperfine parameters are close to those of Fe^{3+} ions in the tetrahedral sites of the $\gamma\text{-Fe}_2\text{O}_3$ crystal structure. Thus, considering the values of the isomer shift, quadrupole splitting, and hyperfine magnetic field of both sextets derived upon spectrum fitting, the iron oxide phase is of non-stoichiometric origin with chemical features closer to $\gamma\text{-Fe}_2\text{O}_3$ and minor amount of non-oxidized Fe^{2+} ions in the octahedral positions. Besides the sextet components, a doublet is clearly seen in the room-temperature ^{57}Fe Mössbauer spectrum; it may be ascribed to ionic Fe^{3+} and/or very small iron(III) nanoparticles (with sizes far below 15 nm) showing superparamagnetic behavior.

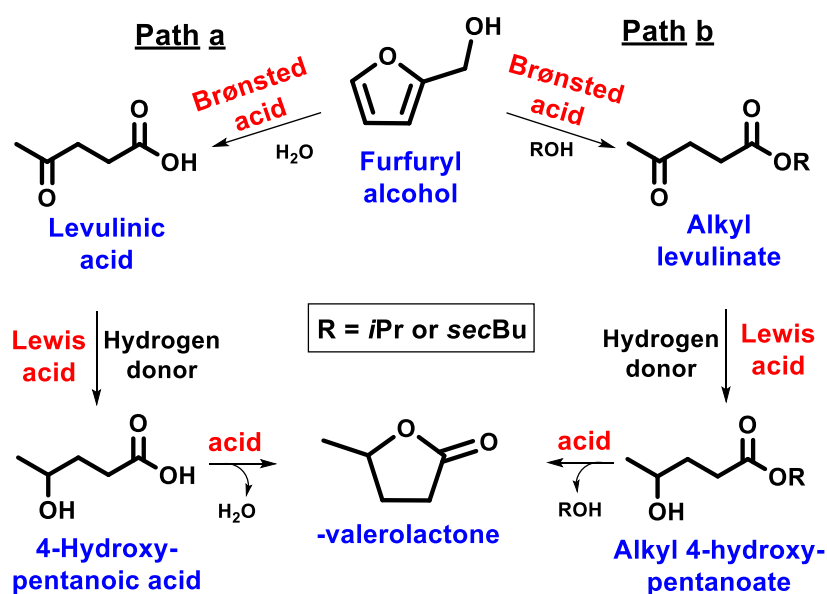
3.3.2 - Catalytic evaluation

After the full characterization of the magnetically recoverable zeolite, the evaluation of its catalytic activity in furfuryl alcohol valorization reactions was conducted. In this regard, the investigation started by the analysis of a reaction set-up using 26 μL of furfuryl alcohol and 75 mg of the catalyst

100. N. N. Greenwood and T. C. Gibb, Mössbauer Spectroscopy; Chapman and Hall Ltd.: London, UK, 1971.

having 2-propanol as solvent at 90 °C. To our delight, the formation of GVL with high selectivity was observed, albeit with a moderated conversion (52% conversion with 97% selectivity to GVL).

The overall reaction pathway for the synthesis of γ -valerolactone from furfuryl alcohol comprises a one-pot sequential process. Firstly, the FA is converted to levulinic acid or alkyl levulinates through a hydrolysis (Scheme 3.14, Path a) or alcoholysis (Scheme 3.14, Path b) reaction catalyzed by Brønsted acids.



SCHEME 3.14 Reaction pathway for the synthesis of γ -valerolactone from furfuryl alcohol.

Next, the levulinic acid (LA) or alkyl levulinate (AL) products are converted to 4-hydroxypentanoic acid or 4-hydroxypentanoates, respectively, through a transfer-hydrogenation reaction catalyzed by Lewis acids in the presence of a secondary alcohol that also serves as hydrogen donor. Finally, the 4-hydroxypentanoic acid or 4-hydroxypentanoates suffer an acid catalyzed cyclization reaction, forming the GVL product.

In order to improve the chemical conversion of FA to GVL, the evaluation of the reaction parameters, e.g. the effects of temperature, catalyst loading and FA:2-propanol ratio was carried out (Figures 3.15a-c). In this study, the temperature (Figure 3.15a) appears to exert a substantial effect on the reaction

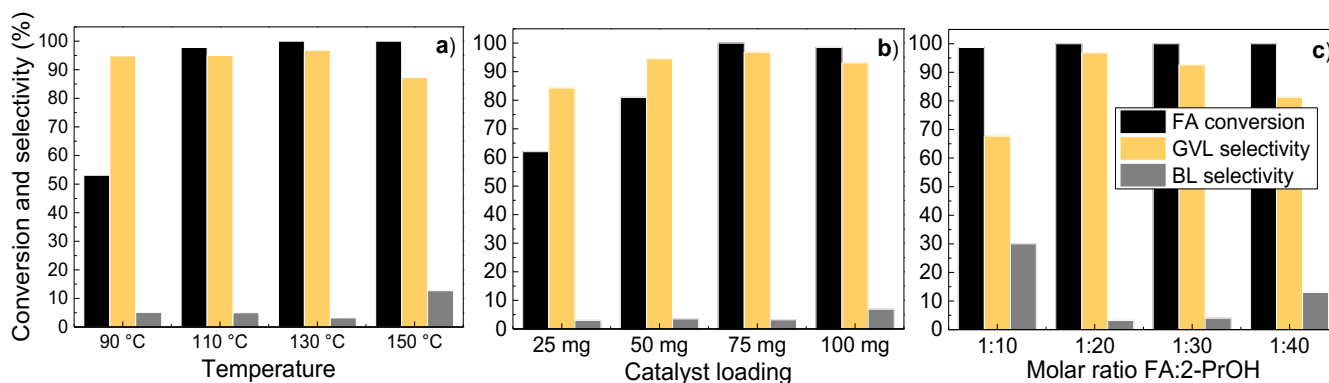
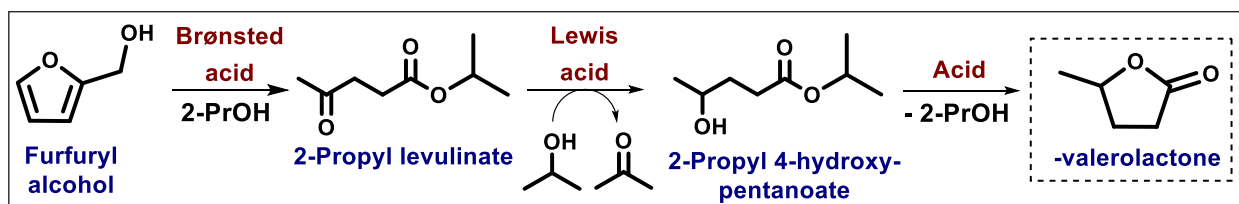


FIGURE 3.15 - Evaluation of reaction parameters for the conversion of FA to GVL in 2-propanol.

outcome, as the conversion increased significantly with the increase in temperature from 90 to 110 °C and attained its maximum at 130 °C (53%, 97% and full conversion, respectively) in the reaction using 50 mg of catalyst and molar ratio FA:2-propanol of 1:20. However, further heating caused a slight decrease in the selectivity to GVL

Knowing the best temperature for the conversion of FA to GVL in 2-propanol, the catalyst loading was next examined at 130 °C and a molar ratio of FA:2-propanol 1:20 (Figure 3.15b). It is possible to notice that both the conversion and selectivity to GVL achieved their highest values when using 75 mg of catalyst (full conversion with 97% selectivity).

Furthermore, diluting the reaction medium from 1:10 to 1:20 (FA:2-propanol) in the reaction at 130 °C with 50 mg of catalyst showed a minor effect in the reaction conversion, but a significant impact in the selectivity to GVL (68% to 97%); further dilution caused slight erosions in selectivity (Figure 3.15c).

Thereafter, the influence of the solvent and the nature of the hydrogen donor was evaluated by increasing its carbon side chain (from 2-

propanol to 2-butanol). Surprisingly, when the reaction was carried out in 2-butanol, the major product discerned was 2-butyl levulinate (BL, Figure 3.16).

The change in chemical selectivity might be related not only to the different hydrogen donor abilities of the alcohols, but also to physicochemical properties, for instance, the boiling point of the ketone produced from their oxidation.¹⁰¹ In order to have an insight into the conversion of FA to BL, the reaction conditions were re-evaluated having 2-butanol as solvent and hydrogen donor (Figures 3.16a-c). As before, the temperature plays a pivotal role in the reaction conversion using 50 mg of catalyst and a 1:20 molar ratio FA-2-butanol, since when the reaction was heated up from 90 °C to 110 °C, the conversion increased from 48 to 98%, achieving virtually full conversion at 130°C (Figure 3.16a). The selectivity, however, was not considerably affected by any of the factors and BL was obtained as the major product.

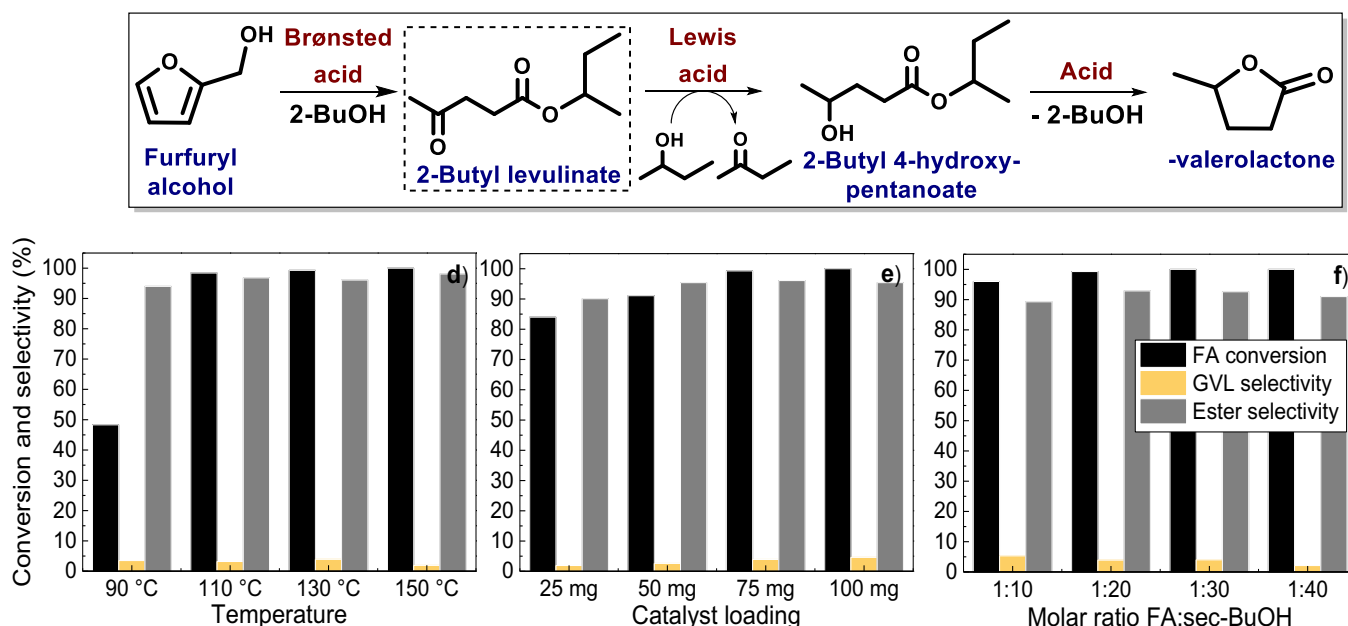


FIGURE 3.16 - Evaluation of reaction parameters in the conversion of FA to BL in 2-butanol.

101. (a) Corma, A.; Domine, M. E.; Nemeth, L.; Valencia, S. J. *Am. Chem. Soc.*, **124**:3194, 2002. (b) Corma, A.; Domin, M. E.; Valencia, S. J. *Catal.*, **215**:294, 2003. (c) J. Jae, Zheng, W.; Lobo, R. F.; Vlachos, D. G *ChemSusChem*, **6**:1158, 2013.

With the optimal conditions in hand for the FA conversion to GVL in 2-propanol and to BL in 2-butanol, the feasibility of the reuse of the HZSM-5 magnetic zeolite catalyst was then evaluated (Figures 3.17a and 3.17b). In this recycling study, after each reaction run, the catalyst was magnetically separated, washed with acetone, dried under vacuum overnight at 50 °C and reused.

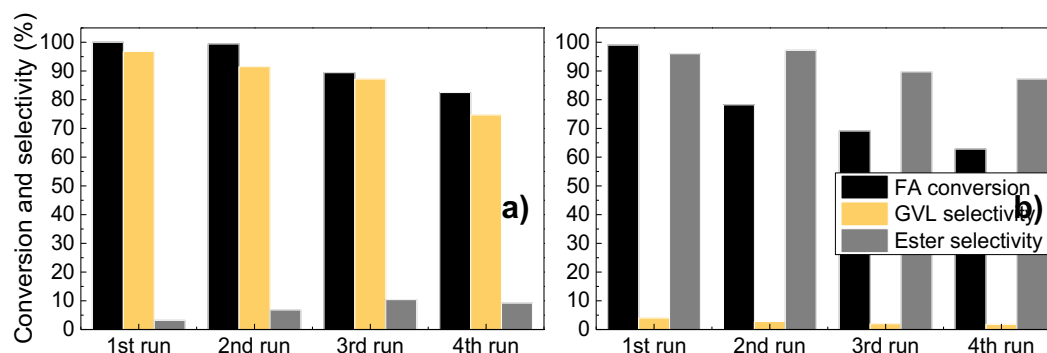


FIGURE 3.17 - Evaluation of the catalyst recyclability in the synthesis of a) GVL in 2-propanol and b) BL in 2-butanol.

Remarkably, after 4 reaction runs, the catalyst was able to keep a good FA conversion and selectivity to GVL in 2-propanol (Figure 3.17a). On the other hand, the FA conversion to BL in 2-butanol suffered a moderate drop in the conversion, from 99% in the first run to 63% in the 4th run, albeit keeping high levels of selectivity (Figure 3.17b). As reported, the partial or total deactivation of zeolite-based catalysts in biomass valorization reactions might be assigned to the blockage of the catalytic sites due to the formation of decomposition products on its surface.¹⁰²

In order to shed some light in both reaction processes, an evaluation of the composition of the reaction medium in 2-propanol and in 2-butanol as function of time (Figures 3.18a and 3.18b, respectively) was conducted. It is noteworthy that both reactions presented high FA conversion and selectivity to GVL in 2-propanol and BL in 2-butanol even after only 30 minutes. On the other

Ennaert, T.; Van Aelst, J.; Dijkmans, J.; De Clercq, R.; Schutyser, W.; Dusselier, M.; Verboekend, D.; Sels, B. F. *Chem. Soc. Rev.*, **45**:584, 2016.

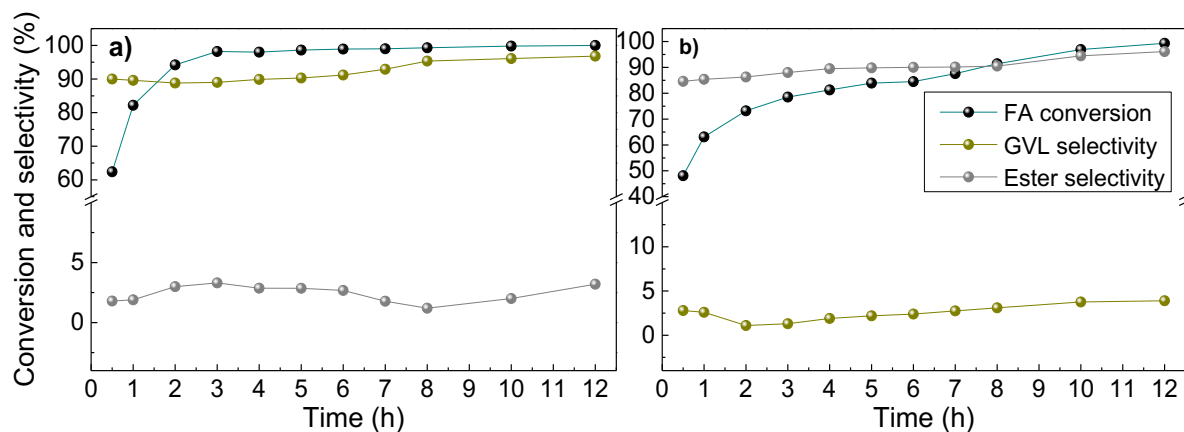


FIGURE 3.18 - Evaluation of reaction composition over time. a) FA to GVL and b) FA to BL.

hand, the reaction in 2-propanol almost achieves its completion (98% conversion) within 3h, while the reaction in 2-butanol takes 12 h to reach 99% conversion.

Aiming to comprehend the extent to which the amount of water present in the reaction medium influences the possible catalyst deactivation,¹⁰³ control experiments were performed with varying amounts of water in the reactions (Figures 3.19a and 3.19b). When the reactions were conducted with 1% of water (%v/v), both the reactions in 2-propanol and 2-butanol maintained high conversion and selectivity, although traces of LA appeared among the products in the reaction with 2-butanol.

After an exhaustive evaluation of the water amount, we were gratified to be able to selectively produce levulinic acid as the major product of the reaction in 2-butanol (when 5% water was added, see the highlighted part in Figure 3.19b). Unfortunately, the recyclability of the catalyst in this reaction was not as successful as the ones of the conversion of FA to GVL or BL, which is probably a consequence of the presence of water in the reaction medium. In this case, the conversion dropped from almost 90% in the first run to approximately 25% in the second run. Remarkably though, ICP-OES analysis of the reaction

103. (a) Jun, K. W.; Lee, H. S.; Roh, H. S.; Park, S. E. *Bull. Korean Chem. Soc.*, **24**:106, 2003. (b) Gayubo, A. G.; Aguayo, A. T.; Atutxa, A.; Valle, B.; Bilbao, J. *Catal. Today*, **107-108**:410, 2005. (c) Bleken, F. L.; Barbera, K.; Bonino, F.; Olsbye, U.; Lillerud, K. P.; Bordiga, S.; Beato, P.; Janssens, T. V. W.; Svelle, S. J. *Catal.*, **307**:62, 2013.

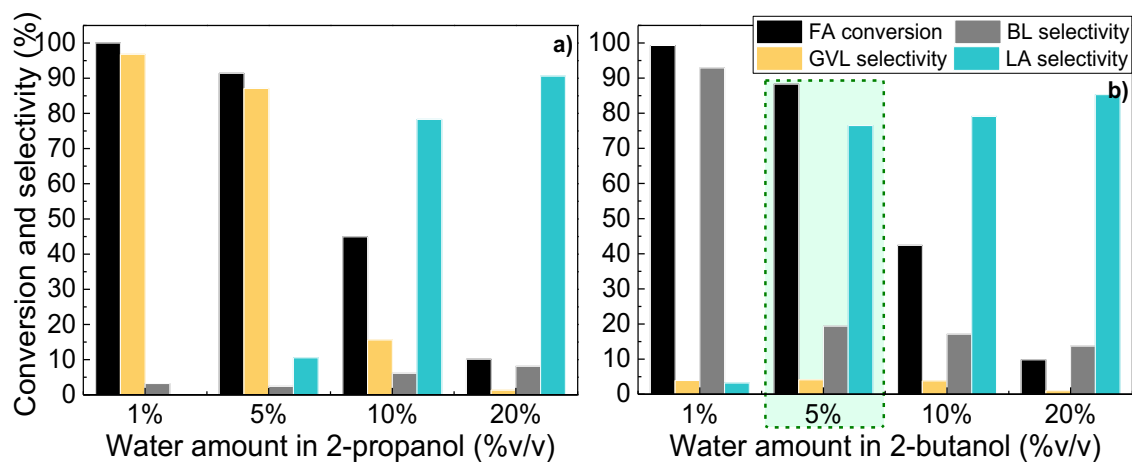


FIGURE 3.19 - Evaluation of water addition in the catalytic conversion of FA to a) GVL and b) BL.

media after the withdrawal of the catalyst showed only traces of aluminum and iron, which implies that metal leaching occurs in a very small extent in this system and can virtually be neglected.

3.4 - Conclusions

In summary, a new methodology for the selective synthesis of GVL directly from furfuryl alcohol via a tandem alcoholysis/hydrogenation/cyclization sequence using a magnetically recoverable HZSM-5 catalyst was developed.

The process can be viewed under the concept of diversity oriented synthesis, that is, a process in which the same starting material (in this case, furfuryl alcohol) is subjected to a range of reagents yielding different molecular skeletons. The general protocol enables the production of various highly valuable platform chemicals by simply changing the solvent used in the reaction; with 2-butanol, the major product was 2-butyl levulinate, and a mixture of water/2-butanol delivered levulinic acid as the main product.

Additionally, it was possible to recycle and reuse the catalyst in several reaction cycles with slender changes in the conversion and selectivity. The results disclosed in this chapter generated a manuscript that has been accepted for publication.

3.5 - Experimental

3.5.1 - Synthesis of the Fe₃O₄ microspheres

The magnetic Fe₃O₄ microspheres were prepared via a modified solvothermal reaction.^{95b} Briefly, FeCl₃·6H₂O (3.9 g), trisodium citrate (1.2 g), and sodium acetate (NaOAc, 7.2 g) were dissolved in ethylene glycol (60 mL) under magnetic stirring. The resulting homogeneous yellow/orange solution was transferred to a 200 mL Teflon-lined stainless-steel autoclave and placed in an oven at 200 °C for 10 h. After cooling to room temperature, the obtained black product was isolated with the aid of a magnet and washed several times with deionized water and ethanol. The magnetite microspheres were then dispersed and stored in distilled water for further use.

3.5.2 - Functionalization of the Fe₃O₄ microspheres with PDDA

The magnetite microspheres were functionalized with PDDA following the procedure described by Lv and co-workers.^{95a} In a typical procedure, wet magnetite nanospheres (1.0 g) were added to an aqueous ammonia solution (2.0 wt%, 30.0 mL) and magnetically stirred at room temperature for 30 min. Then, the PDDA solution (5 mL, 20 wt% in H₂O) was added and the mixture was stirred at room temperature for 24 h. The PDDA-functionalized magnetite microspheres were magnetically separated from the solution and kept in water for further functionalization with the zeolite.

3.5.3 - Synthesis of NaZSM-5 zeolite (Si/Al =14)

In a typical procedure, sodium aluminate (300 mg) and potassium hydroxide (540 mg) were added to deionized water (13 mL) and magnetically stirred to obtain a homogeneous solution. Next, the tetrapropylammonium

hydroxide solution (TPAOH, 11.8 mL, 1.0M sol. in H₂O) was added and the solution was stirred for 1 h, followed by the addition of tetraethyl orthosilicate (20 mL). The resulting gel was stirred (~700 rpm) at room temperature for 24 h and transferred to a Teflon-lined stainless steel autoclave (maximum capacity of 100 mL) and hydrothermally treated at 170 °C for 24 h. The material was cooled to room temperature, washed with distilled water until pH ~7 and dried at 60 °C under vacuum for 24 h. The white powder was calcinated at 550 °C for 5 h under air atmosphere.

3.5.4 - Preparation of magnetically recoverable catalyst – magnetite microspheres embedded on HZSM-5 zeolite (Fe₃O₄-HZSM-5)

The magnetite microspheres functionalized with PDDA (300 mg) were dispersed in distilled water (50 mL) followed by the addition of the NaZSM-5 zeolite powder (2.2 g) and the mixture was stirred for 48 h at room temperature. The ensuing composite Fe₃O₄-PDDA-NaZSM-5 was magnetically separated from the aqueous mixture and dried at 60 °C for 24 h under vacuum. The material was then calcinated under air atmosphere at 550 °C for 5 h resulting in the magnetically recoverable material with the zeolite in its sodic form. In order to convert the sodic form of the zeolite (NaZSM-5) to its acid form (HZSM-5), an ion-exchange with ammonium cations was performed using a solution of ammonium nitrate (NH₄NO₃). For this transformation, the core-shell magnetic zeolite (1.0 g) was dispersed in an aqueous solution of NH₄NO₃ (100 mL, 1.0 mol L⁻¹) and the mixture was vigorously stirred (1000 rpm) at 80 °C for 2 h. Subsequently, the material separated from the media with the aid of an external magnet and resubmitted to cationic exchange process twice more. The brown solid was then dried at 60 °C under vacuum for 24 hours and calcinated under air atmosphere at 550 °C for 5 h.

3.5.5 Characterization of the support and the Fe₃O₄-HZSM-5 catalyst

The particle size and morphological studies of the Fe₃O₄ microspheres and the γ -Fe₂O₃-HZSM-5 catalyst were performed by TEM. Transmission Electron Microscopy (TEM) analysis was accomplished using JEOL JEM 2010F at 160kV of accelerating voltage. Microscopic images were obtained by HRTEM TITAN 60-300 with X-FEG type emission gun, operating at 80 kV. This microscope is equipped with Cs image corrector and a STEM high-angle annular dark-field detector (HAADF). The point resolution is 0.06 nm in HRTEM mode. The elemental mappings were obtained by STEM-Energy Dispersive X-ray Spectroscopy (EDS) with acquisition time of 20 min. For HRTEM analyses, the powder samples were dispersed in ethanol and 5 min ultrasonicated. One drop of this solution was placed on a copper grid with holey carbon film. The sample was dried at room temperature.

X-ray diffraction patterns were recorded with a PANalytical X'Pert PRO MPD (PANalytical, Netherlands) diffractometer in the Bragg-Brentano geometry, Co-K α radiation (40 kV, 30 mA, $\lambda = 0.1789$ nm) equipped with an X'Celerator detector and programmable divergence and diffracted beam anti-scatter slits. The measurement range was $2\theta:5^\circ - 105^\circ$ with a step size of 0.017° . The identification of crystalline phases was performed using the High Score Plus software (PANalytical) that includes the PDF-4+ database.

The experimental content of aluminum and silicon were determined by x-ray fluorescence (XRF) in a Shimadzu RayNY EDS-720 X-ray spectrometer equipped with an X-ray tube (Rh target) with a 5-50 KV tube voltage and tube current in the range of 1 to 1000 μ A, a Si(Li) solid state detector with energy resolution of 165 eV at 5.96 KeV K α Mn line cooled with liquid nitrogen. The sample was irradiated in a 3mm² spot size under vacuum of $\sim 10^{-6}$ torr.

TPD measurements were conducted in a Micromeritics Autochem II 2920 Chemisorption Analyzer equipment with a TCD (Thermal Conductivity

Detector) detector. For this, 50 mg of the sample were pre-treated thermally under 30 mL.min⁻¹ helium flow at a heating rate of 10 °C min⁻¹ until 600 °C and kept at this temperature for 30 minutes. After this period, the reactor was cooled to 120 °C, and the He flow was kept for 60 minutes. Next, the adsorption of ammonia was performed through the passing of a 15% mixture of NH₃ in He for 30 minutes over the sample. After saturation, the sample was purged with He for 1 hour to remove the excess of ammonia. Finally, the temperature desorption was initiated under a 30 mL min⁻¹ He flow in a 15 °C min⁻¹ heating rate until 600 °C. To quantify the acid sites, the area under the curve of the graph of TCD signal x temperature was calculated.

The infrared spectrum of adsorbed pyridine was recorded on a Fourier Transform Infrared spectrophotometer model Prestigi-21 in the range of 1800–1400 cm⁻¹ wavenumber. For the qualitative acidity determination, 50 mg of sample were subjected to a heat treatment in a tubular furnace at 300 °C and 100 mL min⁻¹ N₂ flow for 1 h. Gaseous pyridine was then adsorbed on the samples for 1 h at 150 °C with a N₂ gas carrier flow at 100 mL min⁻¹. Next, the N₂ flow was kept constant for 1 h at 150 °C for the removal of the physically adsorbed pyridine.

The transmission ⁵⁷Fe Mössbauer spectra were recorded employing a Mössbauer spectrometer operating at a constant acceleration mode and equipped with 50 mCi ⁵⁷Co(Rh) source. For fitting the collected ⁵⁷Fe Mössbauer spectrum, the MossWinn software program was used;¹ prior to fitting, the signal-to-noise ratio was enhanced employing the routines incorporated into MossWinn software program and the statistical procedure developed by Prochazka et al.² The isomer shift values were referred to α-Fe at room temperature.

ICP-OES measurements were conducted in a Thermo Fisher Scientific, iCAP 6300 Duo, with a CID (Charge Injection Device) detector.

3.5.6 - Catalytic evaluation

In a typical catalytic test, furfuryl alcohol (26 μL), 2-propanol or 2-butanol (1500 μL) and the magnetically recoverable catalyst (75 mg) were added to a glass vial containing a magnetic stir bar. The vial was sealed with a Teflon lid and an aluminum cap and immersed in a pre-heated oil bath at 130 $^{\circ}\text{C}$ and magnetically stirred at 700 rpm for 8h. After completion of the reaction, the vial was cooled to room temperature and the catalyst was separated with the aid of a magnet and a small amount of the reaction liquid (50 μL) was removed from the vial, diluted in absolute ethanol and the products were analyzed using GC-FID; the retention times of the products were compared to those of commercial standards.

3.5.7 – Analyses of the reaction products

The samples were analyzed using an Agilent 6820 gas chromatograph equipped with an Agilent DB-5 capillary column (30 m x 0.32 mm, 0.5 μm) under the operation parameters: temperature of inlet of 250 $^{\circ}\text{C}$, temperature of flame ionization detector of 250 $^{\circ}\text{C}$, temperature ramp of the oven from 100 to 250 $^{\circ}\text{C}$ at a rate of 10 $^{\circ}\text{C min}^{-1}$. CG-MS analyses were conducted in a Shimadzu GCMS-QP2010S Gas Chromatograph coupled to a MS detector equipped with a ZB-5MS column (30 m x 0.25 mm x 0.25 μm) under the operation parameters: temperature of inlet of 250 $^{\circ}\text{C}$, temperature of the interface of 300 $^{\circ}\text{C}$, temperature ramp of the oven from 50 to 250 $^{\circ}\text{C}$ at a rate of 10 $^{\circ}\text{C min}^{-1}$.

Chapter 4

4.

Sulfonic acid-functionalized dendritic mesoporous silica nanospheres: synthesis, characterization and application on the valorization of furfural and carbohydrates

General overview

This chapter will address the first attempt on the design, synthesis and characterization of a catalyst constituted by sulfonic acid-functionalized dendritic mesoporous silica nanospheres for application in the valorization of bio-derived furfural and carbohydrates. A brief introduction regarding the use of mesoporous and sulfonic-acid-functionalized materials will be presented.

4.1 Introduction

According to IUPAC,¹⁰⁴ porous materials can be divided into three classes depending on their pore size: microporous (pore size < 2nm), mesoporous (pore size in the range of 2-50 nm), and macroporous (pore size >50nm) materials.

Zeolites are the most famous microporous materials, and since the 1950s, when the first zeolites were synthesized in laboratory, they have been widely applied in the field of catalysis. Their main feature is the possibility of shape selective chemical transformations, a consequence of their well-defined pore architecture and dimensions.⁸⁹ However, this property may also be seen as their main disadvantage: since zeolites are microporous materials, the size of their pores is very small and limits their application in transformations that involve bulky molecules.

104. Sing, K.S.W.; Everett, D.H.; Haul, R.A.W.; Moscou, L.; Pierotti, R.A.; Rouquerol, J.; Siemieniewska, T. *Pure Appl. Chem.*, **57**:603, 1985.

In this way, great attention has been devoted to the synthesis of materials with enlarged pore sizes, more specifically, into the mesopores range, what in theory would allow larger molecules to enter, react and leave the pore system of the material.¹⁰⁵

One of the most famous mesoporous materials till date is MCM-41 (Mobil Composition of Matter No. 41), a type of silica with highly ordered hexagonal pores with a very narrow pore size distribution. This material was described in 1992, followed by other interesting similar materials, such as MCM-48, which displays a cubic mesostructure and MCM-50, with lamellar structure. Other mesoporous types of mesoporous silica include HMS (hexagonal mesoporous silica) and MSU (Michigan State University material), which displays worm-like structures. Another very popular type of mesoporous silica used as catalytic support in the last few years is SBA-15 (Santa Barbara No. 15), which is similar to MCM-41 with 2D hexagonal mesoporous structure, but with thicker walls, which confers to it higher thermal and hydrothermal stabilities. The factors that define the different types of silica during their synthesis are the type of surfactant used, the solvent, temperature, pressure, the silica precursor and the presence of pore swelling agents. Figure 4.1 shows some of the most popular types of mesoporous silica.¹⁰⁵

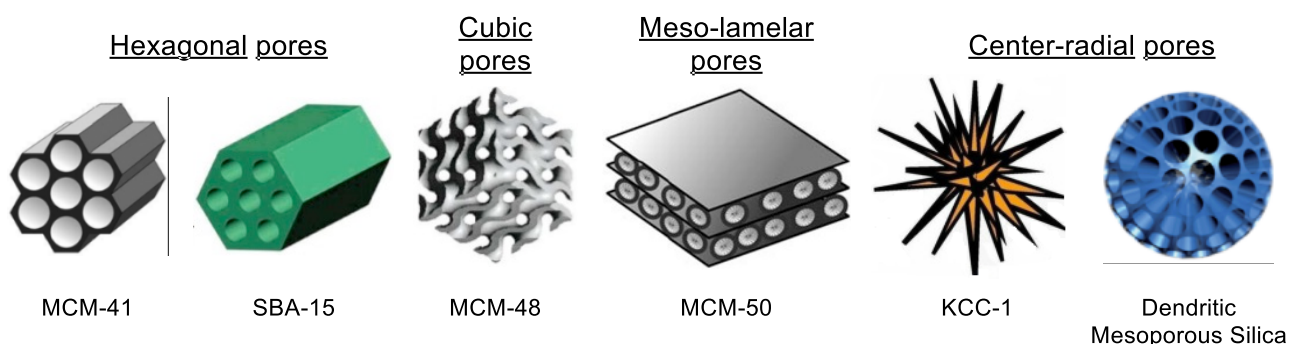


FIGURE 4.1 - Reprinted with permission from ref. 106. Copyright 2014 American Chemical Society.

105. (a) Taguchi, A.; Schüth, F. *Micropor. Mesopor. Mater.*, **77**:1, 2005. (b) Perego, C.; Millini, R. *Chem. Soc. Rev.*, **42**:3956, 2013. (c) Pal, N.; Bhaumik, A. *RSC Adv.*, **5**:24363, 2015.

In 2009, dendritic mesoporous silica, a new type of silica mesoporous material, was developed and, since then, has become widely popular, finding applications in catalysis, environmental and biomedical sciences. This type of material is constituted by spherical silica micro-/nanoparticles with center-radial pore structures with large pore channels and highly accessible surface areas. It is composed by silica fibers or wrinkles that act as building units that are arranged along the center-radial direction, that is, from the center to the surface of the particles.¹⁰⁶

Due to their marked properties, mesoporous silica materials have been widely used as supports for catalysts in the valorization of bio-derived compounds, being SBA-15 by far the most used one. For instance, G. Wang's group reported, in 2011, a method for the conversion of xylose to furfural using a catalyst constituted by sulfated alumina-zirconia supported in SBA-15, obtaining xylose conversions superior to 98% and selectivity to furfural around 53% - the dehydration of xylose was previously described in Schemes 3.2 and 3.3.¹⁰⁷ A similar work was published by G. Wang's group in the same year using sulfonic acid-functionalized SBA-15; in this case, a selectivity of 65% to xylose was achieved.¹⁰⁸ Another interesting work on the same reaction was reported by Arias's group in 2012 using SBA-15-supported arenesulfonic acids and, remarkably, they were able to transform xylose to furfural with conversions up to 96% and selectivities up to 85%.¹⁰⁹ In these reports, the byproducts formed in the reactions were attributed to furfural polymerization.

Later in 2011, Zheng's group disclosed a method for the sequential hydrogenation/esterification of furfural in the presence of acetic acid using a

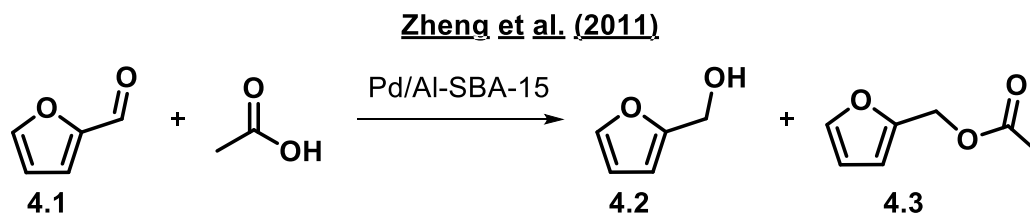
106. Du, X.; Qiao, S. Z. *Small*, **11**:392, 2015.

107. Shi, X.; Wu, Y.; Li, P.; Yi, H.; Yang, M.; Wang, G. *Carbohydrate Res.*, **346**:480, 2011.

108. Shi, X.; Wu, Y.; Yi, H.; Rui, G.; Li, P.; Yang, M.; Wang, G. *Energies*, **4**:669, 2011.

109. Agirrezabal-Telleria, I.; Requies, J.; Güemez, M.B.; Arias, P.L. *Applied Catal. B-Environ.*, **115-116**, 169, 2012.

Pd/Al-SBA-15 catalyst, which showed to be superior to other known palladium catalysts such as Pd/C (Scheme 4.1).¹¹⁰



SCHEME 4.1 - Sequential reduction/esterification of furfural promoted by a Pd/Al-SBA-15 catalyst.

Additional applications of these materials in the conversion of bio-derived compounds include the reduction of furfural to furfuryl alcohol using SBA-15-supported copper and cobalt catalysts.¹¹¹ Other mesoporous silica used in this type of reaction is MCM-41; it has been reported to catalyze pyrolysis of lignocellulosic biomass to produce bio-oil,¹¹² in the conversion of xylose to furfural,¹¹³ and production of HMF from sugars.¹¹⁴ As for mesoporous silica with radial pores, due to their fairly recent discovery their application in the conversion of bio-derived compounds is still not very well reported. Till date, only one example can be found in literature; in this report, Saraji and co-workers report the functionalization of KCC-1 silica with sulfonic acid and its use in the conversion of fructose to HMF.¹¹⁵

110. Yu, W.; Tang, Y.; Mo, L.; Chen, P.; Lou, H.; Zheng, X. *Catal. Commun.*, **13**:35, 2011.

111. (a) Vargas-Hernández, D.; Rubio-Caballero, J. M.; Santamaría-González, J.; Moreno-Tost, R.; Mérida-Robles, J. M.; Pérez-Cruza, M. A.; Jiménez-López, A.; Hernández-Huesca, R.; Maireles-Torres, P. *J. Mol. Catal. A*, **383-384**:106, 2014. (b) Audemar, M.; Ciotonea, C.; Vigier, K. D. O.; Royer, S.; Ungureanu, A.; Dragoi, B.; Dumitriu, E.; Jérôme, F. *ChemSusChem*, **8**:1885, 2015.

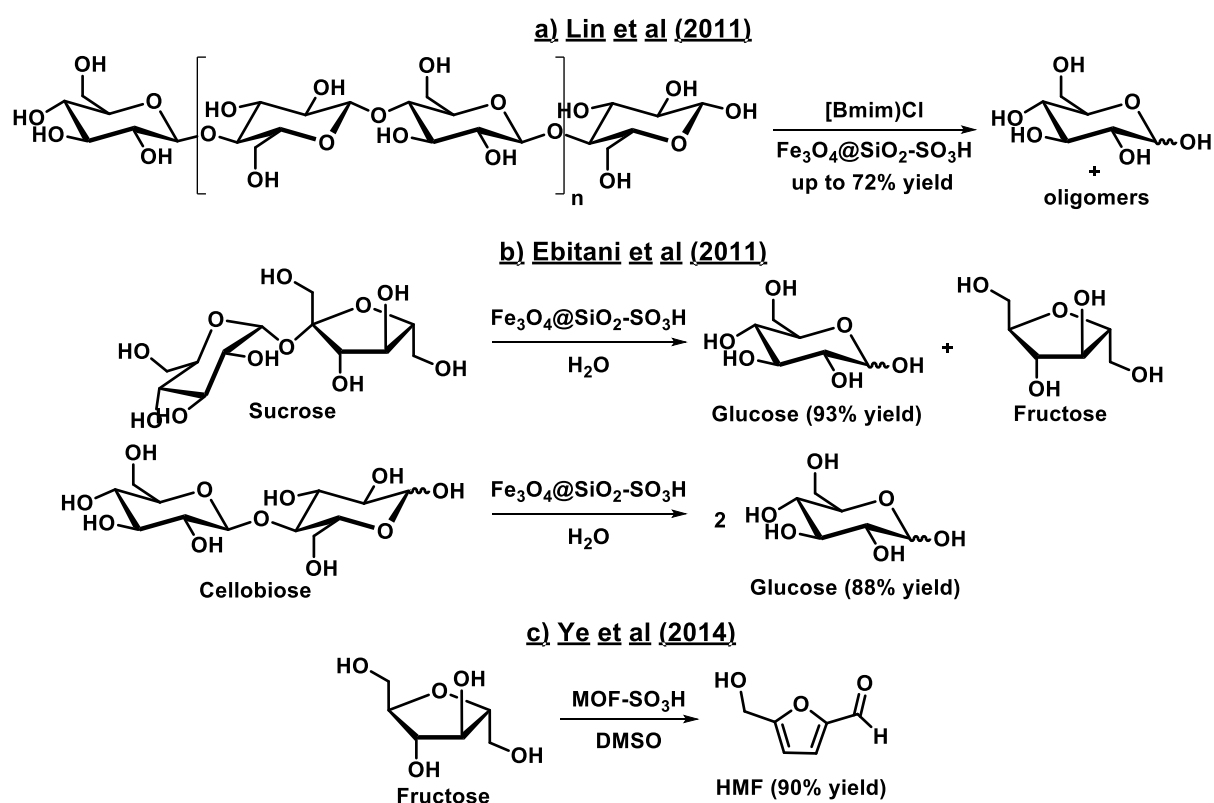
112. (a) Iliopoulou, E. F.; Antonakou, E. V.; Karakouliac, S.A.; Vasalos, I.A.; Lappas, A.A.; Triantafyllidis, K.S. *Chem. Eng. J.*, **134**:51, 2007. (b) Adam, J.; Blazsó, M.; Mészáros, E.; Stöcker, M.; Nilsen, M. H.; Bouzga, A.; Hustada, J. E.; Grønli, M.; Øyed, G., **84**:1494, 2005. (c) Antonakou, E.; Lappas, A.; Nilsen, M. H.; Bouzga, A.; Stöcker, M. *Fuel*, **85**:2202, 2006.

113. Zhang, J.; Zhuang, J.; Lin, L.; Liu, S.; Zhang, Z. *Biomass Bioenerg.* **39**:73, 2012.

114. (a) Jiménez-Morales, I.; Moreno-Recio, M.; Santamaría-González, J.; Maireles-Torres, P. *J. Appl. Catal. B-Environ.* **164**:70, 2015. (b) Liu, A.; Zhang, Z.; Fang, Z.; Liu, B.; Huang, K. J. *Ind. Eng. Chem.* **20**:1977, 2014.

115. Chermahini, A. N.; Shahangi, F.; Dabbagha, H. A.; Sarajia, M. *RSC Adv.*, **6**:3380, 2016.

As discussed above and in the previous chapters, supported sulfonic acid-functionalized materials have been widely used as catalysts not only in the conversion of biomass compounds but also in other numerous types of transformations. Besides mesoporous silica materials, sulfonic acid have also been supported in magnetic supports and used in the hydrolysis of sugars (Scheme 4.2a and 4.2b)¹¹⁶ or in metal-organic frameworks (MOFs) and used in the conversion of fructose to HMF (Scheme 4.2c).¹¹⁷



SCHEME 4.2 – Conversion of sugars using sulfonic acid-functionalized materials as catalysts.

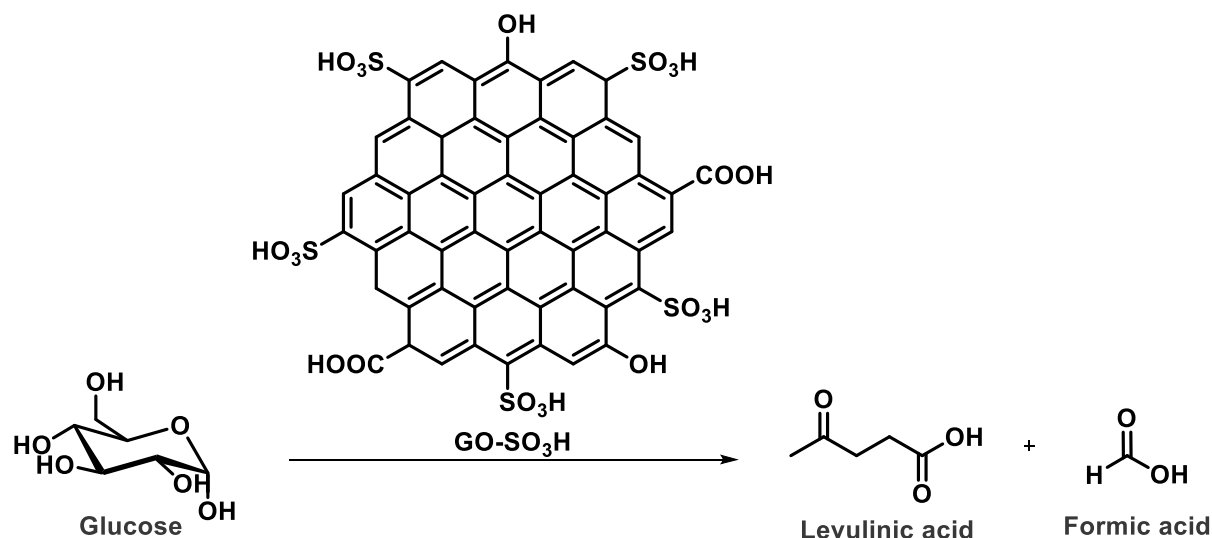
Another very interesting protocol that involves the application of supported sulfonic acids was reported by Chang's group in 2013.¹¹⁸ In this work,

116. (a) Xiong, Y.; Zhang, Z.; Wang, X.; Liu, B.; Lin, J. Chem. Eng. J. **235**:349, 2014. (b) Takagaki, A.; Nishimura, M.; Nishimura, S.; Ebitani, K. Chem. Letters, **40**:1195, 2011.

117. Chen, J.; Li, K.; Chen, L.; Liu, R.; Huang, X.; Ye, D. Green Chem., **16**:2490, 2014.

118. Upare, P. P.; Yoon, J.-W.; Kim, M. Y.; Kang, H.-Y.; Hwang, D. W.; Hwang, Y. K.; Kung, H. H.; Chang, J.-S. Green Chem., **15**:2935, 2013.

the group achieved the conversion of hexose sugars to levulinic acid using a catalyst constituted by sulfonic acid supported on graphene oxide (Scheme 4.3).



SCHEME 4.3 – Conversion of glucose to levulinic acid promoted by a sulfonic acid-functionalized graphene catalyst.

In this work, the catalyst was prepared through the reaction of graphene oxide with chlorosulfonic acid in chloroform. Differently from previous reports, where the Brønsted acidity of sulfonic acids was explored to promote the transformations, in this work the group was able to prove the existence of Lewis acid sites in the catalyst and envisioned the use of this catalysts for a transformation that requires both types of acid sites. The Lewis acidity of sulfonic acids had already been reported by Tanabe in 1990, which demonstrated that the generation of this strong Lewis acidity is related to sulfonation or the dehydration of the Brønsted acid sites.¹¹⁹ In spite of this potential catalytic activity of sulfonic acids, these properties have not been thoroughly explored in reactions that require this type of acid sites.

119. (a) Tanabe, K.; Hattori, H.; Yamaguchi, T. *Crit. Rev. Surf. Chem.*, **1**:1, 1990. (b) Hua, W.; Yue, Y.; Gao, Z. *J. Mol. Catal. A: Gen.*, **170**:195, 2001.

4.2 - Aims-Objectives

Considering the almost unexplored potential of sulfonic acids as catalysts in Lewis acid-demanding reactions and the great appeal of the valorization of bio-derived compounds, the aim of the work described in this chapter was the design, synthesis and characterization of a novel sulfonic acid functionalized-mesoporous silica catalyst for application in the conversion of furfural and sugars to alkyl levulinates. Specific objectives of this chapter include:

- ✓ The synthesis of a metal-free catalyst with Brønsted and Lewis acid sites constituted by sulfonic acid-functionalized dendritic silica nanospheres;
- ✓ The full characterization of the catalyst;
- ✓ The evaluation catalytic activity of in the valorization of hexose and pentose sugars and their derivatives;
- ✓ The evaluation the influence of recyclability of catalyst;
- ✓ The comparison of the synthesized catalyst with other sulfonic acid-functionalized materials.

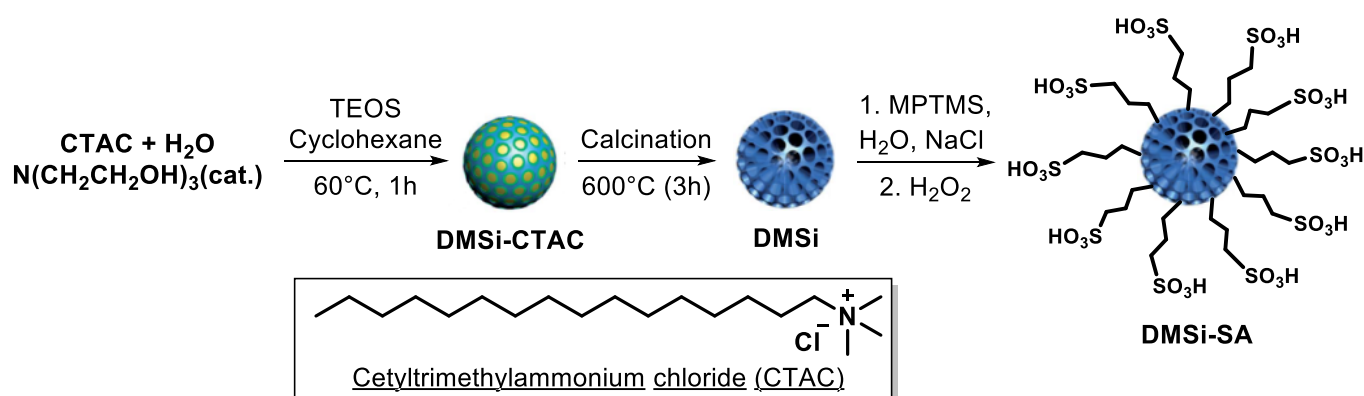
4.3 - Results and discussion

4.5.1 - Catalyst characterization

The material chosen to be used as catalyst support was dendritic mesoporous silica (DMSi) nanospheres due to their advantageous properties and relatively easy preparation process. As for the active phase, we decided to explore the Lewis acidity displayed by sulfonic acids, and, therefore, obtaining a catalyst that displays dual acidic character, of both Lewis and Brønsted types.

The preparation of the catalyst is outlined in Scheme 4.4. The support was prepared using tetraethyl orthosilicate (TEOS) in the biphasic system oil-

water stratification approach described by Yang and co-workers.¹²⁰ The support was then functionalized by grafting mercaptopropyl groups to the surface of the DMSi nanospheres using a hydrothermal saline promoted grafting; in this approach, an aqueous NaCl solution is used as solvent in order to promote the activation of the silica surface towards the functionalization with mercaptopropyltriethoxysilane (MPTMS). The last step of the catalyst's synthesis is the conversion the mercapto groups to acid sulfonic via a mild oxidation protocol using hydrogen peroxide as oxidizing agent.¹²¹



SCHEME 4.4 – Preparation of the catalyst comprised by sulfonic acid-functionalized dendritic mesoporous silica.

In order to investigate the morphology of the newly developed catalyst and have an insight on its composition, TEM and SEM-EDS analysis were performed (Figure 4.2).

The TEM image of the DMSi nanospheres depicted in Figure 4.2a showed that the nanospheres are monodisperse with a uniform shape; the histogram containing the particle count showed in Figure 4.2c confirms that indeed the particles present a very narrow size distribution with a mean size of 53 nm. Figure 4.2b shows the sophisticated architecture of the dendritic particles, which present center-radial pore structure with 6 nm open mesopores channels.

120. Shen, D.; Yang, J.; Li, X.; Zhou, L.; Zhang, R.; Li, W.; Chen, L.; Wang, R.; Zhang, F.; Zhao, D. *Nano Lett.*, **14**:923, 2014.

121. Pirez, C.; Lee, A. F.; Manayil, J. C.; Parlett, C. M. A.; Wilson, K. *Green Chem.*, **16**:4506, 2014.

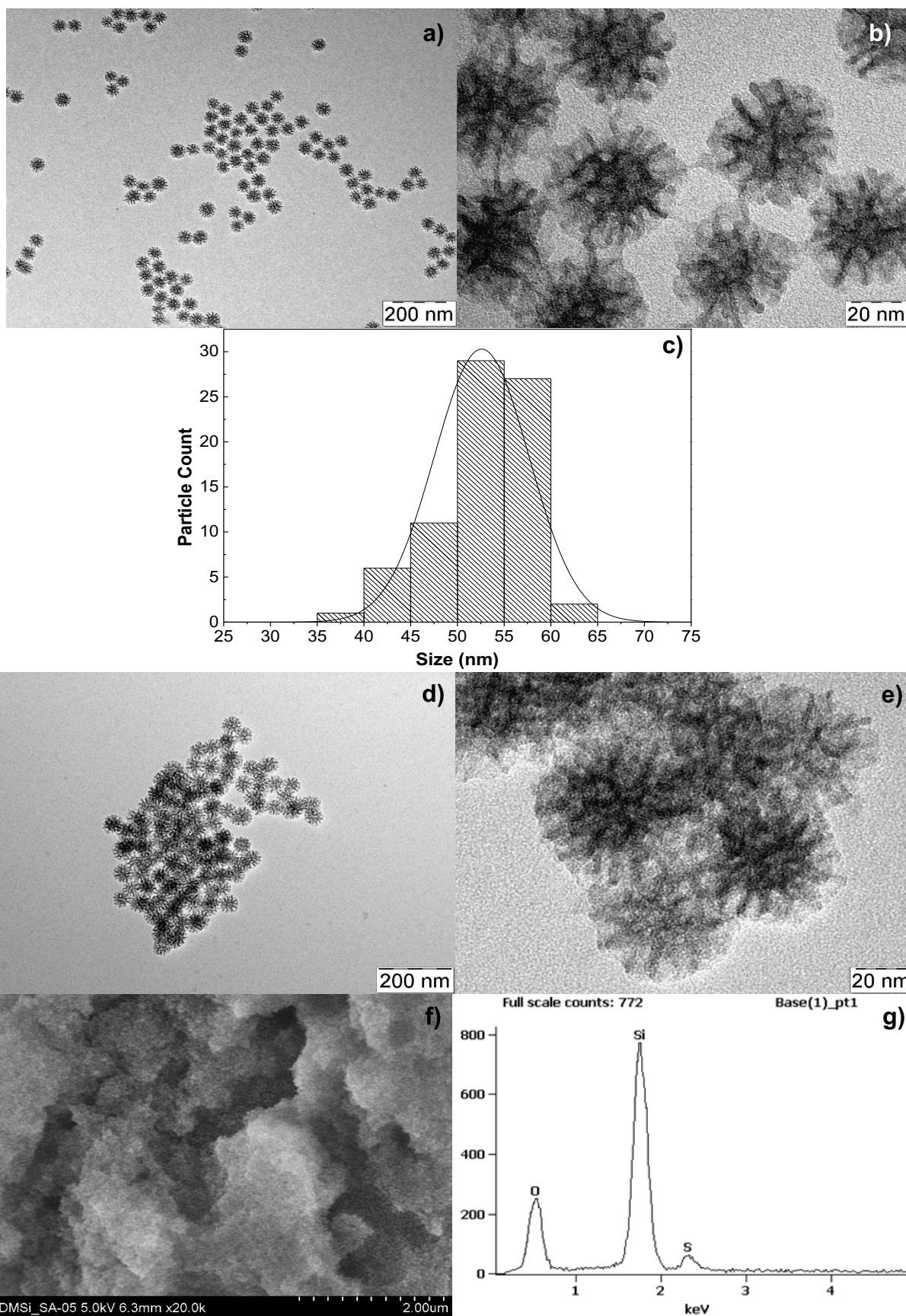


FIGURE 4.2 – a) and b) TEM images of DMSi, c) size distribution analysis of DMSi, d) and e) TEM images of DMSi-SA, f) SEM image of DMSi-SA and g) EDS spectrum of DMSi-SA.

The images of the catalyst DMSi-SA (Figures 4.2d and 4.2e) confirms that the functionalization with sulfonic acid did not lead to significant changes in the morphology of the material. Furthermore, the SEM-EDS technique confirmed the presence of silicon, oxygen and sulfur atoms on the DMSi-SA catalyst (Figures 4.2f and 4.2g).

Although mesoporous silica is an amorphous material, the ordered structure of the mesopores in it may generate diffraction peaks at low angles. In that way, this analysis was conducted and confirmed the presence of ordered mesopores in the structure, as characterized by the peaks at $2\theta = 0.5^\circ$ and 1.7° ; the occurrence of two different peaks may be related to the presence of two sizes of mesopores in the material.¹²⁰

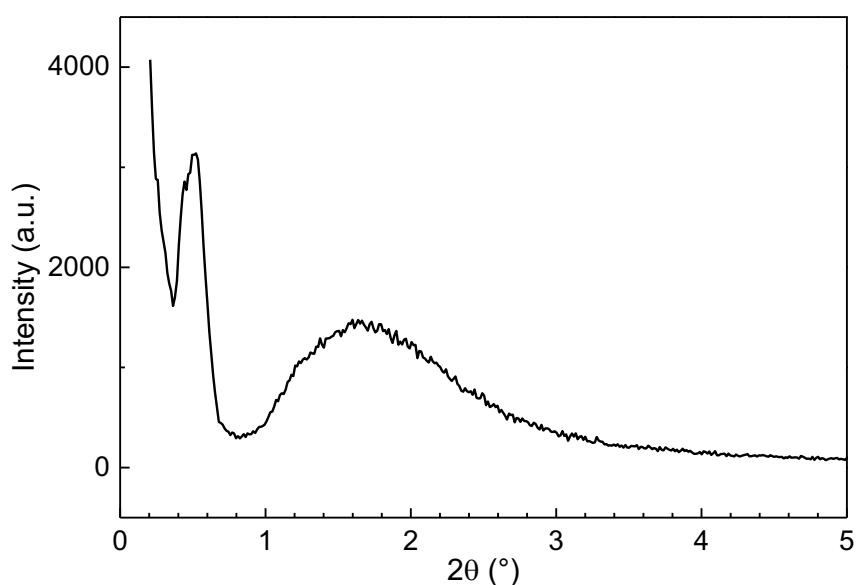


FIGURE 4.3 – Low angle x-ray diffractogram of DMSi-SA.

Afterwards, the textural characterization of the pure DMSi nanospheres as well as the final catalyst were conducted. The nitrogen adsorption and desorption isotherms are depicted in Figure 4.4 and the textural properties of the silica materials are described in Table 4.1. The isotherm of the pure silica (DMSi) nanospheres could be classified as type IV with hysteresis loop type H2, characteristic of mesoporous materials with cylindrical pores. Furthermore, the

DMSi nanospheres exhibit a high specific surface area, which are in agreement with the values reported by Wang and co-workers.¹²⁰

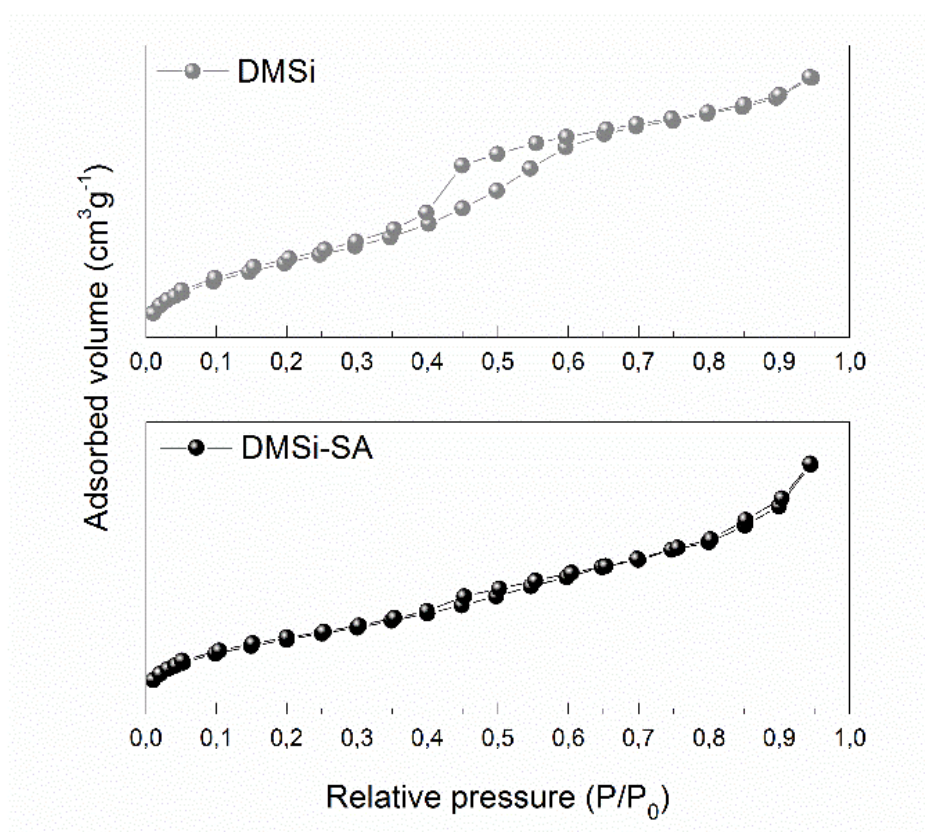


FIGURE 4.4 - Nitrogen adsorption/desorption isotherms of (A) DMSi and (B) DMSi-

It is noteworthy that both the specific surface area and the pore volume of the catalyst underwent a significant decrease when compared to the silica nanospheres, what could be expected considering that the functionalization with the organic groups occurs on the surface and inside the pores of the nanospheres, leading to pore blockage.

TABLE 4.1 - Textural properties of the silica nanospheres and the functionalized materials.

Sample	$S_{B.E.T.} (m^2 g^{-1})$	$D_p (nm)$	$V_p (cm^3 g^{-1})$
DMSi	527	6.4	1.1
DMSi-SA	236	5.8	0.9

With the aim to study the dispersion of the sulfonic groups in the DMSi nanospheres, HR-TEM accompanied by chemical mapping analyses were performed (Figure 4.5).

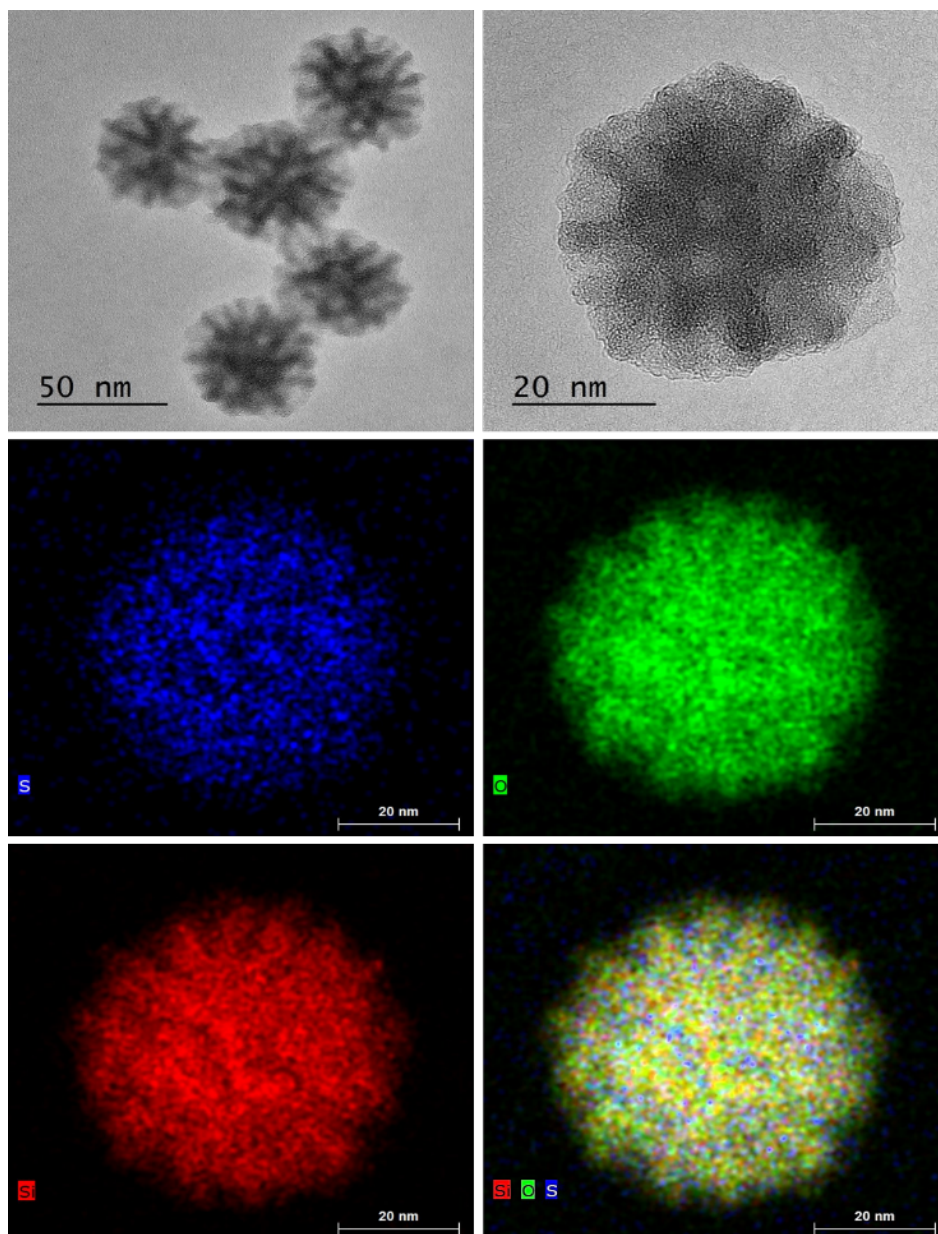


FIGURE 4.5 - HRTEM and chemical mapping in the sulfonic acid functionalized DMSi-SA catalyst.

It is possible to notice in Figure 4.5b that the dendritic silica nanospheres present open mesopores with estimated diameter of approximately 6 nm, confirming the TEM observations. Additionally, the chemical mapping showed that the sulfur atoms are well distributed on the silica nanosphere in both

the surface and inside the mesopores, which implies that the methodology employed for the grafting of the thio-compound to the support was highly effective.

In order to verify the conversion of mercaptopropyl to the sulfonic acid counterparts, and therefore, quantify the Brønsted acidic sites in the catalyst, an aqueous titration has been performed. The obtained value was 0.89 mmol. Comparing this value with the one obtained for the total sulfur amount of present in the sample determined by x-ray fluorescence, which was of 1.8 mmol g⁻¹ it is possible to infer that only half of the mercapto groups were converted to sulfonic acid.

Aiming to confirm the oxidation state of the sulfur atoms in the sample and the possible occurrence of partially oxidized species, x-ray photoelectron spectroscopy (XPS) analyses were performed (Figure 4.6).

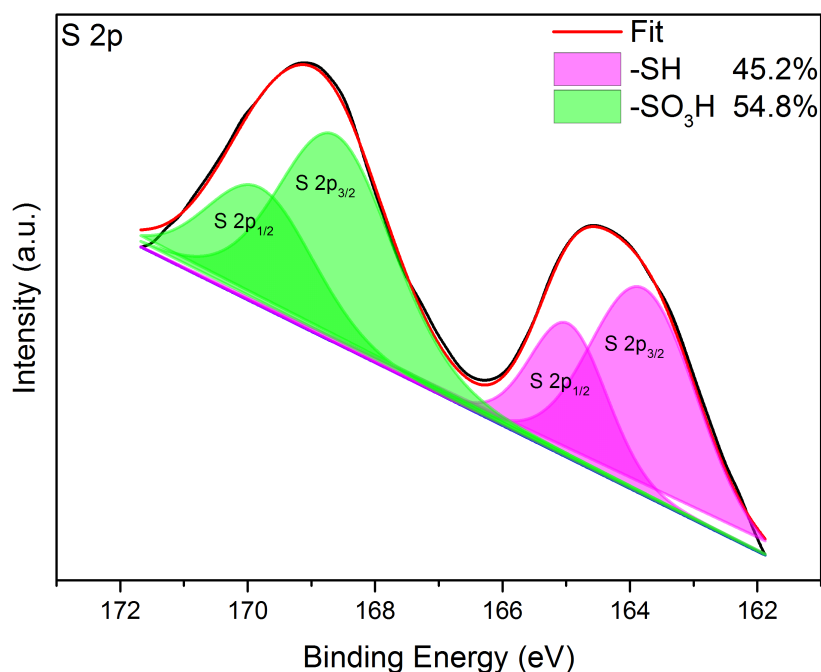


FIGURE 4.6 – XPS spectra of the DMSi-SA catalyst.

XPS is one of the most important techniques for studying the chemical state of the atoms present in the surface layer region of solid materials and determine the chemical environment around the atoms present in the surface

of the samples. The most significant results were obtained when studying the energy S2p core level. The S2p spectra in Figure 4.6 depicts two peaks (fitted by two doublets at 168.6, 169.7 and 163.9, 165.1 eV) assigned to sulfur in $-\text{SO}_3\text{H}$ and $-\text{SH}$ groups, respectively. Approximately half sulfur content exists in the form of $-\text{SO}_3\text{H}$, which corroborates the joint results obtained by XRF and titration.¹²²

In order to determine the nature of the acidic sites present in the sample an infrared of adsorbed pyridine was conducted (Figure 4.7). The infrared spectrum of adsorbed pyridine of the support showed only bands related to the interaction of pyridine with silanol groups, which behave as weak Brønsted acid sites: the band in 1447 cm^{-1} is related to H-bonded silanol groups, while the one in 1596 cm^{-1} is from free silanol groups. As for the spectrum of the catalyst DMSi-SA, the band in 1596 cm^{-1} is ascribed to the stretching of C-C in the aromatic ring of the pyridinium ion, which indicates the presence of strong Brønsted acid sites in

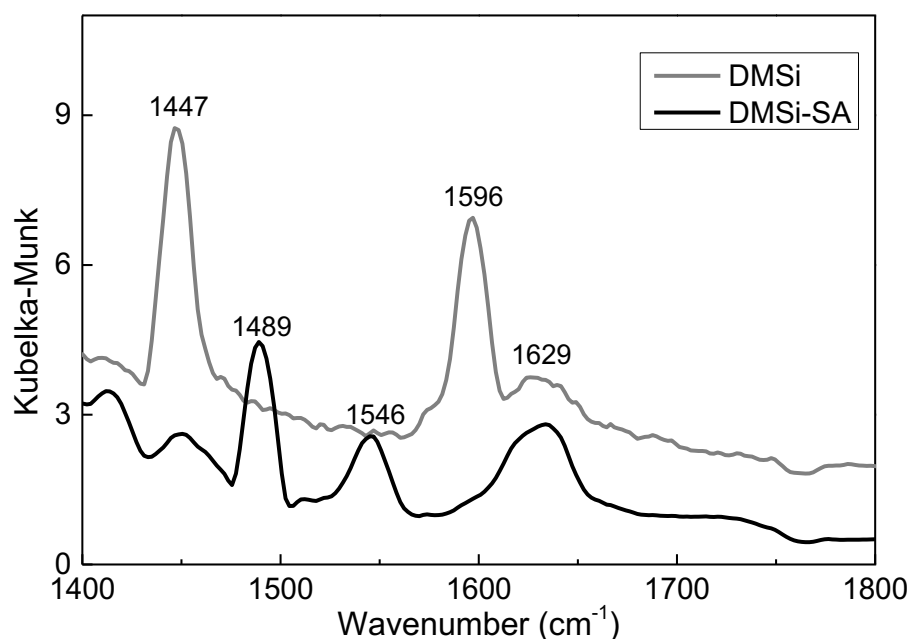


FIGURE 4.7 – Infrared of adsorbed pyridine of the support DMSi and the catalyst DMSi-SA.

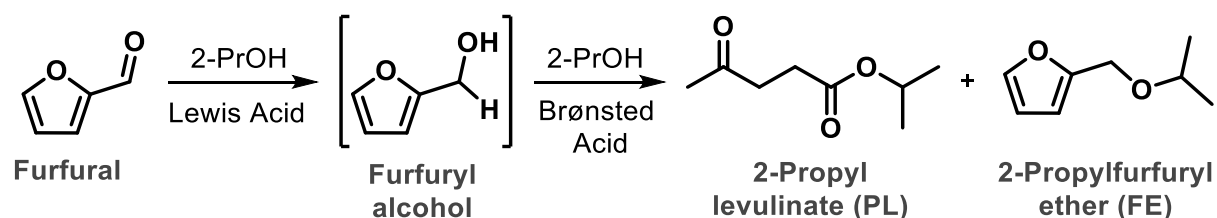
122. Russo, P. A.; Antunes, M. M.; Neves, P.; Wiper, P. V.; Fazio, E.; Neri, F.; Barreca, F.; Mafra, L.; Pillinger, M.; Pinna, N.; Valente, A. A. *J. Mater. Chem. A*, **2**:11813, 2014.

the sample; the band in 1489 appears due to the presence of both Lewis and Brønsted acid sites.¹²³ The band in 1629 cm^{-1} , which appears in the spectra of both samples, is a result of the interaction of pyridine with water.¹¹⁸

Having the sulfonic acid-functionalized dendritic mesoporous silica nanosphere thoroughly characterized in hands, the next step was the evaluation of its catalytic activity conversion of hexoses, pentoses and their derivatives to value-added chemicals.

4.5.2 - Catalytic evaluation

As depicted in Scheme 4.5, the first step in the conversion of furfural to alkyl levulinates is the transfer hydrogenation of furfural to furfuryl alcohol. As discussed in Chapter 3, section 3.1.1 (Page 87), this reaction is a notorious protocol for the reduction of carbonyl compounds using secondary alcohols as hydrogen source and requires Lewis acid catalysts. The second step is a alcoholysis that comprises a series of steps, as showed in Scheme 3.6 (Page 87).



SCHEME 4.5 – Conversion of furfural to 2-propyl levulinate.

In that way, the optimization studies on the conversion of furfural to propyl levulinates through a one-pot sequential transfer hydrogenation/alcoholysis sequence using isopropanol as solvent and hydrogen donor in the first step and reactant in the second by studying the effect of the temperature (Figure 4.8). It is possible to note that the increase of the temperature

123. (a) Hamoudi, S.; Kaliaguine, S.; *Micropor. Mesopor. Mat.*, **59**:195, 2003. (b) Zhang, X.; Zhao, Y.; Xu, S.; Yang, Y.; Liu, J.; Wei, Y.; Yang, Q. *Nat. Commun.*, **5**:3170, 2014.

has a dramatic effect on both the conversion and selectivity of the reaction. When the temperature was raised from 90 to 130°C led to an enhancement in both conversion and selectivity to the ester product, but a further increase to 150 °C caused a marked drop in selectivity albeit a great increase in the conversion. In the case of the catalyst loading, both the conversion and selectivity to the ester increased with the catalyst loading, achieving its maximum with 100 mg of catalyst (55% conversion and 98% selectivity). As for the solvent amount, its increase was deleterious to the reaction selectivity.

In summary, further studies optimization studies are required to improve the conversion of the reaction. Since the conversion appears to be

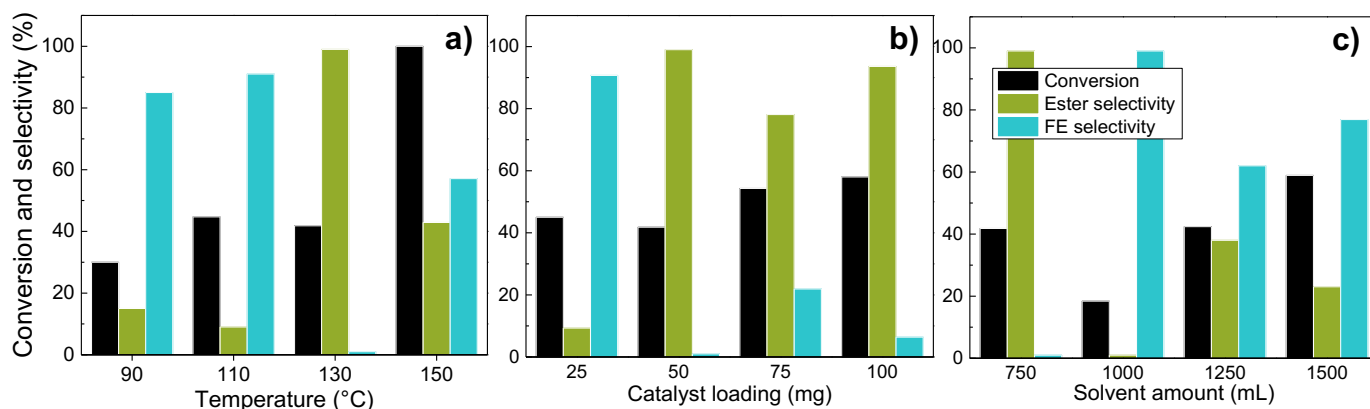
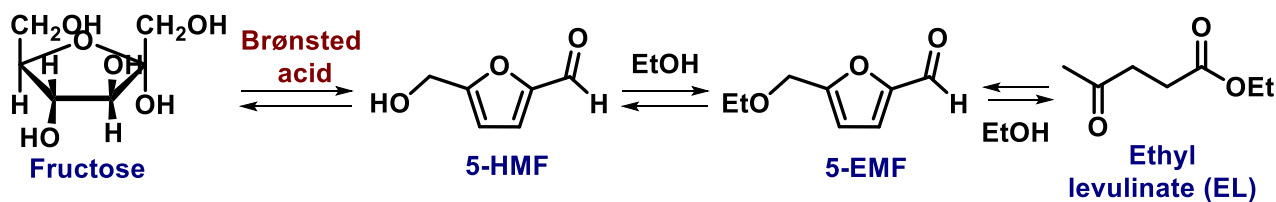


FIGURE 4.8 – Evaluation of reaction parameters in the conversion of furfural to 2-propyl levulinate.

strongly dependent on the catalyst loading, we intend to conduct a more detailed study to quantify the Lewis acid sites on the sample and their influence in the conversion and selectivity.

The catalytic activity of DMSi-SA was also evaluated in the conversion of fructose to 5-HMF and ethyl levulinate (Scheme 4.6). In this reaction, fructose is initially dehydrated to 5-HMF in the presence of Brønsted acids and may be converted *in situ* to 5-EMF; next, the ring opening of 5-EMF followed by a decarboxylation step that releases formic acid affords ethyl levulinate.



Accordingly, for the optimization of the reaction conditions for this transformation (Figure 4.9) the reaction was set up in an Ace® pressure tube using 50 mg of catalyst at 170 °C and kept at this temperature for a determined time. It is possible to notice from Figure 4.9a that both the conversion and selectivity change considerably over time. As expected, the conversion increases over time, achieving its maximum at 12h of reaction. On the other hand, the selectivity decreased significantly with reaction time. Therefore, the best reaction conditions seemed to be achieved in 6h of reaction, with a conversion of 80% and selectivity

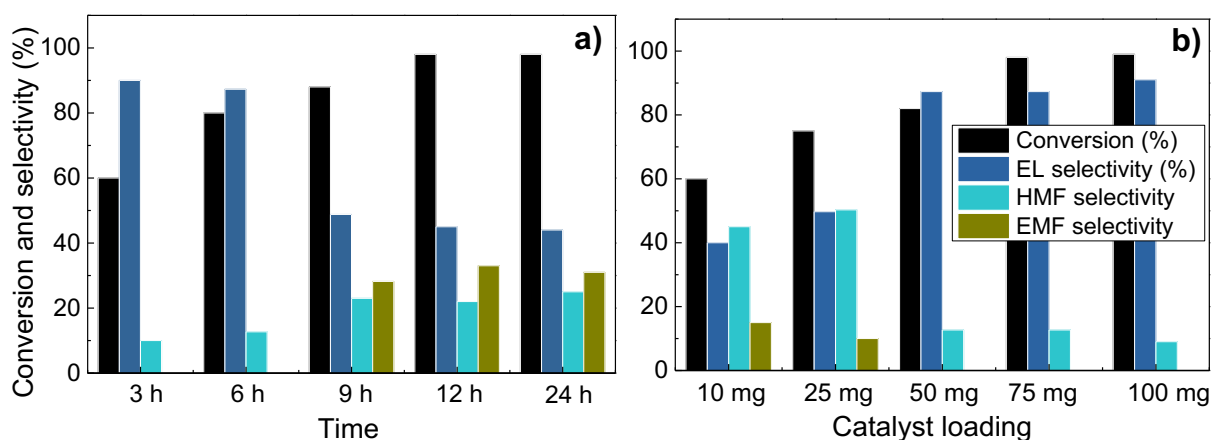


FIGURE 4.9 – Evaluation of a) reaction time and b) catalyst loading in the conversion of fructose to ethyl levulinate at 170 °C.

of 87% to ethyl levulinate.

The evaluation of the catalyst loading (Figure 4.9b), conducted at the same temperature, showed that both the conversion and selectivity increase with the amount of catalyst in the reaction medium; remarkably, when using 100 mg of catalyst, a conversion of over 95% was achieved with 90% of selectivity to ethyl levulinate.

Knowing that the catalyst amount plays a fundamental role in the reaction and setting 6h as the ideal reaction time, the catalyst loading was reevaluated at a lower temperature (120°C) with the intent of determining how the temperature could influence the outcome of the reaction (Figure 4.10). Although the conversion followed the same tendency and increased considerably with the catalyst loading, the selectivity to ethyl levulinate remained below 60% even when using 100 mg of catalyst.

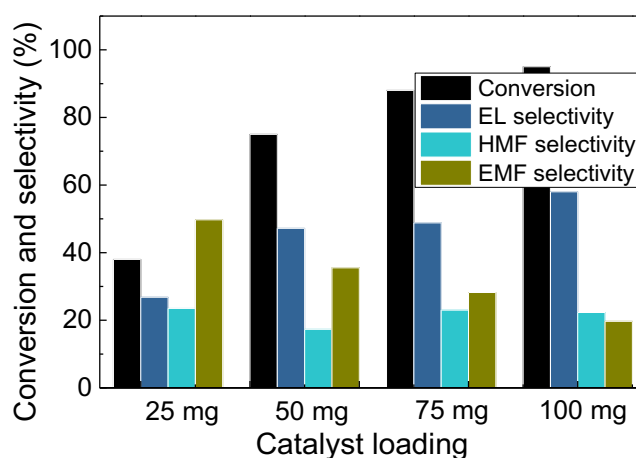
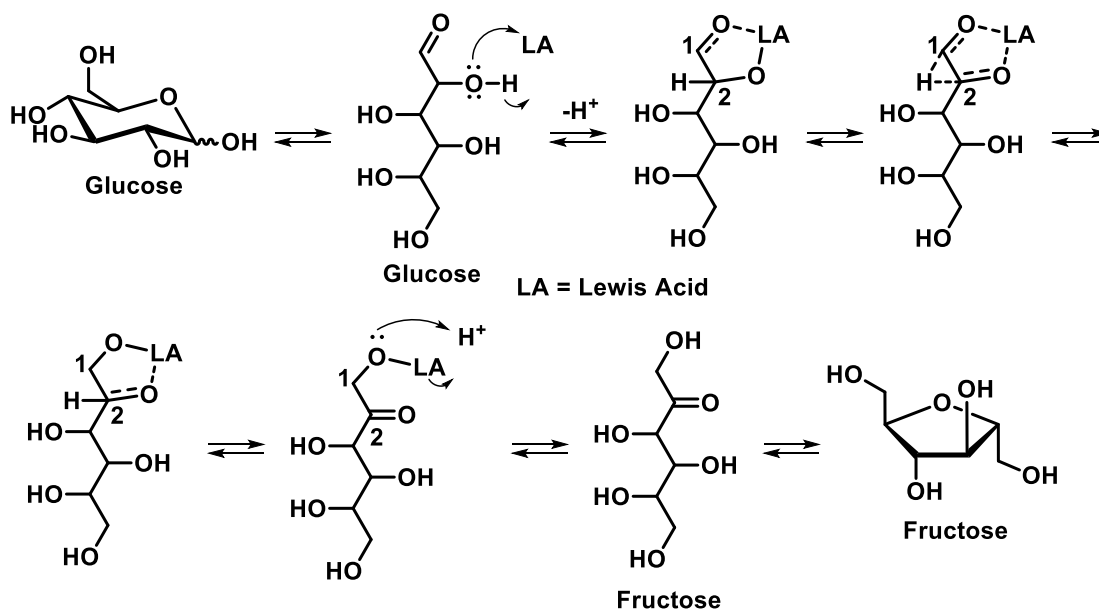


FIGURE 4.10 - Evaluation of the catalyst loading in the conversion of fructose to ethyl levulinate at 120°C.

Having the previous optimized conditions in hand for the conversion of fructose to ethyl levulinate, the possibility of the application of this protocol for glucose was evaluated; this transformation is very interesting, especially when one considers that the conversion of glucose to fructose requires Lewis acids catalyst (Scheme 4.7). Therefore, we envisioned that the DMSi-SA would be effective in this reaction; to our delight, the catalyst was able to promote this transformation, but a low conversion was achieved (15%), albeit a selectivity superior to 90%. However, further optimization is necessary in order to improve the outcome of this process.



SCHEME 4.7 – Mechanism of the isomerization of glucose to fructose.

4.4- Conclusions and perspectives

In summary, a new metal-free catalyst that displays both Lewis and Brønsted acid sites was prepared and thoroughly characterized. The catalyst showed exceptional activity in the conversion of furfural to alkyl levulinate and fructose to ethyl levulinate. However, the obtention of 5-HMF from fructose with good selectivities still remains a challenge. Additionally, the conversion of other hexoses (e.g. glucose) and pentoses (e.g. xylose) and their derivatives to value-added chemicals is another interesting perspective of this work.

4.5 - Experimental

4.5.1 - Synthesis of dendritic mesoporous silica (DMSi) nanospheres

The DMSi nanospheres used as support for the catalyst were synthesized following a procedure described by Yang and co-workers.¹²⁰ A solution containing distilled water (72 mL), cetyltrimethylammonium chloride (CTAC, 48 mL, 25 wt% aqueous solution) and trietanolamine (TEA, 360 μ L) was stirred at 500 rpm for 1 h at 60 °C. A solution containing tetraethylorthosilicate

(TEOS, 8 mL) and cyclohexane (32 mL) was then added dropwise to the CTAC solution. The mixture was kept under reflux at 60 °C for 20 h under slow magnetic stirring (200 rpm). The resultant material was cooled to room temperature and centrifuged at 13000 rpm for 20 min, followed by washing with distilled water several times. Next, the white material was dried at 60 °C for 24 h followed by trituration and calcination at 600 °C in air atmosphere for 3 h.

4.5.2 - Functionalization of DMSi nanospheres with sulfonic acid groups

The sulfonic acid-functionalized DMSi nanospheres were obtained following a two-step approach recently described by Pirez and co-workers.¹²¹ 1 g of the calcinated DMSi nanospheres was added to a solution containing distilled water (30 mL) and sodium chloride (200 mg) under vigorous stirring at room temperature for 30 min. Then, 3-mercaptopropyl trimethoxysilane (MPTMS, 1 mL) was added to the mixture, which was refluxed at 100 °C under magnetic stirring (600 rpm) for 24 h. The mercaptopropyl functionalized material (DMSi-MP) was filtered under vacuum and washed several times with distilled water followed by drying at 50 °C under vacuum overnight. The thiol groups were next converted into sulfonic groups by a mild oxidation approach using hydrogen peroxide as oxidant. For this step, the dried and trituated DMSi-MP (~1.6 g) was added into a 30% hydrogen peroxide solution (30 mL) and vigorously stirred (1000 rpm) at room temperature for 24 h. The resultant material was filtered under vacuum and washed several times with methanol, followed by drying at 50 °C under vacuum for 24 h. The dendritic mesoporous silica functionalized with sulfonic acid groups was named as DMSi-SA.

4.5.3 Characterization of the DMSi support and the DMSi-SA catalyst

The particle size and morphological studies of the DMSi support and DMSi-SA catalyst were performed by TEM. Transmission Electron Microscopy

(TEM) analysis was accomplished using JEOL JEM 2010F at 160kV of accelerating voltage. Microscopic images were obtained by HRTEM TITAN 60-300 with X-FEG type emission gun, operating at 80 kV. This microscope is equipped with Cs image corrector and a STEM high-angle annular dark-field detector (HAADF). The point resolution is 0.06 nm in HRTEM mode. The elemental mappings were obtained by STEM-Energy Dispersive X-ray Spectroscopy (EDS) with acquisition time of 20 min. For HRTEM analyses, the powder samples were dispersed in ethanol and 5 min ultrasonicated. One drop of this solution was placed on a copper grid with holey carbon film. The sample was dried at room temperature.

Low angle x-ray diffraction patterns were recorded with a PANalytical X'Pert PRO MPD (PANalytical, Netherlands) diffractometer in the Bragg-Brentano geometry, Co-K α radiation (40 kV, 30 mA, $\lambda = 0.1789$ nm) equipped with an X'Celerator detector and programmable divergence and diffracted beam anti-scatter slits. The measurement range was $2\theta:0^\circ - 5^\circ$ with a step size of 0.017° .

Samples were analyzed using an Agilent 6820 gas chromatograph equipped with an Agilent DB-5 capillary column (30 m x 0.32 mm, 0.5 μ m) under the operation parameters: temperature of inlet of 100 °C, temperature of flame ionization detector of 250 °C, temperature ramp of the oven from 100 to 250 °C at a rate of 10 °C min⁻¹.

The infrared spectrum of adsorbed pyridine was recorded on a Fourier Transform Infrared spectrophotometer model Prestigi-21 in the range of 1800–1400 cm⁻¹ wavenumber. For the qualitative acidity determination, 50 mg of sample were subjected to a heat treatment in a tubular furnace at 300 °C and 100 mL min⁻¹ N₂ flow for 1 h. Gaseous pyridine was then adsorbed on the samples for 1 h at 150 °C with a N₂ gas carrier flow at 100 mL min⁻¹. Next, the N₂ flow was kept constant for 1 h at 150 °C for the removal of the physically adsorbed pyridine.

XPS surface investigation has been performed on the PHI 5000 VersaProbe II XPS system (Physical Electronics) with monochromatic Al-K α source (15 kV, 50 W) with photon energy of 1486.7 eV. Dual beam charge compensation was used for all measurements. All the spectra were measured in the vacuum of 1.4×10^{-7} Pa and at the room temperature of 22 °C. For the high resolution spectra the pass energy was set up to 23.500 eV and step size 0.200 eV. The spectra were evaluated with the MultiPak (Ulvac - PHI, Inc.) software. All binding energy (BE) values were referenced to the C1s peak at 284.80 eV.

The aqueous titration of the catalyst was conducted using thymol blue as indicator. The sample was previously submitted by an ionic exchange with KCl and the resulting HCl was titrated with an NaOH solution previously standardized using potassium hydrogen phthalate (KHC₈H₄O₄). All analysis were performed as triplicates and in different batches of the catalyst.

4.5.4 - Catalytic evaluation of DMSi-SA nanospheres on furfural conversion to alkyl levulinates

To a 10 mL glass vial sealed with a Teflon lid and an aluminum cap, furfural (0.34 mmol, 28 μ L), of 2-propanol or 2-butanol (750 μ L) and DMSi-SA (50 mg) were added, followed by the addition of a magnetic stir bar. The vial was sealed and immersed in a pre-heated silicon oil bath at the desired temperature and the reaction was magnetically stirred (700 rpm) for 24 h. After this, the vial was cooled at room temperature and a small amount (\sim 50 μ L) of the resulting liquid was removed, filtered using a syringe filter, diluted in absolute ethanol and analyzed by GC-FID and GC-MS techniques. The retention time of the reagents and products were compared with those of commercially available standards. In order to evaluate the degree of polymerization of furfural, some samples were injected using DMF as internal standard.

4.5.5 - Catalytic evaluation of DMSi-SA nanospheres on fructose conversion to alkyl levulinates

To a 15 mL Ace® pressure tube, fructose (200 mg, 1.1 mmol), ethanol (2 mL) and DMSi-SA (50 mg) were added, followed by the addition of a magnetic stir bar. The tube was sealed and immersed in a pre-heated silicon oil bath at the desired temperature and the reaction was magnetically stirred (700 rpm) for 6 h. After this, the vial was cooled at room temperature and a small amount (~50 µL) of the resulting liquid was removed, filtered using a syringe filter, diluted in ethyl acetate and analyzed by GC-FID and GC-MS techniques using DMF as internal standard. The retention time of the reagents and products were compared with those of commercially available standards.

4.5.6 - Analyses of the reaction products

The samples were analyzed using an Agilent 6820 gas chromatograph equipped with an Agilent DB-5 capillary column (30 m x 0.32 mm, 0.5 µm) under the operation parameters: temperature of inlet of 250 °C, temperature of flame ionization detector of 250 °C, temperature ramp of the oven from 100 to 250 °C at a rate of 10 °C min⁻¹. CG-MS analyses were conducted in a Shimadzu GCMS-QP2010S Gas Chromatograph coupled to a MS detector equipped with a ZB-5MS column (30 m x 0.25 mm x 0.25 µm) under the operation parameters: temperature of inlet of 250 °C, temperature of the interface of 300 °C, temperature ramp of the oven from 50 to 250 °C at a rate of 10 °C min⁻¹.

References

1. IUPAC. Compendium of Chemical Terminology, 2nd ed. (the "Gold Book"). Compiled by McNaught, A. D. and Wilkinson, A. Blackwell Scientific Publications, Oxford, 1997.
2. (a) BRAVO-SUÁREZ, J. J.; KIDDER, M. K.; SCHWARTZ, V. Novel Materials for Catalysis and Fuels Processing. ACS Symposium Series. 1st ed. American Chemical Society, Washington-DC, 2013. (b) HAGEN, J. Industrial Catalysis: A Practical Approach. 2nd ed., Hoboken, John Wiley & Sons, 2005.
3. ANASTAS, P. T.; WARNER, J. C. Green Chemistry: Theory and Practice. 1st ed, Oxford Science Publications, Oxford, 1998.
4. VAN LEEUWEN, P.W.N.M. Homogeneous Catalysis: Understanding the Art. New York, Springer-Verlag, 2004.
5. NØRSKOV, J. K.; STUDDT, F.; ABILD-PEDERSEN, F.; BLIGAARD, T. Fundamental Concepts in Heterogeneous Catalysis. Hoboken, John Wiley & Sons, 2014.
6. ASTRUC, D.; LU, F.; ARANZAES, J. R. "Nanoparticles as recyclable catalysts: The frontier between homogeneous and heterogeneous catalysis". *Angew. Chem. Int. Ed.*, **44**:7852, 2005.
7. SCHLÖGL, R.; HAMID, S. B. A. "Nanocatalysis: mature science revisited or something really new?". *Angew. Chem. Int. Ed.*, **43**:1628, 2004.
8. LI, H.; LUK, Y.-Y. ; MRKSICH, M. "Catalytic asymmetric dihydroxylation by gold colloids functionalized with self-assembled monolayers". *Langmuir*, **15**:4957, 1999.
9. MOTORINA, I.; CRUDDEN, C. M. "Asymmetric dihydroxylation of olefins using cinchona alkaloids on highly ordered inorganic supports". *Org. Lett.*, **3**:2325, 2001.
10. KONIECZNY, S.; LEURS, M.; TILLER, J. C. "Polymer enzyme conjugates as chiral ligands for Sharpless dihydroxylation of alkenes in organic solvents". *ChemBioChem*, **16**:83, 2015.
11. SHILPA, N.; MANNA, J.; RANA, R. K. "Bioinspired nanoparticle-assembly route to a hybrid scaffold: designing a robust heterogeneous catalyst for asymmetric dihydroxylation of olefins". *Eur. J. Inorg. Chem.*, **2015**:4965, 2015.
12. HAN, Q., HE, C.; ZHAO, M., QI, B.; NIU, J.; DUAN, C. "Engineering chiral polyoxometalate hybrid metal-organic frameworks for asymmetric dihydroxylation of olefins". *J. Am. Chem. Soc.*, **135**:10186, 2013.
13. ZHANG, G.; WANG, Y.; WEN, X.; DING, C.; LI, Y. "Dual-functional click-triazole: a metal chelator and immobilization linker for the construction of a heterogeneous palladium catalyst and its application for the aerobic oxidation of alcohols". *Chem. Commun.*, **48**:2979, 2012.
14. KASAPLAR, P.; RODRÍGUEZ-ESCRICH, C.; PERICAS, M. A. "Continuous flow, highly enantioselective Michael additions catalyzed by a PS-supported squaramide". *Org. Lett.*, **15**:3498, 2013.

- 15.** REDDY, B. V. S.; VENKATESWARLU, A.; REDDY, G. N.; REDDY, Y. V. R. "Chitosan-SO₃H: an efficient, biodegradable, and recyclable solid acid for the synthesis of quinoline derivatives via Friedländer annulation" *Tetrahedron Lett.*, **54**:5767, 2013.
- 16.** (a) GAWANDE, M. B.; BRANCO, P. S.; VARMA, R. S. "Nano-magnetite (Fe₃O₄) as a support for recyclable catalysts in the development of sustainable methodologies". *Chem. Soc. Rev.*, **42**:3371, 2013. (b) GAWANDE, M. B.; MONGA, Y.; ZBORIL, R.; SHARMA, R. K. "Silica-decorated magnetic nanocomposites for catalytic applications". *Coordin. Chem. Rev.*, **288**:118, 2015. (c) GAWANDE, M. B.; GOSWAMI, A.; ASEFA, T., GUO, H.; BIRADAR, A. V., PENG, D.-L.; ZBORIL, R.; VARMA, R. S. "Core-shell nanoparticles: synthesis and applications in catalysis and electrocatalysis". *Chem. Soc. Rev.*, **44**:7540, 2015. (d) SHYLESH, S.; SCHNEMANN, V.; THIEL, W. R. "Magnetically separable nanocatalysts: bridges between homogeneous and heterogeneous catalysis". *Angew. Chem. Int. Ed.*, **49**: 3428, 2010. (e) POLSHETTIWAR, V.; LUQUE, R.; FIIHRI, A.; ZHU, H.; BOUHRARA, M.; BASSET, J.-M. "Magnetically recoverable nanocatalysts". *Chem. Rev.*, **111**:3036, 2011.
- 17.** (a) ROSSI, L. M.; COSTA, N. J. S.; SILVA, F. P.; WOJCIESZAK, R. "Magnetic nanomaterials in catalysis: advanced catalysts for magnetic separation and beyond". *Green Chem.*, **16**:290, 2014. (b) WANG, D.; ASTRUC, D. "Fast-growing field of magnetically recyclable nanocatalysts". *Chem. Rev.*, **114**:6949, 2014.
- 18.** (a) LU, A.-H.; SALABAS, E. L.; SCHÜTH, F. "Magnetic nanoparticles: synthesis, protection, functionalization, and application". *Angew. Chem. Int. Ed.*, **46**:1222, 2007. (b) CHAUDHURI, R. G.; PARIJA, S. "Core/shell nanoparticles: classes, properties, synthesis mechanisms, characterization, and applications" *Chem. Rev.*, **112**:2373, 2012. (c) VATTA, L. L.; SANDERSON, R. D.; KOCH, K. R. "Magnetic nanoparticles: properties and potential applications". *Pure Appl. Chem.*, **78**:1793, 2006.
- 19.** XU, Z.; SHEN, C.; HOU, Y.; GAO, H.; SUN, S. "Oleylamine as both reducing agent and stabilizer in a facile synthesis of magnetite nanoparticles". *Chem. Mater.*, **21**:1778, 2009.
- 20.** LANGEVIN, D. "Micelles and microemulsions". *Annu. Rev. Phys. Chem.*, **43**:341, 1992.
- 21.** LIU, J.; SUN, Z.; DENG, Y.; ZOU, Y.; LI, C.; GUO, X.; XIONG, L.; GAO, Y.; LI, F.; ZHAO, D. "Highly water-dispersible biocompatible magnetite particles with low cytotoxicity stabilized by citrate groups". *Angew. Chem. Int. Ed.*, **48**:5875, 2009.
- 22.** (a) GUERRERO-MARTÍNEZ, A.; PÉREZ-JUSTE, J.; LIZ-MARZÁN, L. M. "Recent progress on silica coating of nanoparticles and related nanomaterials". *Adv. Mater.*, **22**:1182, 2010. (b) JANA, N. R.; EARHART, C.; YING, J. Y. "Synthesis of water-soluble and functionalized nanoparticles by silica coating". *Chem. Mater.*, **19**:5074, 2007.
- 23.** BAEZA, A.; GUILLENA, G.; RAMÛN, D. J. "Magnetite and metal-impregnated magnetite catalysts in organic synthesis: a very old concept with new promising perspectives". *ChemCatChem*, **8**:49, 2016.
- 24.** (a) ZAERA, F. *Chem. Soc. Rev.*, **42**:2746, 2013. "Nanostructured materials for applications in heterogeneous catalysis". (b) MCMORN, P.; HUTCHINGS, G. J. "Heterogeneous enantioselective catalysts: strategies for the immobilisation of homogeneous catalysts". *Chem. Soc. Rev.*, **33**:108, 2004. (c) SHELDON, R. A.; BEKKUM, H. Fine

Chemicals through Heterogeneous Catalysis, 1st ed., John Wiley & Sons, Wiley-VCH, Weinheim, New York, 2001.

- 25.** MARSET, X.; PÉREZ, J. M.; RAMÓN, D. J. “Cross-dehydrogenative coupling reaction using copper oxide impregnated on magnetite in deep eutectic solvents”. *Green Chem.*, **18**:826, 2016.
- 26.** SMITH, E. L.; ABBOTT, A. P.; RYDER, K. S. “Deep eutectic solvents (DESS) and their applications”. *Chem. Rev.*, **114**:11060, 2014.
- 27.** (a) LIU, P.; HAO, J.-W.; MOA, L.-P.; ZHANG, Z.-H. “Recent advances in the application of deep eutectic solvents as sustainable media as well as catalysts in organic reactions”. *RSC Adv.*, **5**:48675, 2015. (b) ALONSO, D. A.; BAEZA, A.; CHINCHILLA, R.; GUILLENA, G.; PASTOR, I. M.; RAMÓN, D. J. “Deep eutectic solvents: the organic reaction medium of the century”. *Eur. J. Org. Chem.* **2016**:612, 2016.
- 28.** SHELKE, S. N.; BANKAR, S. R.; MHASKE, G. R.; KADAM, S. S.; MURADE, D. K.; BHORKADE, S. B.; RATHI, A. K.; BUNDALESKI, N.; TEODORO, O. M. N. D.; ZBORIL, R.; VARMA, R. S.; GAWANDE, M. B. “Iron oxide-supported copper oxide nanoparticles (Nanocat-Fe-CuO): magnetically recyclable catalysts for the synthesis of pyrazole derivatives, 4-methoxyaniline, and Ullmann-type condensation reactions”. *ACS Sustainable Chem. Eng.* **2**: 1699, 2014.
- 29.** KOTANI, M.; KOIKE, T.; YAMAGUCHI, K.; MIZUNO, N. “Ruthenium hydroxide on magnetite as a magnetically separable heterogeneous catalyst for liquid-phase oxidation and reduction”. *Green Chem.* **8**:735, 2006.
- 30.** LIU, J.; PENG, X.; SUN, W.; ZHAO, Y.; XIA, C. “Magnetically separable Pd catalyst for carbonylative sonogashira coupling reactions for the synthesis of α , β -alkynyl ketones”. *Org. Lett.*, **10**:3933, 2008.
- 31.** LUO, S.; ZHENG, X.; XU, H.; G MI, X.; ZHANG, L.; CHENG, J.-P. “Magnetic nanoparticle-supported Morita–Baylis–Hillman catalysts”. *Adv. Synth. Catal.*, **349**:2431, 2007.
- 32.** (a) LUO, S.; ZHENG, X.; CHENG, J.-P. “Asymmetric bifunctional primary aminocatalysis on magnetic nanoparticles”. *Chem. Commun.*, **2008**:5719, 2008. (b) ZHENG, X.; ZHANG, L.; LI, J.; LUO, S.; CHENG, J.-P. “Magnetic nanoparticle supported polyoxometalates (POMs) via non-covalent π - π interaction: reusable acid catalysts and catalyst supports for chiral amines”. *Chem. Commun.*, **47**: 12325, 2011. (c) GLEESON, O.; DAVIES, G.-L.; PESCHIULLI, A.; TEKORIUTE, R.; GUNKO, Y. K.; CONNON, S. J. “The immobilisation of chiral organocatalysts on magnetic nanoparticles: the support particle cannot always be considered inert”. *Org. Biomol. Chem.*, **9**:7929, 2011. (d) ROY, S.; PERICÀS, M. A. “Functionalized nanoparticles as catalysts for enantioselective processes”. *Org. Biomol. Chem.*, **7**: 2669, 2009.
- 33.** RIENTE, P.; YADAV, J.; PERICÀS, M. A. “A click strategy for the immobilization of MacMillan organocatalysts onto polymers and magnetic nanoparticles”. *Org. Lett.*, **14**:3668, 2012.

- 34.** KAWAMURA, M.; SATO, K. "Magnetic nanoparticle-supported crown ethers". *Chem. Commun.*, **2007**:3404, 2007.
- 35.** SOBHANI, S.; VAHIDI, Z.; ZERAATKAR, Z.; KHODADADI, S. "A Pd complex of a NNN pincer ligand supported on γ -Fe₂O₃@SiO₂ as the first magnetically recoverable heterogeneous catalyst for C–P bond forming reactions". *RSC Adv.*, **5**:36552, 2015.
- 36.** ZHENG, X.; LUO, S.; ZHANG, L.; CHENG, J.-P. "Magnetic nanoparticle supported ionic liquid catalysts for CO₂ cycloaddition reactions". *Green Chem.*, **11**:455, 2009.
- 37.** CIOC, R. C.; RUIJTER, E.; ORRU, R. V. A. "Multicomponent reactions: advanced tools for sustainable organic synthesis". *Green Chem.*, **16**:2958, 2014.
- 38.** STRECKER, A. "Ueber die künstliche bildung der milchsäure und einen neuen, dem glycocoll homologen körper". *Liebigs. Ann. Chem.*, **27**:75, 1850.
- 39.** RADZISZEWSKI, B. "Ueber die constitution des lophins und verwandter verbindunge". *Ber. Dtsch. Chem. Ges.*, **15**:1499, 1882.
- 40.** HANTZSCH, A. "Ueber die synthese pyridinartiger verbindungen aus acetessigäther und aldehydammoniak". *Liebigs. Ann. Chem.*, **215**:1, 1882.
- 41.** BIGINELLI, P. "Ueber aldehyduramide des acetessigäthers". *Chemische Berichte*, **24**:1317, 1891.
- 42.** MANNICH, C.; KROSCHE, W. "Ueber ein kondensations produkt aus formaldehyd, ammoniak und antipyrin" *Arch. Pharm.*, **250**:647, 1912.
- 43.** BUCHERER, H. T.; LIEB, V. A. "Über die bildung substituierter hydantoine aus aldehyden und ketonen. Synthese von hydantoinen" *J. Prakt. Chem.*, **140**:151, 1934.
- 44.** UGI, I; MEYER, R.; FETZER, U.; STEINBRÜCKNER, C. "Versuche mit Isonitrilen". *Angew. Chem.* **71**:386, 1959.
- 45.** PASSERINI, M.; SIMONE, L. "Formation of α -hydroxycarboxamides on treatment of an isonitrile with a carboxylic acid and an aldehyde or ketone". *Gazz. Chim. Ital.* **51**:126, 1921.
- 46.** (a) GANEM, B. "Strategies for Innovation in Multicomponent Reaction Design". *Acc. Chem. Res.*, **42**:463, 2009. (b) CLIMENT, M. J.; CORMA, A.; IBORRA, S. "Homogeneous and heterogeneous catalysts for multicomponent reactions". *RSC Adv.*, **2**:16, 2012. (c) BIGGS-HOUCK, J. E.; YOUNAI, A.; SHAW, J. T. "Recent advances in multicomponent reactions for diversity-oriented synthesis". *Curr. Opin. Chem. Biol.*, **14**:371, 2010.
- 47.** (a) KOUKABI, N.; KOLVARI, E.; KHAZAEI, A.; ZOLFIGOL, M. A.; SHIRMARDI-SHAGHASEMIC, B.; KHAVASID, H. R. "Hantzsch reaction on free nano-Fe₂O₃ catalyst: excellent reactivity combined with facile catalyst recovery and recyclability". *Chem. Commun.*, **47**:9230, 2011. (b) GHASEMZADEH, M. A.; SAFAEI-GHOMI, J.; MOLAEI, H. "Fe₃O₄ nanoparticles: As an efficient, green and magnetically reusable catalyst for the one-pot synthesis of 1,8-dioxo-decahydroacridine derivatives under solvent-free conditions". *C. R. Chimie*, **15**:969, 2012. (c) DANDIA, A.; JAIN, A. K.; SHARMA, S. "CuFe₂O₄ nanoparticles

as a highly efficient and magnetically recoverable catalyst for the synthesis of medicinally privileged spiropyrimidine scaffolds". *RSC Adv.*, **3**:2924, 2013. (d) ROSTAMNIA, S.; NURI, A.; XIN, H.; POURJAVADI, A; HOSSEINI, S. H. "Water dispersed magnetic nanoparticles (H_2O -DMNPs) of $\gamma\text{-Fe}_2\text{O}_3$ for multicomponent coupling reactions: a green, single-pot technique for the synthesis of tetrahydro-4*H*-chromenes and hexahydroquinoline carboxylates". *Tetrahedron Lett.*, **54**:3344, 2013. (e) GHahremanzadeh, R.; RASHID, Z.; ZARNANI, A. H.; NAEIMI, H. "Synthesis of novel spirooxindoles in water by using MnFe_2O_4 nanoparticles as an efficient magnetically recoverable and reusable catalyst". *Appl. Catal. A-Gen.*, **467**:270, 2013. (f) LI, B.-L.; ZHANG, M.; HU, H.-C.; DUB, X.; ZHANG, Z.-H. "Nano- CoFe_2O_4 supported molybdenum as an efficient and magnetically recoverable catalyst for a one-pot, four-component synthesis of functionalized pyrroles". *New J. Chem.*, **38**:2435, 2014.

48. (a) ALIAGA, M. J.; RAMÓN, D. J.; YUS, M. "Impregnated copper on magnetite: an efficient and green catalyst for the multicomponent preparation of propargylamines under solvent free conditions". *Org. Biomol. Chem.*, **8**: 43, 2010. (b) GAWANDE, M. B.; VELHINHO, A.; NOGUEIRA, I. D.; GHUMMAN, C. A. A.; TEODORO, O. M. N. D.; BRANCO, P. S. "A facile synthesis of cysteine-ferrite magnetic nanoparticles for application in multicomponent reactions-a sustainable protocol". *RSC Adv.* **2**:6144, 2012.

49. (a) BAIG, R. B. N.; VARMA, R. S. "A highly active magnetically recoverable nano ferrite-glutathione-copper (nano-FGT-Cu) catalyst for Huisgen 1,3-dipolar cycloadditions". *Green Chem.*, **14**:625, 2012. (b) XIONG, X.; CAI, L. "Application of magnetic nanoparticle-supported CuBr: a highly efficient and reusable catalyst for the one-pot and scale-up synthesis of 1,2,3-triazoles under microwave-assisted conditions". *Catal. Sci. Technol.*, **3**:1301, 2013. (c) DEGHANI, F.; SARDARIAN, A. R.; ESMAEILPOUR, M. "Salen complex of Cu(II) supported on superparamagnetic $\text{Fe}_3\text{O}_4@SiO_2$ nanoparticles: An efficient and recyclable catalyst for synthesis of 1- and 5-substituted 1*H*-tetrazoles". *J. Organomet. Chem.*, **743**:87, 2013.

50. GAWANDE, M. B.; VELHINHO, A.; NOGUEIRA, I. D.; GHUMMAN, C. A. A.; TEODORO, O. M. N. D.; BRANCO, P. S. "A facile synthesis of cysteine-ferrite magnetic nanoparticles for application in multicomponent reactions - a sustainable protocol". *RSC Advances*, **2**:6144, 2012.

51. (a) PANDA, S. S.; KHANNA, P.; KHANNA, L. "Biginelli reaction: a green perspective". *Curr. Org. Synth.* **16**:507, 2012. (b) MAJID, M. H.; ASADI, S.; BOSHRA, B. M. "Recent progress in asymmetric Biginelli reaction". *Molecular Diversity*, **17**:389, 2013. (c) GRAAFF, C.; RUIJTER, E.; ORRU, R. V. A. "Recent developments in asymmetric multicomponent reactions". *Chem. Soc. Rev.*, **41**: 3969, 2012.

52. KAPPE, C. O. "Recent advances in the Biginelli dihydropyrimidine synthesis. New tricks from an old dog". *Acc. Chem. Res.*, **33**:879, 2000.

53. (a) LACOTTE, P.; BUISSON, D. A.; AMBROISE, Y. "Synthesis, evaluation and absolute configuration assignment of novel dihydropyrimidin-2-ones as picomolar sodium iodide symporter inhibitors". *Eur. J. Med. Chem.*, **62**: 722, 2013. (b) CRESPO, A.; MAATOUGUI, A. E.; BIAGINI, P.; AZUAJE, J.; COELHO, A.; BREA, J.; LOZA, M. I.; CADAVID, M. I.; GARCÍA-MERA, X.; GUTIÉRREZ-DE-TERÁNAND, H.; SOTELO, E. "Discovery of 3, 4-dihydropyrimidin-2(1*H*)-ones as a novel class of potent and selective A2B adenosine receptor antagonists". *ACS Med. Chem. Lett.*, **4**:1031, 2013.

54. (a) CLARK, J. H.; MACQUARRIE, D. J.; SHERWOOD, J. "The combined role of catalysis and solvent effects on the Biginelli reaction: improving efficiency and sustainability". *Chem. Eur. J.* **19**:5174, 2013. (b) SHEN, Z.-L.; XU, X.-P.; JI, S.-J. "Brønsted Base-Catalyzed One-Pot Three-Component Biginelli-Type Reaction: An Efficient Synthesis of 4,5,6-Triaryl-3,4-dihydropyrimidin-2(1*H*)-one and Mechanistic Study". *J. Org. Chem.* **75**:1162, 2010. (c) NANDI, G. C.; SAMAIAND, S.; SINGH, M. S. "Biginelli and Hantzsch-type reactions leading to highly functionalized dihydropyrimidinone, thiocoumarin, and pyridopyrimidinone frameworks via ring annulation with β -oxodithioesters". *J. Org. Chem.*, **75**:7785, 2010. (d) RAMOS, L. M.; GUIDO, B. C.; NOBREGA, C. C.; CORRÊA, J. R.; SILVA, R. G.; OLIVEIRA, H. C. B.; GOMES, A. F.; GOZZO, F. C.; NETO, B. A. D. "The Biginelli reaction with an imidazolium-tagged recyclable iron catalyst: kinetics, mechanism, and antitumoral activity" *Chem. Eur. J.*, **19**: 4156, 2013. (e) SHARMA, N.; SHARMA, U. K.; KUMAR, R.; RICHA, SINHA, A. K. "Green and recyclable glycine nitrate (GlyNO₃) ionic liquid triggered multicomponent Biginelli reaction for the efficient synthesis of dihydropyrimidinones" *RSC Adv.*, **2**:10648, 2012. (f) ZHU, C.; YANG, B.; ZHAO, Y.; FU, C.; TAO, L.; WEI, Y. "A new insight into the Biginelli reaction: the dawn of multicomponent click chemistry?" *Polym. Chem.*, **4**:5395, 2013.

55. MONDAL, J.; SEN, T.; BHAUMIK, A. "Fe₃O₄@mesoporous SBA-15: a robust and magnetically recoverable catalyst for one-pot synthesis of 3,4-dihydropyrimidin-2(1*H*)-ones via the Biginelli reaction". *Dalton Trans.*, **41**:6173, 2012.

56. KOLVARI, E.; KOUKABI, N.; ARMANDPOUR, O. "A simple and efficient synthesis of 3,4-dihydropyrimidin-2-(1*H*)-ones via Biginelli reaction catalyzed by nanomagnetic-supported sulfonic acid". *Tetrahedron* **70**:1383, 2014.

57. (a) NAZARI, S.; SAADAT, S.; FARD, P. K.; GORJIZADEH, M.; NEZHAD, E. R.; AFSHARI, M. "Imidazole functionalized magnetic Fe₃O₄ nanoparticles as a novel heterogeneous and efficient catalyst for synthesis of dihydropyrimidinones by Biginelli reaction". *Monatsh Chem* **144**:1877, 2013. (b) ZARNEGAR, Z.; SAFARI, J. "Magnetic nanoparticles supported imidazolium-based ionic liquids as nanocatalyst in microwave-mediated solvent-free Biginelli reaction" *J Nanopart Res.*, **16**:2509, 2014. (c) SAFARI, J.; ZARNEGAR, Z. "Brønsted acidic ionic liquid based magnetic nanoparticles: a new promoter for the Biginelli synthesis of 3,4-dihydropyrimidin-2(1*H*)-ones/thiones". *New J. Chem.*, **38**:358, 2014.

58. (a) GIRIJA, D.; NAIK, H. S. B.; KUMAR, B. V.; SUDHAMANI, C. N.; HARISH, K. N. "Fe₃O₄ nanoparticle supported Ni(II) complexes: A magnetically recoverable catalyst for Biginelli Reaction". *Arab. J. Chem.* doi:10.1016/j.arabjc.2014.08.008. (b) MOBINIKHALEDI, A.; FOROUGHIFAR, N.; KHAJEH-AMIRI, A. "1*N*-Propylcarbamothioyl benzamide complex of Bi(III) supported on superparamagnetic Fe₃O₄/SiO₂ nanoparticles as a highly efficient and magnetically recoverable heterogeneous nanocatalyst for the one-pot synthesis of 3,4-dihydropyrimidin-2(1*H*)-ones/thiones (DHPMs) via the Biginelli reaction". *Reac Kinet Mech Cat* **17**:59, 2016. (c) SHEYKHAN, M.; YAHYAZADEH, A.; RAHEMIZADEH, Z. "Cu-EDTA-modified APTMS-Fe₃O₄@SiO₂ core-shell nanocatalyst: a novel magnetic recoverable catalyst for the Biginelli reaction". *RSC Adv.*, **6**:34553, 2016. (d) SAFARI, J.; ZARNEGAR, Z. "Biginelli reaction on Fe₃O₄-MWCNT nanocomposite: excellent reactivity and facile recyclability of the catalyst combined with ultrasound irradiation". *RSC Advances*, **3**:17962, 2013. (e) WANG, A.; LIU, X.; SU, Z.; JING, H. "New magnetic nanocomposites of ZrO₂-Al₂O₃-Fe₃O₄ as green solid acid catalysts in organic reactions". *Catal. Sci. Technol.*, **4**:71, 2014. (f) NEZHAD, E. R.; ABBASI, Z.;

MOGHADDAM, M. R.; ATTAEI, M. A. "Ni²⁺ supported on hydroxyapatite-core@shell γ -Fe₂O₃ nanoparticles as new and green catalyst for the synthesis of 3,4-dihydropyrimidin-2(1H)-ones under solvent-free condition". *Iran. Chem. Commun.*, **1**:35, 2013.

59. (a) NOWAK, I.; ZIOLEK, M. "Niobium compounds: preparation, characterization, and application in heterogeneous catalysis" *Chem. Rev.*, **99**: 3603, 1999. (b) GARCÍA-SANCHO, C.; SÁDABA, I.; MORENO-TOST, R.; MÉRIDA-ROBLES, J.; SANTAMARÍA-GONZÁLEZ, J.; LÓPEZ-GRANADOS, M.; MAIRELES-TORRES, P. "Dehydration of xylose to furfural over MCM-41-supported niobium-oxide catalysts". *ChemSusChem*, **6**:635, 2013. (c) EKHSAN, J. M.; LEE, S. L.; NUR, H. "Niobium oxide and phosphoric acid impregnated silica–titania as oxidative-acidic bifunctional catalyst" *Appl. Catal. A-Gen.*, **471**:142, 2014. (d) TIOZZO, C.; BISIO, C.; CARNIATOAND, F.; GUIDOTTIA, M. "Grafted non-ordered niobium-silica materials: Versatile catalysts for the selective epoxidation of various unsaturated fine chemicals". *Catal. Today* **235**:49, 2014. (e) CHAGAS, P.; OLIVEIRA, H. S.; MAMBRINI, R.; HYARIC, M. L.; ALMEIDA, M. V.; OLIVEIRA, L. C. A. "A novel hydrofobic niobium oxyhydroxide as catalyst: Selective cyclohexene oxidation to epoxide" *Appl. Catal. A-Gen.* **454**:88, 2013.

60. (a) MARIN, M. L.; HALLETT-TAPLEY, G. L.; IMPELLIZZERI, S.; FASCIANI, C.; SIMONCELLI, S.; NETTO-FERREIRA, J. C.; SCAIANO, J. C. "Synthesis, acid properties and catalysis by niobium oxide nanostructured materials". *Catal. Sci. Technol.*, **4**: 3044, 2014. (b) USHIKUBO, T.; IIZUKA, T.; HATTORI, H.; TANABE, K. "Preparation of highly acidic hydrated niobium oxide". *Catal. Today* **16**:291, 1993. (c) ARMAROLI, T.; BUSCA, G.; CARLINI, C.; GIUTTARI, M.; GALLETTIB, A. M. R.; SBRANA, G. "Acid sites characterization of niobium phosphate catalysts and their activity in fructose dehydration to 5-hydroxymethyl-2-furaldehyde". *J. Mol. Cat. A-Chem.* **151**: 233, 2000. (d) TANABE, K. "Niobic acid as an unusual acidic solid material". *Mater. Chem. Phys.*, **17**:217, 1987.

61. Arpini, B. H.; Bartolomeu, A. A.; Andrade, C. K. Z.; Silva-Filho, L. C.; Lacerda, V. "Recent Advances in Using Niobium Compounds as Catalysts in Organic Chemistry". *Curr. Org. Synth.*, **12**:570, 2015.

62. ALVIM, H. G. O.; LIMA, T. B.; OLIVEIRA, A. L.; OLIVEIRA, H. C. B.; SILVA, F. M.; GOZZO, F. C.; SOUZA, R. Y.; SILVA, W. A.; NETO, B. A. D. "Facts, presumptions, and myths on the solvent-free and catalyst-free Biginelli reaction. What is catalysis for?" *J. Org. Chem.*, **79**:3383, 2014.

63. STADLER, A.; KAPPE, C.O. "Microwave-mediated Biginelli reactions revisited. On the nature of rate and yield enhancements" *J. Chem. Soc. Perkin Trans.* **2**:1363, 2000.

64. (a) KAPPE, C. O. "A reexamination of the mechanism of the Biginelli dihydropyrimidine synthesis. Support for an N-acyliminium ion intermediate" *J. Org. Chem.*, **62**:7201, 1997. (b) SWEET, F.; FISSEKIS, J. D. "Synthesis of 3, 4-dihydro-2 (1H)-pyrimidinones and the mechanism of the Biginelli reaction". *J. Am. Chem. Soc.*, **95**:8741, 1973. (c) SOUZA, R. O. M. A.; PENHA, E. T.; MILAGRE, H. M. S.; GARDEN, S. J.; ESTEVES, P. M.; EBERLIN, M. N.; ANTUNES, O. A. C. "The three-Component Biginelli Reaction: a combined experimental and theoretical mechanistic investigation". *Chem. Eur. J.*, **15**: 9799, 2009.

65. LIMA, C. G. S.; SILVA, S.; GONÇALVES, R. H.; LEITE, E. R.; SCHWAB, R. S.; CORRÊA, A. G.; PAIXÃO, M. W. "Highly Efficient and Magnetically Recoverable Niobium Nanocatalyst for the Multicomponent Biginelli Reaction". *ChemCatChem*, **6**:3455, 2014.

- 66.** SPEIGHT, J. G. *An Introduction to Petroleum Technology, Economics, and Politics*, 1st ed., Hoboken, John Wiley & Sons, 2011.
- 67.** (a) CORTRIGHT, R. D.; DAVDA, R. R.; DUMESIC, J. A. "Hydrogen from catalytic reforming of biomass-derived hydrocarbons in liquid water". *Nature*, **418**:964, 2002. (b) HUBER, G. W.; CHHEDA, J. N.; BARRETT, C. J.; DUMESIC, J. A. "Production of liquid alkanes by aqueous-phase processing of biomass-derived carbohydrates". *Science*, **308**:1446, 2005. (c) ROMÁN-LESHKOV, Y.; BARRETT, C. J.; LIU, Z. Y.; DUMESIC, J. A. "Production of dimethylfuran for liquid fuels from biomass-derived carbohydrates". *Nature*, **447**:982, 2007. (d) CHHEDA, J. N.; HUBER, G. W.; DUMESIC, J. A. "Liquid-phase catalytic processing of biomass-derived oxygenated hydrocarbons to fuels and chemicals". *Angew. Chem. Int. Ed.*, **46**:7164, 2007 (e) SERRANO-RUIZ, J. C.; LUQUE, R.; SEPÚLVEDA-ESCRIBANO, A. "Transformations of biomass-derived platform molecules: from high added-value chemicals to fuels via aqueous-phase processing". *Chem. Soc. Rev.*, **40**:5266, 2011. (f) CLIMENT, M. J.; CORMA, A.; IBORRA, S. "Conversion of biomass platform molecules into fuel additives and liquid hydrocarbon fuels". *Green Chem.*, **16**:516, 2014.
- 68.** ALONSO, D. M.; BOND, J. Q.; DUMESIC, J. A. "Catalytic conversion of biomass to biofuels" *Green Chem.*, **12**:1493, 2010.
- 69.** LEE, J. W. *Advanced Biofuels and Bioproducts*, 1st ed, New York, Springer-Verlag, 2013.
- 70.** WERTZ, J.-L.; BÉDUÉ, O. *Lignocellulosic Biorefineries*, 1st ed, Lausanne, EPFL Press, 2013.
- 71.** MOHAN, D.; PITTMAN JR., C. U.; STEELE, P. H. "Pyrolysis of wood/biomass for bio-oil: a critical review". *Energy & Fuels*, **20**:848, 2006.
- 72.** (a) MOSIER, N.; WYMAN, C. E.; DALE, B. E.; ELANDER, R. T.; LEE, Y. Y.; HOLTZAPPLE, M.; LADISCH, M. R. "Features of promising technologies for pretreatment of lignocellulosic biomass". *Bioresour. Technol.*, **96**:673, 2005. (b) CHAKAR, F. S.; RAGAUSKAS, A. J. "Review of current and future softwood kraft lignin process chemistry". *Ind. Crops Prod.*, **20**:131, 2004.
- 73.** (a) THAKUR, V. K.; THAKUR, M. K.; RAGHAVAN, P.; KESSLER, M. R. "Progress in green polymer composites from lignin for multifunctional applications: a review" *ACS Sustainable Chem. Eng.* **2**:1072, 2014. (b) AZADI, P.; INDERWILDI, O. R.; FARNOOD, R.; KING, D. A. "Liquid fuels, hydrogen and chemicals from lignin: a critical review". *Renew. Sust. Energ. Rev.* **21**:506, 2013.
- 74.** (a) WYMAN, C. E.; DALE, B. E.; ELANDER, R. T.; HOLTZAPPLE, M.; LADISCH, M. R.; LEE, Y. Y. "Comparative sugar recovery data from laboratory scale application of leading pretreatment technologies to corn stover". *Bioresour. Technol.*, **96**:2026, 2005. (b) LLOYD, T. A.; WYMAN, C. E. "Combined sugar yields for dilute sulfuric acid pretreatment of corn stover followed by enzymatic hydrolysis of the remaining solids". *Bioresour. Technol.*, **96**:1967, 2005.
- 75.** MARTIN, A. M. *Bioconversion of Waste Materials to Industrial Products*, 1st ed, New York, Springer-Verlag, 1998.

- 76.** (a) WANG, T.; NOLTE, M. W.; SHANKS, B. H. "Catalytic dehydration of C₆ carbohydrates for the production of hydroxymethylfurfural (HMF) as a versatile platform chemical" *Green Chem.*, **16**:548, 2014. (b) CHHEDA, J. N.; DUMESIC, J. A. "An overview of dehydration, aldol-condensation and hydrogenation processes for production of liquid alkanes from biomass-derived carbohydrates" *Catal. Today*, **123**:59, 2007.
- 77.** (a) RACKEMANN, D. W.; DOHERTY, W. O. S. "The conversion of lignocellulosics to levulinic acid" *Biofuels, Bioprod. Bioref.* **5**:198, 2011. (b) LEONARD, R. H. "Levulinic acid as a basic chemical raw material". *Ind. Eng. Chem.*, **48**:1330, 1956. (c) Timokhin, B. V.; Baransky, V A.; Eliseeva, G. D. "Levulinic acid in organic synthesis" *RUSS. CHEM. REV.*, **68**:73, 1999.
- 78.** DÉMOLIS, A.; ESSAYEM, N.; RATABOUL, F. "Synthesis and applications of alkyl levulinates". *ACS Sustainable Chem. Eng.*, **2**:1338, 2014.
- 79.** ALONSO, D. M.; WETTSTEIN, S. G.; DUMESIC, J. A. "Gamma-valerolactone, a sustainable platform molecule derived from lignocellulosic biomass". *Green Chem.*, **15**:584, 2013.
- 80.** ROSATELLA, A. A.; SIMEONOV, S. P.; FRADE, R. F. M.; AFONSO, C. A. M. "5-Hydroxymethylfurfural (HMF) as a building block platform: biological properties, synthesis and synthetic applications" *Green Chem.*, **13**:754, 2011.
- 81.** (a) LANGE, J. P.; VAN DE GRAAF, W.D.; HAAN, R. J. "Conversion of furfuryl alcohol into ethyl levulinate using solid acid catalysts". *ChemSusChem*, **2**:437, 2009. (b) YAN, K.; CHEN, A. "Selective hydrogenation of furfural and levulinic acid to biofuels on the ecofriendly Cu-Fe catalyst". *Fuel*, **115**:101, 2014. (c) KIJEŃSKI, J.; WINIAREK, P.; PARYJCZAK, T.; LEWICKI, A.; MIKOŁAJSKA, A. "Platinum deposited on monolayer supports in selective hydrogenation of furfural to furfuryl alcohol". *Appl. Catal. A:Gen.*, **233**:171, 2002. (d) JAE, J.; ZHENG, W.; LOBO, R. F.; VLACHOS, D. G. "Production of dimethylfuran from hydroxymethylfurfural through catalytic transfer hydrogenation with ruthenium supported on carbon". *ChemSusChem*, **6**:1158, 2013. (e) PANAGIOTOPOULOU, P.; MARTIN, N.; VLACHOS, D. G. "Effect of hydrogen donor on liquid phase catalytic transfer hydrogenation of furfural over a Ru/RuO₂/C catalyst". *J. Mol. Catal. A-Chem.*, **392**:223, 2014. (f) CHIA, M.; DUMESIC, J. A. "Liquid-phase catalytic transfer hydrogenation and cyclization of levulinic acid and its esters to γ -valerolactone over metal oxide catalysts". *Chem. Commun.*, **47**:12233, 2011.
- 82.** BUI, L.; LUO, H.; GUNTHER, W. R.; ROMÁN-LESHKOV, W. "Domino reaction catalyzed by zeolites with Brønsted and Lewis acid sites for the production of γ -valerolactone from furfural". *Angew. Chem.* **125**:8180, 2013.
- 83.** (a) YAN, Z.; LIN, L.; LIU, S. "Synthesis of γ -valerolactone by hydrogenation of biomass-derived levulinic acid over Ru/C catalyst" *Energ. Fuel.*, **23**:3853, 2009. (b) GALLETTI, A. M. R.; ANTONETTI, C.; DE LUISE, V.; MARTINELLI, M. "A sustainable process for the production of γ -valerolactone by hydrogenation of biomass-derived levulinic acid". *Green Chem.*, **14**:688, 694. (c) UPARE, P. P.; LEE, J.-M.; HWANG, D. W.; HALLIGUDI, S. B.; HWANG, Y. K.; CHANG, J.-S. "Selective hydrogenation of levulinic acid to γ -valerolactone over carbon-supported noble metal catalysts". *J. Ind. Eng. Chem.*, **17**:287, 287. (d) HENGNE, A. M.; RODE, C. V. "Cu-ZrO₂ nanocomposite catalyst for selective hydrogenation of levulinic acid and its ester to γ -valerolactone". *Green Chem.*, **14**:1064, 2012. (e)

WETTSTEIN, S. G.; BOND, J. Q.; ALONSO, D. M.; PHAM, H. N.; DATYE, A. K.; DUMESIC, J. A. "RuSn bimetallic catalysts for selective hydrogenation of levulinic acid to γ -valerolactone". *Appl. Catal. B-Environ.*, **117-118**:321, 2012. (f) LI, W.; XIE, J.-H.; LINA, H.; ZHOU, Q.-L. "Highly efficient hydrogenation of biomass-derived levulinic acid to γ -valerolactone catalyzed by iridium pincer complexes". *Green Chem.*, **14**:2388, 2012. (g) DENG, L.; ZHAO, Y.; LI, J.; FU, Y.; LIAO, B.; GUO, Q.-X. "Conversion of levulinic acid and formic acid into γ -valerolactone over heterogeneous catalysts". *ChemSusChem*, **3**:1172, 2010.

84. HORVAT, J.; KLAIĆ, B.; METELKO, B.; ŠUNJIĆ, V. "Mechanism of levulinic acid formation". *Tetrahedron Lett.*, **26**:2111, 1985.

85. (a) GILKEY, M. J.; XU, B. "Heterogeneous catalytic transfer hydrogenation as an effective pathway in biomass upgrading". *ACS Catal.*, **6**:1420, 2016. (b) WANG, D.; ASTRUC, D. "The golden age of transfer hydrogenation". *Chem. Rev.*, **115**:6621, 2015.

86. HENGNE, A. M.; KAMBLE, S. B.; RODE, C. V. "Single pot conversion of furfuryl alcohol to levulinic esters and γ -valerolactone in the presence of sulfonic acid functionalized ILs and metal catalysts". *Green Chem.*, **15**:2540, 2013.

87. CHEN, B.; LI, F.; HUANG, Z.; LU, T.; YUAN, Y.; YUAN, G. "Integrated catalytic process to directly convert furfural to levulinate ester with high selectivity". *ChemSusChem*, **7**:202, 2014.

88. (a) DENG, L.; LI, J.; LAI, D. M.; FU, Y.; GUO, Q. X. "Catalytic conversion of biomass-derived carbohydrates into γ -valerolactone without using an external H₂ supply". *Angew. Chem. Int. Ed.*, **48**:6529, 2009. (b) DU, X.-L.; HE, L.; ZHAO, S.; LIU, Y.-M.; CAO, Y.; HE, H.-Y.; FAN, K.-N. "Hydrogen-independent reductive transformation of carbohydrate biomass into γ -valerolactone and pyrrolidone derivatives with supported gold catalysts". *Angew. Chemie*, **123**:7961, 2011. (c) QI, L.; HORVÁTH, I. T. "Catalytic conversion of fructose to γ -valerolactone in γ -valerolactone" *ACS Catal.*, **2**:2247, 2012. (d) YUAN, J.; LI, S.; YU, L.; LIU, Y.; CAO, Y.; HE, H.; FAN, K.-N. "Copper-based catalysts for the efficient conversion of carbohydrate biomass into γ -valerolactone in the absence of externally added hydrogen". *Energy Environ. Sci.*, **6**:3308, 2013 (e) CUI, J.; TAN, J.; DENG, T.; CUI, X.; ZHENG, H.; ZHU, Y.; LI, Y. "Direct conversion of carbohydrates to γ -valerolactone facilitated by a solvent effect". *Green Chem.*, **17**:3084, 2015. (f) ZHOU, H.; SONG, J.; KANG, X.; HU, J.; YANG, Y.; FAN, H.; MENG, Q.; HAN, B. "One-pot conversion of carbohydrates into gamma-valerolactone catalyzed by highly cross-linked ionic liquid polymer and Co/TiO₂". *RSC Adv.*, **5**:15267, 2015.

89. (a) AUERBACH, S. M.; CARRADO, K. A.; DUTTA, P. K. *Handbook of Zeolite Science and Technology*, Boca Raton, CRC Press, 2003. (b) XU, R.; PANG, W.; YU, J.; HUO, Q.; CHEN, J. *Chemistry of Zeolites and Related Porous Materials: Synthesis and Structure*, 1st ed, Hoboken, John Wiley & Sons, 2007. (c) CEJKA, J.; CORMA, A.; ZONES, S. *Zeolites and Catalysis: Synthesis, Reactions and Applications*, 1st ed, John Wiley & Sons, 2010.

90. KAMIMURA, Y.; TANAHASHI, S.; ITABASHI, K.; SUGAWARA, A.; WAKIHARA, T.; SHIMOJIMA, A.; OKUBO, TATSUYA. "Crystallization behavior of zeolite beta in OSDA-free, seed-assisted synthesis". *J. Phys. Chem. C*, **115**:744, 2011.

- 91.** (a) YU, Z.; LI, S.; WANG, Q.; ZHENG, A.; JUN, X.; CHEN, L.; DENG, F. “Brønsted/Lewis acid synergy in H-ZSM-5 and H-MOR zeolites studied by ^1H and ^{27}Al DQ-MAS solid-state NMR spectroscopy”. *J. Phys. Chem. C*, **115**:22320, 2011. (b) LONYI, F.; VALYON, J. “On the interpretation of the NH_3 -TPD patterns of H-ZSM-5 and H-modernite”. *Micropor. Mesopor. Mater.*, **47**:293, 2001. (c) COSTER, D.; BLUMENFELD, A. L.; FRIPIAT, J. J. “Lewis acid sites and surface aluminum in aluminas and zeolites: a high-resolution NMR study”. *J. Phys. Chem.*, **98**:6201, 1994. (d) CHUKIN, G. D.; KULIKOV, A. S.; SERGIENKO, S. A. “Nature of Lewis acidity in H-zeolites”. *React. Kinet. Catal. L*, **27**:287, 1985.
- 92.** (a) NADGERI, J. M.; HIYOSHI, N.; YAMAGUCHI, A.; SATO, O.; SHIRAI, M. “Liquid phase hydrogenation of methyl levulinate over the mixture of supported ruthenium catalyst and zeolite in water”. *Appl. Catal. A-Gen.*, **470**:215, 2014. (b) LUO, H. Y.; CONSOLI, D. F.; GUNTHER, W. R.; ROMÁN-LESHKOV, Y. “Investigation of the reaction kinetics of isolated Lewis acid sites in Beta zeolites for the Meerwein–Ponndorf–Verley reduction of methyl levulinate to γ -valerolactone” *J. Catal.*, **320**:198, 2014. (c) WANG, J.; JAENICKEA, S.; CHUAH, G.-K. “Zirconium–Beta zeolite as a robust catalyst for the transformation of levulinic acid to γ -valerolactone via Meerwein–Ponndorf–Verley reduction”. *RSC Adv.*, **4**:13481, 2014.
- 93.** CAO, Q.; GUAN, J.; PENG, G.; HOU, T.; ZHOU, J.; MU, X. “Solid acid-catalyzed conversion of furfuryl alcohol to alkyl tetrahydrofurfuryl ether” *Catal. Commun.*, **58**:76, 2015.
- 94.** MELLMER, M. A.; GALLO, J. M. R.; ALONSO, D. M.; DUMESIC, J. A. “selective production of levulinic acid from furfuryl alcohol in THF solvent systems over H-ZSM-5” *ACS Catal.*, **5**:3354, 2015.
- 95.** (a) LV, Q.; LI, G.; LU, H.; CAI, W.; HUANG, H.; CHENG, C. “Preparation of magnetic zeolite $\gamma\text{-Fe}_2\text{O}_3/\text{TS-1}$ with core/shell structure and application in photocatalytic degradation”. *Microporous Mesoporous Mater.*, **203**:202, 2015. (b) LIU, J.; SUN, Z.; DENG, Y.; ZOU, Y.; LI, C.; GUO, X.; XIONG, L.; GAO, Y.; LI, F.; ZHAO, D. “Highly water-dispersible biocompatible magnetite particles with low cytotoxicity stabilized by citrate groups”. *Angew. Chem. Int. Ed.*, **48**:5875, 2009.
- 96.** (a) HATTORI, H.; ONO, Y. *Solid Acid Catalysis: From Fundamentals to Applications*, 1st ed., Boca Raton, CRC Press, 2015. (b) BHATIA, S. *Zeolite Catalysts: Principles and Applications*, Boca Raton, CRC Press, 1989. (c) LERCHER, J. A.; GRUNDLING, C.; EDER-MIRTH, G. Infrared studies of the surface acidity of oxides and zeolites using adsorbed probe molecules. *Catal. Today*, **27**:353, 1996.
- 97.** (a) JIN, F.; LI, Y. “A FTIR and TPD examination of the distributive properties of acid sites on ZSM-5 zeolite with pyridine as a probe molecule”. *Catal. Today*, **145**:101, 2009. (b) BUZZONI, R.; BORDIGA, S.; RICCHIARDI, G.; LAMBERTI, C.; ZECCHINA, A. “Interaction of Pyridine with Acidic (H-ZSM5, H- β , H-MORD Zeolites) and Superacidic (H-Nafion Membrane) Systems: An IR Investigation”. *Langmuir*, **12**:930, 1996.
- 98.** (a) YOSHIDA, Y.; LANGOUCHE, G. *Mössbauer Spectroscopy*, 1st ed, New York, Springer-Verlag, 2013. (b) SHARMA, V. K.; KLINGELHÖFER, G.; NISHIDA, T. *Mössbauer Spectroscopy: Applications in Chemistry, Biology, and Nanotechnology*, 1st ed, Hoboken, John Wiley & Sons, 2013.

- 99.** TUCEK, J.; ZBORIL, R.; PETRIDIS, D. J. “Maghemite nanoparticles by view of Mössbauer spectroscopy” *Nanosci. Nanotechnol.*, **6**:926, 2006.
- 100.** N. N. GREENWOOD AND T. C. GIBB, *Mössbauer Spectroscopy*, Chapman and Hall Ltd, London, 1971.
- 101.** (a) CORMA, A.; DOMINE, M. E.; NEMETH, L.; VALENCIA, S. “Al-free Sn-Beta zeolite as a catalyst for the selective reduction of carbonyl compounds (Meerwein-Ponndorf-Verley reaction)”. *J. Am. Chem. Soc.*, **124**:3194, 2002. (b) CORMA, A.; DOMIN, M. E.; VALENCIA, S. “Water-resistant solid Lewis acid catalysts: Meerwein–Ponndorf–Verley and Oppenauer reactions catalyzed by tin-beta zeolite”. *J. Catal.*, **215**:294, 2003. (c) J. JAE, ZHENG, W.; LOBO, R. F.; VLACHOS, D. G. “Production of dimethylfuran from hydroxymethylfurfural through catalytic transfer hydrogenation with ruthenium supported on carbon”. *ChemSusChem*, **6**:1158, 2013.
- 102.** ENNAERT, T.; VAN AELST, J.; DIJKMANS, J.; DE CLERCQ, R.; SCHUTYSER, W.; DUSSELIER, M.; VERBOEKEND, D.; SELS, B. F. “Potential and challenges of zeolite chemistry in the catalytic conversion of biomass”. *Chem. Soc. Rev.*, **45**:584, 2016.
- 103.** (a) JUN, K. W.; LEE, H. S.; ROH, H. S.; PARK, S. E. “Highly water-enhanced H-ZSM-5 catalysts for dehydration of methanol to dimethyl ether”. *Bull. Korean Chem. Soc.*, **24**:106, 2003. (b) GAYUBO, A. G.; AGUAYO, A. T.; ATUTXA, A.; VALLE, B.; BILBAO. “Regeneration of a HZSM-5 zeolite catalyst deactivated in the transformation of aqueous ethanol into hydrocarbons”. *J. Catal. Today*, **107-108**:410, 2005. (c) BLEKEN, F. L.; BARBERA, K.; BONINO, F.; OLSBYE, U.; LILLERUD, K. P.; BORDIGA, S.; BEATO, P.; JANSSENS, T. V. W.; SVELLE, S. “Catalyst deactivation by coke formation in microporous and desilicated zeolite H-ZSM-5 during the conversion of methanol to hydrocarbons” *J. Catal.*, **307**:62, 2013.
- 104.** SING, K.S.W.; EVERETT, D.H.; HAUL, R.A.W.; MOSCOU, L.; PIEROTTI, R.A.; ROUQUEROL, J.; SIEMIENIEWSKA, T. “Physical and biophysical chemistry division commission on colloid and surface chemistry including catalysis”. *Pure Appl. Chem.*, **57**:603, 1985.
- 105.** (a) TAGUCHI, A.; SCHÜTH, F. “Ordered mesoporous materials in catalysis”. *Micropor. Mesopor. Mater.*, **77**:1, 2005. (b) PEREGO, C.; MILLINI, R. “Porous materials in catalysis: challenges for mesoporous materials”. *Chem. Soc. Rev.*, **42**:3956, 2013. (c) PAL, N.; BHAUMIK, A. “Mesoporous materials: versatile supports in heterogeneous catalysis for liquid phase catalytic transformations”. *RSC Adv.*, **5**:24363, 2015.
- 106.** DU, X.; QIAO, S. Z. “Dendritic silica particles with center-radial pore channels: promising platforms for catalysis and biomedical applications”. *Small*, **11**:392, 2015.
- 107.** SHI, X.; WU, Y.; LI, P.; YI, H.; YANG, M.; WANG, G. “Catalytic conversion of xylose to furfural over the solid acid $\text{SO}_4^{2-}/\text{ZrO}_2\text{-Al}_2\text{O}_3/\text{SBA-15}$ catalysts”. *Carbohydrate Res.*, **346**:480, 2011.
- 108.** SHI, X.; WU, Y.; YI, H.; RUI, G.; LI, P.; YANG, M.; WANG, G. “Selective preparation of furfural from xylose over sulfonic acid functionalized mesoporous SBA-15 materials”. *Energies*, **4**:669, 2011.

- 109.** AGIRREZABAL-TELLERIA, I.; REQUIES, J.; GÜEMEZ, M.B.; ARIAS, P.L. “Pore size tuning of functionalized SBA-15 catalysts for the selective production of furfural from xylose”. *Applied Catal. B- Environ.*, **115-116**:169, 2012.
- 110.** YU, W.; TANG, Y.; MO, L.; CHEN, P.; LOU, H.; ZHENG, X. “Bifunctional Pd/Al-SBA-15 catalyzed one-step hydrogenation–esterification of furfural and acetic acid: A model reaction for catalytic upgrading of bio-oil”. *Catal. Commun.*, **13**:35, 2011.
- 111.** (a) VARGAS-HERNÁNDEZ, D.; RUBIO-CABALLERO, J. M.; SANTAMARÍA-GONZÁLEZ, J.; MORENO-TOST, R.; MÉRIDA-ROBLES, J. M.; PÉREZ-CRUZA, M. A.; JIMÉNEZ-LÓPEZ, A.; HERNÁNDEZ-HUESCA, R.; MAIRELES-TORRES, P. “Furfuryl alcohol from furfural hydrogenation over copper supported on SBA-15 silica catalysts”. *J. Mol. Catal. A*, **383-384**:106, 2014. (b) AUDEMAR, M.; CIOTONEA, C.; VIGIER, K. D. O.; ROYER, S.; UNGUREANU, A.; DRAGOI, B.; DUMITRIU, E.; JÉRÔME, F. “Selective hydrogenation of furfural to furfuryl alcohol in the presence of a recyclable cobalt/SBA-15 catalyst”. *ChemSusChem*, **8**:1885, 2015.
- 112.** (a) ILIOPOULOU, E. F.; ANTONAKOU, E. V.; KARAKOULIAC, S.A.; VASALOS, I.A.; LAPPAS, A.A.; TRIANTAFYLIDIS, K.S. Catalytic conversion of biomass pyrolysis products by mesoporous materials: effect of steam stability and acidity of Al-MCM-41 catalysts”. *Chem. Eng. J.*, **134**:51, 2007. (b) ADAM, J.; BLAZSÓ, M.; MÉSZÁROS, E.; STÖCKER, M.; NILSEN, M. H.; BOUZGA, A.; HUSTADA, J. E.; GRØNLIA, M.; ØYED, G. “Pyrolysis of biomass in the presence of Al-MCM-41 type catalysts”. *Fuel*, **84**:1494, 2005. (c) ANTONAKOU, E.; LAPPAS, A.; NILSEN, M. H.; BOUZGA, A.; STÖCKER, M. “Evaluation of various types of Al-MCM-41 materials as catalysts in biomass pyrolysis for the production of bio-fuels and chemicals”. *Fuel*, **85**:2202, 2006.
- 113.** ZHANG, J.; ZHUANG, J.; LIN, L.; LIU, S.; ZHANG, Z. “Conversion of D-xylose into furfural with mesoporous molecular sieve MCM-41 as catalyst and butanol as the extraction phase”. *Biomass Bioenerg.* **39**:73, 2012.
- 114.** (a) JIMÉNEZ-MORALES, I.; MORENO-RECIO, M.; SANTAMARÍA-GONZÁLEZ, J.; MAIRELES-TORRES, P. J. “Production of 5-hydroxymethylfurfural from glucose using aluminium doped MCM-41 silica as acid catalyst”. *Appl. Catal. B-Environ.* **164**:70, 2015. (b) LIU, A.; ZHANG, Z.; FANG, Z.; LIU, B.; HUANG, K. J. “Synthesis of 5-ethoxymethylfurfural from 5-hydroxymethylfurfural and fructose in ethanol catalyzed by MCM-41 supported phosphotungstic acid”. *Ind. Eng. Chem.* **20**:1977, 2014.
- 115.** CHERMAHINI, A. N.; SHAHANGI, F.; DABBAGHA, H. A.; SARAJIA, M. “Production of 5-hydroxymethylfurfural from fructose using a spherically fibrous KCC-1 silica catalyst”. *RSC Adv.*, **6**:3380, 2016.
- 116.** (a) XIONG, Y.; ZHANG, Z.; WANG, X.; LIU, B.; LIN, J. “Hydrolysis of cellulose in ionic liquids catalyzed by a magnetically-recoverable solid acid catalyst”. *Chem. Eng. J.* **235**:349, 2014. (b) TAKAGAKI, A.; NISHIMURA, M.; NISHIMURA, S.; EBITANI, K. “Hydrolysis of sugars using magnetic silica nanoparticles with sulfonic acid groups”. *Chem. Letters*, **40**:1195, 2011.
- 117.** CHEN, J.; LI, K.; CHEN, L.; LIU, R.; HUANG, X.; YE, D. “Conversion of fructose into 5-hydroxymethylfurfural catalyzed by recyclable sulfonic acid-functionalized metal–organic frameworks”. *Green Chem.*, **16**:2490, 2014.

- 118.** UPARE, P. P.; YOON, J.-W.; KIM, M. Y.; KANG, H.-Y.; HWANG, D. W.; HWANG, Y. K.; KUNG, H. H.; CHANG, J.-S. “Chemical conversion of biomass-derived hexose sugars to levulinic acid over sulfonic acid-functionalized graphene oxide catalysts”. *Green Chem.*, **15**:2935, 2013.
- 119.** (a) TANABE, K.; HATTORI, H.; YAMAGUCHI, T. “Surface properties of solid superacids”. *Crit. Rev. Surf. Chem.*, **1**:1, 1990. (b) HUA, W.; YUE, Y.; GAO, Z. “Acidity enhancement of SBA mesoporous molecular sieve by modification with $\text{SO}_4^{2-}/\text{ZrO}_2$ ”. *J. Mol. Catal. A: Gen.*, **170**:195, 2001.
- 120.** SHEN, D.; YANG, J.; LI, X.; ZHOU, L.; ZHANG, R.; LI, W.; CHEN, L.; WANG, R.; ZHANG, F.; ZHAO, D. “Biphase stratification approach to three-dimensional dendritic biodegradable mesoporous silica nanospheres”. *Nano Lett.*, **14**:923, 2014.
- 121.** PIREZ, C.; LEE, A. F.; MANAYIL, J. C.; PARLETT, C. M. A.; WILSON, K. “Hydrothermal saline promoted grafting: a route to sulfonic acid SBA-15 silica with ultra-high acid site loading for biodiesel synthesis”. *Green Chem.*, **16**:4506, 2014.
- 122.** RUSSO, P. A.; ANTUNES, M. M.; NEVES, P.; WIPER, P. V.; FAZIO, E.; NERI, F.; BARRECA, F.; MAFRA, L.; PILLINGER, M.; PINNA, N.; VALENTE, A. A. J. “Solid acids with SO_3H groups and tunable surface properties: versatile catalysts for biomass conversion”. *Mater. Chem. A*, **2**:11813, 2014.
- 123.** (a) HAMOUDI, S.; KALIAGUINE, S. “Sulfonic acid-functionalized periodic mesoporous organosilica”. *Micropor. Mesopor. Mat.*, **59**:195, 2003. (b) Zhang, X.; Zhao, Y.; Xu, S.; Yang, Y.; Liu, J.; Wei, Y.; Yang, Q. “Polystyrene sulphonic acid resins with enhanced acid strength via macromolecular self-assembly within confined nanospace”. *Nat. Commun.*, **5**:3170, 2014.

Appendices

Appendix 1:
 ^1H NMR and ^{13}C NMR spectra of the DHMP products

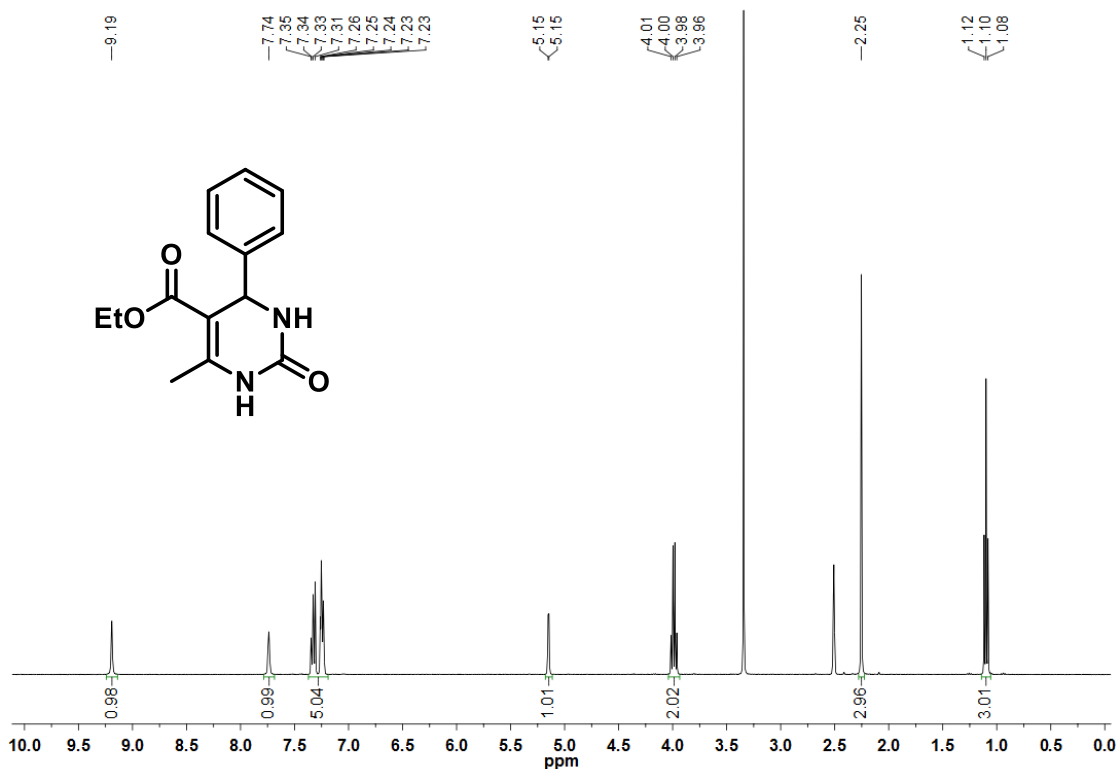


FIGURE A1 - ^1H -NMR spectrum of compound 2.37a.

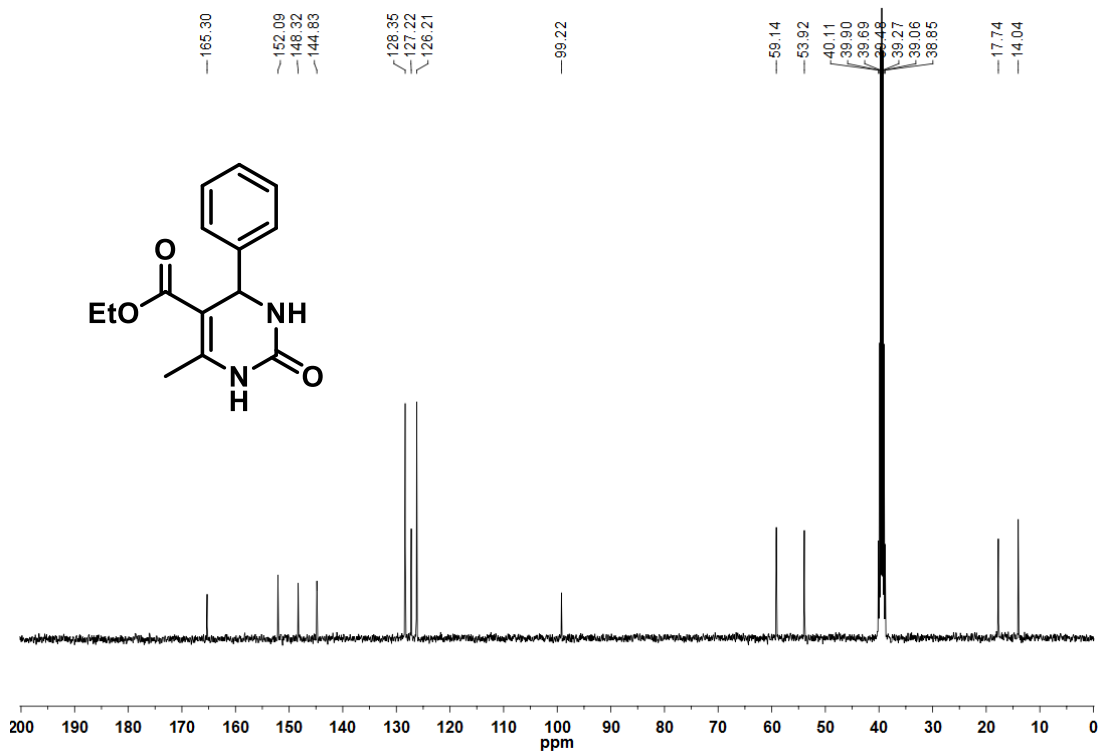


FIGURE A2 - ^{13}C -NMR spectrum of compound 2.37a.

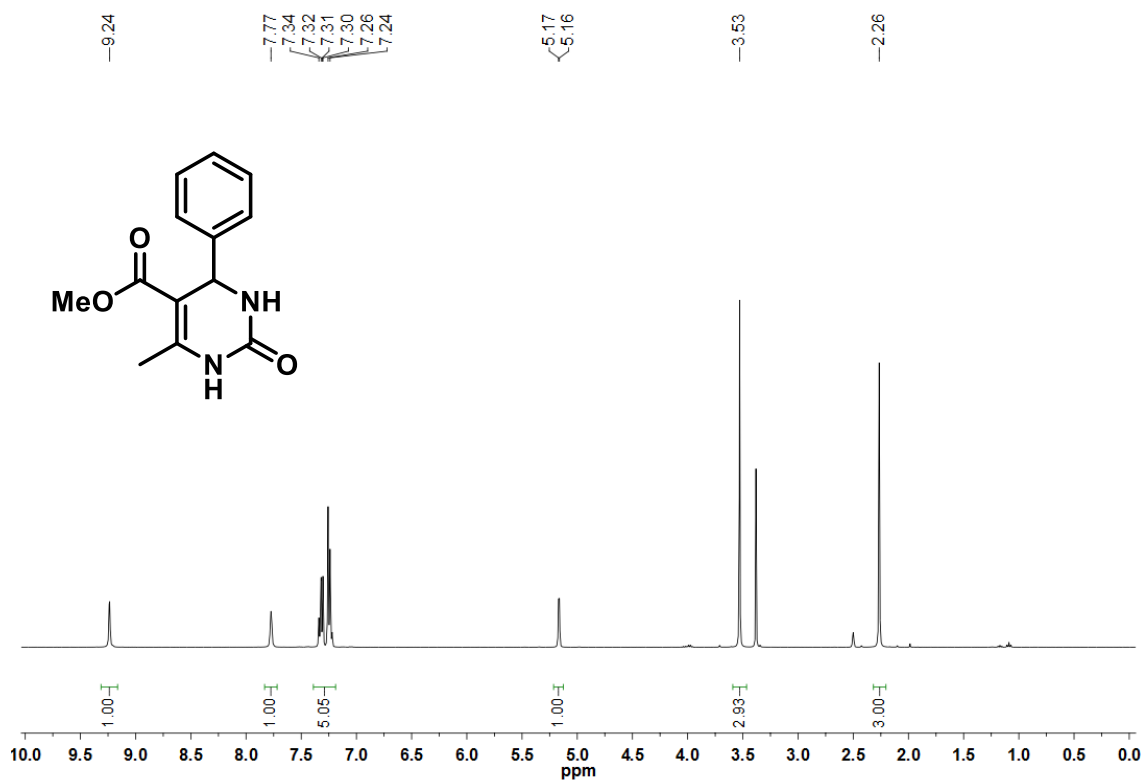


FIGURE A3 - $^1\text{H-NMR}$ spectra of compound **2.37b**.

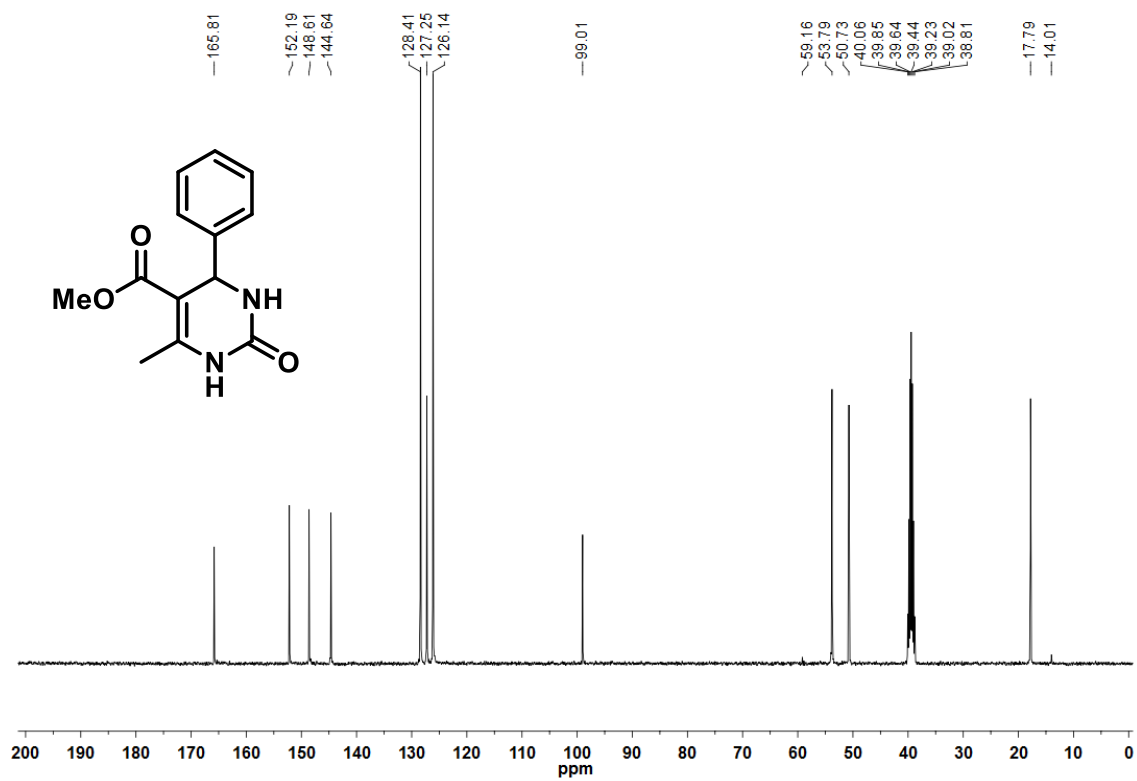


FIGURE A4 - $^{13}\text{C-NMR}$ spectra of compound **2.37b**.

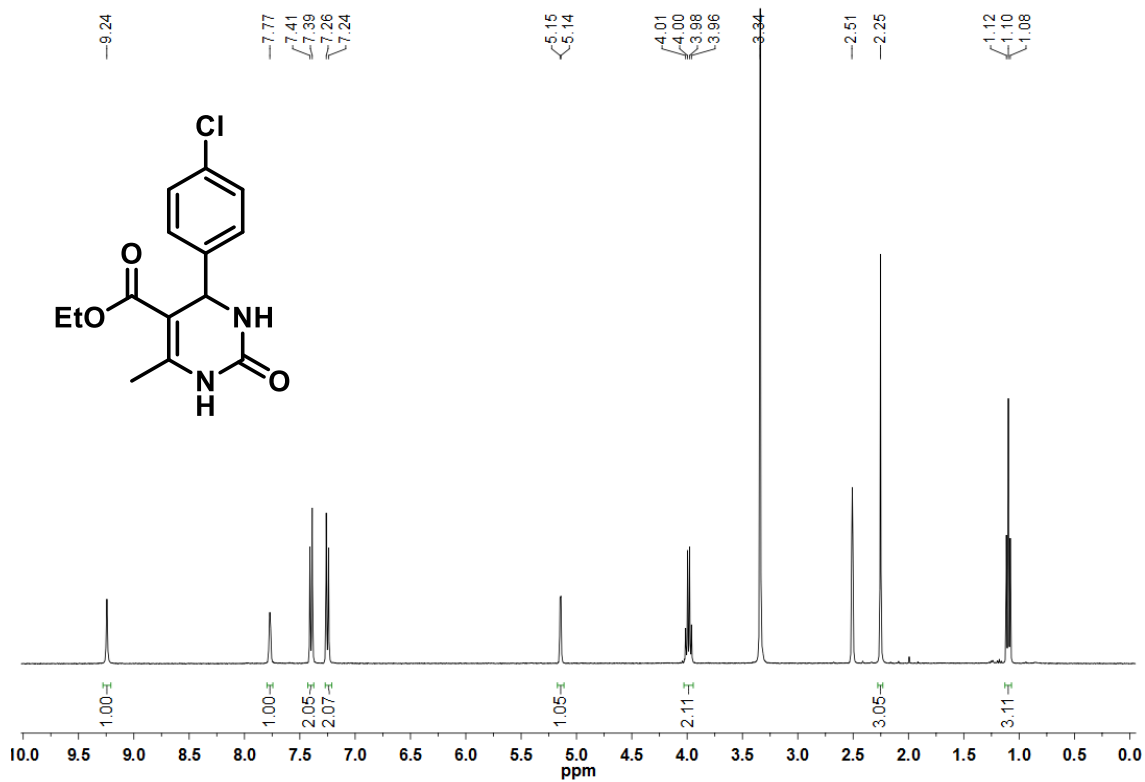


FIGURE A5 - $^1\text{H-NMR}$ spectrum of compound **2.37c**.

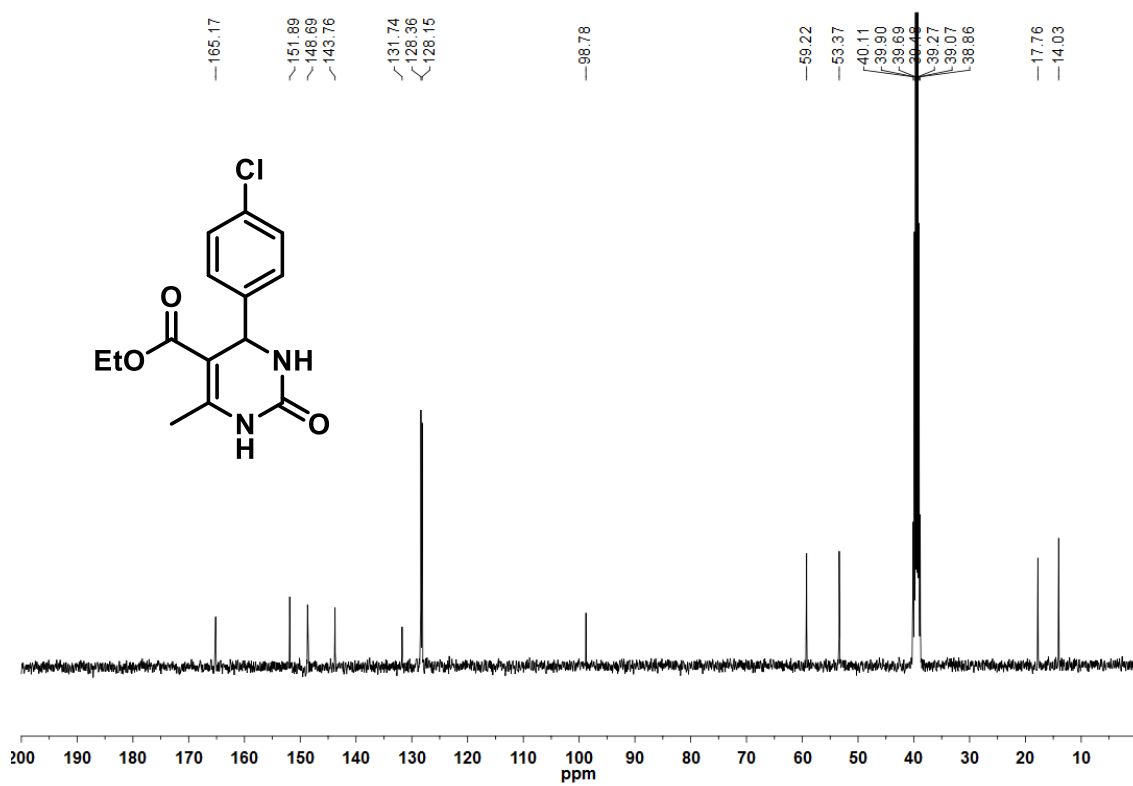


FIGURE A6 - $^{13}\text{C-NMR}$ spectrum of compound **2.37c**.

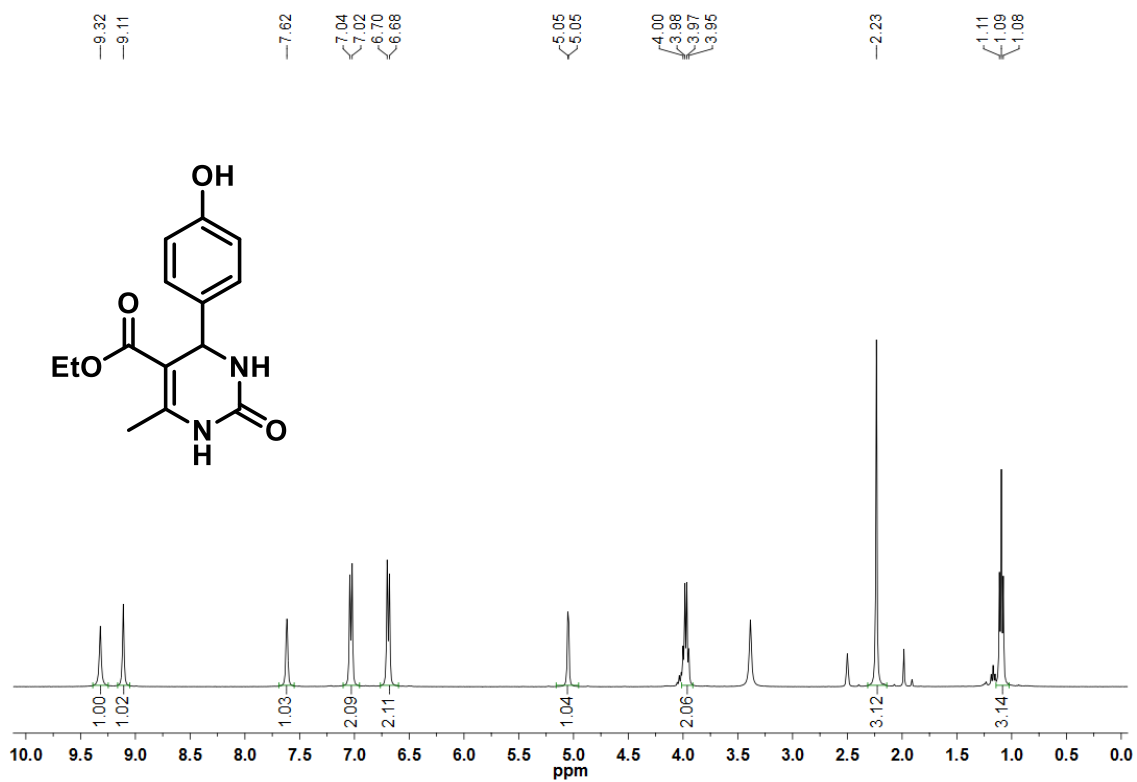


FIGURE A7 - ¹H-NMR spectrum of compound 2.37d.

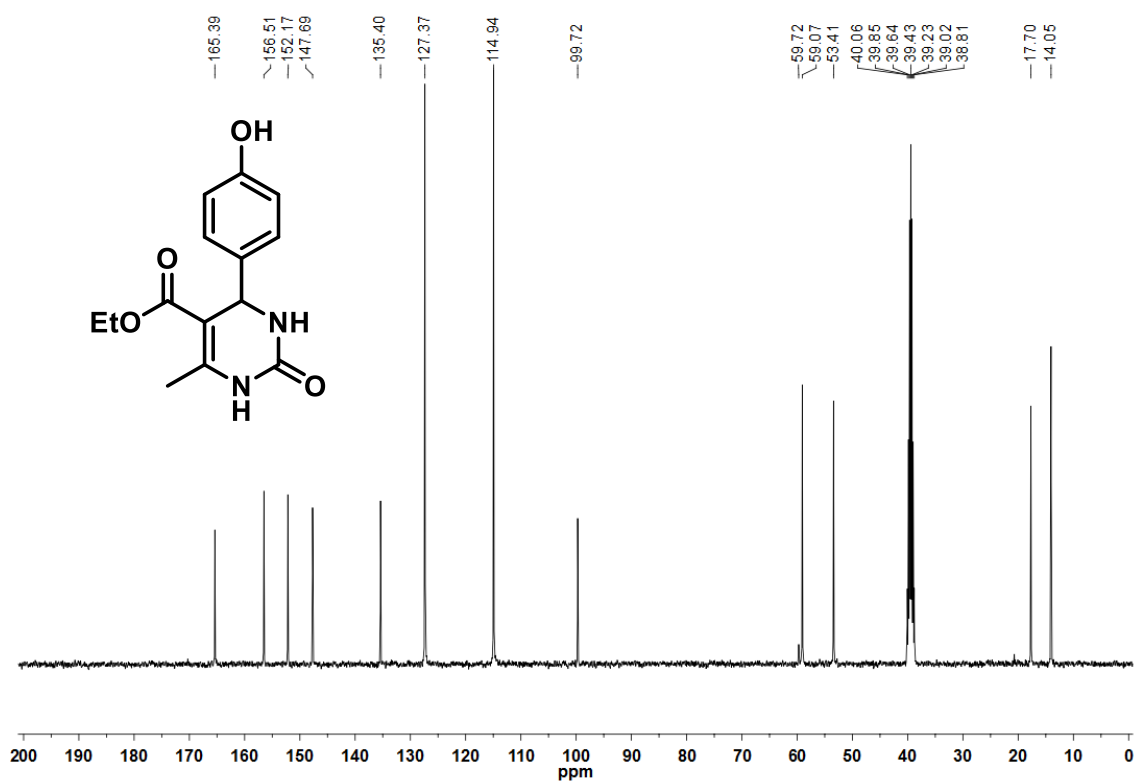


FIGURE A8 - ¹³C-NMR spectra of compound 2.37d.

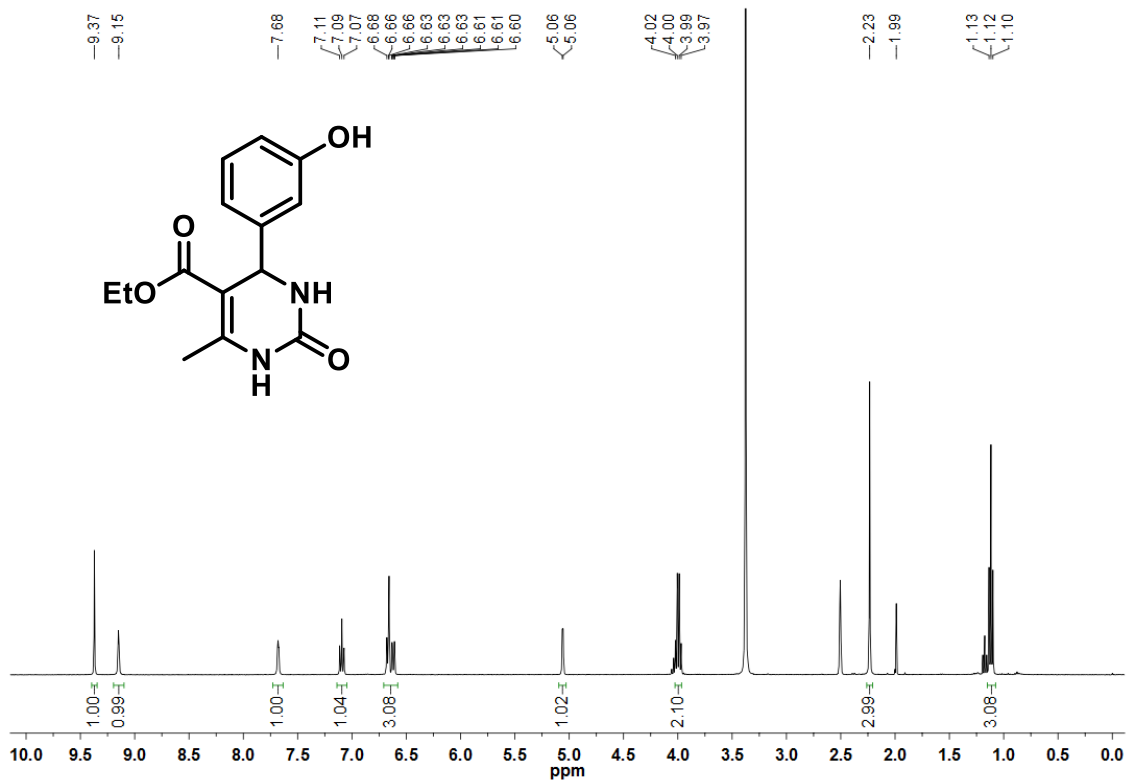


FIGURE A9 - ¹H-NMR spectrum of compound 2.37e.

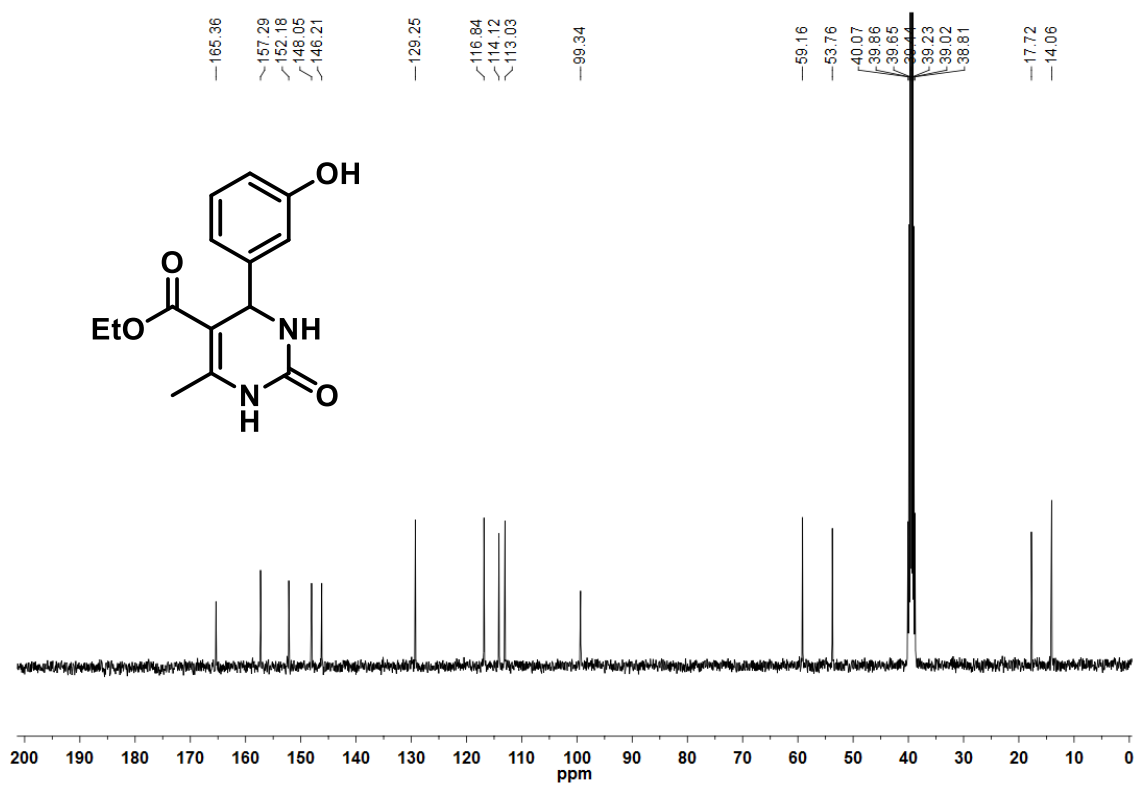


FIGURE A10 - ¹³C-NMR spectra of compound 2.37e.

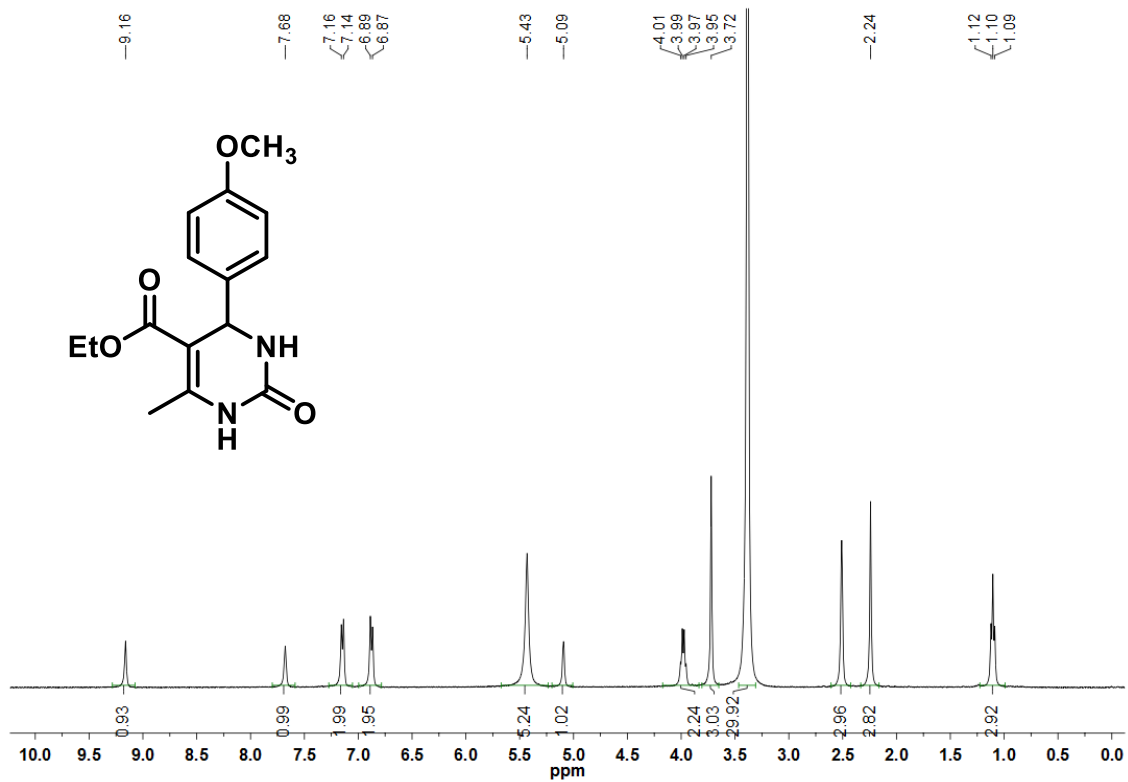


FIGURE A11 - ¹H-NMR spectrum of compound 2.37f.

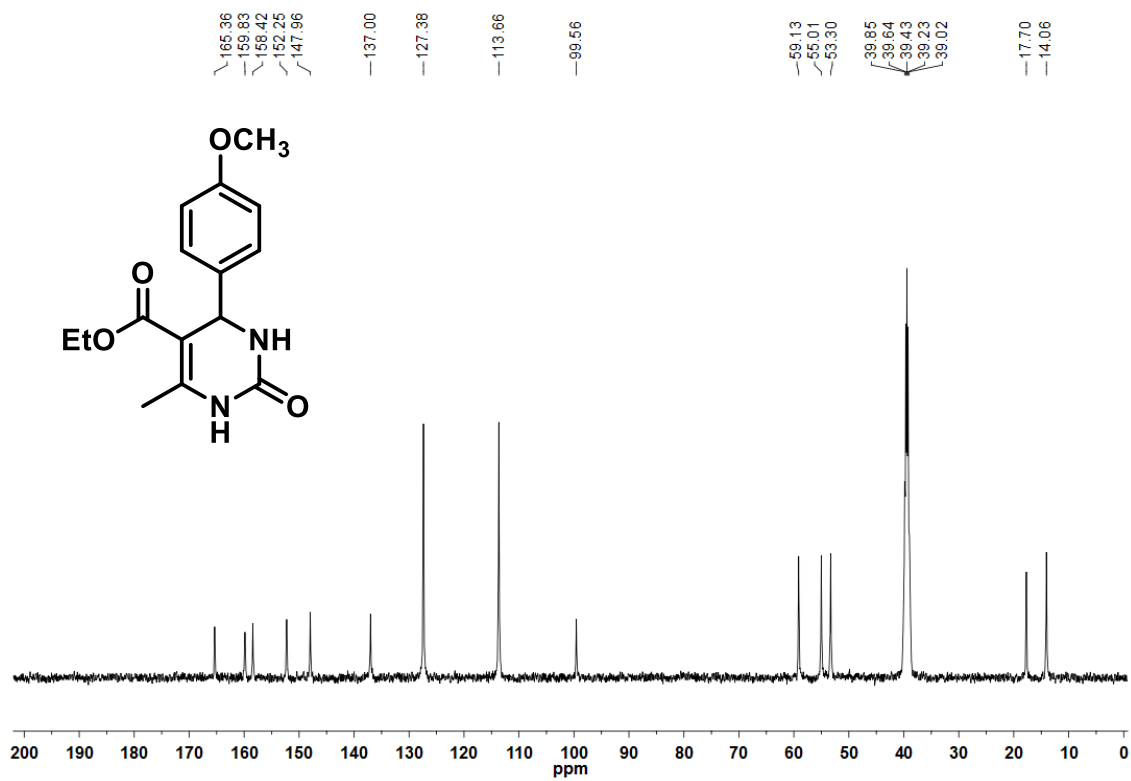


FIGURE A12 - ¹³C-NMR spectrum of compound 2.37f.

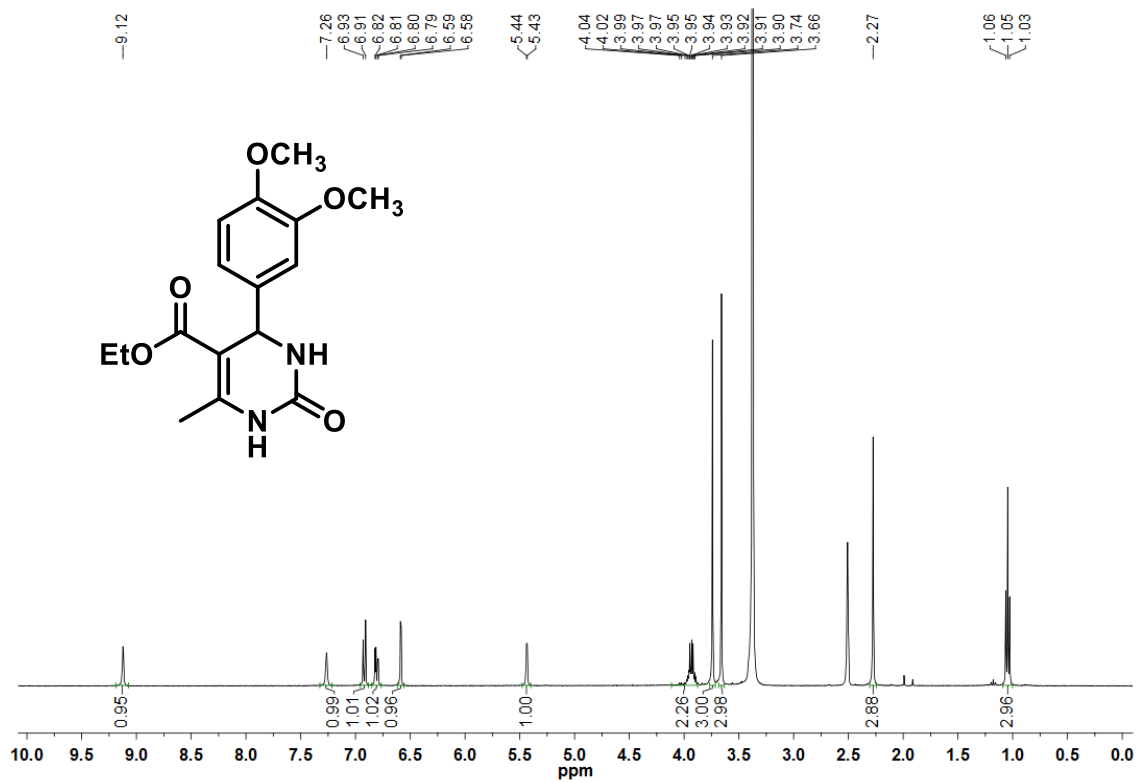


FIGURE A13 - ¹H-NMR spectrum of compound 2.37g.

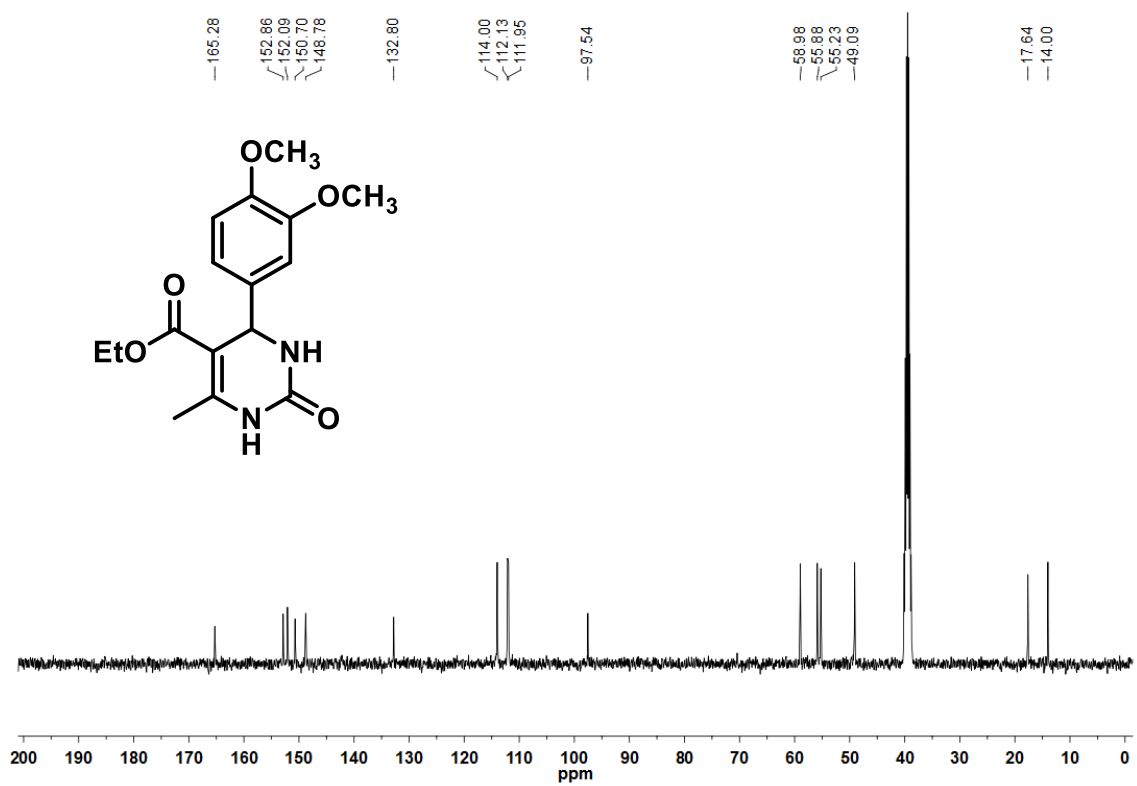


FIGURE A14 - ¹³C-NMR spectra of compound 2.37g.

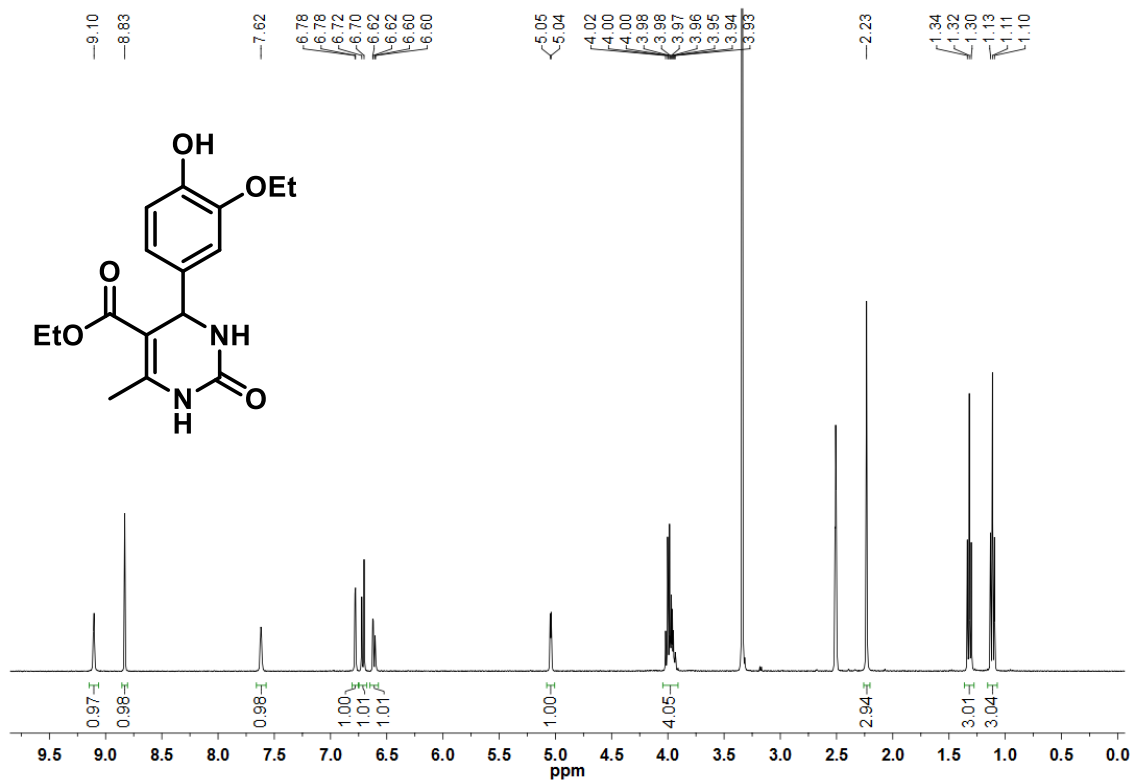


FIGURE A15 - ¹H-NMR spectrum of compound 2.37h.

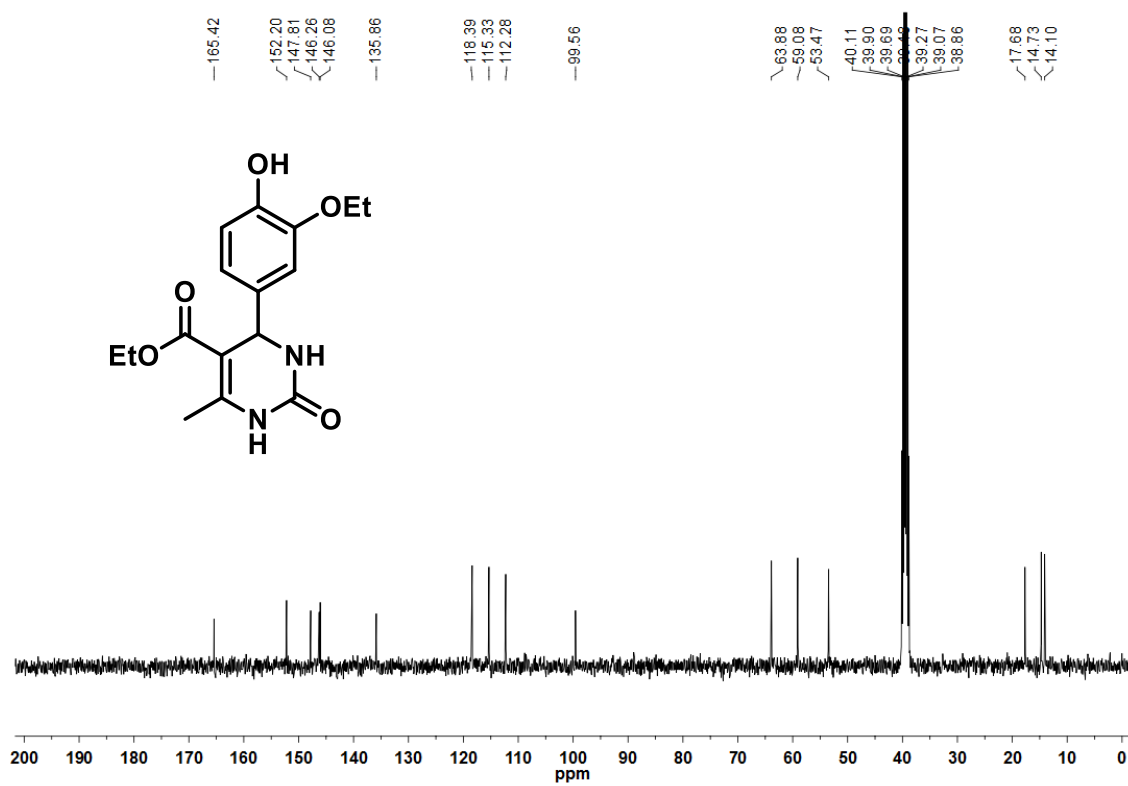


FIGURE A16 - ¹³C-NMR spectra of compound 2.37h.

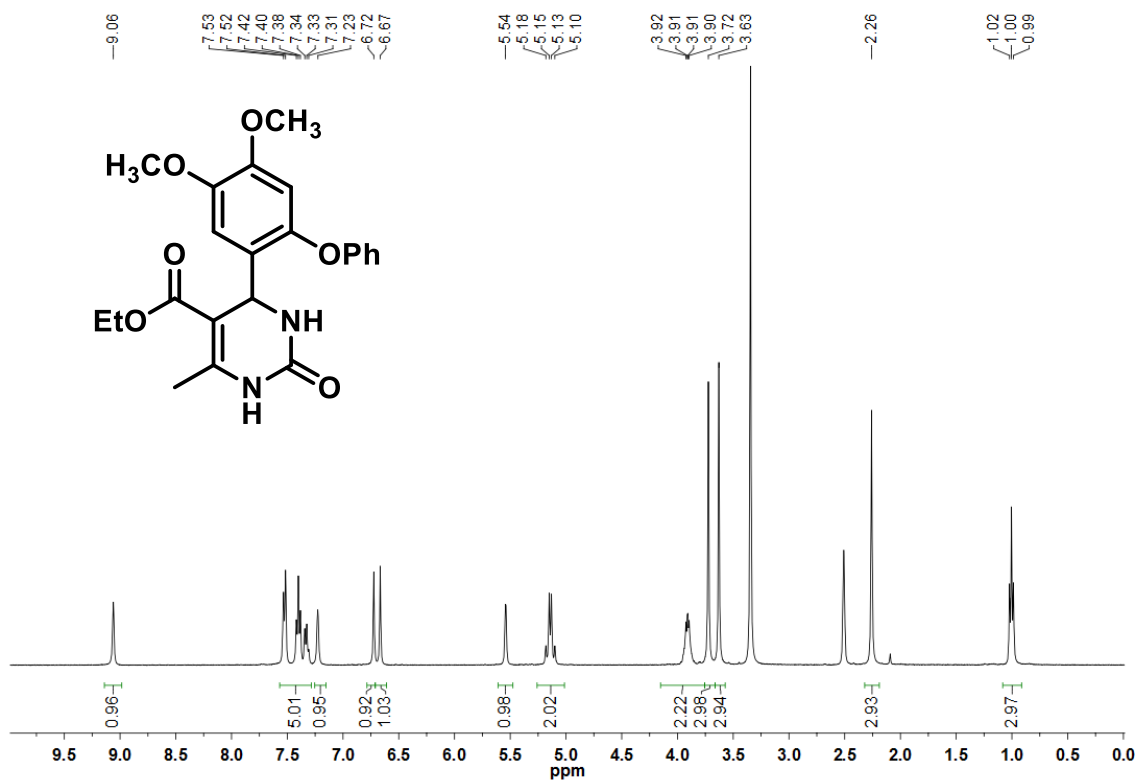


FIGURE A17 - ¹H-NMR spectrum of compound 2.37i.

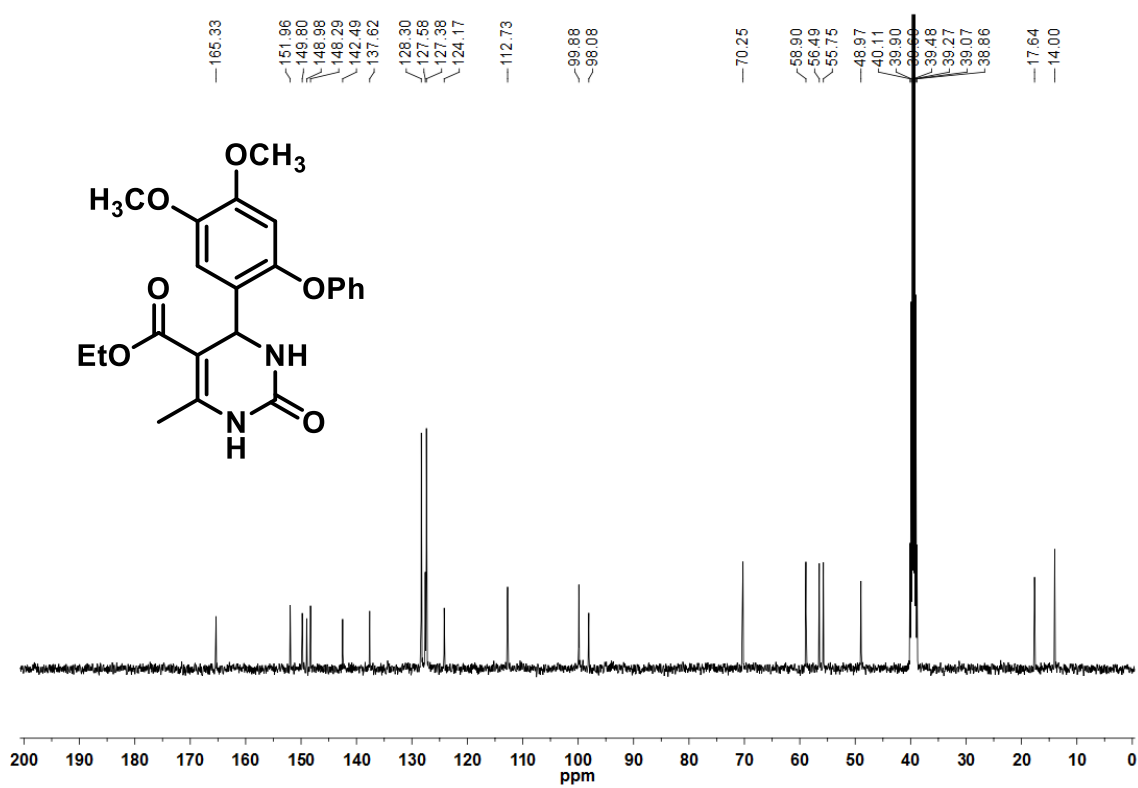


FIGURE A18 - ¹³C-NMR spectra of compound 2.37i .

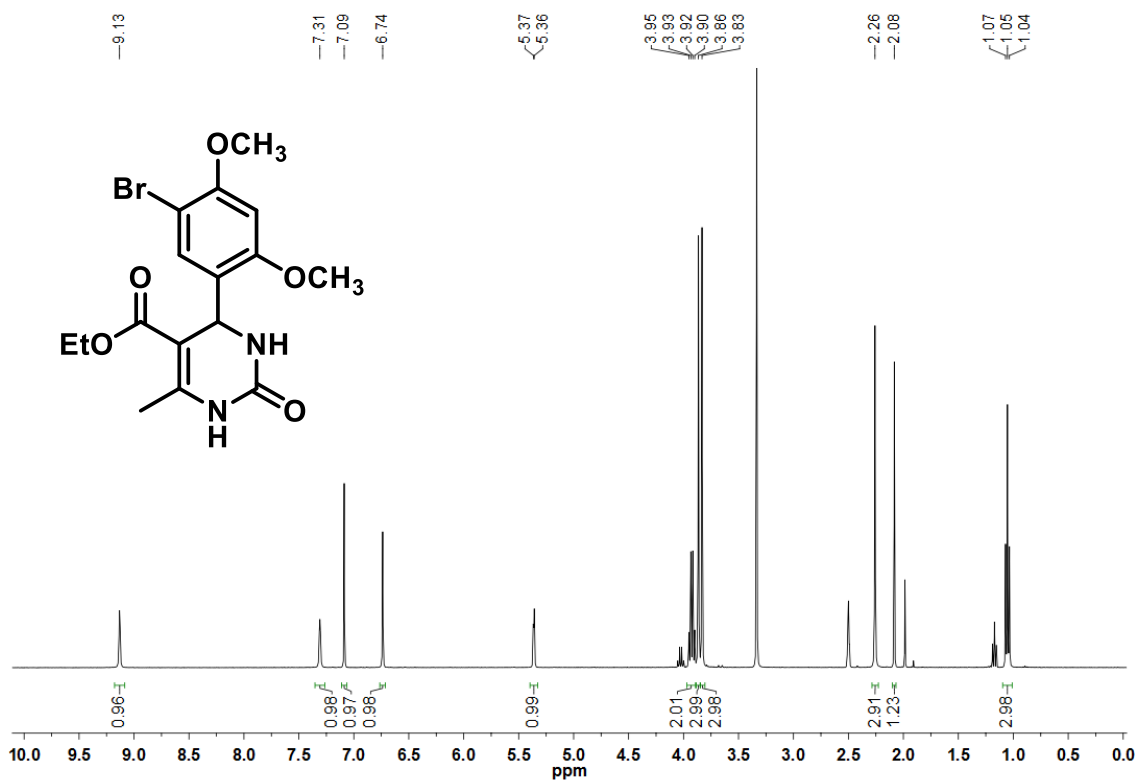


FIGURE A19 - $^1\text{H-NMR}$ spectrum of compound **2.37j**.

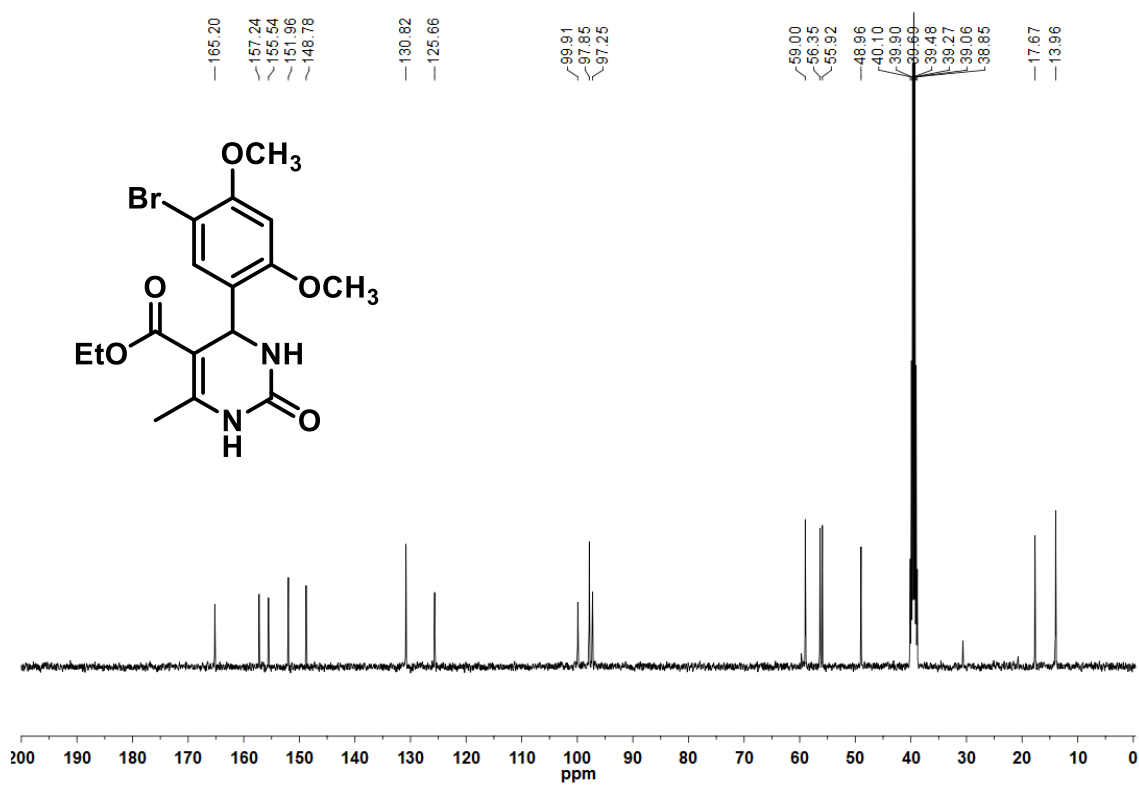


FIGURE A20 - $^{13}\text{C-NMR}$ spectra of compound **2.37j**.

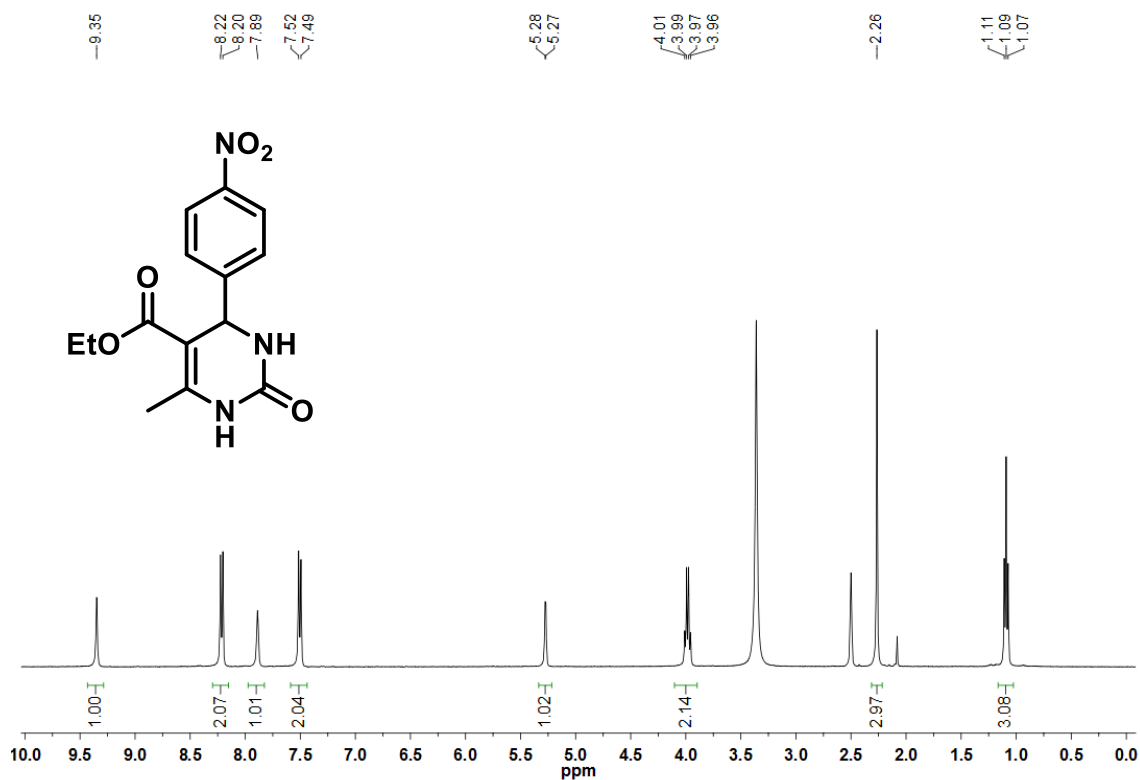


FIGURE A21 - ¹H-NMR spectrum of compound **2.37k**.

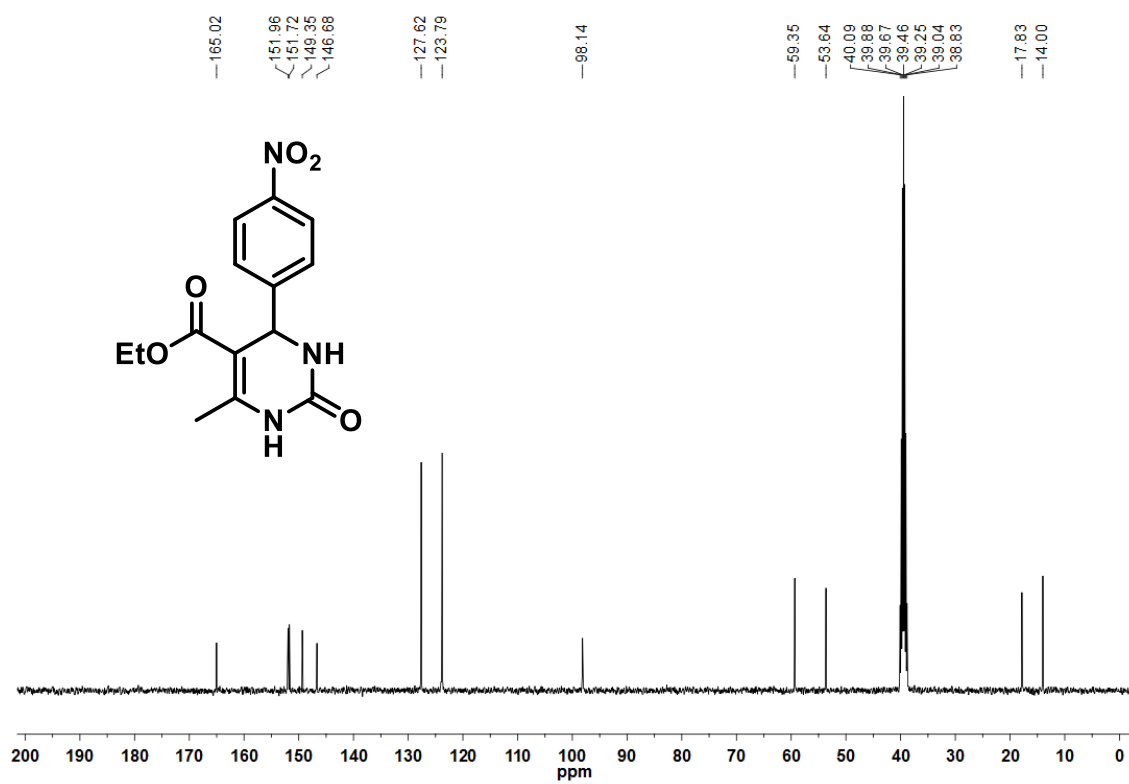


FIGURE A22 - ¹³C-NMR spectra of compound **2.37k**.

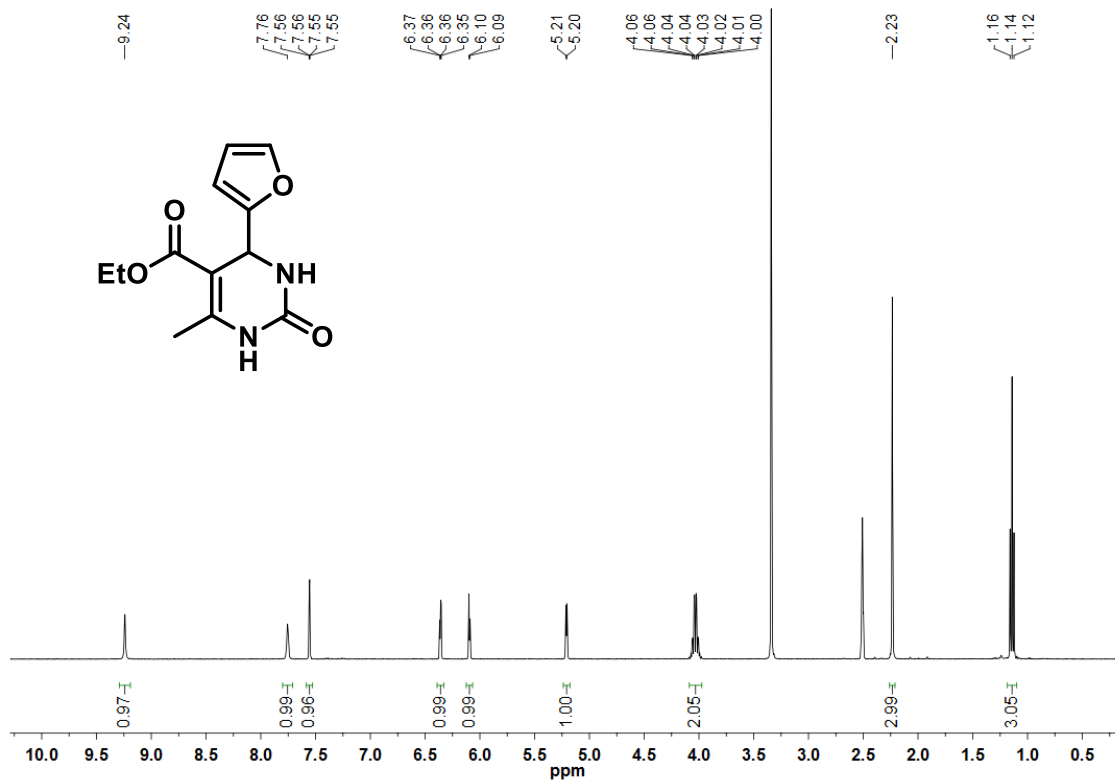


FIGURE A23 - ¹H-NMR spectrum of compound 2.371.

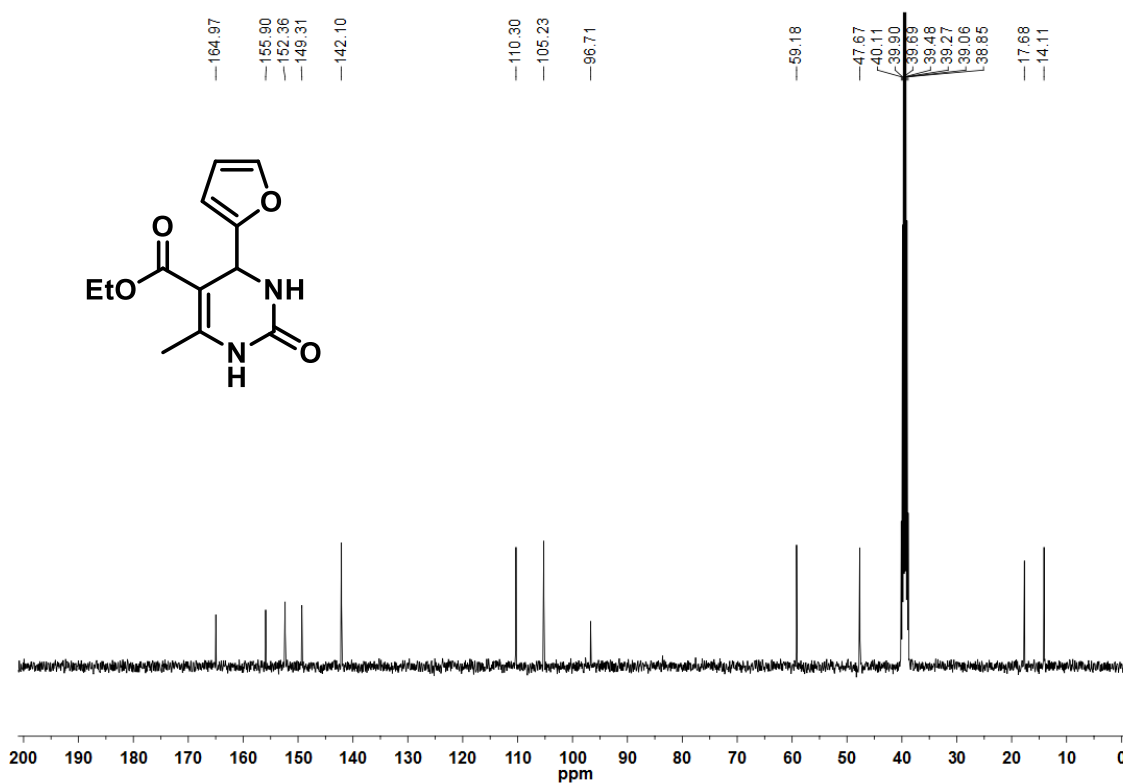


FIGURE A24 - ¹³C-NMR spectra of compound 2.371.

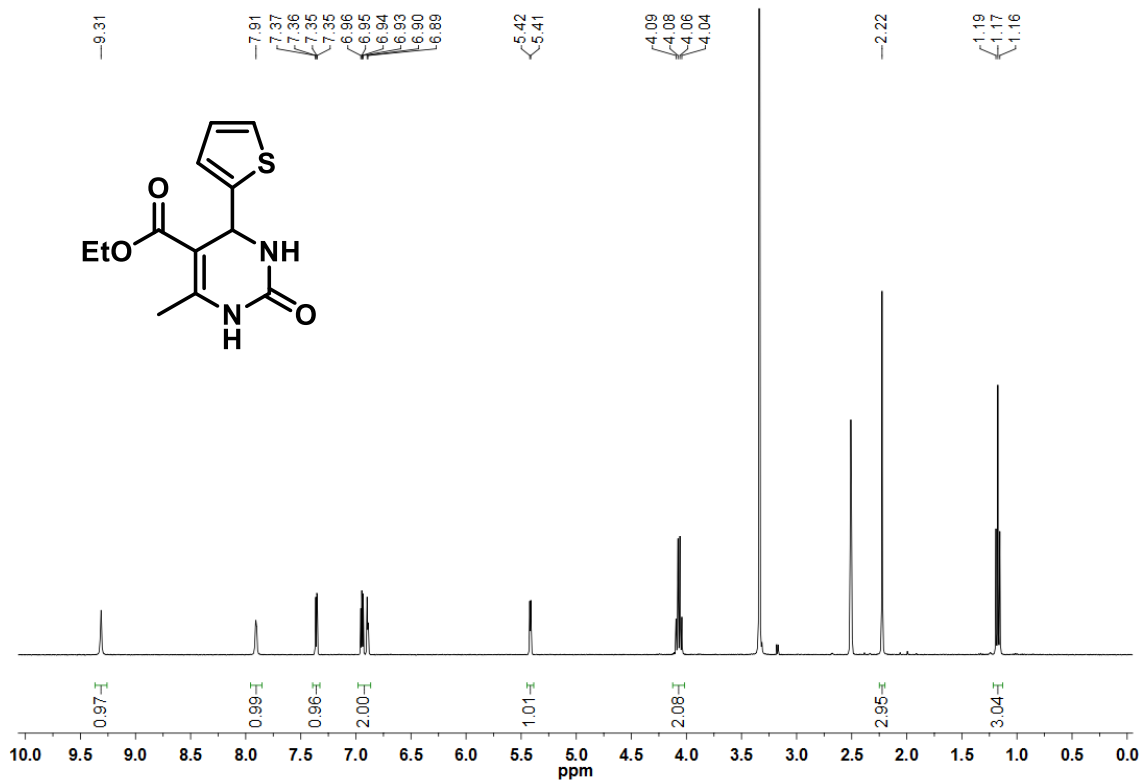


FIGURE A25 - ¹H-NMR spectrum of compound **2.37m**.

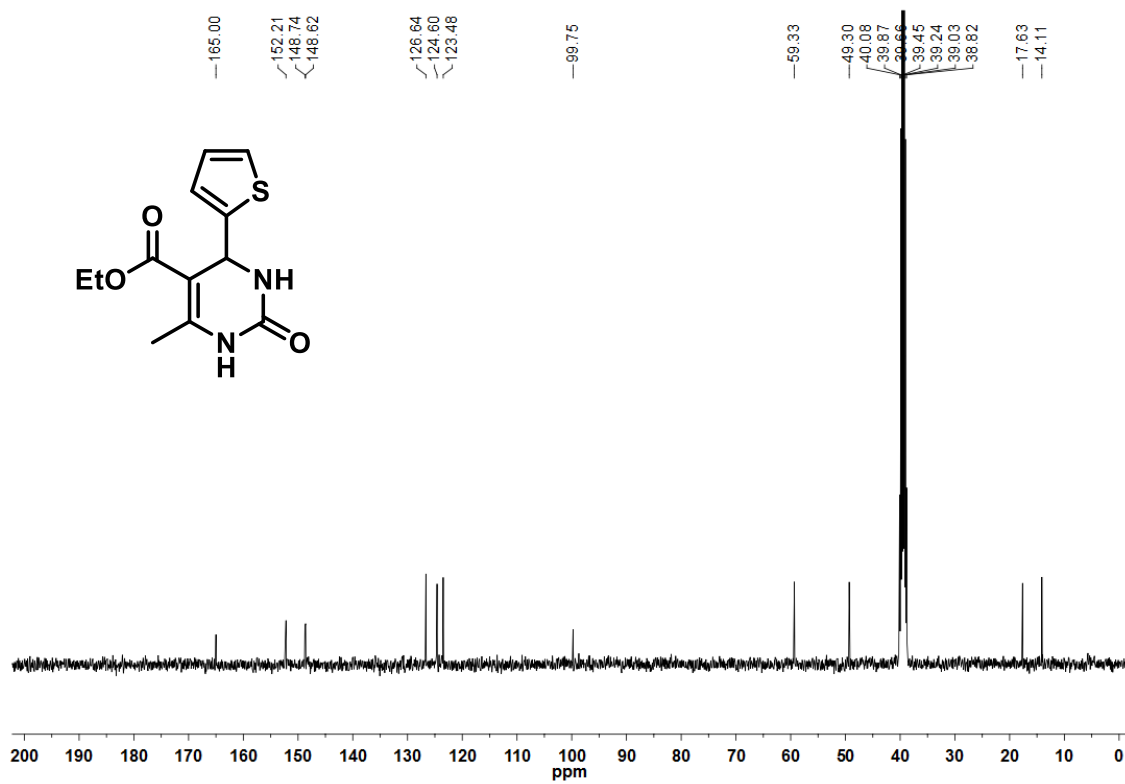


FIGURE A26 - ¹³C-NMR spectra of compound **2.37m**.

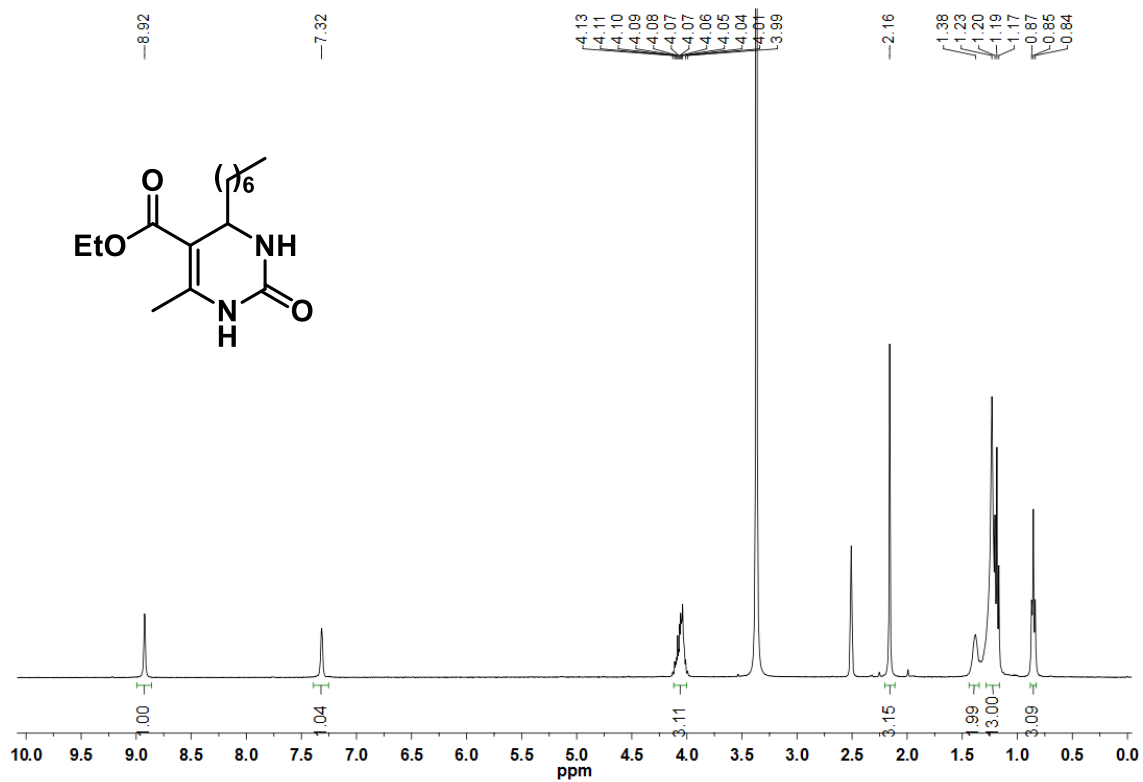


FIGURE A27 - ¹H-NMR spectrum of compound 2.37n.

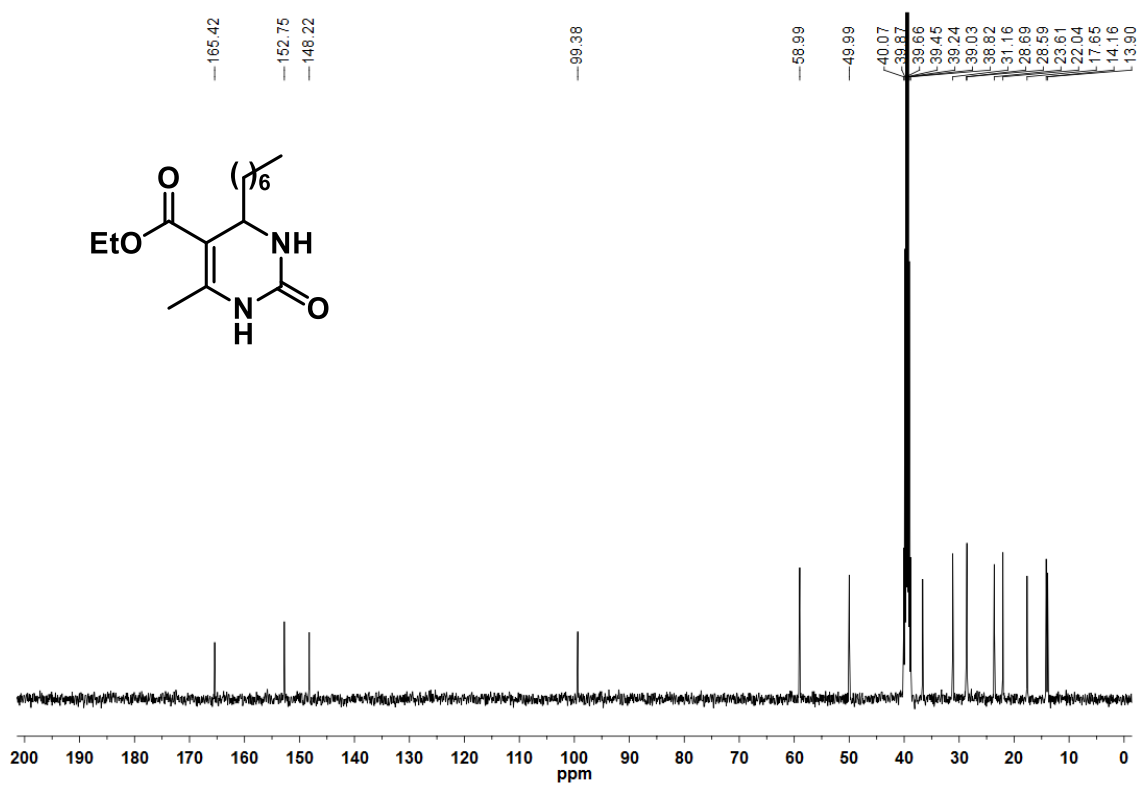


FIGURE A28 - ¹³C-NMR spectra of compound 2.37n.

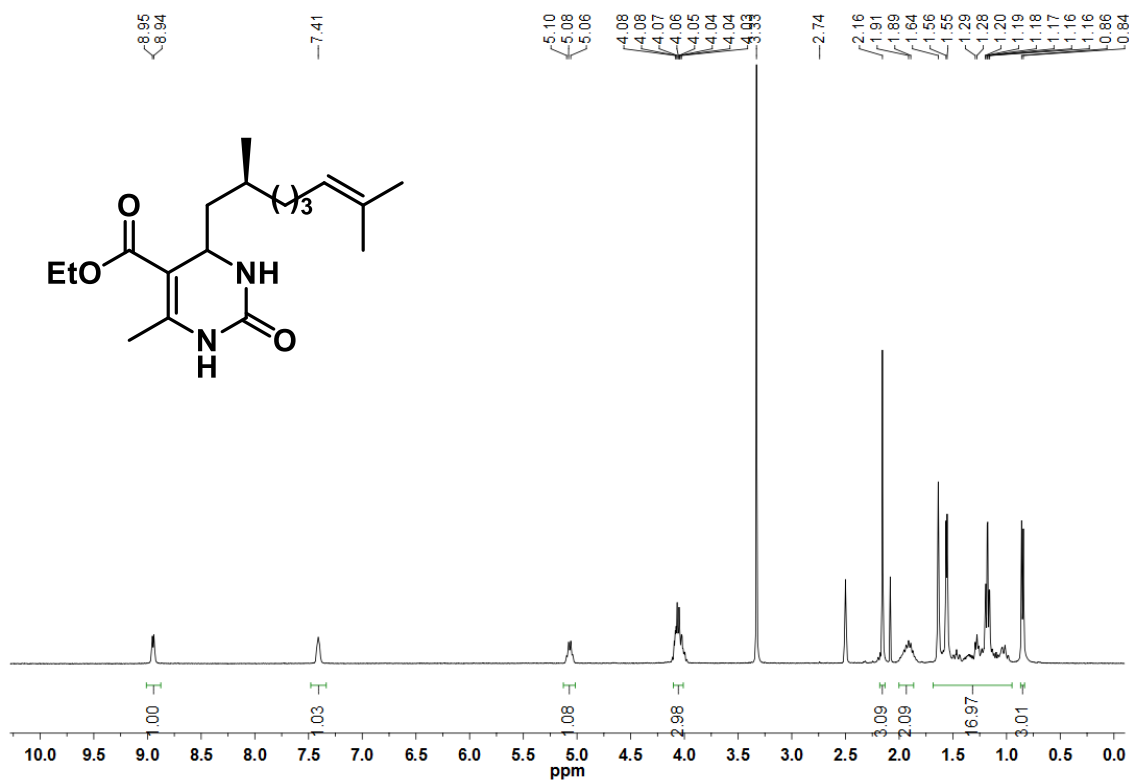


FIGURE A29 - $^1\text{H-NMR}$ spectrum of compound **2.37o**.

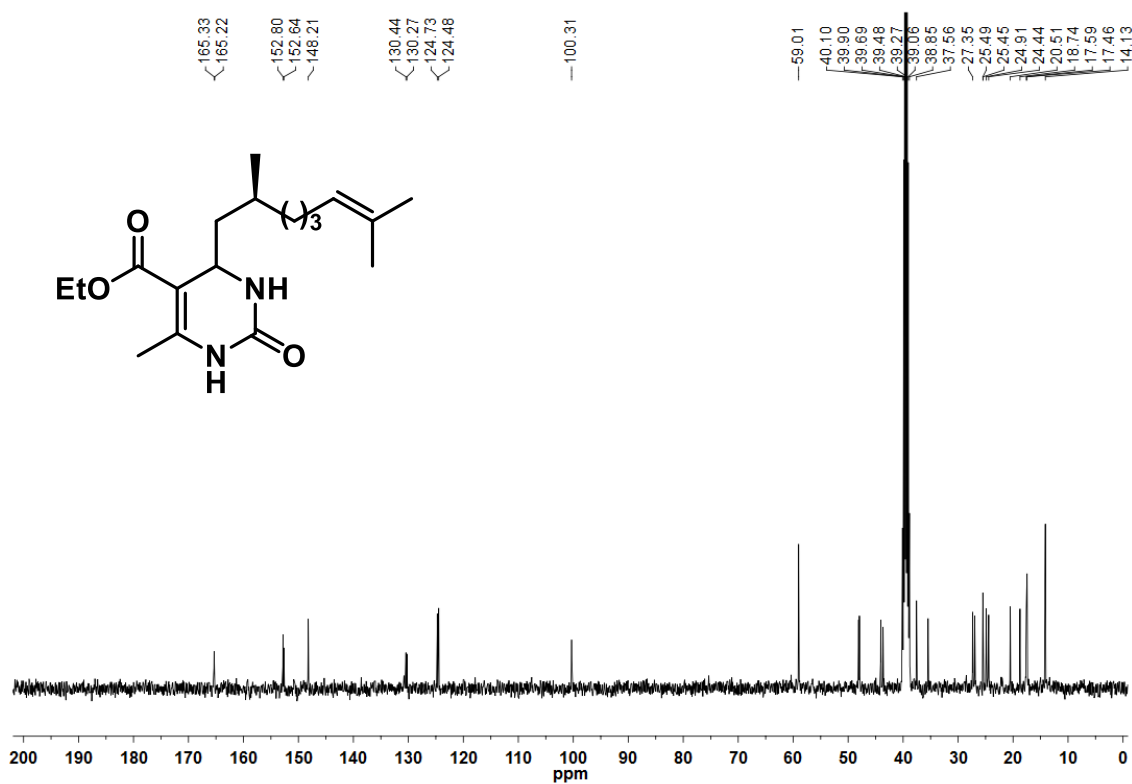


FIGURE A30 - $^{13}\text{C-NMR}$ spectra of compound **2.37o**.

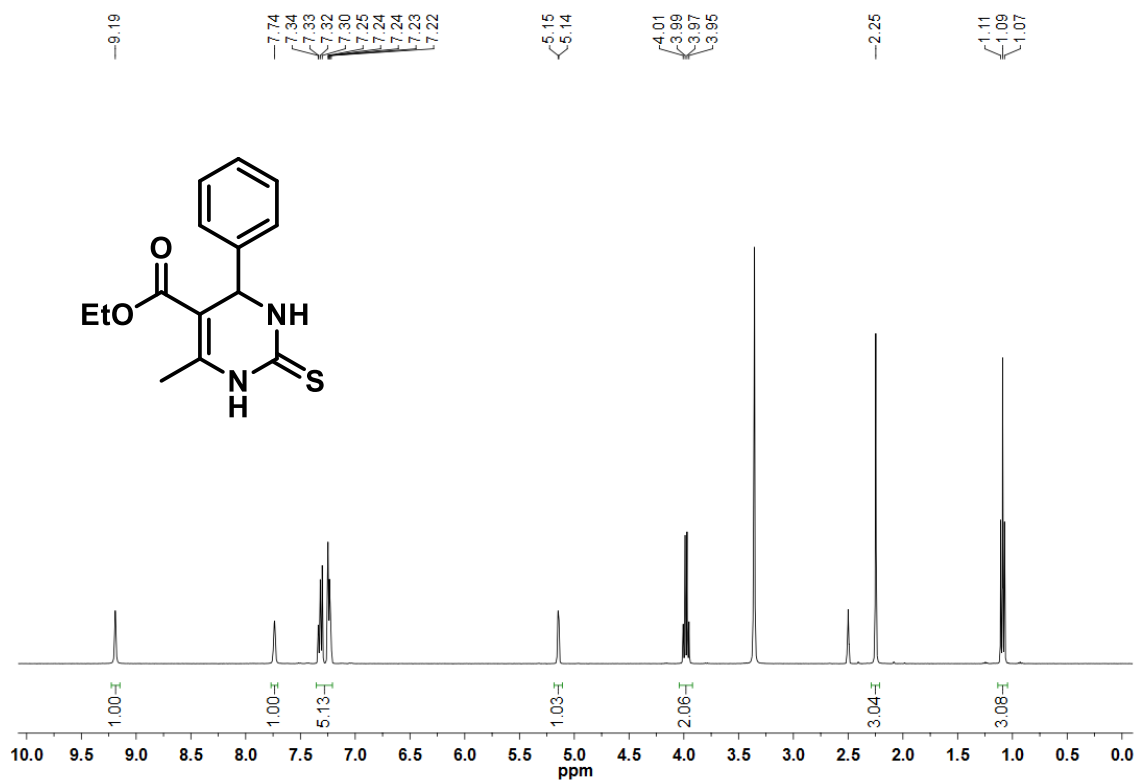


FIGURE A31 - ¹H-NMR spectrum of compound 2.37p.

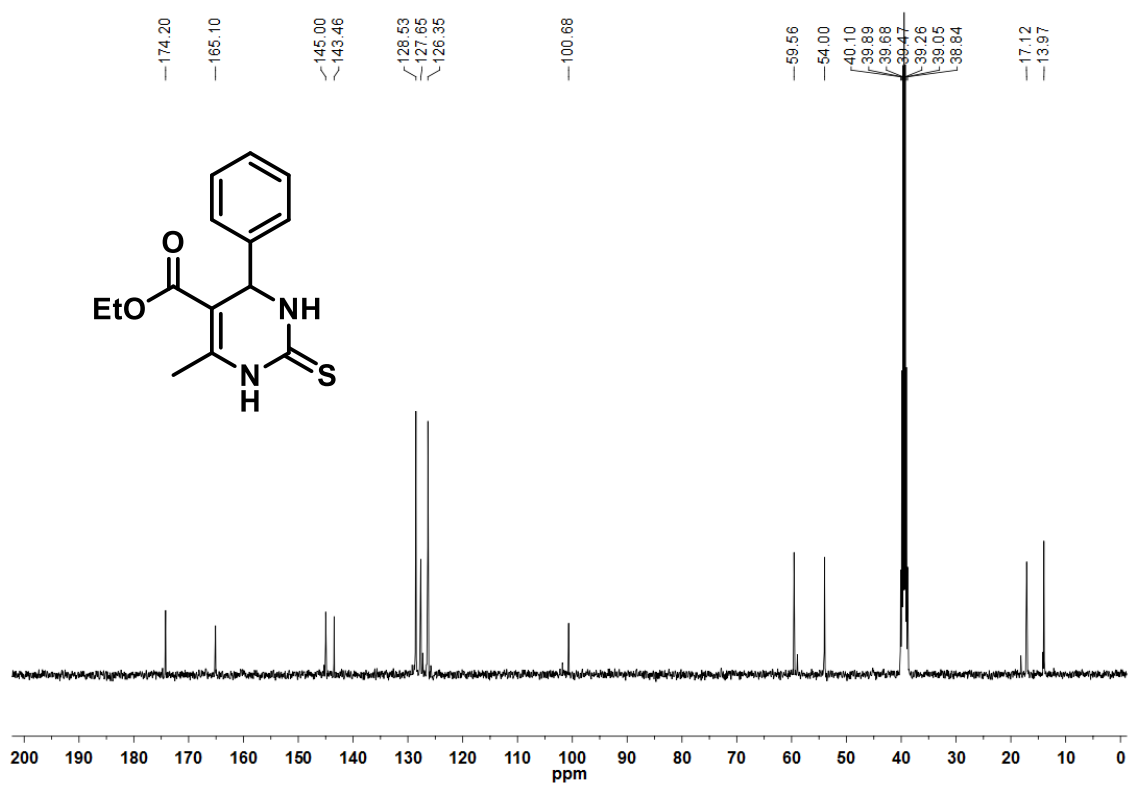


FIGURE A32 - ¹³C-NMR spectra of compound 2.37p.

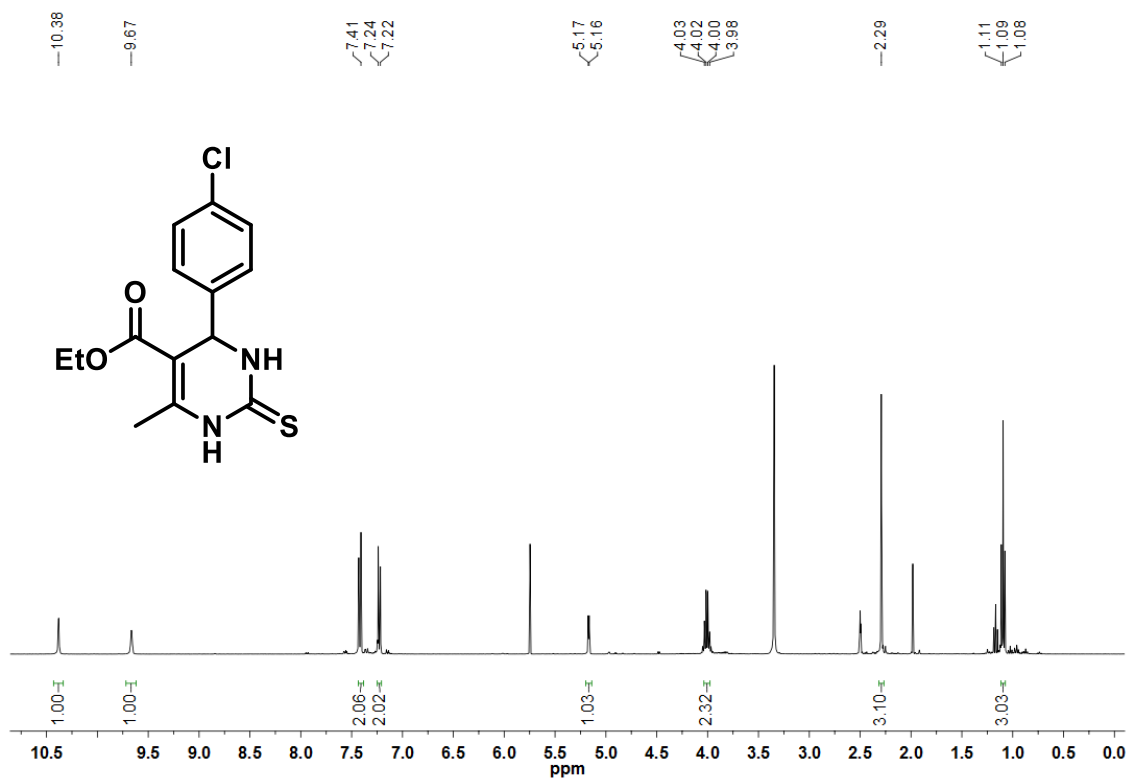


FIGURE A33 - ¹H-NMR spectrum of compound 2.37q.

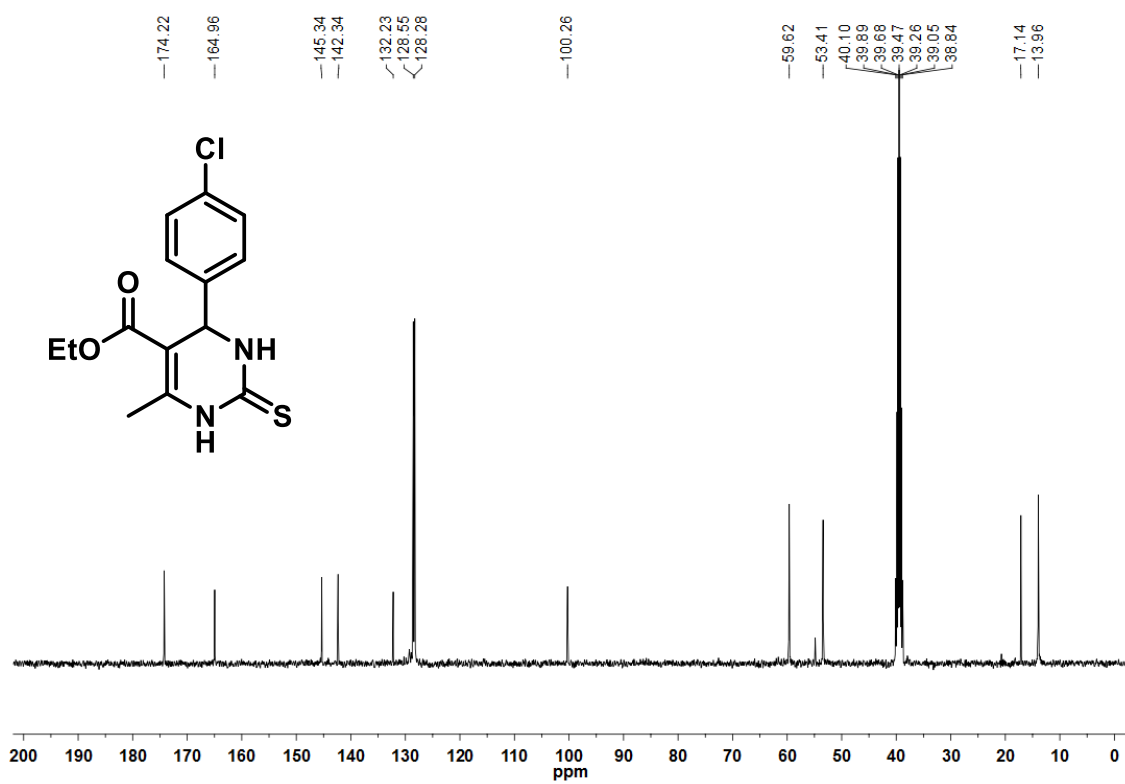


FIGURE A34 - ¹³C-NMR spectra of compound 2.37q.

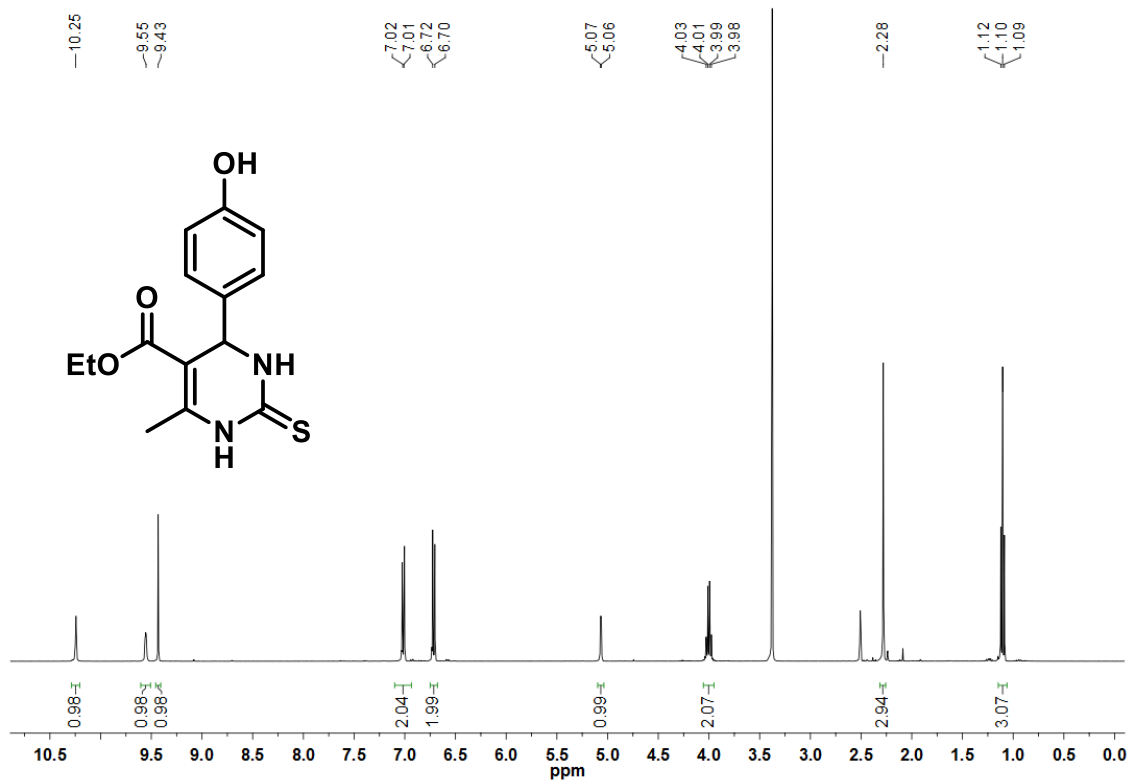


FIGURE A35 - ¹H-NMR spectrum of compound 2.37r.

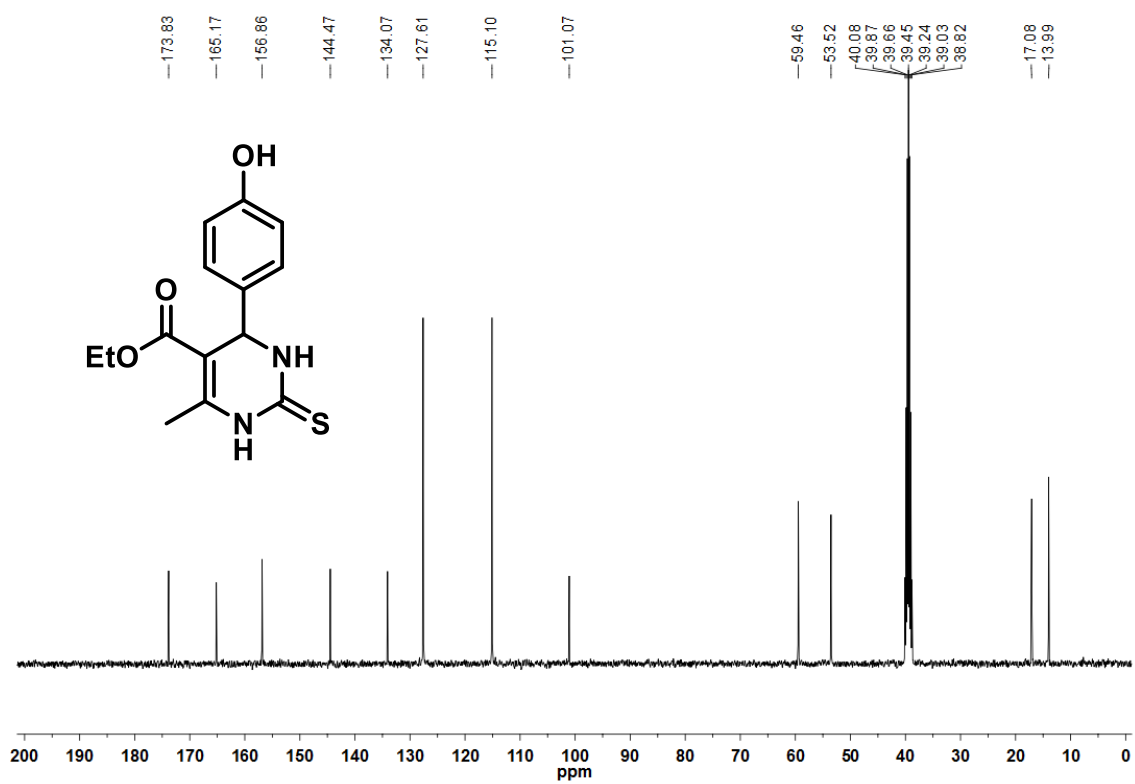


FIGURE A36 - ¹³C-NMR spectra of compound 2.37r.

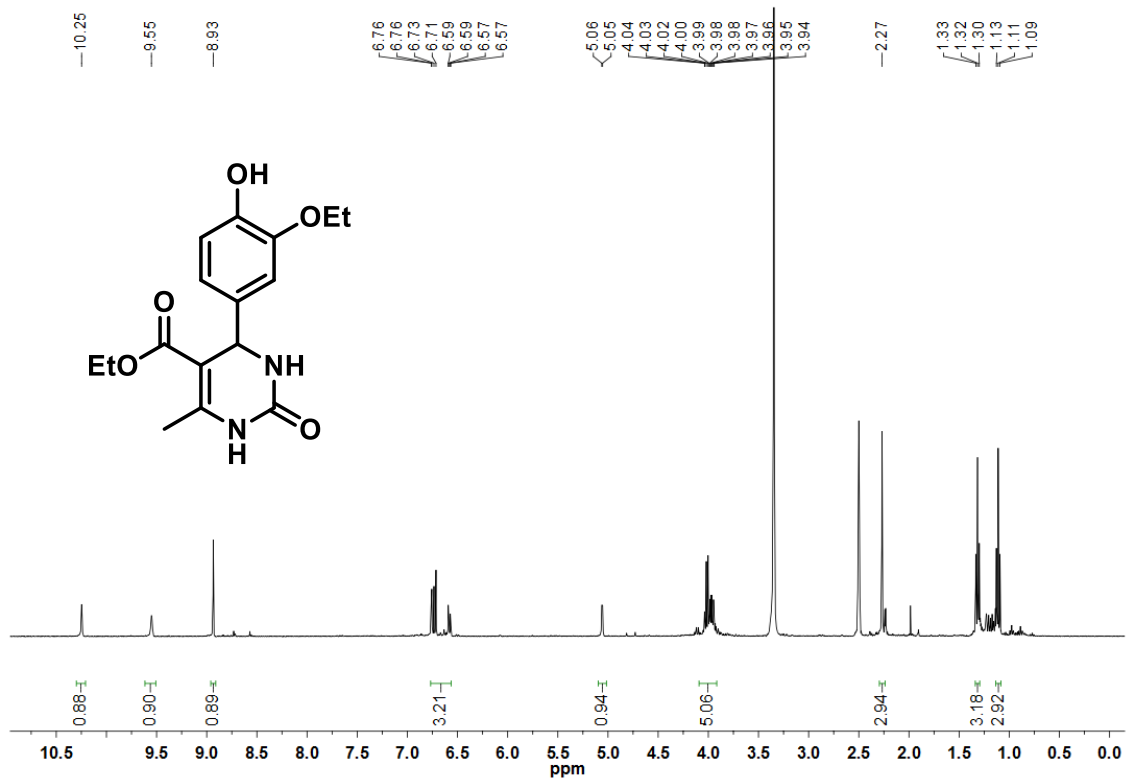


FIGURE A37 - ¹H-NMR spectrum of compound 2.37s.

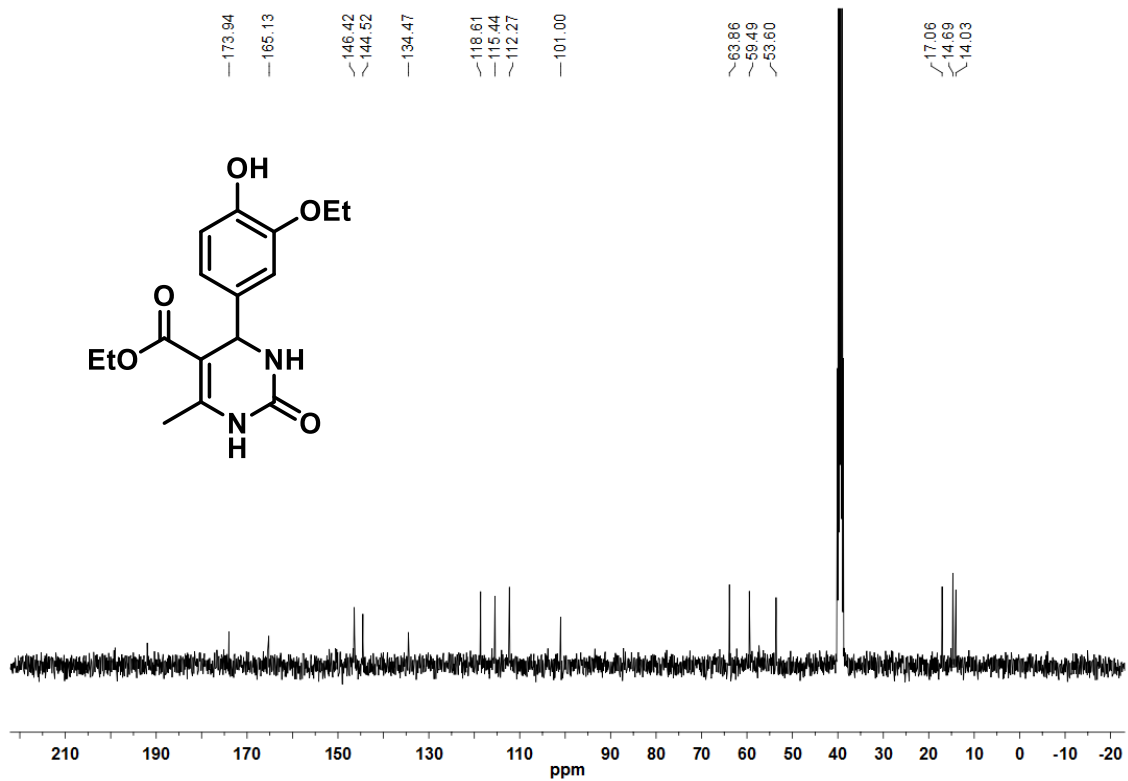


FIGURE A38 - ¹³C-NMR spectra of compound 2.37s.

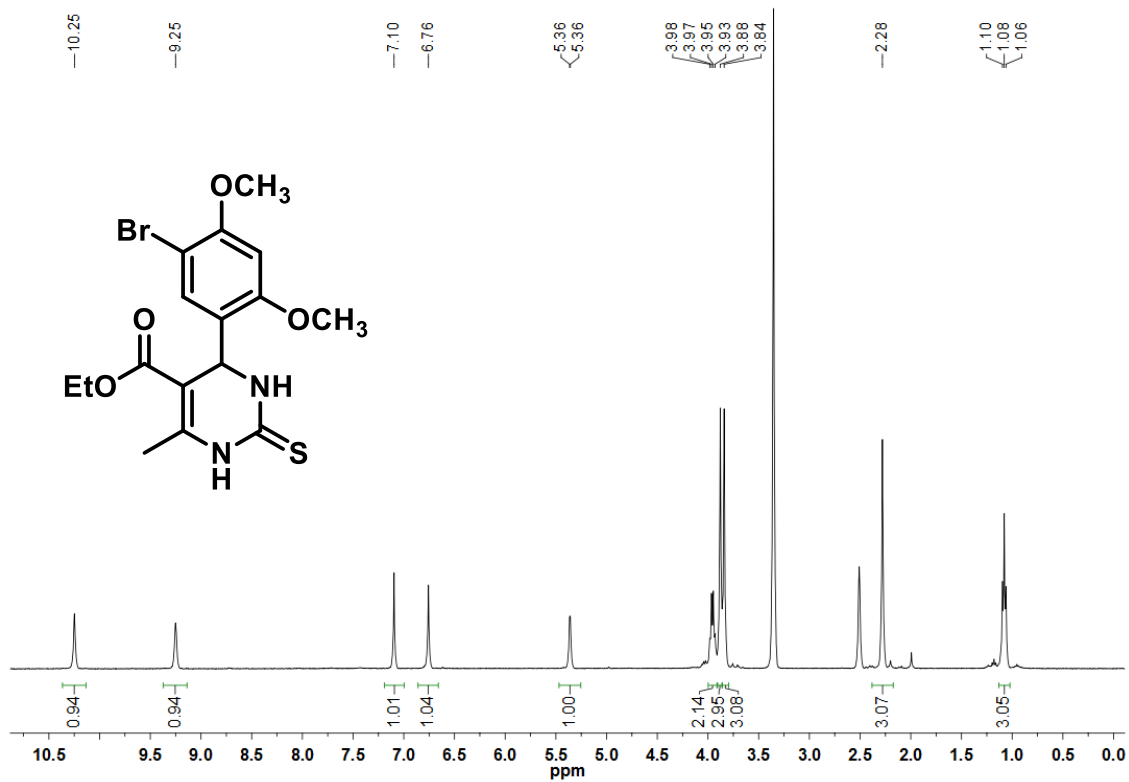


FIGURE A39 - ¹H-NMR spectrum of compound 2.37t.

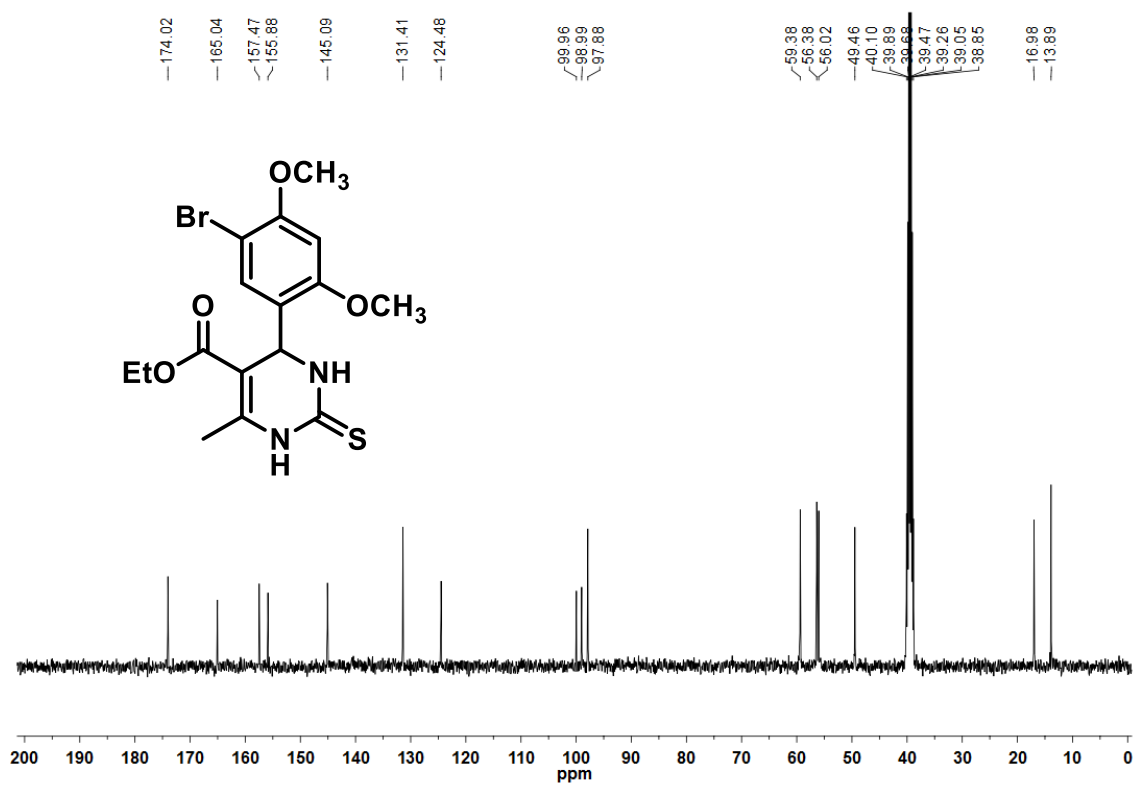


FIGURE A40 - ¹³C-NMR spectra of compound 2.37t.

Appendix 2:

Selected chromatograms of standards and reactions reported in Chapters 3 and 4.

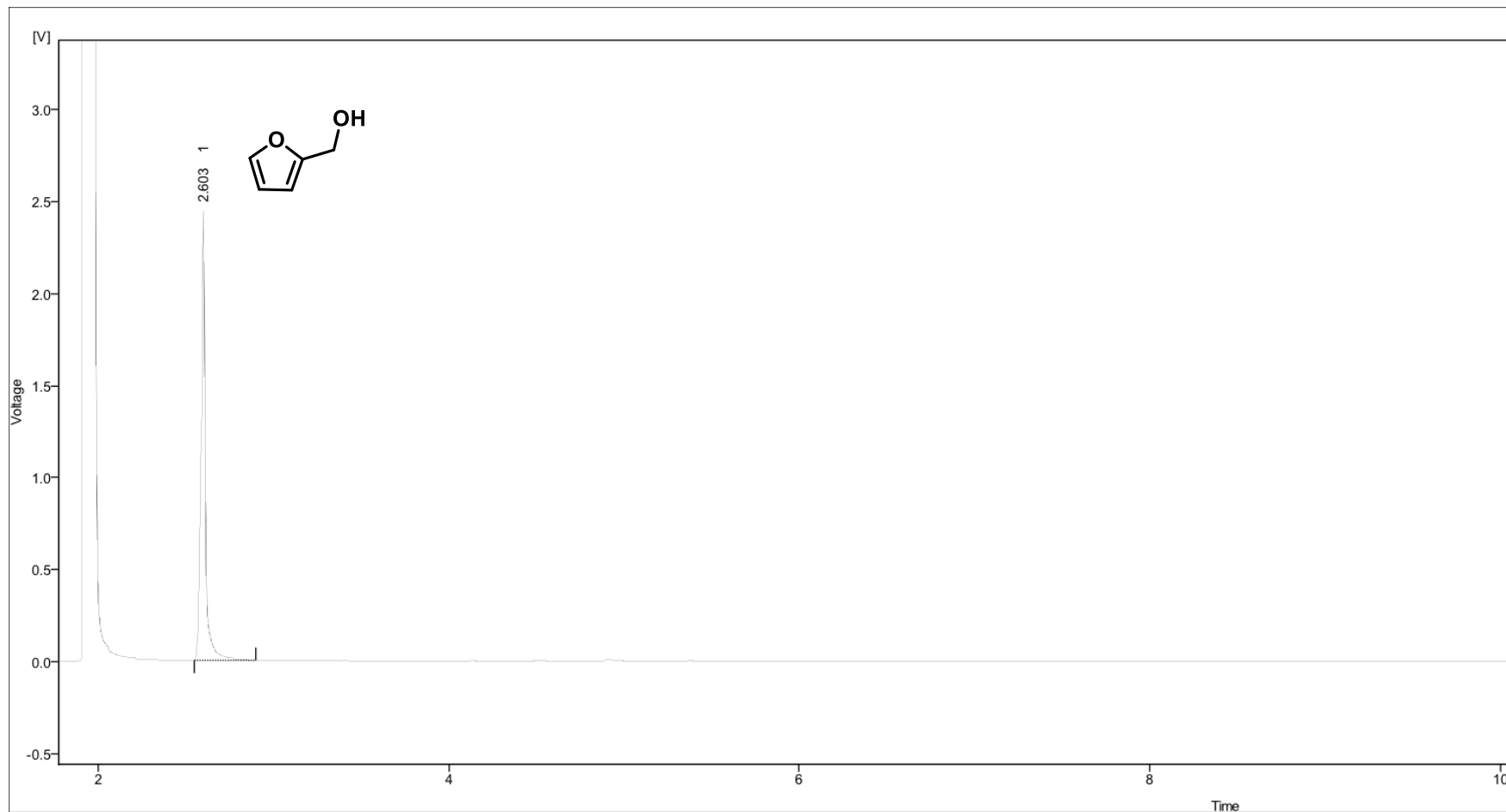


FIGURE A41 – GC-FID chromatogram of the furfuryl alcohol standard.

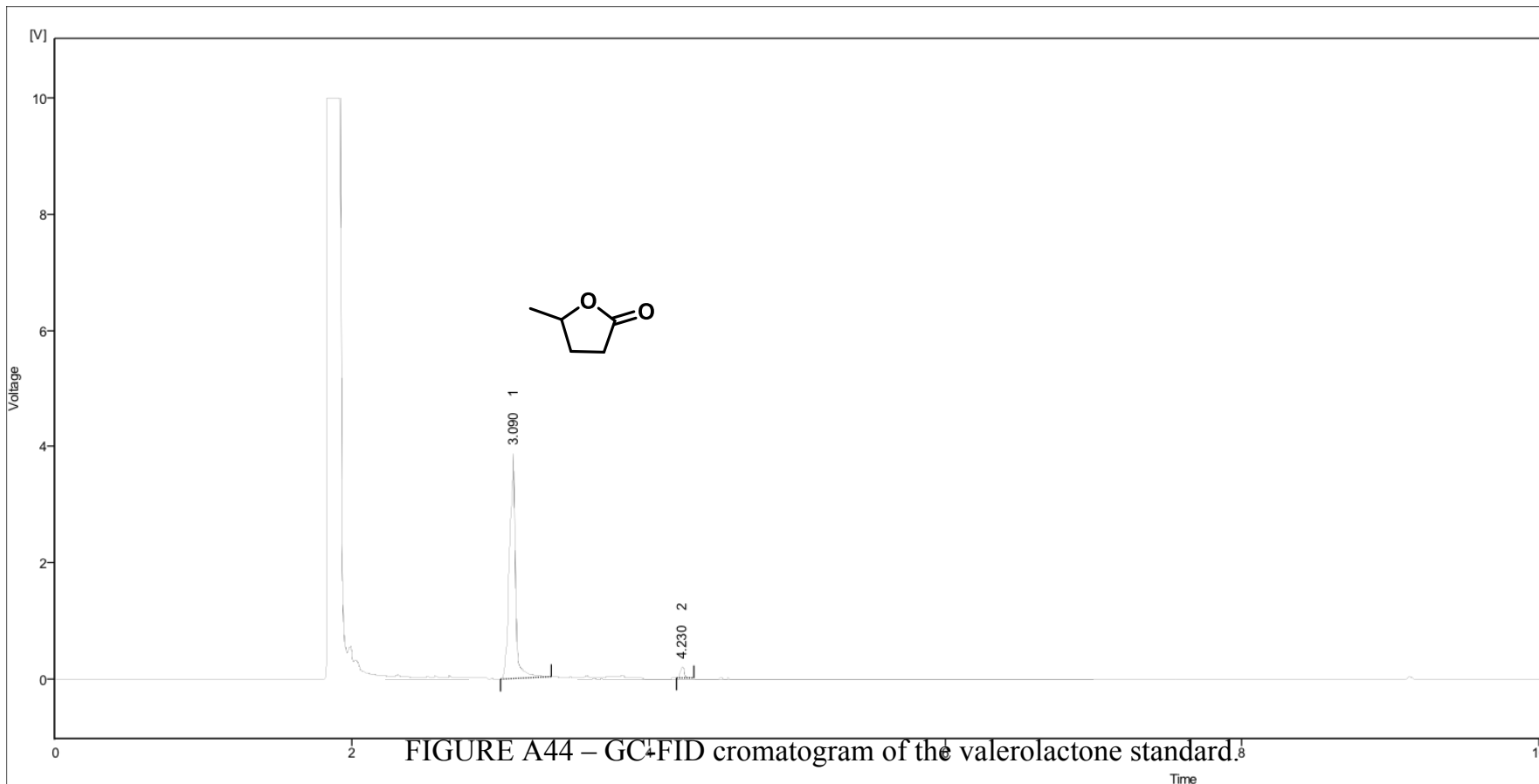


FIGURE A44 – GC-FID chromatogram of the valerolactone standard.

FIGURE A42 – GC-FID chromatogram of the valerolactone standard.

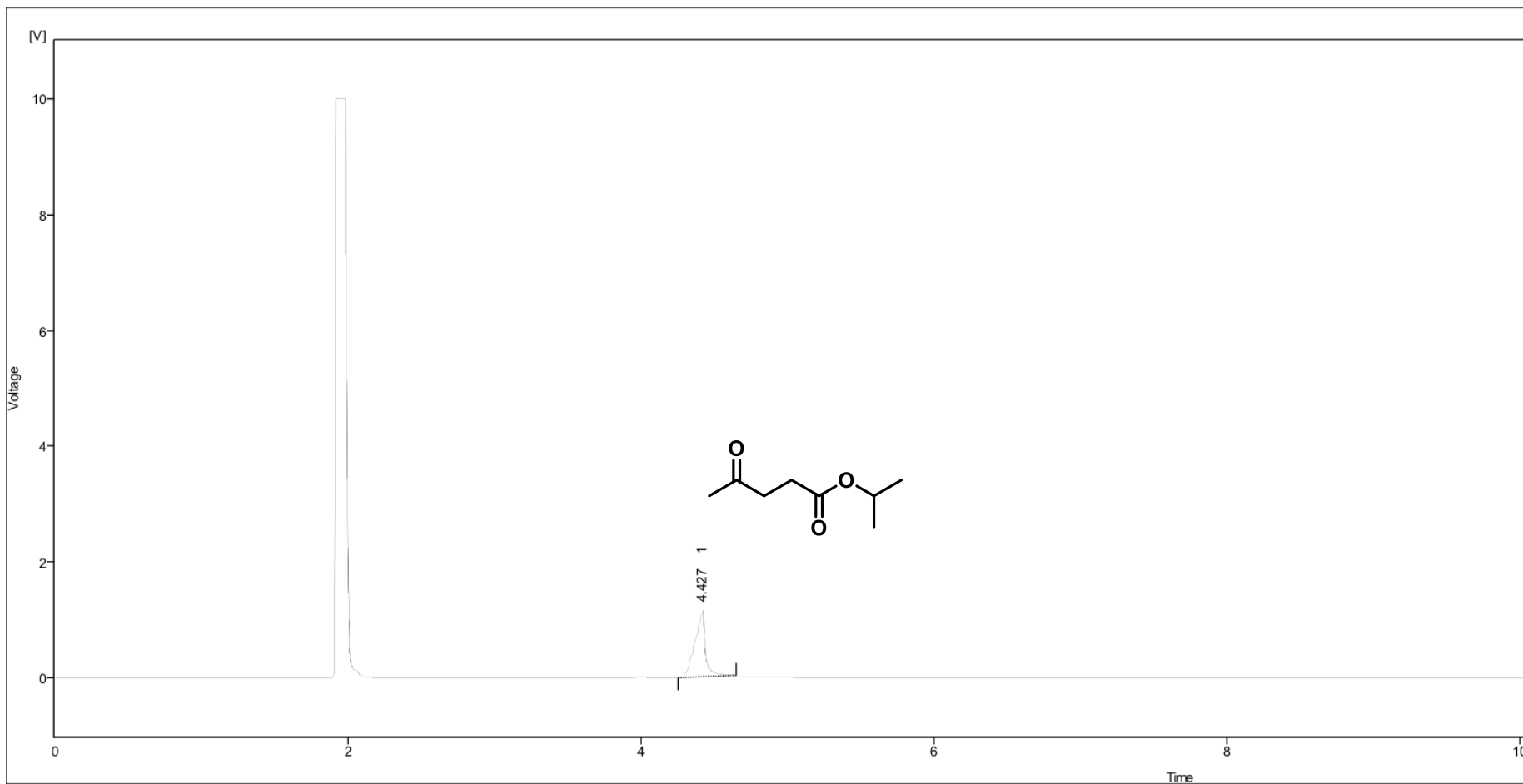


FIGURE A43 – GC-FID chromatogram of the propyl levulinate standard.

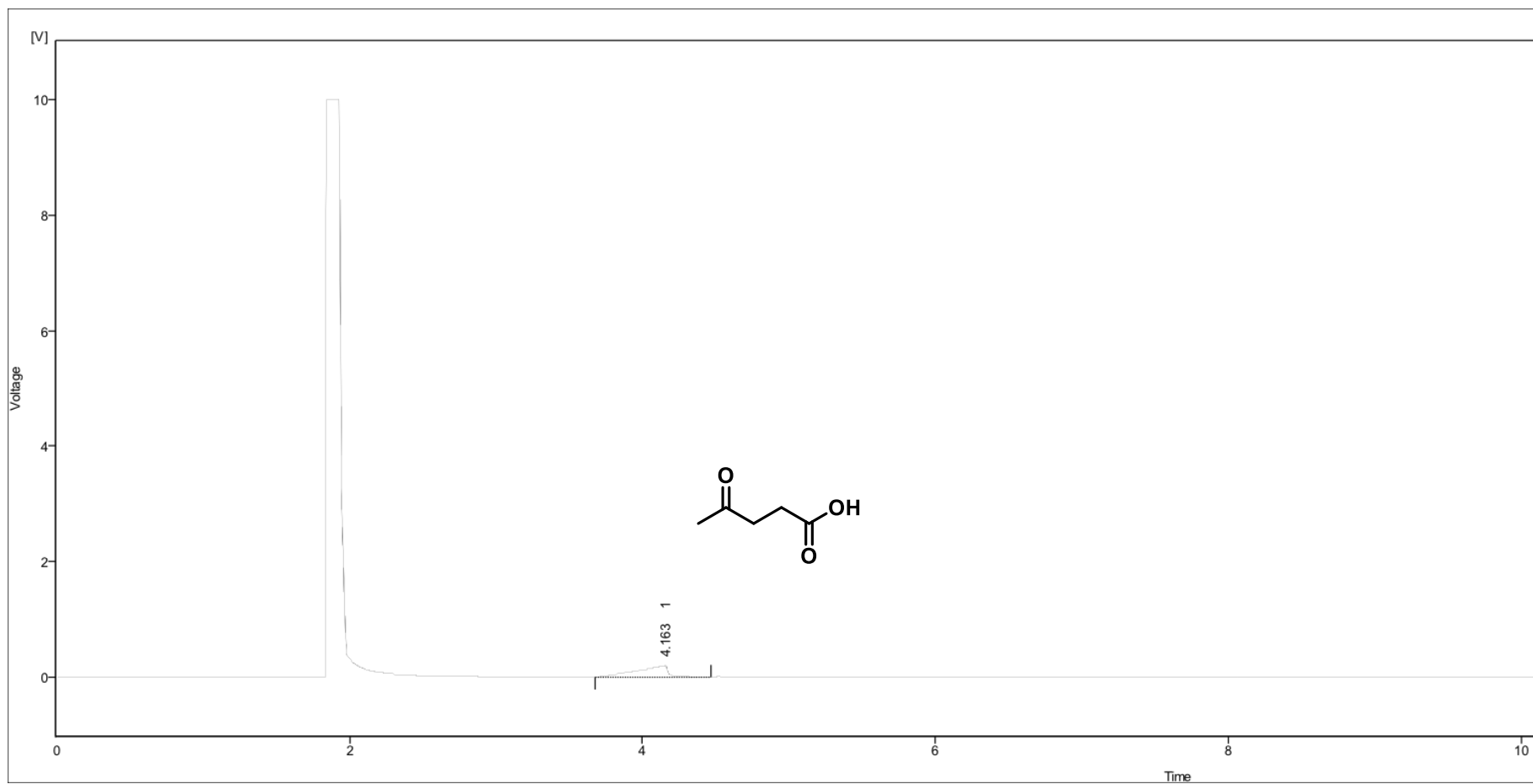


FIGURE A44 – GC-FID chromatogram of the levulinic acid standard.

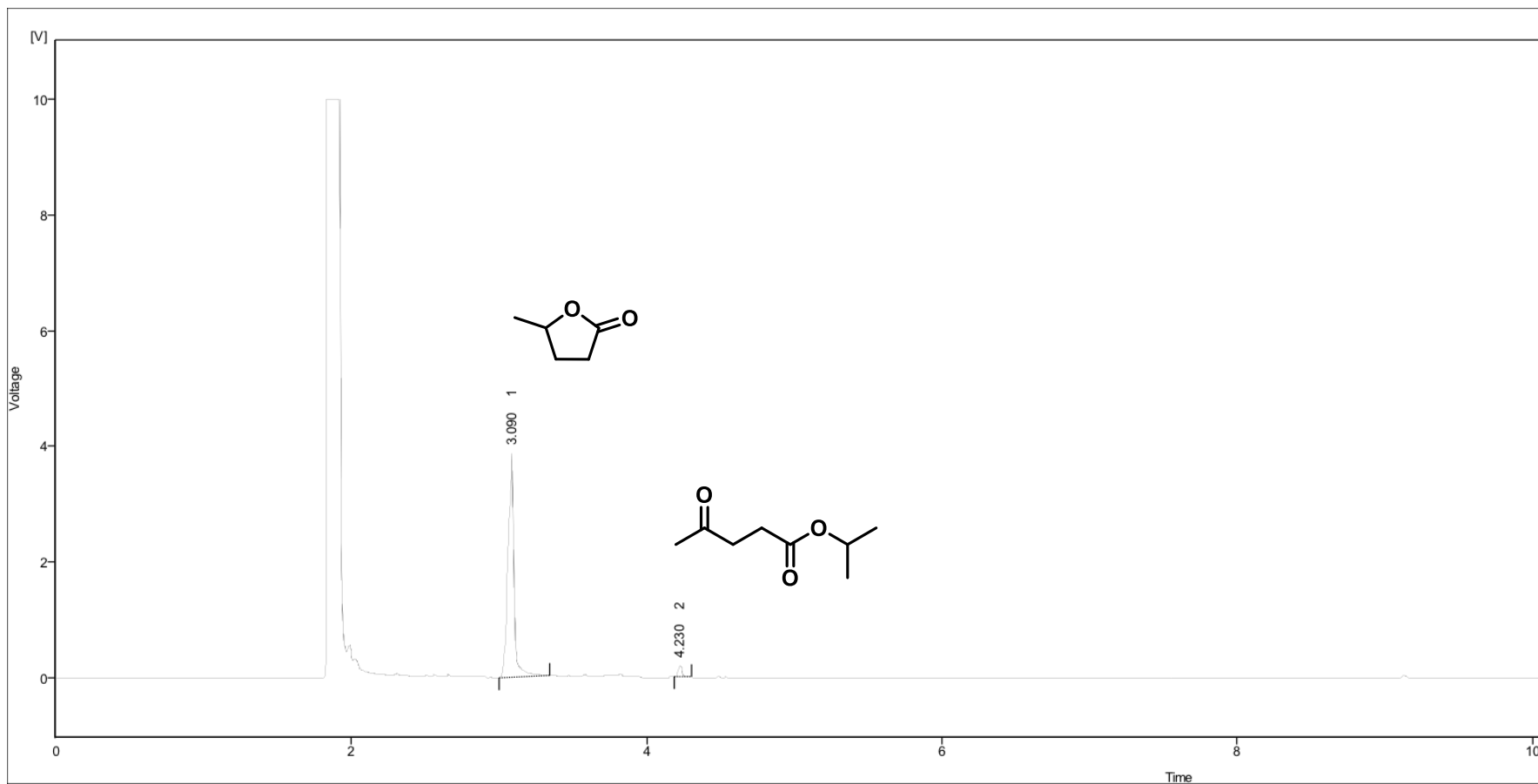


FIGURE A45 – GC-FID chromatogram of reaction in 2-propanol in optimized conditons.

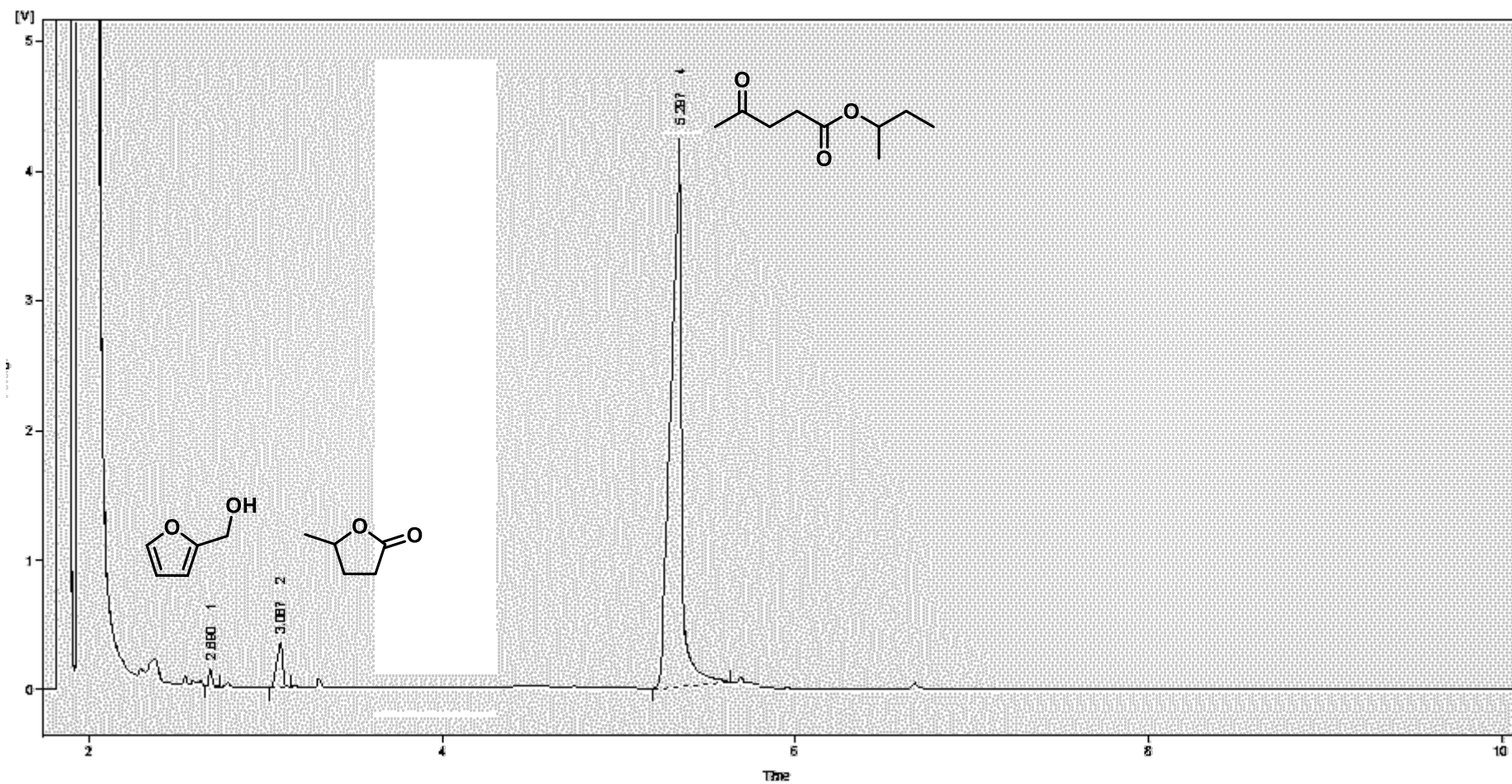


FIGURE A46 – GC-FID chromatogram of reaction in 2-butanol in optimized conditons.

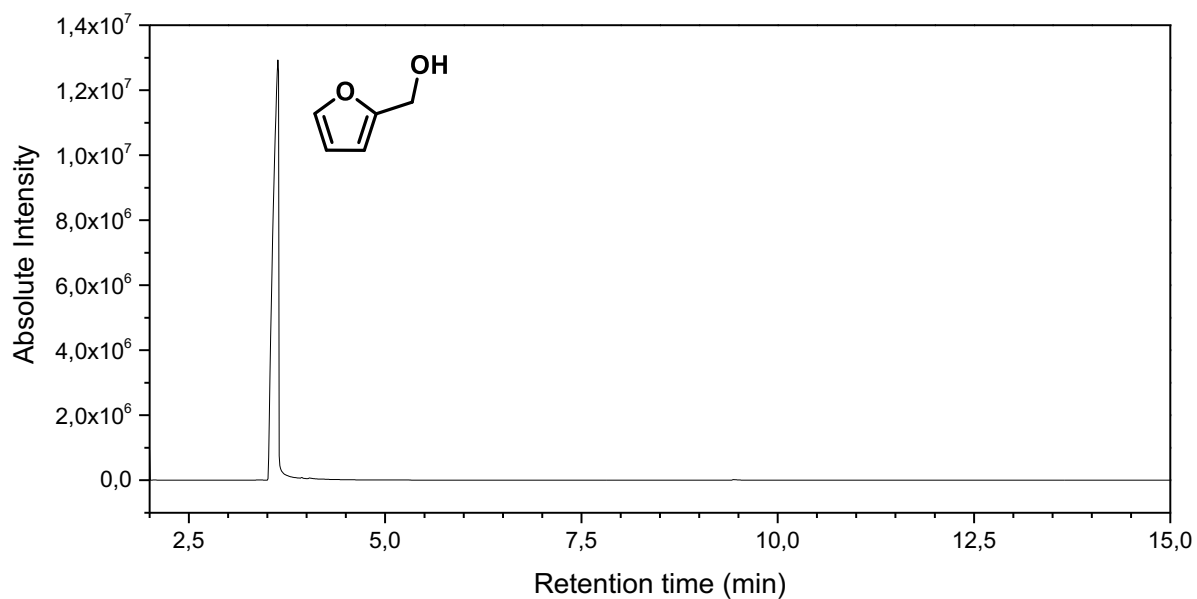


FIGURE A47 - Chromatogram of the furfuryl alcohol standard.

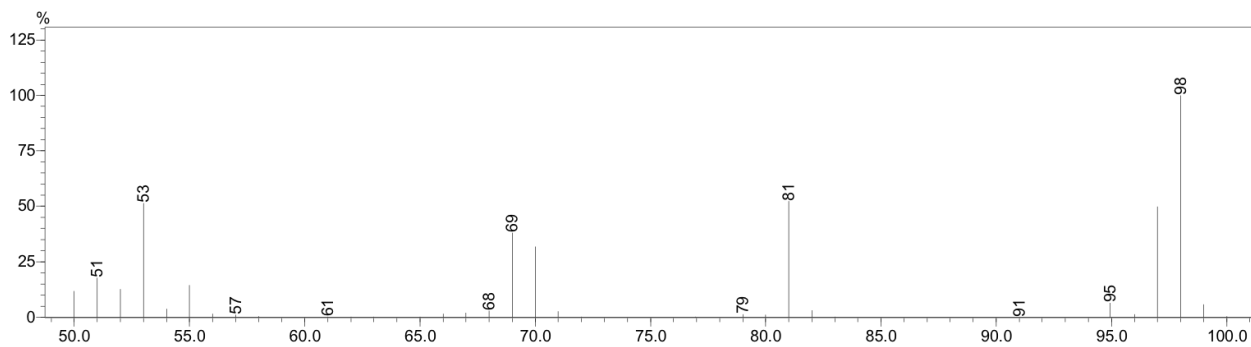


FIGURE A48 - Mass spectrum for the furfuryl alcohol standard.

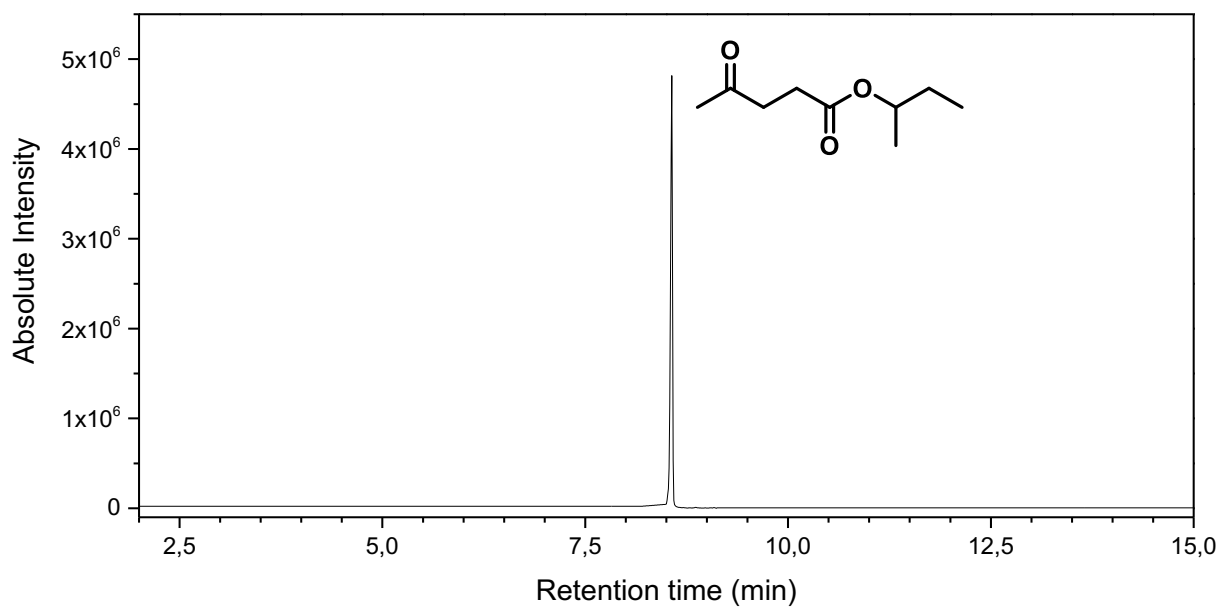


FIGURE A49 - Chromatogram of the 2-butyl levulinate standard.

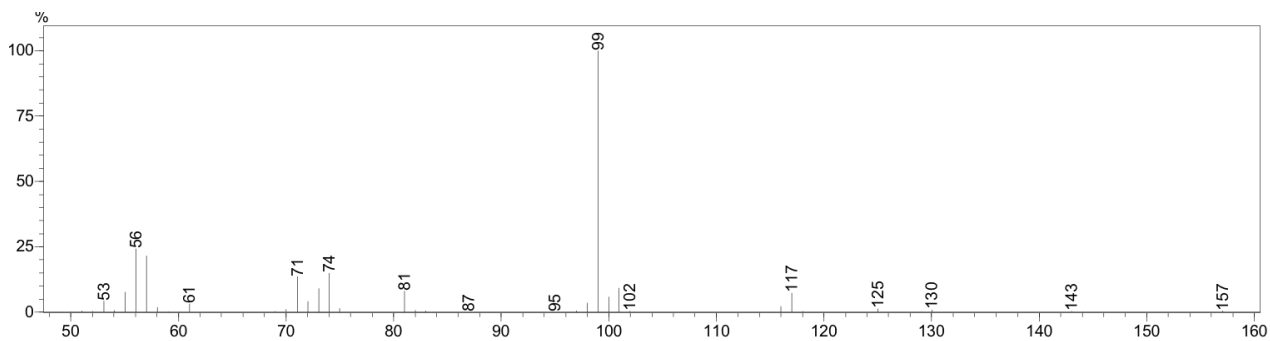


FIGURE A50 - Mass spectrum for the 2-butyl levulinate standard.

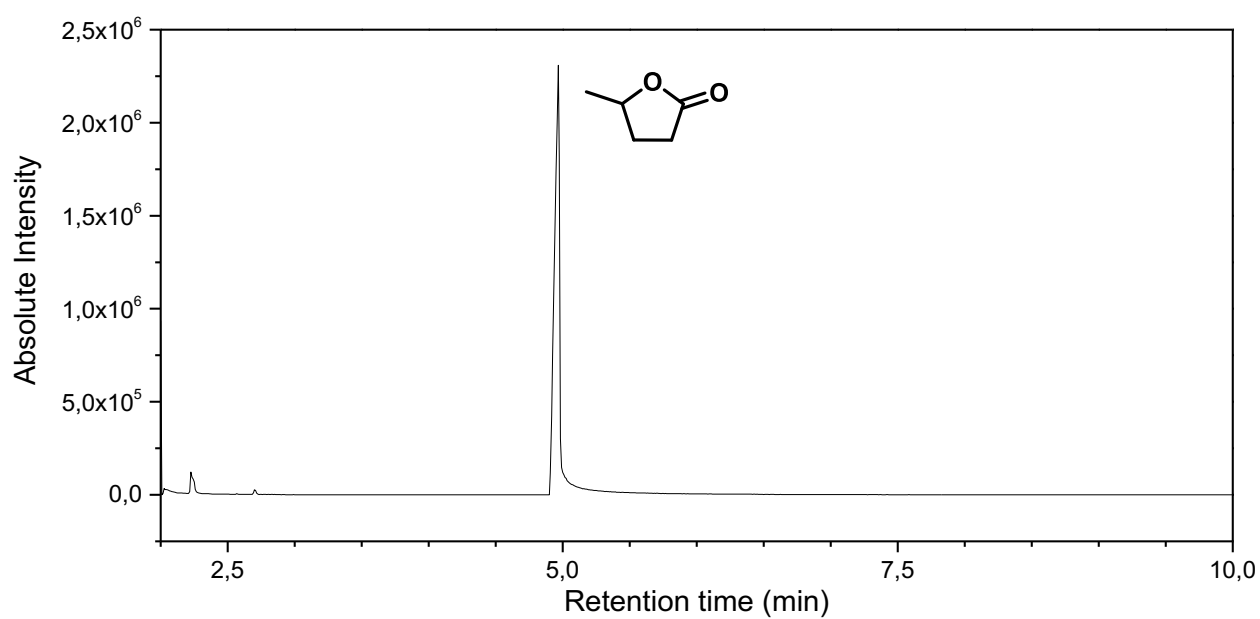


FIGURE A51 - Chromatogram of the GVL standard.

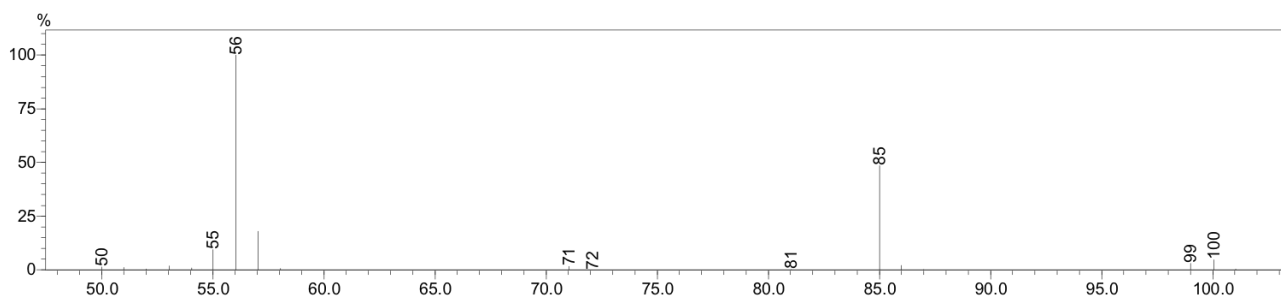


FIGURE A52 - Mass spectrum for the GVL standard.

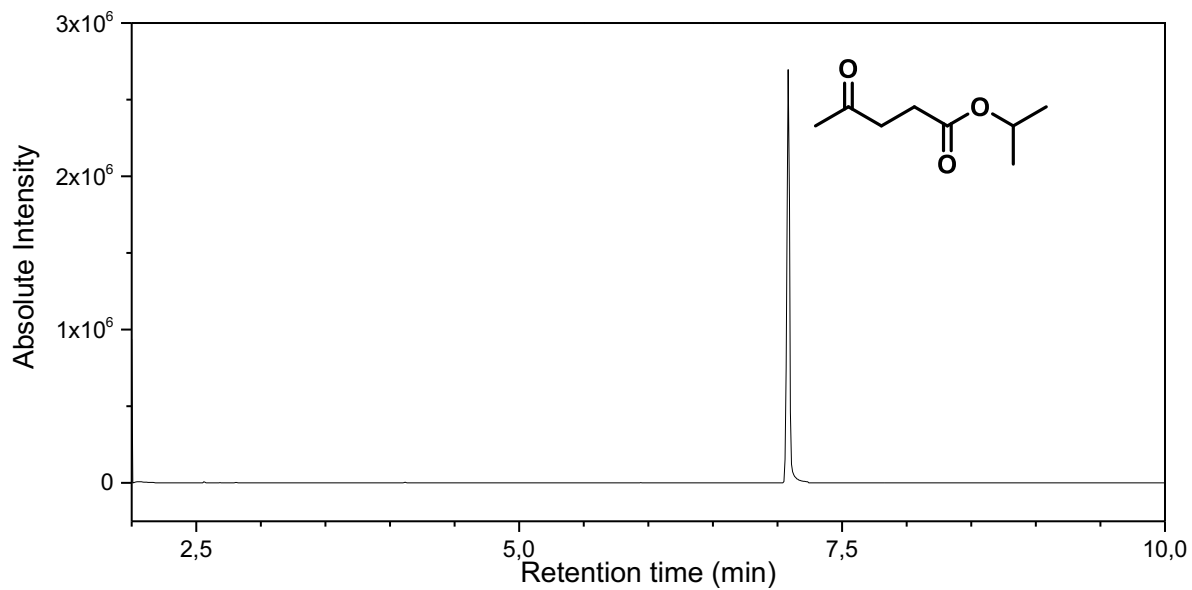


FIGURE A53 - Chromatogram of the 2-propyl levulinate standard.

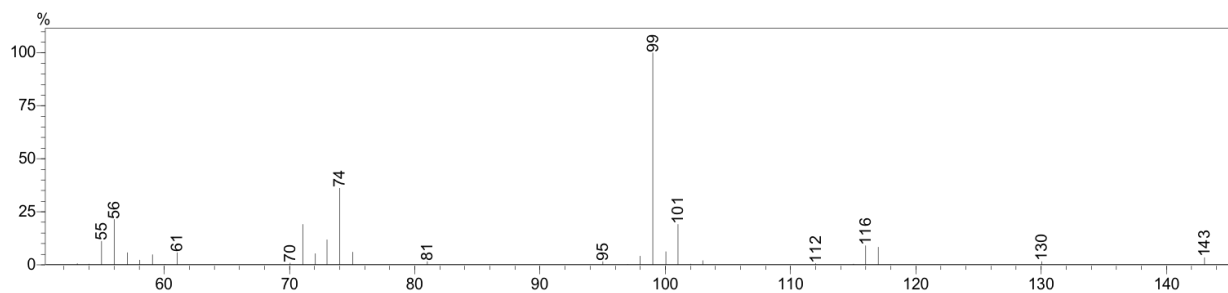


FIGURE A54 - Mass spectrum for the 2-propyl levulinate standard.

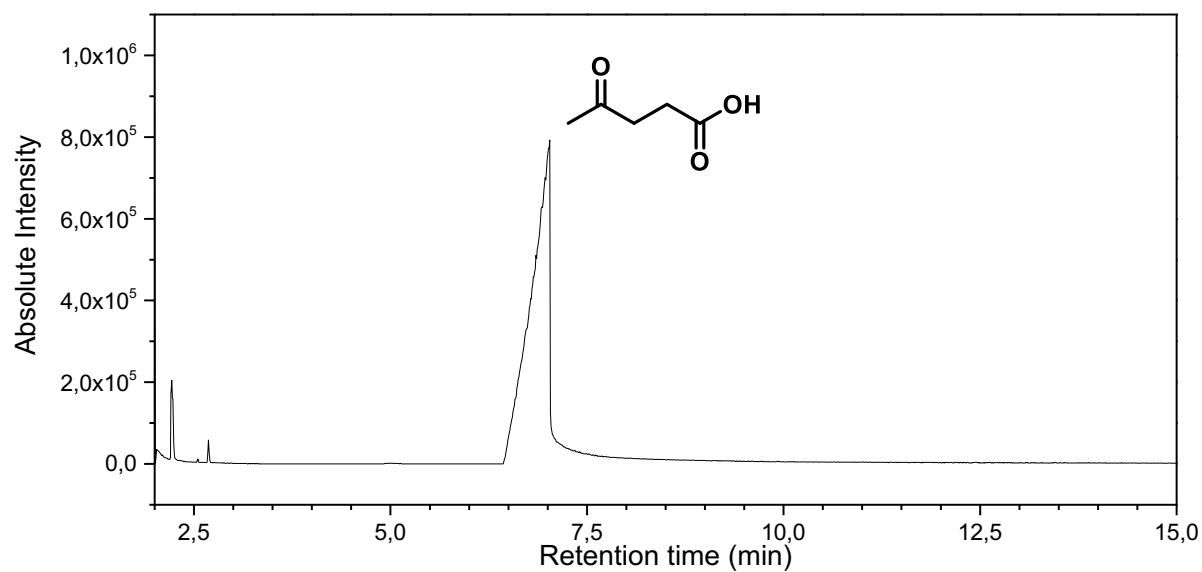


FIGURE A55 - Chromatogram of the levulinic acid standard.

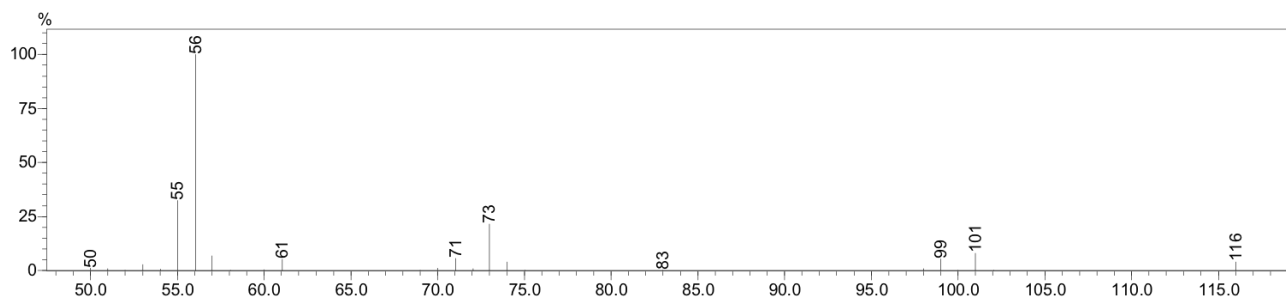


FIGURE A56 - Mass spectrum for the levulinic acid standard.

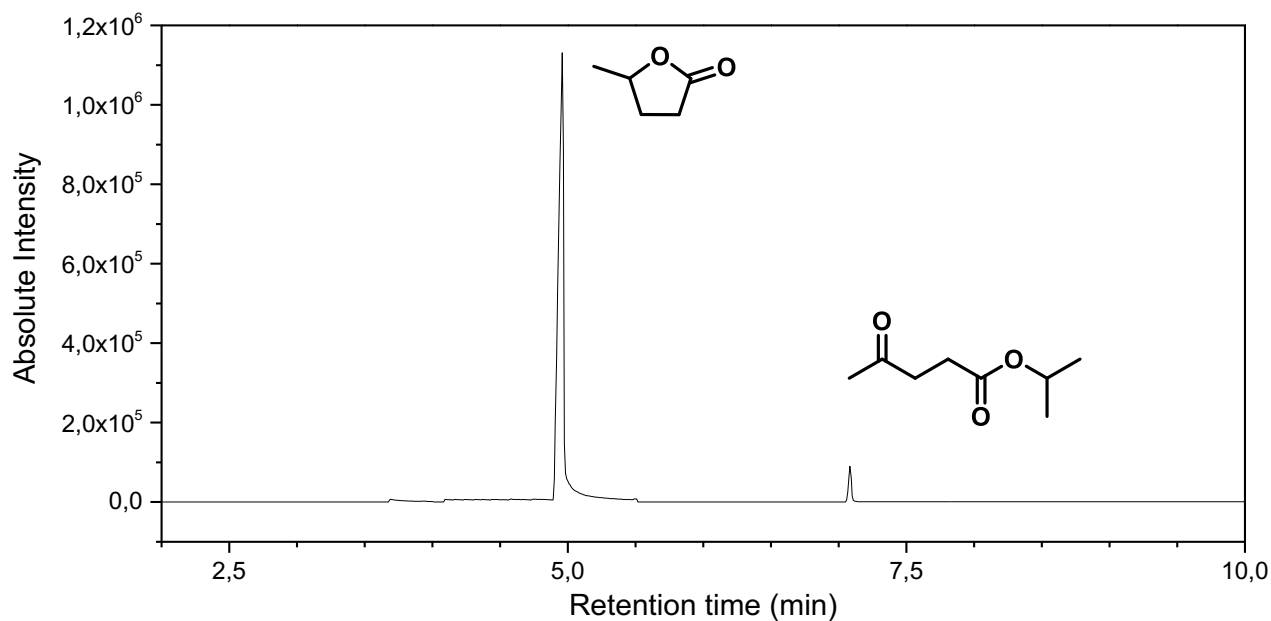


FIGURE A57 - Chromatogram of the reaction in optimized conditions in 2-propanol.

Table A1 - Data extracted from the chromatogram of the reaction in optimized conditions in 2-propanol.

Peak #	Initial time	End time	Ret. time	Peak Area	% Area
1	4.92	5.28	4.96	54912	96.8
2	7.05	7.12	7.08	1815	3.2

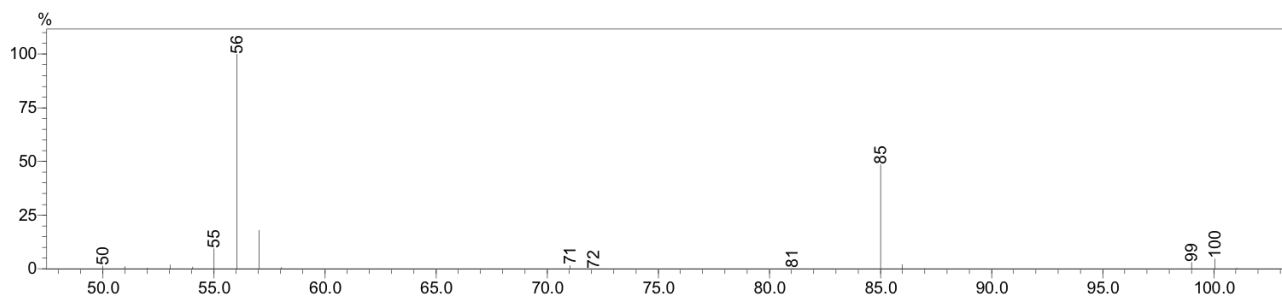


FIGURE A58 - Mass spectrum of peak #1 of the reaction in optimized conditions in 2-propanol.

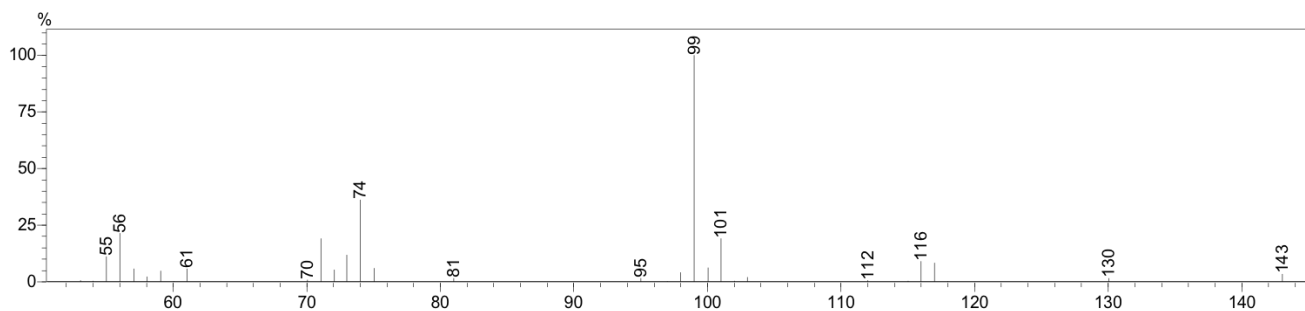


FIGURE A59 - Mass spectrum of peak #2 of the reaction in optimized conditions in 2-propanol.

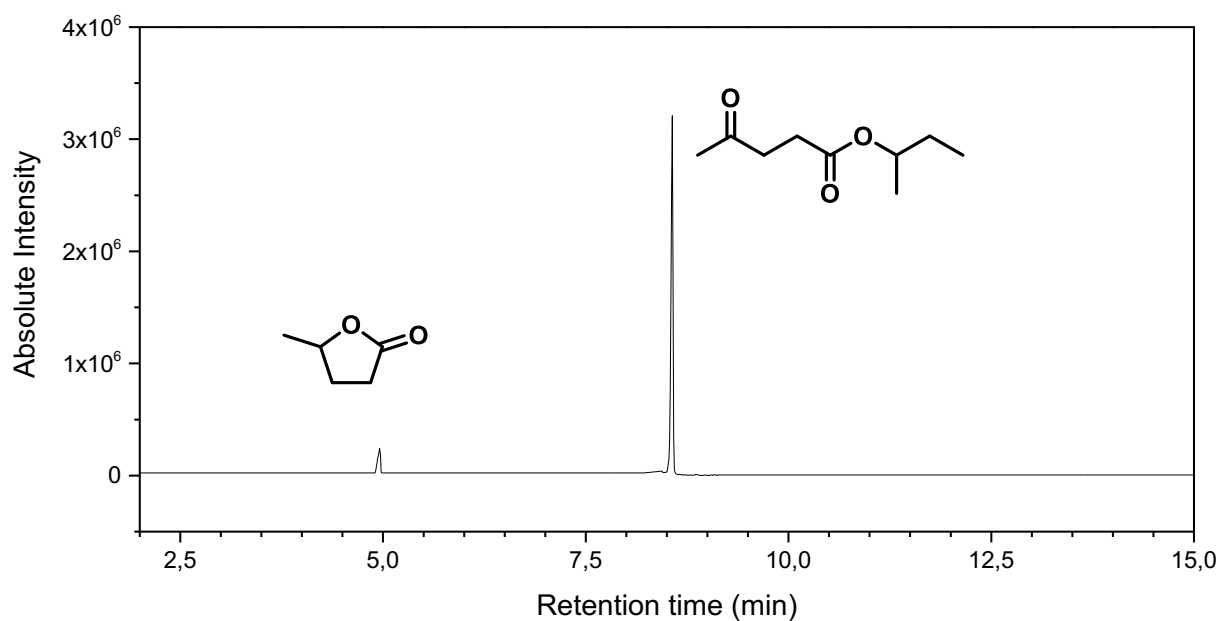


FIGURE A60 - Chromatogram of the reaction in optimized conditions in 2-butanol.

Table A2 - Data extracted from the chromatogram of the reaction in optimized conditions in 2-propanol.

Peak #	Initial time	End time	Ret. time	Peak Area	% Area
1	4.91	5.37	5.96	3323	3.3
2	8.45	8.62	8.57	100537	96.7

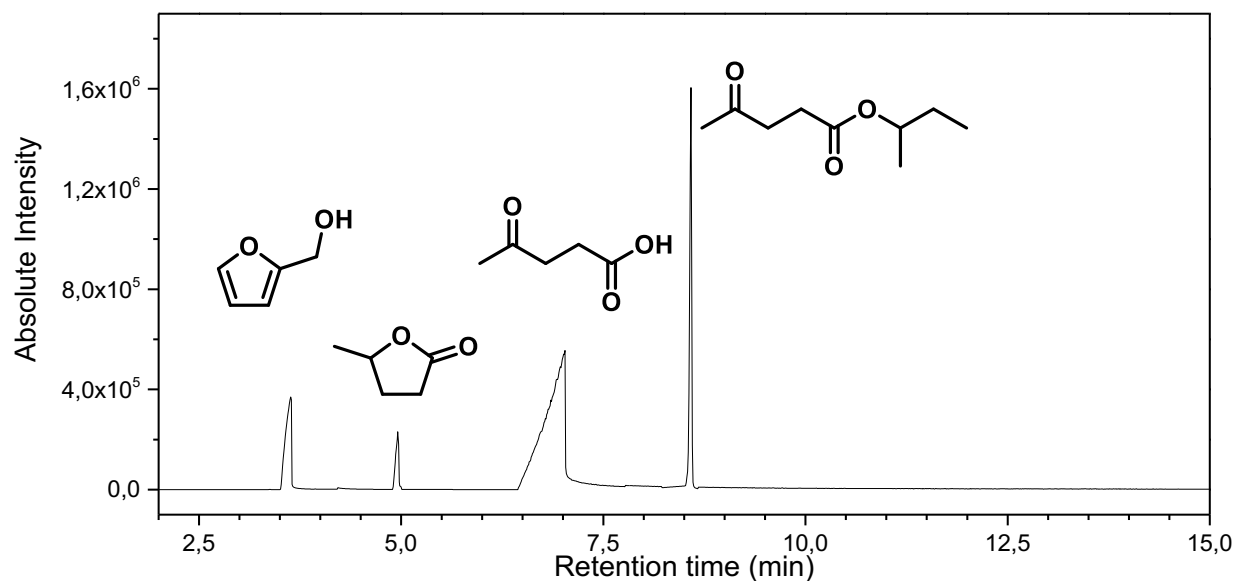


FIGURE A61 - Chromatogram of the reaction in 2-butanol in the presence of 5% of water.

Table A3 - Data extracted from the chromatogram of the reaction in 2-butanol in the presence of 5% of water.

Peak #	Initial time	End time	Ret. time	Peak Area	% Area
1	3.47	3.49	3.69	29688	11,7
2	4.82	5.40	4.96	9186	3,6
3	6.46	7.14	7.02	171401	67,5
4	8.52	8.64	8.58	43467	17,1

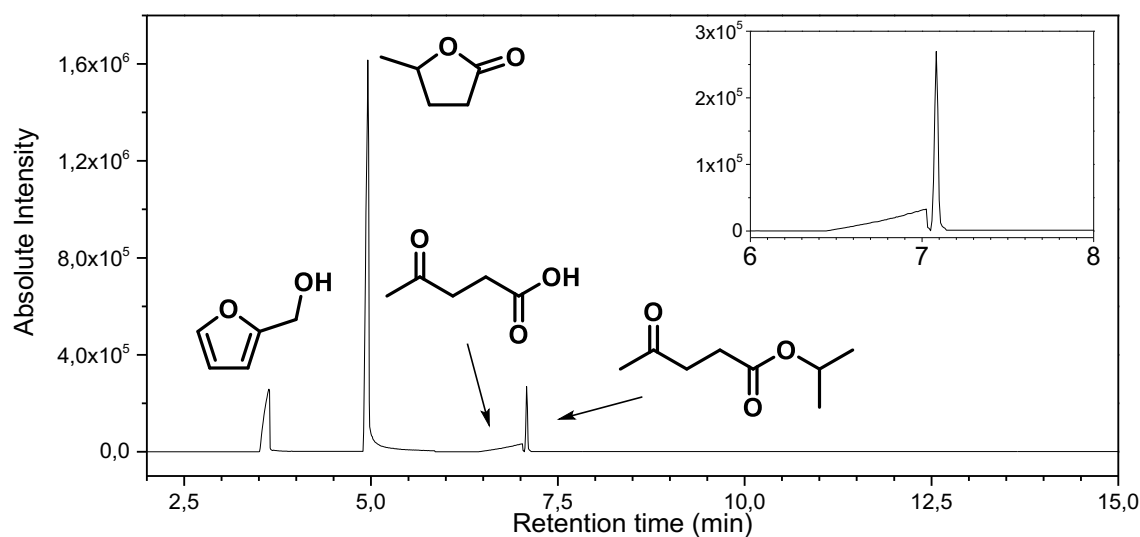


FIGURE A62 - Chromatogram of the reaction in 2-propanol in the presence of 5% of water.

Table A4 - Data extracted from the chromatogram of the reaction in 2-propanol in the presence of 5% water.

Peak #	Initial time	End time	Ret. time	Peak Area	% Area
1	3.50	3.49	3.69	10391	8,6
2	4.86	5.52	4.96	96189	79,6
3	6.44	7.12	7.02	2650	2,2
4	8.52	8.62	8.58	11596	9,6

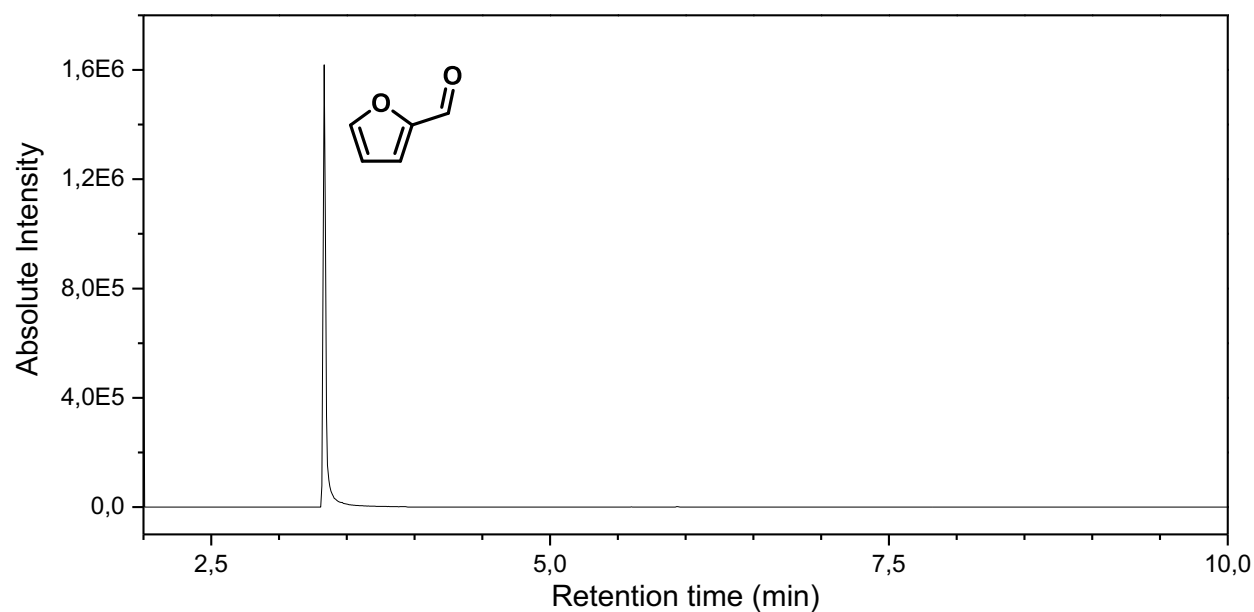


FIGURE A63 – GC-MS cromatogram of the furfural standard.

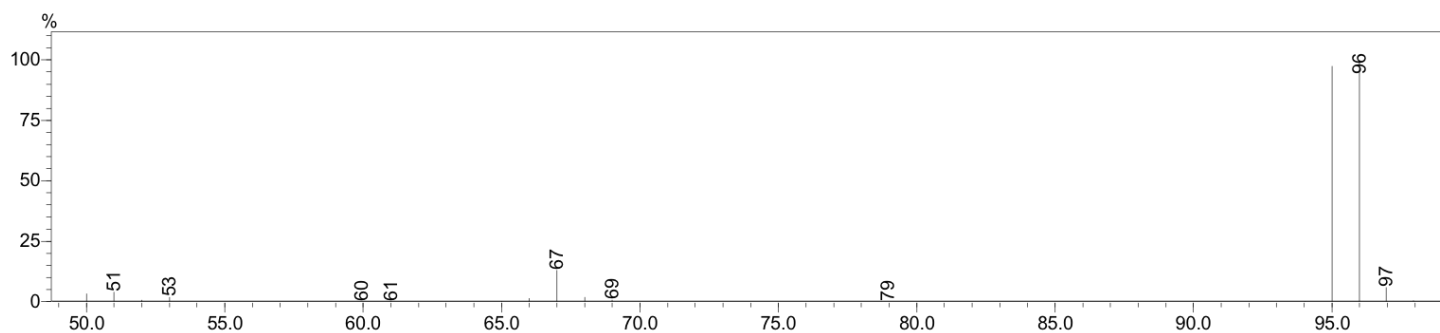


FIGURE A64 – Mass spectrum of the furfural standard.

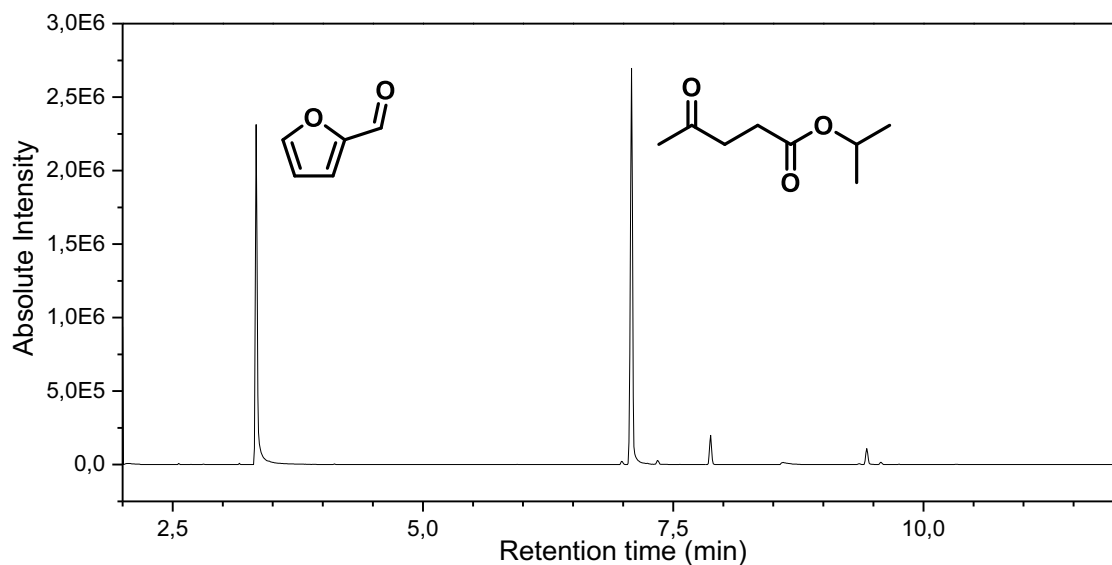


FIGURE A65 – GC-MS chromatogram of the reaction of furfural conversion to 2-propyl levulinate in 2-propanol at 130°C using 750µL of solvent and 50 mg of catalyst.

Table A5 - Data extracted from the chromatogram of the reaction of furfural conversion to 2-propyl levulinate in 2-propanol at 130°C using 750µL of solvent and 50 mg of catalyst.

Peak #	Initial time	End time	Ret. time	Peak Area	% Area
1	3.26	3.44	3.33	3074958	41.9
2	7.01	7.17	7.08	3983378	54.3
3	7.80	7.90	7.87	271704	3.7

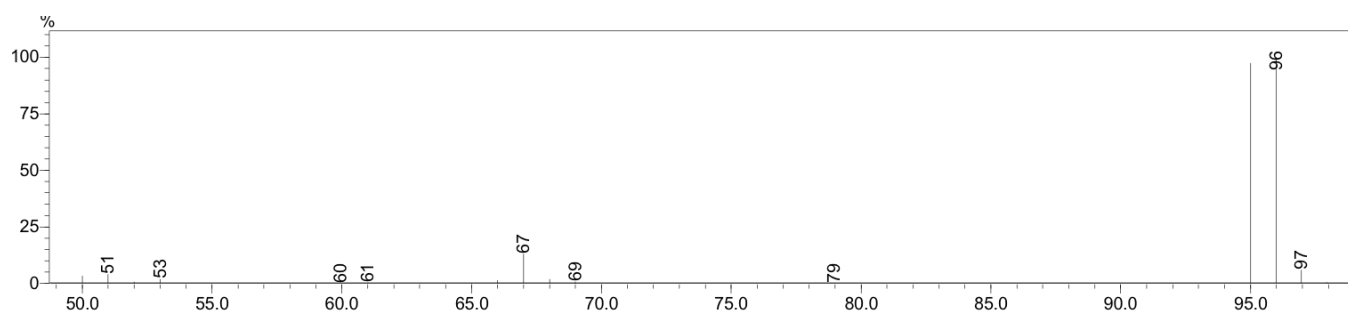


FIGURE A66 – Mass spectrum of the peak #1 in chromatogram of the reaction of furfural conversion to 2-propyl levulinate in 2-propanol.

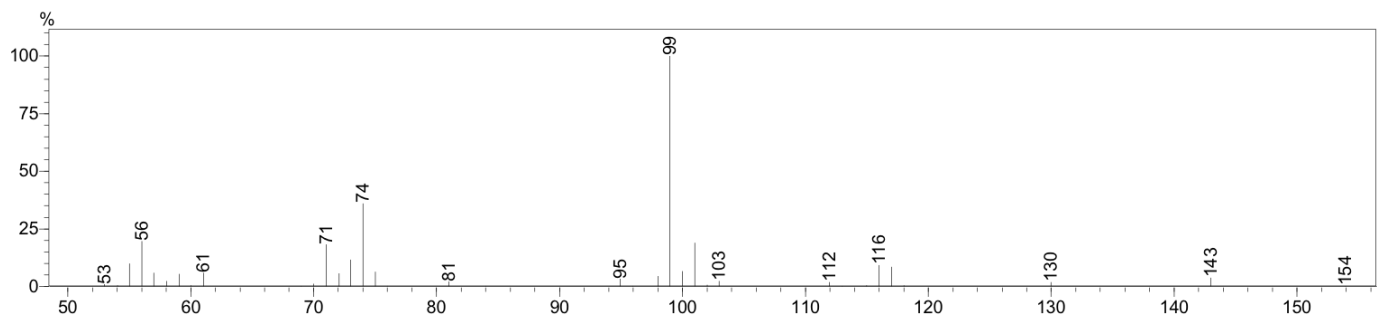


FIGURE A67 – Mass spectrum of the peak #2 in the chromatogram of the reaction of furfural conversion to 2-propyl levulinate in 2-propanol.

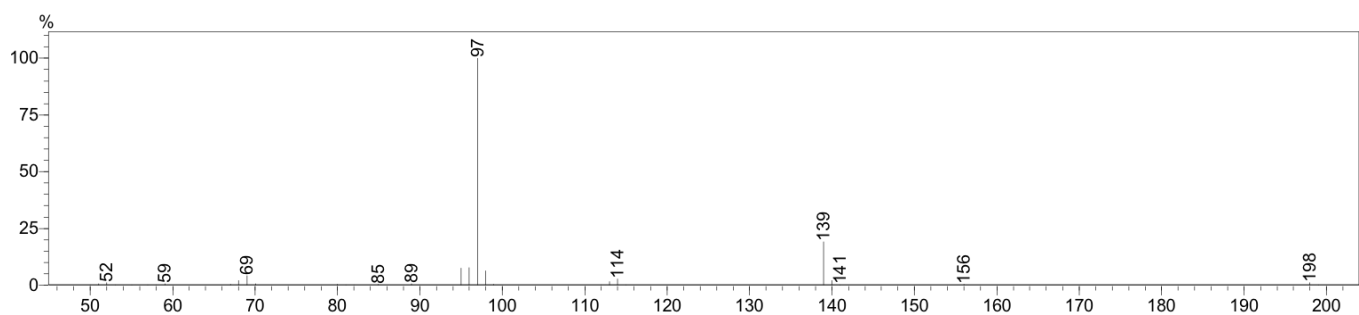


FIGURE A68 – Mass spectrum of the peak #3 in the chromatogram of the reaction of furfural conversion to 2-propyl levulinate in 2-propanol.

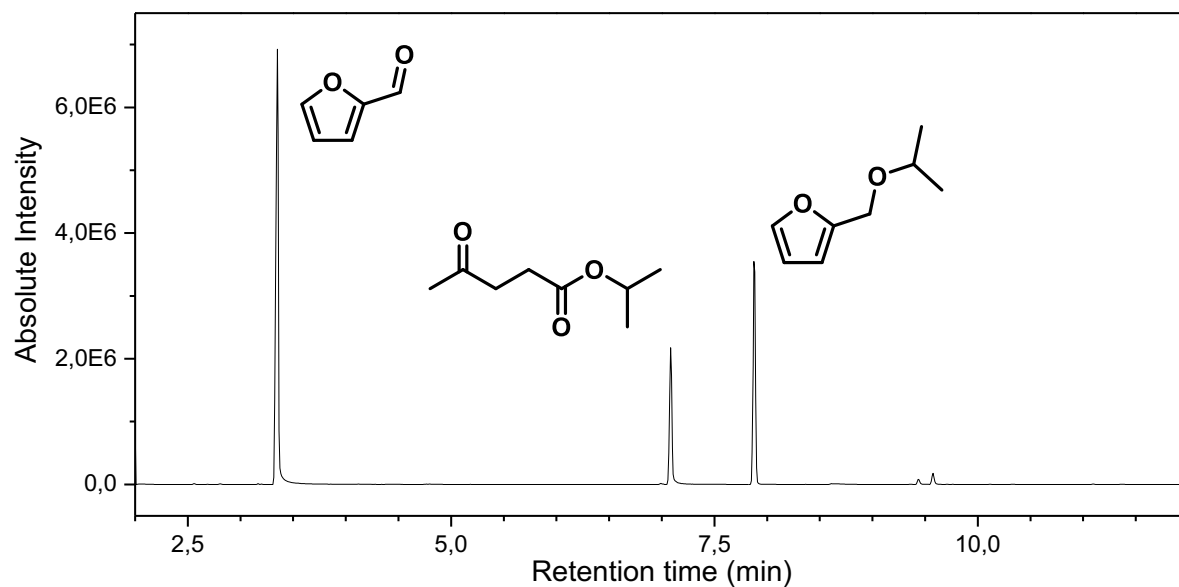


FIGURE A69 – GC-MS chromatogram of the reaction of furfural conversion to 2-propyl levulinate in 2-propanol at 130°C using 1250 μ L of solvent and 50 mg of catalyst.

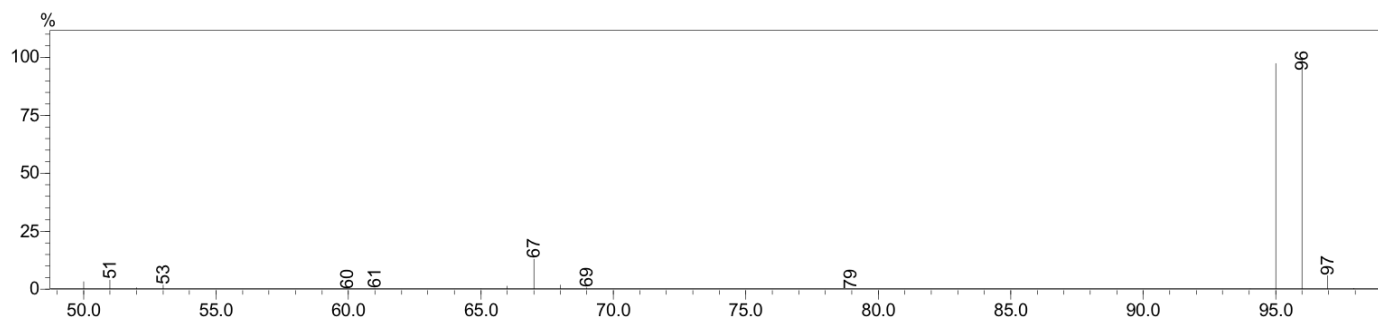


FIGURE A70 – Mass spectrum of the peak #1 in the chromatogram of the reaction of furfural conversion to 2-propyl levulinate in 2-propanol at 130°C using 1250 μ L of solvent and 50 mg of catalyst.

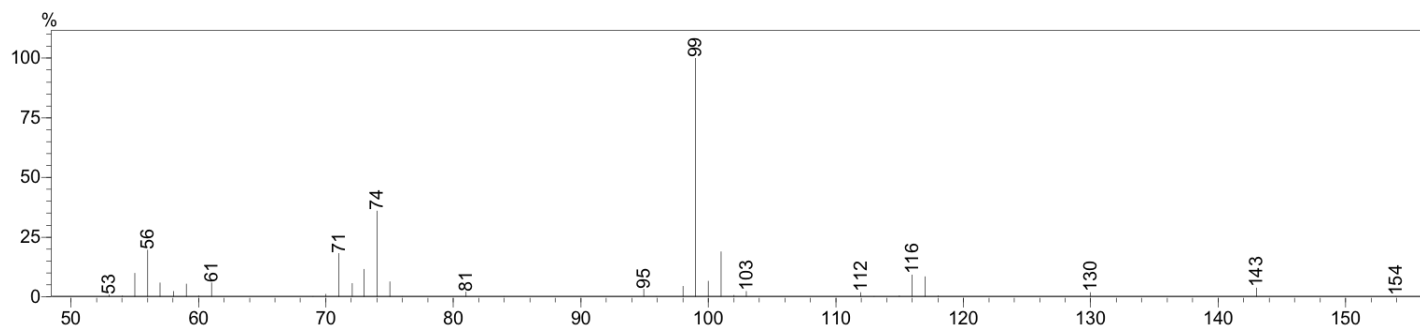


FIGURE A71 – Mass spectrum of the peak #2 in the chromatogram of the reaction of furfural conversion to 2-propyl levulinate in 2-propanol at 130°C using 1250 μ L of solvent and 50 mg of catalyst.

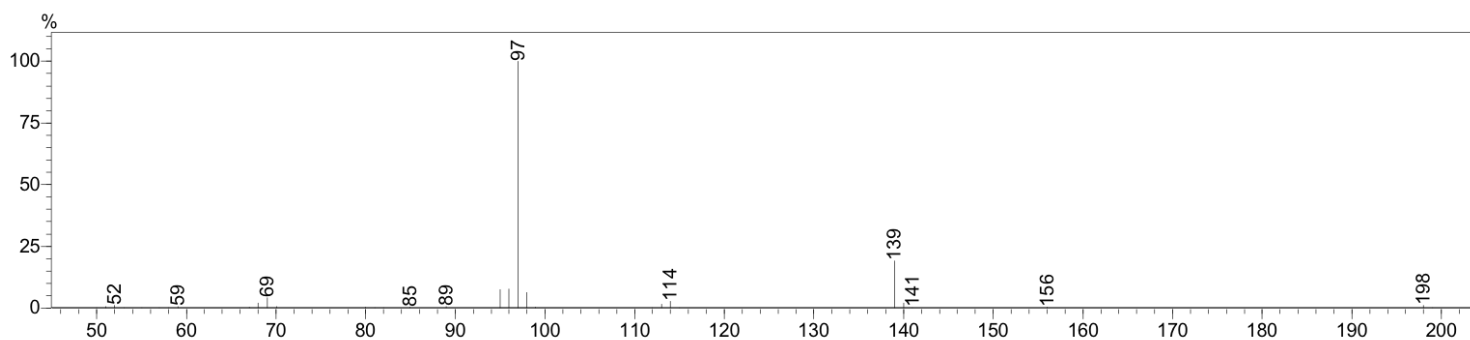


FIGURE A72 – Mass spectrum of the peak #3 in the chromatogram of the reaction of furfural conversion to 2-propyl levulinate in 2-propanol at 130°C using 1250 μ L of solvent and 50 mg of catalyst.

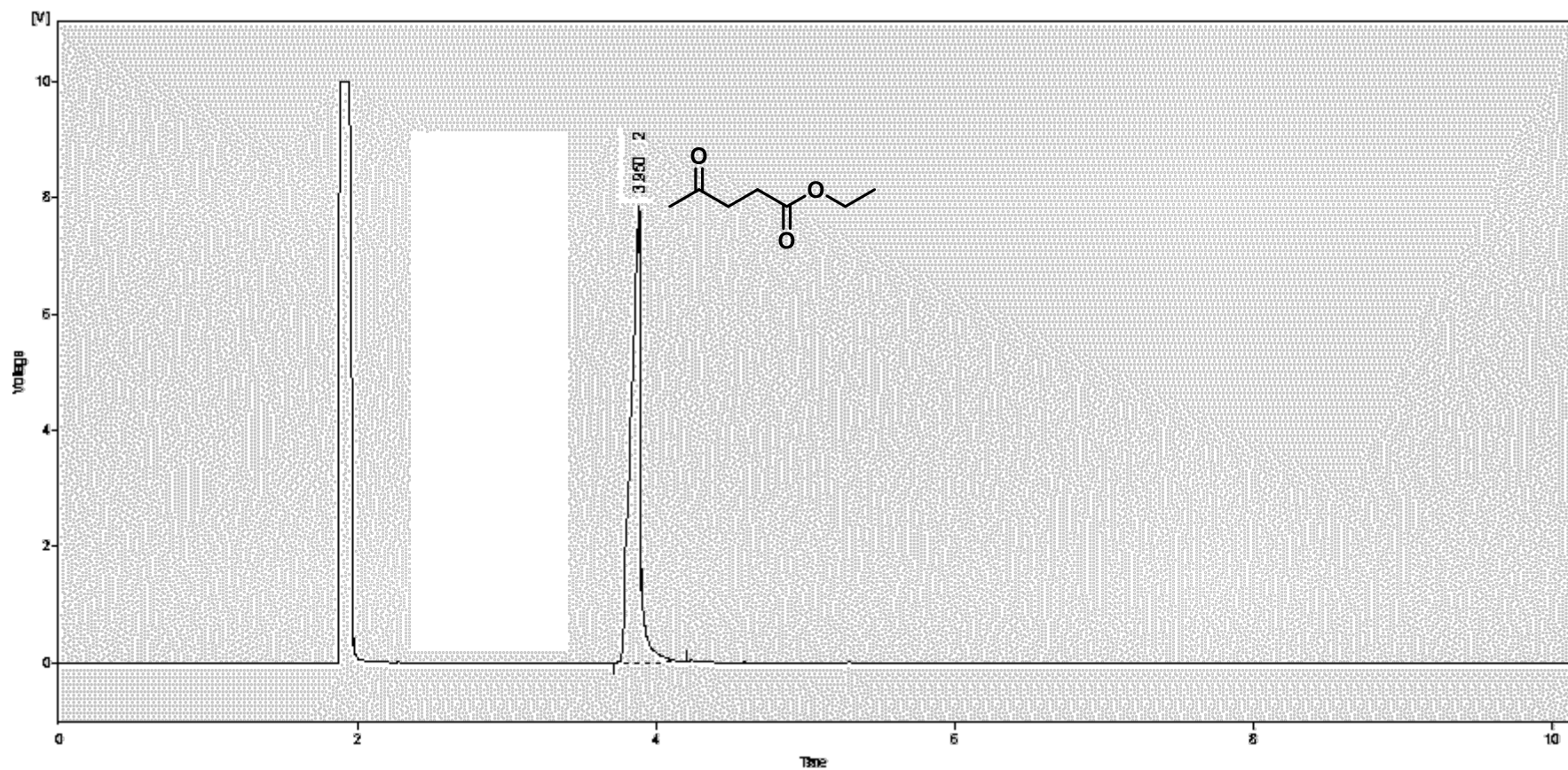


FIGURE A73 – GC-FID chromatogram of the ethyl levulinate standard.

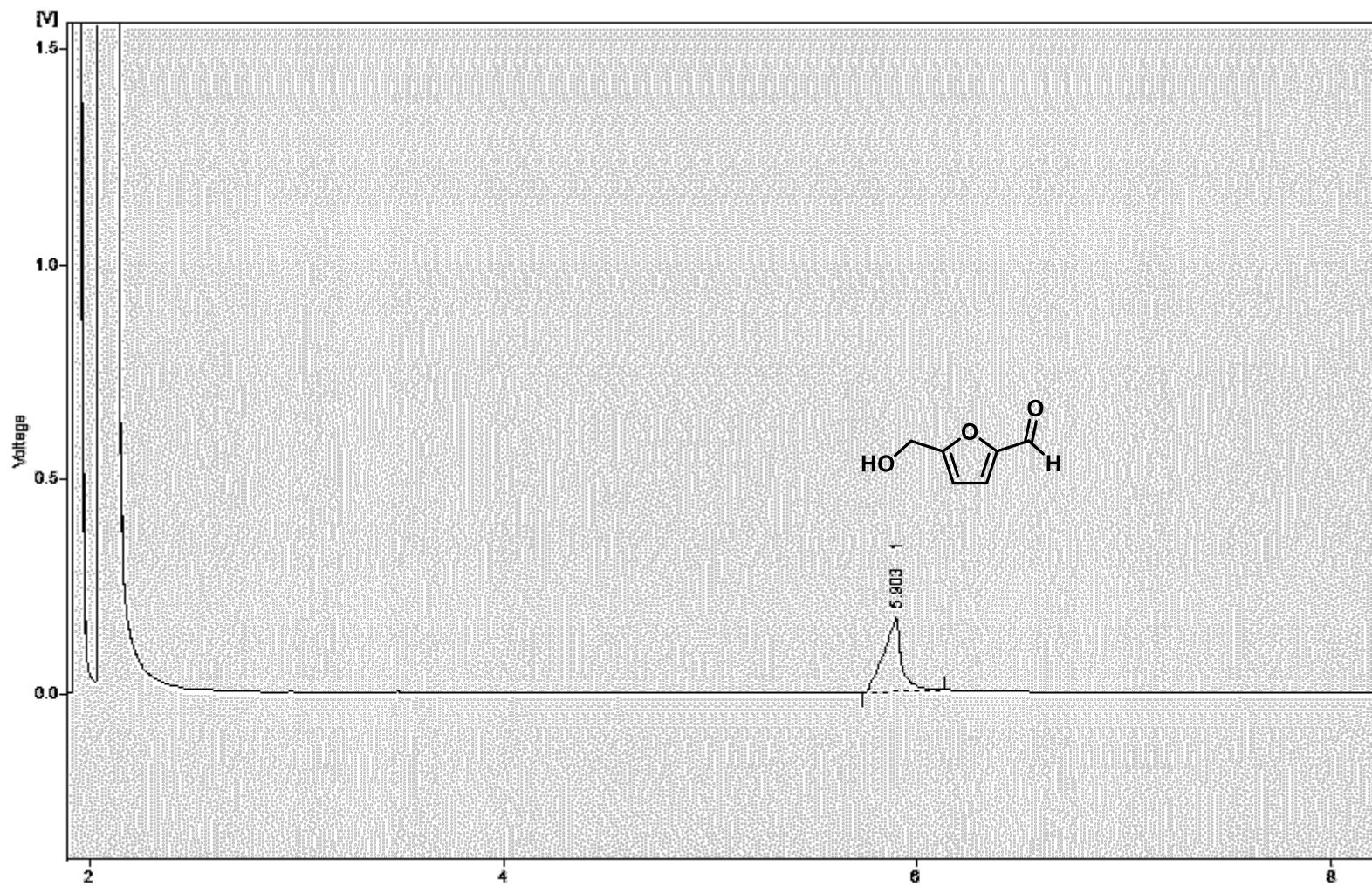


FIGURE A74 – GC-FID chromatogram of the HMF standard.

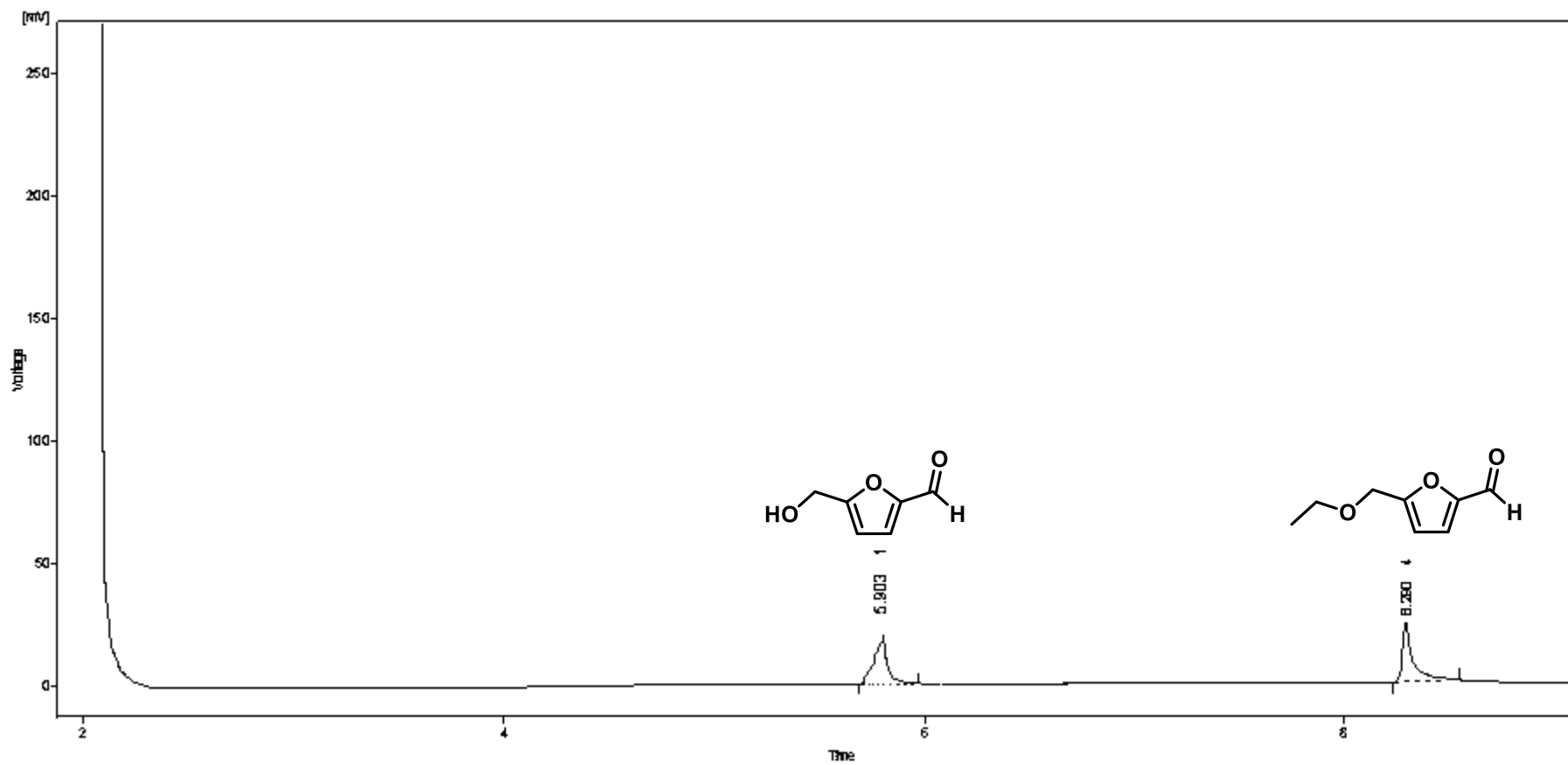


FIGURE A75 – GC-FID chromatogram of the EMF standard.

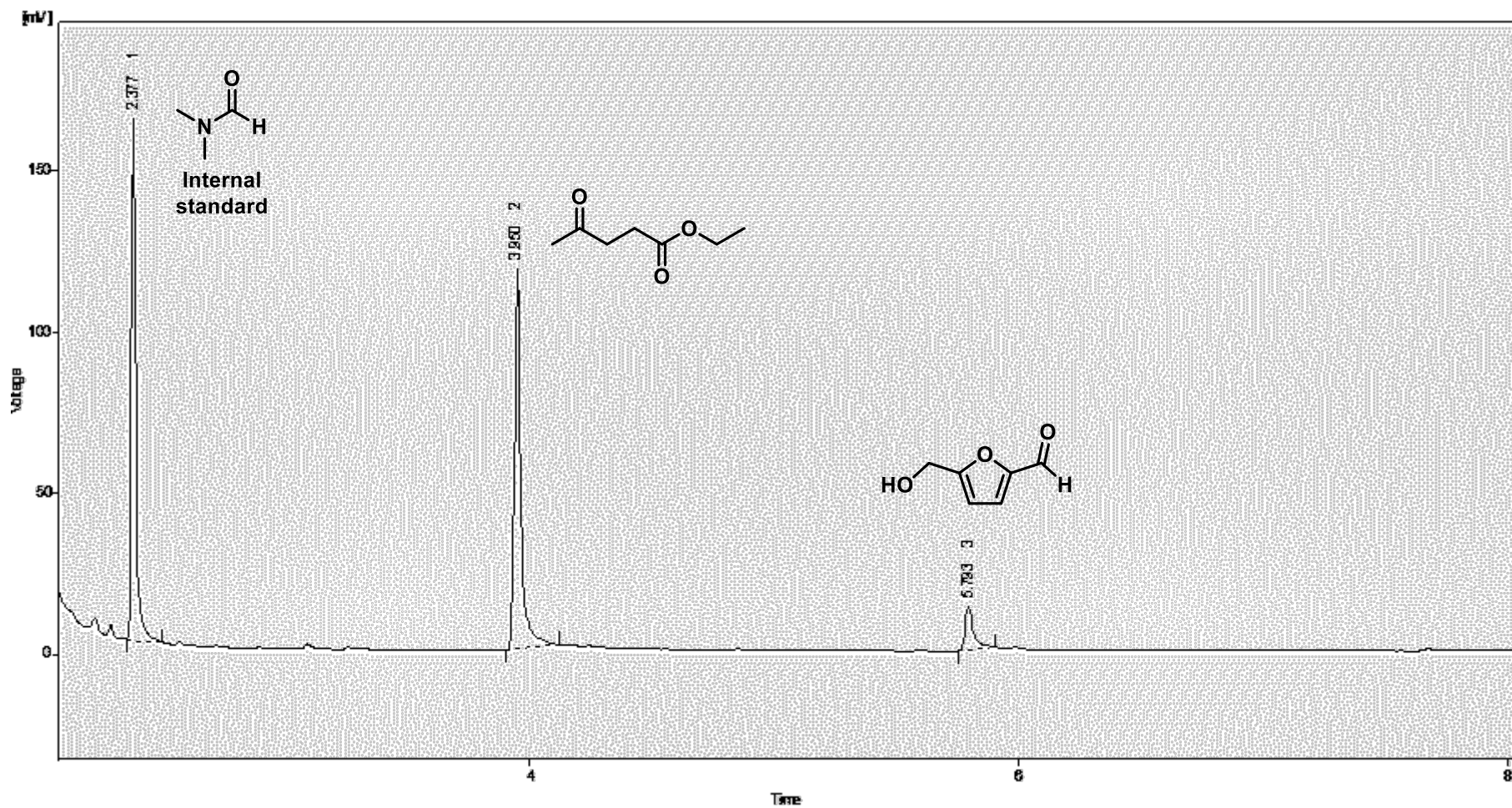


FIGURE A76 – GC- FID chromatogram of the reaction for the conversion of fructose to ethyl levulinate in ethanol at 170°C using 75 mg of catalyst.

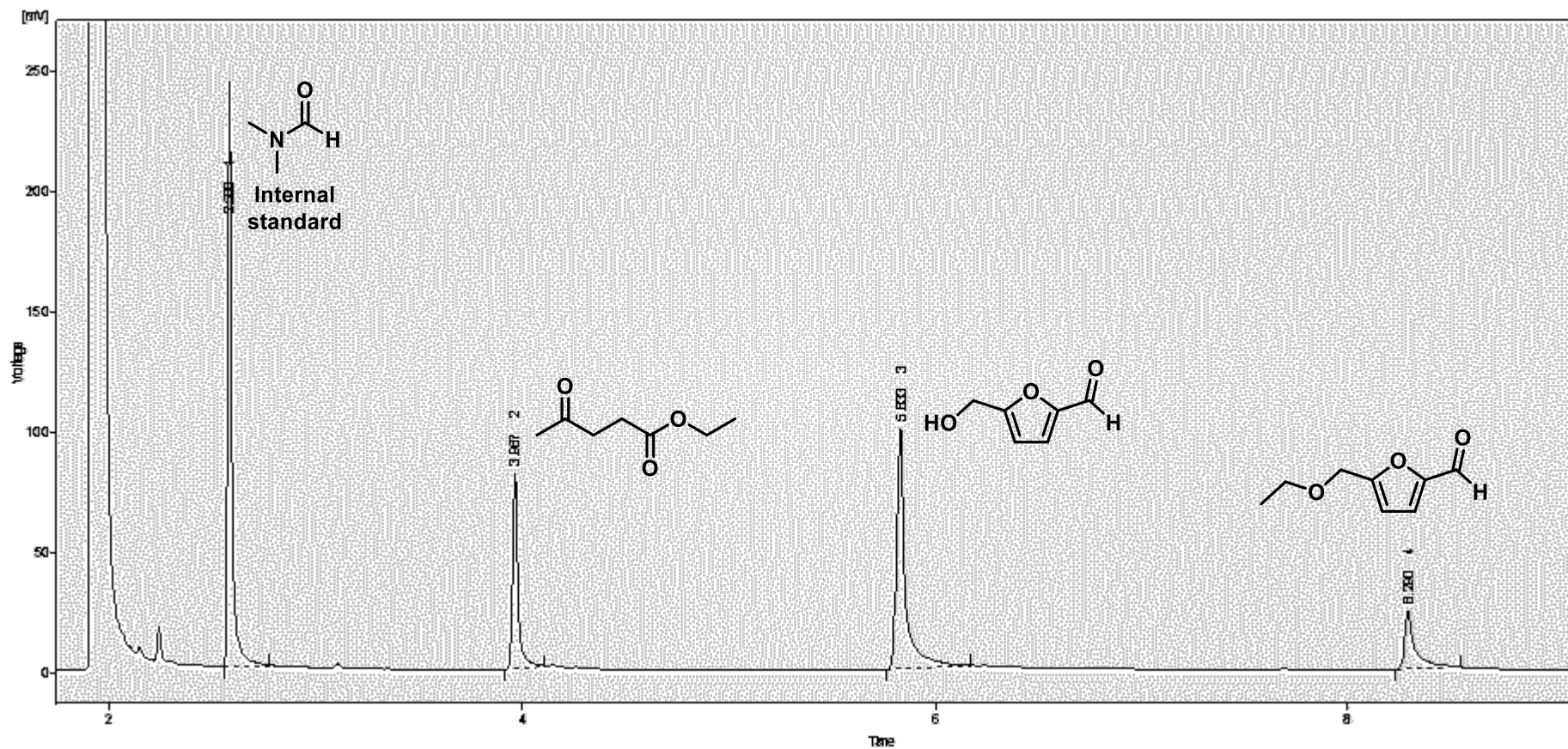


FIGURE A77 – GC- FID cromatogram of the reaction for the conversion of fructose to ethyl levulinate in ethanol at 170°C using 10 mg of catalyst.

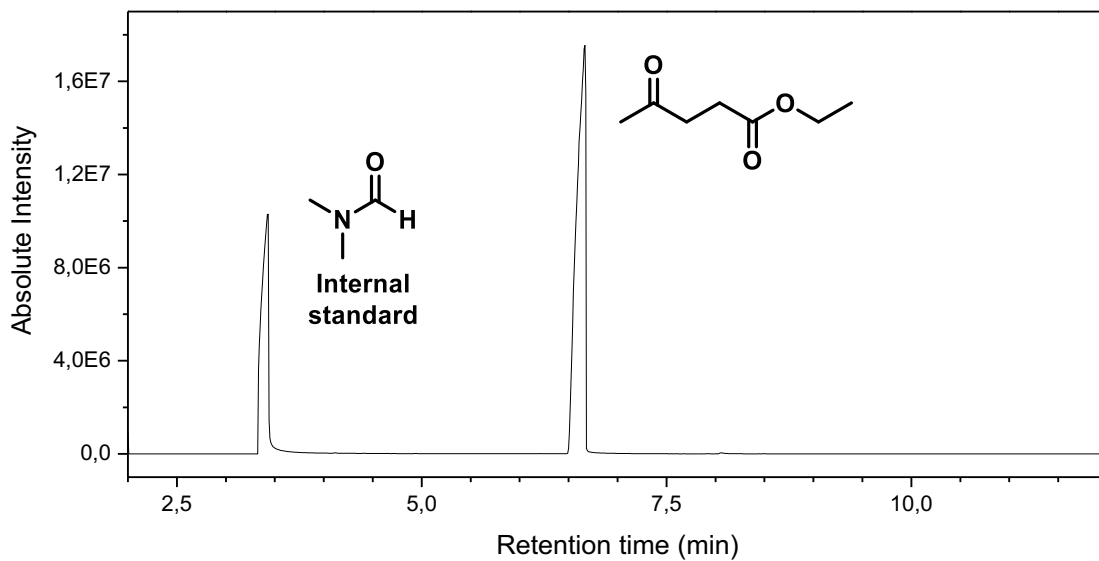


FIGURE A78 - GC-MS chromatogram of the ethyl levulinate standard in the presence of DMF.

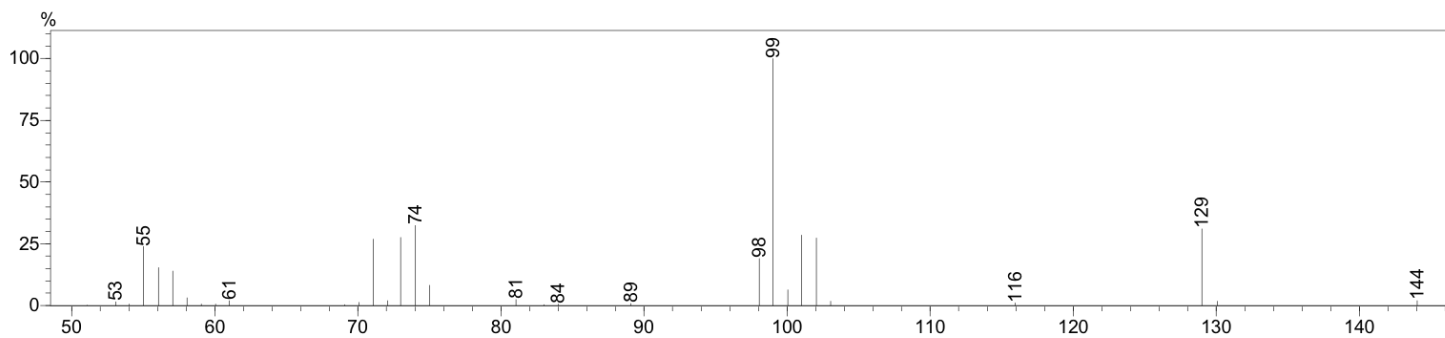


FIGURE A79 – Mass spectrum of the ethyl levulinate standard.

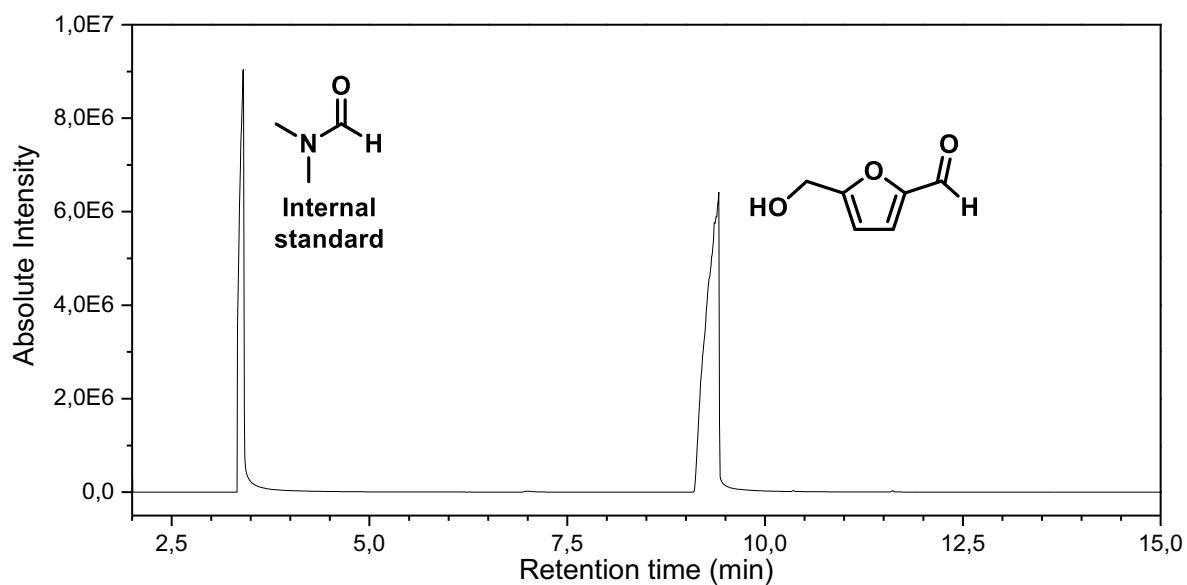


FIGURE A80 - GC-MS chromatogram of the HMF standard in the presence of DMF.

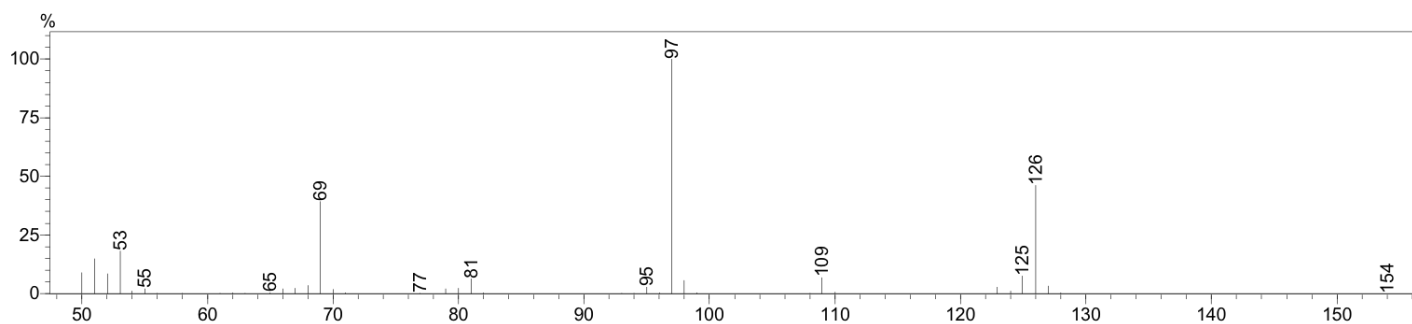


FIGURE A81 – Mass spectrum of the HMF standard.

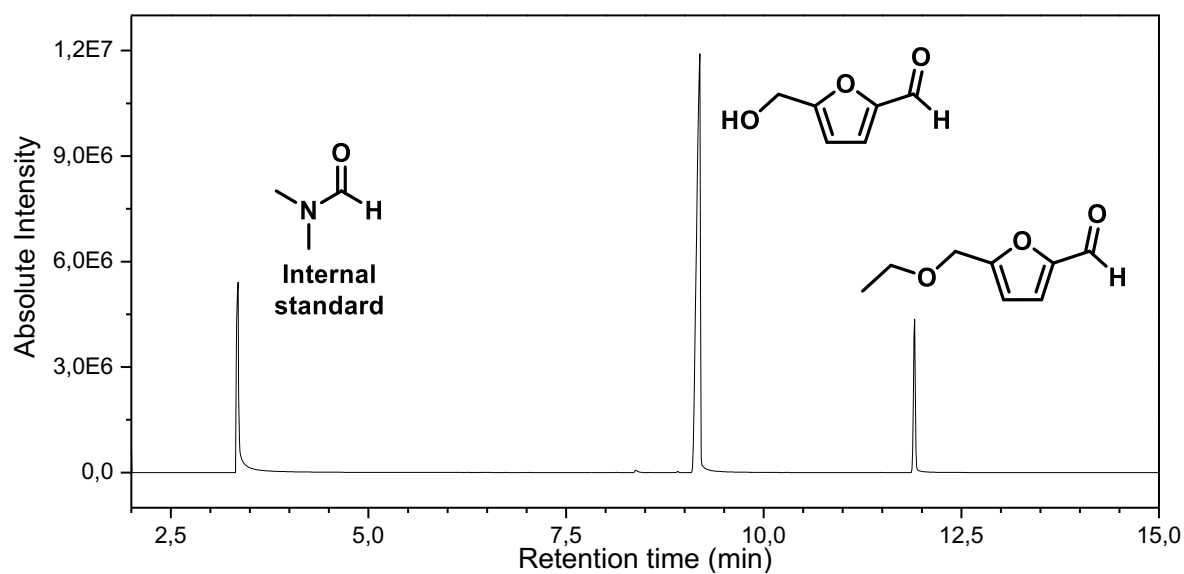


FIGURE A82 - GC-MS cromatogram of the EMF standard in the presence of DMF.

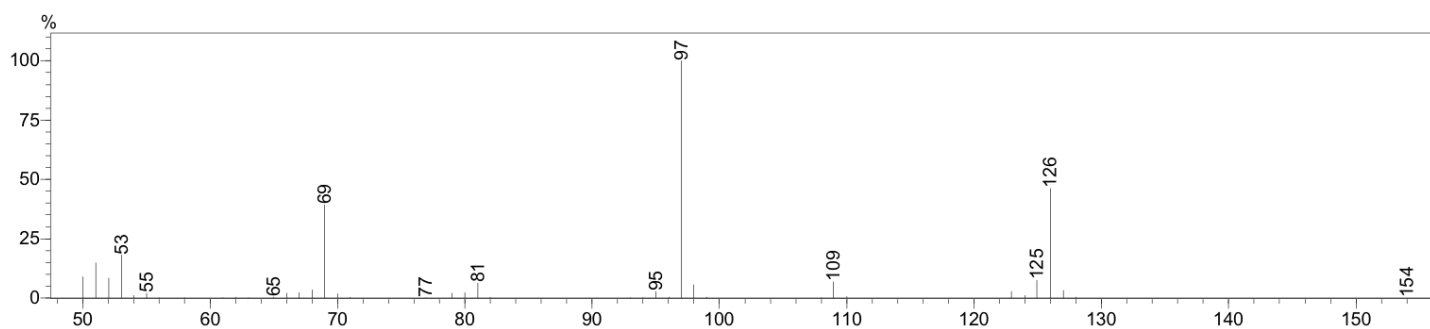


FIGURE A83 - GC-MS of peak #2 in the cromatogram of the EMF standard (identified as HMF).

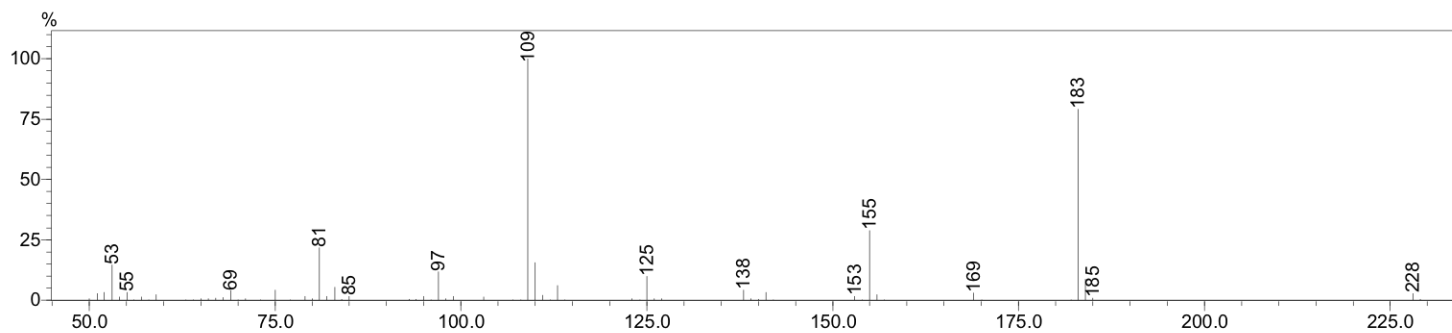


FIGURE A84 - GC-MS of peak #3 in the chromatogram of the EMF standard (identified as EMF).

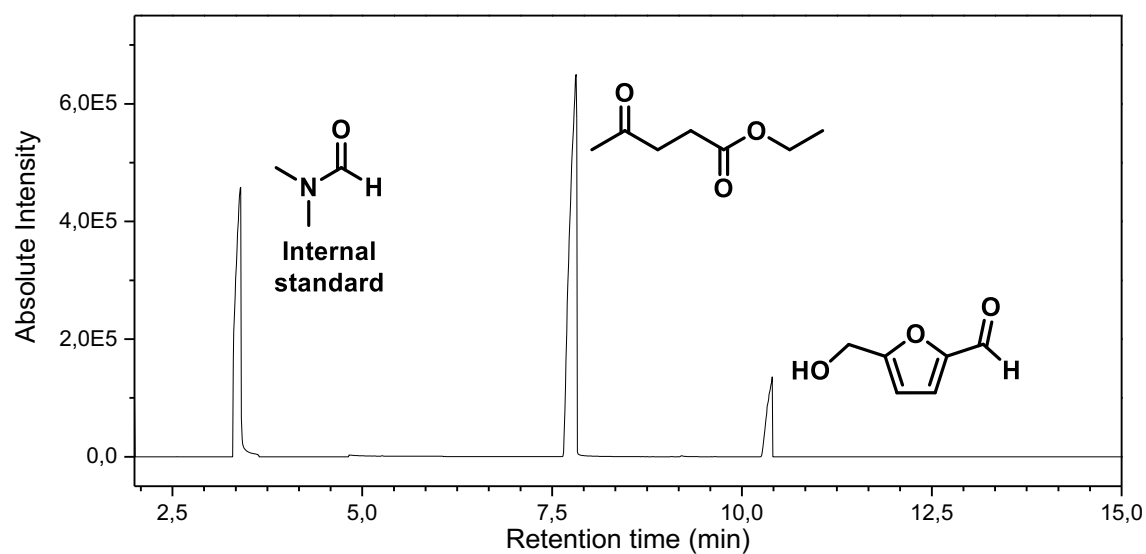


FIGURE A85 – GC- MS chromatogram of the reaction for the conversion of fructose to ethyl levulinate in ethanol at 170°C using 75 mg of catalyst.

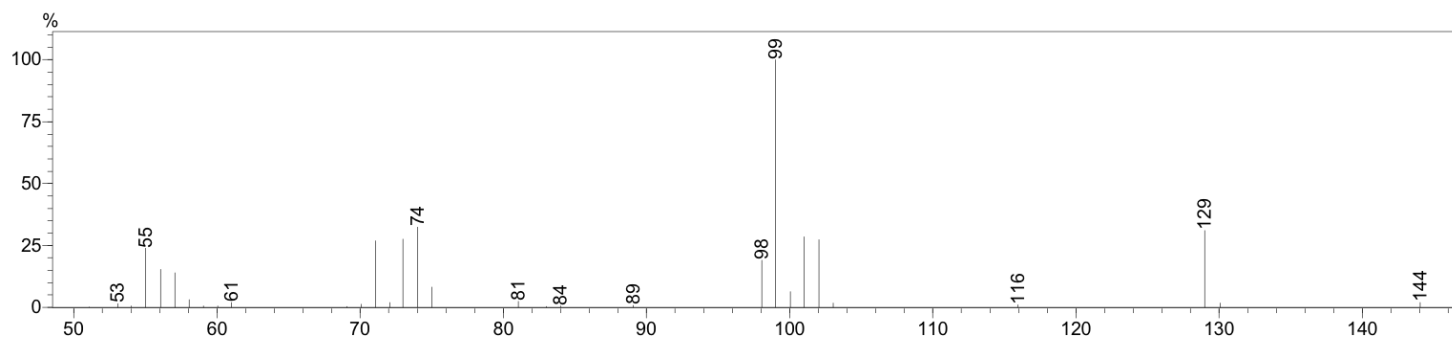


FIGURE A86 - GC-MS of peak #2 in the chromatogram of the reaction for the conversion of fructose to ethyl levulinate in ethanol at 170°C using 75 mg of catalyst.

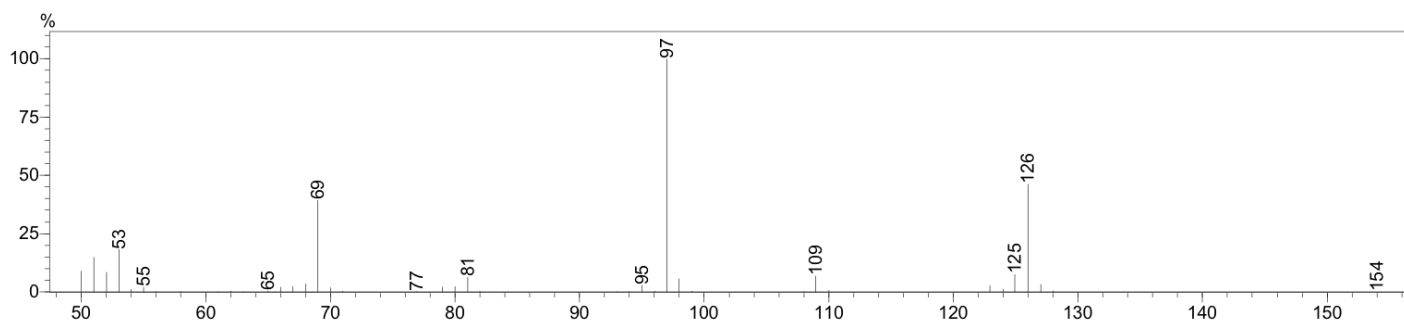


FIGURE A87 - GC-MS of peak #3 in the chromatogram of the reaction for the conversion of fructose to ethyl levulinate in ethanol at 170°C using 75 mg of catalyst.